On the Coarsening of Immiscible Polymer Blends with Cocontinuous Morphology

A DISSERTATION
SUBMITTED TO THE FACULTY OF THE GRADUATE SCHOOL
OF THE UNIVERSITY OF MINNESOTA
BY

Carlos René López-Barrón

IN PARTIAL FULFILLMENT OF THE REQUIREMENTS
FOR THE DEGREE OF
Doctor Of Philosophy

December, 2009

© Carlos René López-Barrón 2009
ALL RIGHTS RESERVED

Acknowledgements

I want to express my gratitude to my advisor, Chris Macosko, for his guidance, enthusiasm and encouragement during the last five years. All what I learned from him, not only academically but in ways to do research, is priceless.

I also want to thank to the many people who contributed to the success of this dissertation in different ways. Thanks to Joel Bell, who introduced me into the topic of cocontinuous blends. Yutaka Miura for his help on the synthesis of the fluorescent monomer. Kwanho Chang and Professor David Morse for providing the theory used to explain the effect of block copolymers on the coarsening of my blends. Randy Ewoldt for helpful discussions on the rheology of my blends during LAOS. To the other members of Macosko group for many interesting discussions on different research topics. Thanks also to the undergraduates working under my mentorship, including Kate Dennehy and Yessica Lie, for their dedication and enthusiasm in the lab. There are also several others without whose expertise this research would have taken quite longer, including Jerry Sedgewick at BIPL, who helped me a great deal in obtaining the first confocal images, and Ravi Chityala at the Minnesota Supercomputer Institute, who helped with the 3D-imaging procedures. Beyond academic and technical help, I treasure the many friendships developed over the past years; especially those of Mike (Castro), Doene, Luca, Hyunwoo, Zhengzi, Dawud (and the soccer team), without whom graduate school would not have been as enjoyable.

Particularly, I want to thank my Mom and Dad for their constant encouragement and faith in me from the early years. Their teachings on personal growth and perseverance have led me to this point of my career. Gracias Ma y Pa. Last but not least, I want to thank Yeny, for her enormous support during these years. She and my kids, Cristobal and Sofia, made this journey very enjoyable. You guys make my life complete.

Dedication

to Yeny, Cristobal and Sofia

and

to my parents

Abstract

Cocontinuous blends are used in a number of applications, including porous media for filtration, dessicant entrained polymers and substrates for drug delivery devices. A major drawback of these materials is that they are thermodynamically unstable, which implies that their morphology evolves into coarser structures when they are above their glass transition (or melting) temperatures. The mechanisms involved in the coarsening process are not fully understood yet.

Three aspects of the coarsening process were addressed in this work: (1) thorough characterization of the microstructure during coarsening via the implementation of novel 3D imaging techniques, (2) modification of interfacial properties via addition of block copolymers in order to hinder the coarsening, and (3) determination of the connection between morphology and viscoelastic response during the coarsening process.

Laser scanning confocal microscopy (LSCM) was used to image fluorescently labeled polystyrene (FLPS)/styrene-ran-acrylonitrile copolymer (SAN) blends. A methodology to obtain 3D micrographs of the blends and analyzed them to extract information of the geometry (size and local curvatures), topology (connectivity) and anisotropy (normal vectors) was implemented. From the analysis of the time evolution of the size and local curvature of the interface, two regimes of coarsening were identified: an early regime, where the characteristic size grows linearly with time and the interface evolves in a self-similar manner, and a late regime where the surface growth is neither linear nor self-similar. The measured decrease of the interface curvature was used to explain this regime transition.

Symmetric diblock copolymers (BC) made of polystyrene (PS) and polymethyl methacrylate (PMMA) were used to compatibilize the blends. A dramatic decrease in the rate of coarsening was observed after adding just 1% of BC. The stabilization

was particularly good for BC with an intermediate molecular weight. This result was explained with a theory based on the equilibrium between micelle dissolution and formation and adsorption and desorption of BC from the interface.

Small amplitude oscillation measurements were performed on both the compatibilized and the non-compatibilized blends. A noticeable extra contribution to the elastic modulus was observed for all the blends with bigger values for the compatibilized blends. A decrease in the elasticity was observed during the coarsening of the blends. This was explained by the decrease in interfacial area. This decrease was slower for the blends with BC, which evinces stabilization of the microstructure.

In an attempt to find a quantitative relation between morphology and rheological response of these materials, a simplification for small deformation to the Doi-Ohta model [Doi, M.; Ohta, T. *J. Chem. Phys.* **1991**, 95, 1242] was proposed. A key parameter in Doi-Ohta's theory is the degree of anisotropy. In this work a method to compute the anisotropy tensor from the analysis of the 3D images was developed. Predictions from the simplification fit rheological data of blends with low interfacial tension in the late regime of coarsening, but failed in the early stage and for high interfacial tension blends.

Contents

List of Tables

List of Figures

Chapter 1

Introduction

Blending two or more existing polymers to produce materials of commercializable properties offers several advantages over developing new polymer molecules. Some of these include reduced research and development expenses, much lower capital related to the scale-up and commercialization and property profile combinations not easily obtained with new polymeric structures [1, 2, 3]. Two very important aspects of polymer blends are whether the blend is miscible or not, and if it is not, its morphology. Although more than 1600 "miscibility windows" has been identified for two, three or four component blends [4], immiscibility dominates the polymer blend technology.

Immiscible blends are characterized by the presence of at least two phases. The properties of these materials (e.g. mechanical strength, rheology, optical, dielectric and barrier properties) are determined by the component properties and the size, shape and spatial distribution of the phases (i.e. the *morphology*). Hence, control of polymer blends morphology has become an area of increasing interest to polymer scientist in the last three decades [5, 6, 7, 2, 1]. The morphologies obtained after mixing immiscible polymers can be classified into four basic categories: dispersed phases (i.e. matrix-droplet), fibrillar, lamellar and cocontinuous structures (see Figure 1.1).

The cocontinuous two phase morphology consists of two continuous and interconnected phases coexisting in a single volume, in such a way that if either of the two phase is extracted a sponge-like structure is obtained (see Figure 1.2). The interest in cocontinuous blends has recently increased because of the unique combination of the component properties unavailable for disperse structures [4, 1]. The patent literature,

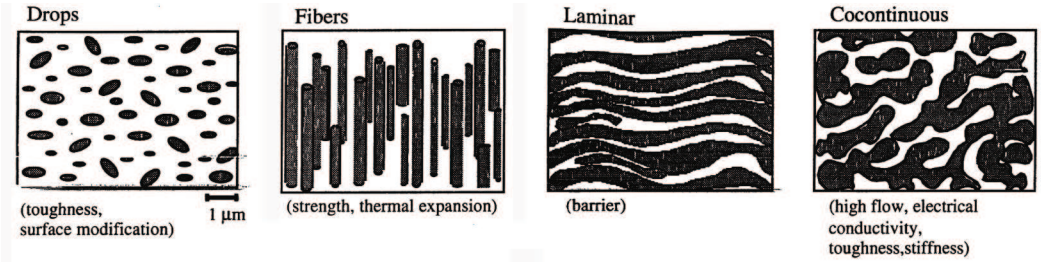

Figure 1.1: Schematic of morphologies produced by polymer-polymer melt blending (adapted from Ref. [6]).

for instance, reveals over 150 inventions related to cocontinuous structures [1]. The applications cover many areas, from enhanced mechanical properties to sophisticated applications such as :

- Porous material for filtration applications. For instance, extracted cocontinuous structures made out of solvent resistant polymers such as polyvinylidene (PVDF), polyamides and polyethylenes, can be used in chromatography and electrophoresis applications [8].

- Devices for controlled drug release. Favis and coworkers [9, 10] recently proposed a method to prepare controlled delivery devices based on cocontinuous polylactide (PLA)/polystyrene blends, after selective extraction of the PLA phase.

- Tissue engineered scaffolds, where two biodegradable polymers are combined into a cocontinuous structure in the prescence of an active substance (usually a drug) that is dispersed into the human body. Extracellular matrices of the body are mimicked by the device, providing scaffold with controlled biodegradation kinetics [11, 12].

- Conductive (and semiconductive) materials, where an inexpensive commodity polymer gives mechanical support to a rather expensive (and usually with poor mechanical properties) conductive materials. In order to assure both conductivity and mechanical integrity, both phases have to be continuous through the material.

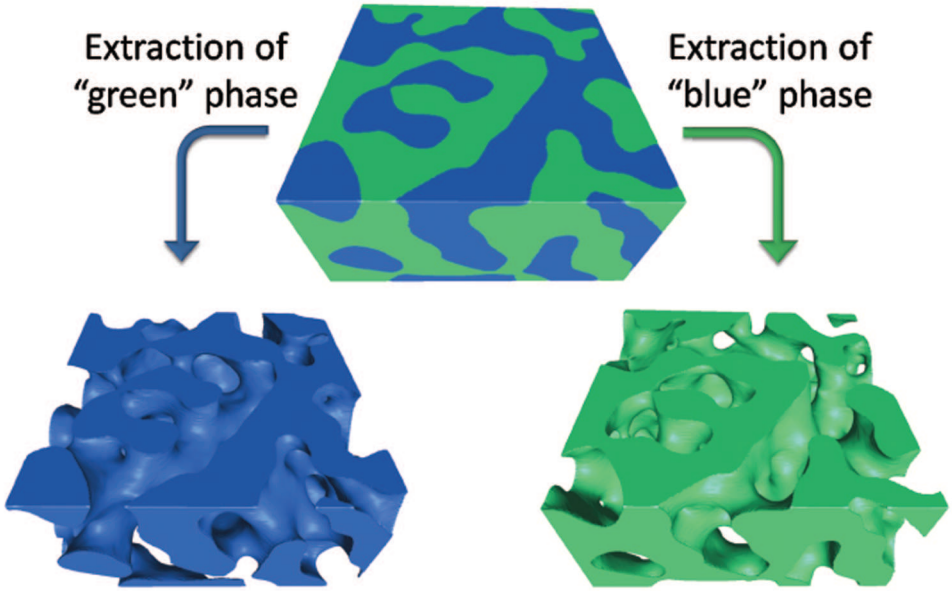

Figure 1.2: Schematic of cocontinuous structures before and after extraction of either of the two phases.

PermaStat®* and StatRite®† are examples of commercially available conductive blends.

- Desiccant entrained polymers for moisture adsorption in drug, food and electronic packaging [13]. These materials are prepared by compounding two polymers and a desiccant agent to create cocontinuous structures where the desiccant is dissolved in one of the polymer phases. The other phase gives mechanical stability to the blends.

From the examples listed above we can deduct that the usefulness of cocontinuous blends depends greatly on the morphology. Nevertheless, due to the connectivity of the domains, cocontinuous blends are intrinsically unstable. The interconnections in this structures are microscopically thin. This implies that, when the blend is above the

*RTP Co `http://www.rtpcompany.com/` Accessed on Sept 25th, 2009.

†The Lubrizol Corporation `http://www.lubrizol.com/EngineeredPolymers/` Accessed on Sept 25th, 2009.

transition (or melting) temperature of the components, a capillary pressure is always driving the liquid out of the thin interconnections [14]. This results in the evolution of the microstructure into coarser structures. Thus, it is plain that understanding the mechanisms involved in the coarsening process, as well as finding ways to control it or even stop it, is crucial in the design and improvement of these materials.

Although research in cocontinuous blends has been intense during the last ten years, there are very few studies on their stability [15, 16, 17, 18, 19]. To date, there is not a general model to predict the rate of coarsening during thermal annealing or the effect of a compatibilizer. In this thesis these two problems are attacked. It is well known that the addition of block copolymers (BC) decreases the rate of coarsening [20, 21, 22]. However the mechanisms of compatibilization is not well understood yet.

On the other hand, it has been shown that the presence of an interface has an effect on the viscoelastic modulus of immiscible blends [23, 24, 25, 26]. This effect is very well understood and modelled for systems with droplet-matrix morphologies [27, 23] but it is still an open question for the case of cocontinuous blends.

Doi and Ohta developed the only known model that relates rheology with morphology of two-phase liquids with complex interfaces [28]. Although this model was developed for mixtures of two liquids with equal volume, it has mostly been tested in dispersed systems [29, 30, 31], except for a single work by Vinckier and Laun [32] who compared experimental results of cocontinuous blends with predictions from Doi-Ohta's model. In this thesis a simplification to Doi-Ohta's model is proposed to account for small amplitude oscillatory shear (SAOS) measurements.

1.1 Overview

The system chosen to study the stability, BC effect and rheology of cocontinuous blends was the blend made of fluorescently-labeled polystyrene (FLPS) and styrene-ran-acrylonitrile copolymer (SAN). These two polymers have very close refractive indices, which makes their blends transparent. Transparent blends are necessary for the microscopy method used throughout this thesis, namely, three dimensional laser scanning confocal microscopy (3D-LSCM).

3D microscopy present several advantages over traditional 2D imaging techniques,

such as accurate measurement of interfacial area, measurement of interfacial curvature and normal vector fields (not obtainable from 2D images). Jinnai and coworkers [33, 34, 35] pioneered in the analysis of interface curvature of partially miscible blends during phase separation using 3D microscopy. Vorhees and coworkers used the methods developed by Jinnai et al. to analyse the microstructure of of metal alloys during topological transitions [36, 37, 38]. In this thesis I followed similar approach as Jinnai to analyse the microstructure of immiscible FLPS/SAN blends.

In Chapter 3 the method to obtain confocal images, 3D recontruction and image analysis are detailed. In the same chapter, a new algorithm to compute local curvatures, namely, the coordinate transformation (CT) method, is implemented and used throughout this thesis. The CT method is tested for accuracy in Appendix A, using a model interface (i.e. the Gyroid surface [39]).

The coarsening of blends with different interfacial tension (Γ) is studied in Chapter 4. The measurement of Γ is described in Appendix C. Two regimes of coarsening were observed and compared to classical theories of spinodal decomposition [40, 14] and to a recent model of coarsening based on contribution of the bending energy to the interfacial tension given by Scholten et al [18]. Due to the failure of these models to explain both growth regimes, a new model based on the evolution of the local curvatures is proposed here, with encouraging results.

The effect of symmetric block copolymers made of polystyrene and polymethylmethacrylate (PS-b-PMMA) on the stability of FLPS/SAN blends were studied in Chapter 5. In general the coarsening was hindered by the addition of BC with better results with higher molecular weights and higher compositions. These results were explained in light of a new theory developed by Morse and Chang [41, 42], which is based on dynamic equilibrium between dissolution and formation of micelles and adsorption and desorption of BC from the blend interface. Results from two other systems were studied by Bell [22] supported the theory as well. These systems are polystyrene(PS)/ high density polyethylene (HDPE) compatibilized with PS-b-PE and PS/PMMA compatibilized with PS-b-PMMA, and are presented here for completeness.

Chapters 6 and 7 present a detailed study of the relation between viscoelastic response morphology of the non compatibilized and compatibilized blends, respectively. These relations were studied after the mixing process and during coarsening. Non

compatibilized 50/50 blends with different Γ and viscosity ratio (p) were considered in Chapter 6. For the case of compatibilized blends (Chapter 7) a model system with p values in the order of 1 and relatively low Γ was used, but with three different compositions. All these measurements were performed under small amplitude oscillation (SAOS) measurements. In addition, Appendix D gives preliminary results of the rheology of cocontinuous blends during oscillatory measurements under large amplitudes (LAOS).

Finally a summary of this thesis and recommendations for future work in this area are given in Chapter 8.

Chapter 2

Materials Synthesis and Characterization

2.1 Introduction

The polymers used throughout this research were fluorescently labeled polystyrene (FLPS) and styrene-acrylonitrile copolymer (SAN). These two polymers were chosen due to their closeness in refractive index, which makes their blend be transparent. Transparency is indispensable for the 3D-microscopy technique used in this work, i.e. laser scanning confocal microscopy (LSCM).

Even when polystyrene and SAN are commercial available, I decided to synthesize both polymers for several reasons, to wit

1. LSCM requires that at least one of the phases emits fluorescence after being excited by a coherent light emitted by the laser system (excitation source) [43, 44]. Therefore a fluorescent dye needs to be added to one of the phases. To assure that the dye is entirely in the fluorescent phase, it is desirable that it is part of the molecule forming that phase. That is why, in this work, styrene was polymerized with a small quantity of a fluorescent monomer to produce FLPS.

2. One of the determinant parameters for the coarsening of cocontinuous blends is the interfacial tension (Γ) [14, 17, 40, 45]. By changing the acrylonitrile content in the SAN, the interfacial tension between FLPS and SAN can be systematically

varied. Three SAN with different AN content were synthesized to study the effect of Γ in the coarsening.

3. Another parameter that affects the formation and stability of cocontinuous blends is the viscosity ratio ($p = \eta_{FLPS}/\eta_{SAN}$) [19, 46]. Three FLPS with different molecular weight were synthesized to study the effect of p in the coarsening. One of them was designed to nearly match the viscosity of the SAN copolymers, i.e. to have $p \sim 1$.

2.2 Polymer synthesis

Both FLPS and SAN were synthesized via free radical polymerization in toluene (30 %vol solution) at 60 °C with azobisisobutyronitrile (AIBN) as initiator. Styrene (S) and acrylonitrile (AN) were both supplied by Aldrich (with 99 % purity). The monomers were freed from inhibitor by shaking twice with 10 % sodium hydroxide solution, washing three times with distilled water, drying over calcium chloride and distilling under reduced pressure. The synthesis of anthracenylmethyl methacrylate (a-MMA) is described in detail in the following section. AIBN was recrystallized from methanol twice and vacuum-dried before used. Toluene solvent (99.8 %, Aldrich) was used as received without further purification.

Solutions containing toluene, 30 %vol of monomer and recrystallized AIBN were added to a three liter three-neck round-bottom flask equiped with a thermometer, a condenser and a mechanical stirrer. The flask was put in a bath with controlled temperature. Polymers with different molecular weights and AN content were prepared by changing the amount of initiator and AN in the formulation. The molar ratios between styrene and total monomer ($f_S = [S]/[M]; [M] = [S] + [AN]$) and between AIBN and monomer ($[AIBN]/[M]$) for all the polymers synthesized are shown in Table 2.1. 1 % of a-MMA was added to the solution for the polystyene synthesis. The reaction time for the polystyrene synthesis was 6 hrs, while for the SAN the reaction was terminated before the conversion reached 10 % to avoid composition drift*. The conversion was

*A set of SAN copolymers previously synthesized with a conversion of 50 % displayed phase separation evidenced by an extra contribution in the elastic modulus at low frequencies (results not shown here)

monitored by gravimetry. The polymers were precipitated in methanol and purified by 2X dissolution in toluene and precipitation in methanol. The final products were dried in a vacuum oven at 60 °C for at least one week.

Table 2.1: Formulations used in the polymer synthesis.

Polymer	f_S	$[AIBN]/[M]$
FLPS40K	1	0.00750
FLPS120K	1	0.00106
FLPS200K	1	0.00035
SAN10	0.96	0.004
SAN20	0.91	0.004
SAN30	0.81	0.004

2.2.1 Synthesis of fluorescent methacrylate monomer

In order to incorporate fluorescence groups into polystyrene polymer chains, a fluorescent monomer was prepared by a single step reaction, illustrated in Figure 2.1. Anthracenylmethyl methacrylate (2) was prepared by derivatization of commercially available 9-anthracenemethanol (1) with methacryloyl chloride in the presence of pyridine in high yield (87 %), following the procedure described by Moon et al.[47]. Briefly, 9-anthracenemethanol (25g), 4-dimethylaminopyridine (DMAP, 100 mg), and a stir bar were placed in a round-bottom flask. Then, dry methylene chloride (250 ml), pyridine (14.2 g), and toluene were sequentially added, and the flask capped. After cooling the flask in an ice water bath, methacryloyl chloride (13.8 g) was added dropwise via syringe. After complete addition the suspension turned to an homogeneous yellow solution. It was allowed to stir for 1 hr. The flask was put in a rotary evaporator to remove most of the solvent. The residue was loaded on a silica gel column and eluted with hexanes/EtOAc (3:1) to fractionate the product (2). The final product was then concentrated by rotary evaporation under vacuum.

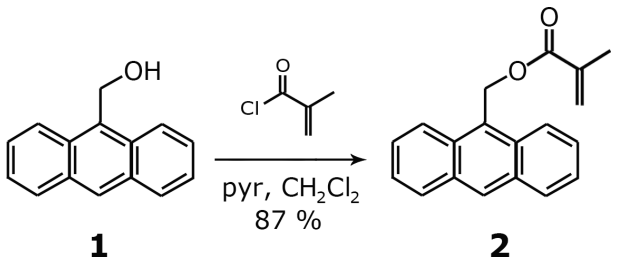

Figure 2.1: Synthetic pathway for the preparation of anthracenylmethyl methacrylate (adapted from [47]).

2.3 Polymer characterization

The properties of the polymers synthesized here are shown in Table 2.2. Their measurements are detailed below.

2.3.1 Molecular weight

Molecular weights were measured by gel permeation chromatography using polystyrene standards. Molecular weigh distributions of the polystyrenes and the SAN copolymers are shown in Figures 2.2 and 2.3, respectively.

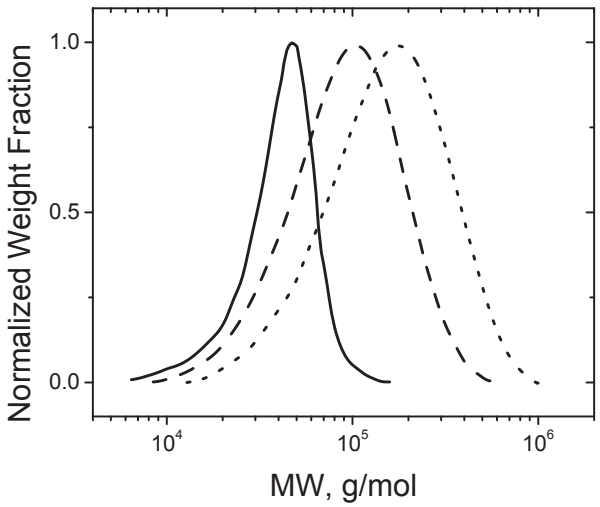

Figure 2.2: Molecular weight distributions of FLPS40K (—), FLPS120K (- -) and FLPS200K (· · ·) measured by GPC using PS standards.

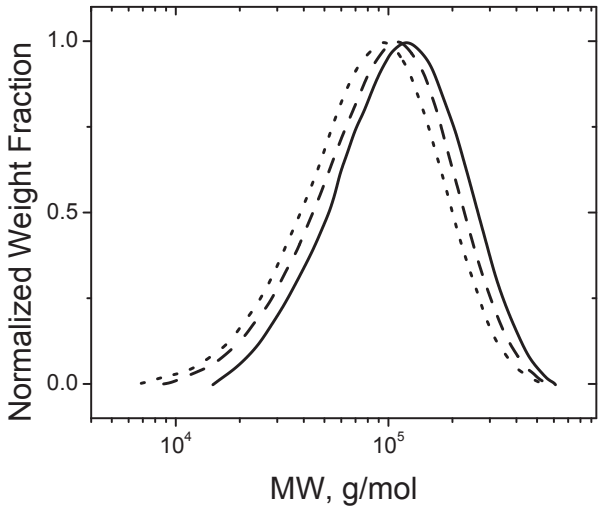

Figure 2.3: Molecular weight distributions of SAN10 (—), SAN20 (- -) and SAN30 ($\cdots$) measured by GPC using PS standards.

2.3.2 Rheological measurements

Dynamic tests of the materials were carried out under dry nitrogen atmosphere at 200 $^{\circ}C$ using a parallel plate ARES rheometer (TA Instruments) in a frequency range of 0.02 to 100 rad/sec. Disk shaped samples with 25 mm diameter and 1.5 mm thickness were pressed using a Wabash hydraulic press at 180 $^{\circ}C$ and subsequently dried at 95 $^{\circ}C$ under vacuum for 24 hours before the tests. Zero shear viscosity of the materials (shown in Table 2.2) was obtained by fitting frequency sweep data (Figure 2.4) with the Cross model. The elastic and viscous moduli as well as $\tan\delta$ are shown in Figure 6.1 (Chapter 6). Note that the viscoelastic properties of FLPS120 are very similar to those of the three SAN copolymers, which, as mentioned before, was one of the reasons to synthesize polystyrenes with specific molecular weight.

Table 2.2: Properties of polymers.

Polymer	M_W kg/mol	M_W/M_n	η_0 Pa-s	AN-content %	n_d
FLPS40K	42.6	1.42	93.1	- -	- -
FLPS120K	122	1.71	1485	- -	1.598 ± 0.001
FLPS200K	193	1.70	6838	- -	- -
SAN10	135	1.55	2110	9.50 ± 1.1	1.587 ± 0.002
SAN20	116	1.63	2376	19.3 ± 0.8	1.580 ± 0.001
SAN30	103	1.67	2510	28.4 ± 1.2	1.569 ± 0.003

2.3.3 SAN copolymer composition

Elemental analysis was done at Midwest Microlab, LLC (`http://www.midwestlab.com/`, accesed in August 28^{th}, 2009) using CHN analysis performed via combustion at 990 C with an elemental analyzer Model 440 CHN/O/S (Exeter Analytical). By determining the ratio of nitrogen to carbon atoms in the SAN it is straightforward to estimate the ratio betwen AN and styrene (see Figure 2.5). 3 samples per polymer were analyzed for statistical significance.

2.3.4 Refractive index

As discussed above, the reason I chose the system PS/SAN was because their refractive indices are very close. Thereupon, the blends prepared with these blends are expected to be transparent. Figure 2.6 show pictures of two different blends, namely, polymethyl methacrylate (PMMA)/SAN20 and FLPS120K/SAN20. Note that the PMMA/SAN20 blend, having a refractive index difference of only 0.1, is completely opaque, while the FLPS/SAN20 with refractive index difference of 0.02, is transparent.

The refractive index of the polymers was measure following the procedure described in the ASTM standard test method D542-95 (for index of refraction of transparent organic plastics). An Abbe refractometer (Bausch Lomb Abbe-3L Refractometer) was

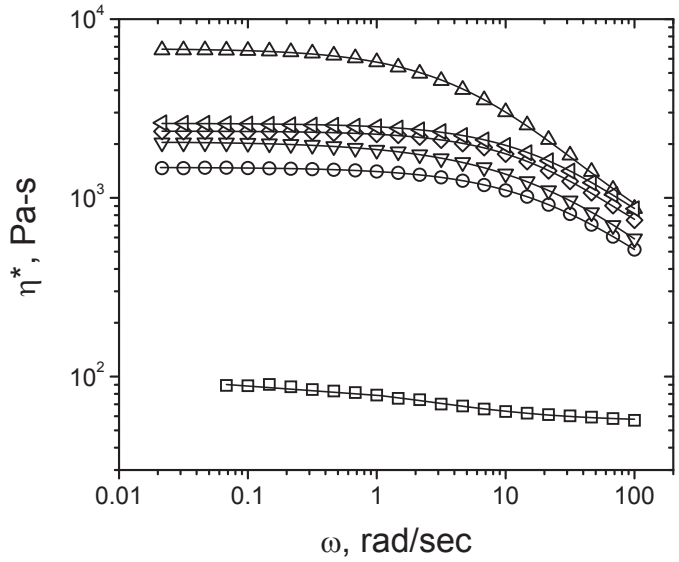

Figure 2.4: Complex viscosity versus frequency for FLPS40K (□), FLPS120K (○), FLPS200K (△), SAN10 (▽), SAN20 (◇) and SAN30 (◁), measured at 200 °C. The solid lines depict Cross model fittings.[48]

used for this test. Specimens with a flat surface measuring 6.5 by 13 mm and a height of 3 mm were prepared by molding and cutting the dryed polymers. The flat surface and a second edge surface perpendicular to the first and on the end of the specimen were polished using fine (No. 000) emery paper followed by a polishing rouge compound suspended in water. A small drop of hydrogenated terphenyl 1-bromonaphthalene (refractive index liquid, $n_d^{25°C} = 1.6200 \pm 0.0002$, Cargille Labs) was placed on the flat surface of the specimen. Then, the specimen was placed in firm contact with the prism

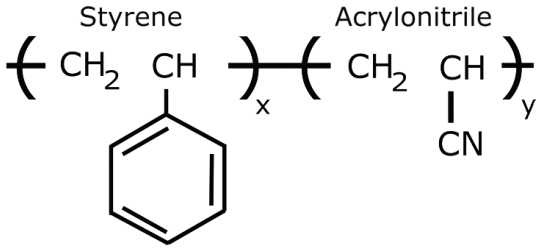

Figure 2.5: Formula of SAN copolymer. AN content ($= 100 \times x/(x+y)$) was measured by CHN analysis.

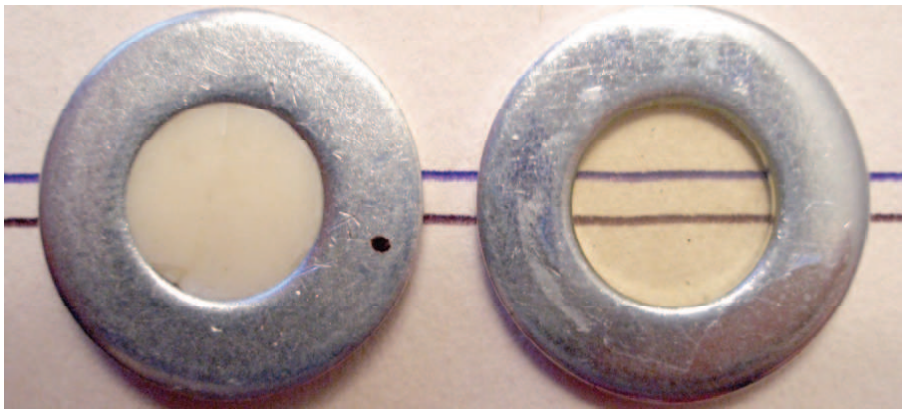

Figure 2.6: Pictures of PMMA/SAN20 and FLPS120K/SAN20 blends. Refractive index differences are, respectively, $|n_{d,PMMA} - n_{d,SAN20}| = 0.1$ and $|n_{d,FLPS} - n_{d,SAN20}| = 0.02$.

of the refractometer with the polished side of the specimen toward the light source. Thereafter, the index of refraction was determined in the same manner as specified for liquids (see [49]). Three specimens per polymer were tested.

Chapter 3

3D Image Analysis of Cocontinuous Structures*

3.1 Introduction

The properties of microstructured polymer blends are strongly influenced by their microstructure [5, 1, 2]. In two-phase blends, the interface between the phases has a non-zero curvature, indicating that an excess free energy is localized at the interface [50, 51]. The necessity to minimize the extra interfacial energy makes the blend thermodynamically unstable. The overall result is that the microstructure evolves into coarser structures (i.e. more planar interfaces) when the blend is above the glass or melt transition temperature of both components. Coarsening is most severe in cocontinuous morphologies where each phase is fully interconnected and coarsening is only slowed by high viscosity or low interfacial tension. Drops, on the other hand, especially if dilute, can be kinetically stable.

In order to understand the microstructure evolution and its relation with the macroscopic properties of the blends, we must be able to characterize the morphology. Two dimensional techniques, such as transmission electron microscopy (TEM) and scanning electron microscopy (SEM), have being extensively used to characterize phase-separated

*Reproduced in part with permission from "Characterizing Interface Shape Evolution in Immiscible Polymer Blends via 3D Image Analysis" Lopez-Barron, C.R.; Macosko, C.W., *Langmuir*, **2009**, 25 (16), 9392–9404. Copyright 2009 American Chemical Society.

structures [1, 46]. 2D images can be used to qualitatively characterize the morphology and to *estimate* the volume fraction and the interfacial area per unit volume [20] if adequate stereological methods are used [52]. These methods are, however, difficult to apply to complicated geometries.† Additionally, the lack of the third dimension can cause misinterpretation of the true morphology [53], e.g. confusing a transversally cut rod with a droplet. The analysis of 3D images solves these drawbacks. Furthermore, 3D images contain information of the interface curvature, which is not available from 2D cuts.

In this study, the morphology of FLPS120K/SAN20 blends was characterized during coarsening using confocal microscopy coupled with 3D reconstruction techniques and differential geometry. Geometrical and topological parameters of the interface were computed via the coordinate transformation (CT) method. The CT method was, for the first time, implemented to analyse 3D reconstructed images.

3.2 3D imaging techniques

Several techniques have been developed to attain 3D visualization of structured blends [53, 36, 54, 55, 56, 57, 58, 59, 60, 61, 62, 63, 35, 64, 65]. Alkemper and Voorhees developed a semi-automatic serial sectioning technique [36] to obtain optical micrographs of different sections and reconstruct the 3D microstructure of Pb-Sn alloys [54]. Transmission electron microtomography (TEMT) has been developed to reveal 3D-structures of block copolymer systems [55, 57, 58, 66]. More recently, Sengupta and Noordermeer [59] used TEMT to visualize three-dimensional morphology in the thermoplastic elastomer blends made of polystyrene-block-(ethylene-co-butylene)-block-polystyrene/poly(propylene)/oil.

X-ray microtomography [60, 53], x-ray phase tomography [61] and three-dimensional nuclear magnetic resonance (NMR) imaging [62] were used to visualize opaque samples with a comparatively large field of view. Pyun et al. imaged the cocontinuous structure of a blend of polystyrene and high density polyethylene with x-ray microtomography[53]. They showed that, as coarsening proceeded, the specific interfacial area obtained from

†Appendix B describe a study where a number of stereological estimators were tested, for the first time, in cocontinuous morphologies.

the analysis of the reconstructed 3D images exceeded the calculated from 2D images obtained with SEM. However they did not apply any stereological correction to the 2D measurements (see Appendix A).

3.2.1 Laser scanning confocal microscopy

Laser scanning confocal mcroscopy (LSCM) is a technique for obtaining high-resolution optical images with depth selectivity [44]. The key feature of confocal microscopy is its ability to acquire in-focus images from selected depths, a process known as optical sectioning. Images are acquired point-by-point and reconstructed with a computer algorithm, allowing three-dimensional reconstructions of topologically-complex objects. For opaque specimens, this is useful for surface profiling, while for non-opaque specimens, interior structures can be imaged. LSCM is a very suitable technique since it does not require time-consuming sample preparation and the image acquisition is fast and non-destructive. However, it has two major drawbacks: one is that at least one of the phases has to fluoresce in order to attain a good contrast in the images; and second is that the sample has to be transparent in order to provide an adequate depth of field [43].

Figure 3.1 shows the basic setup of a confocal microscope. In order to get very high intensities, a laser is used to provide the excitation light. The light (blue) reflects off a dichroic mirror, which directs it to an assembly of vertically and horizontally scanning mirrors (not shown). These motor-driven mirrors scan the laser across the specimen. The dye in the specimen is excited by the laser light and fluoresces. The fluorescent (green) light is descanned by the same mirrors that are used to scan the excitation light (blue) from the laser and then passes through the dichroic mirror. Thereafter, it is focused onto the pinhole. The light that makes it through the pinhole is measured by a detector such as a photomultiplier tube. In confocal microscopy, there is never a complete image of the specimen because at any instant only one point is observed. Thus, for visualization the detector is attached to a computer, which builds up the image one pixel at a time [67].

Verhoogt et al. pioneered in the use of laser scanning confocal microscopy (LSCM) to visualize polymer blends [63]. They compared images of the microstructure of the blend made of SEBS block copolymer and poly(ether ester) from LSCM and SEM. Jinnai and coworkers have extensively utilized LSCM to visualize bicontinuous structures generated

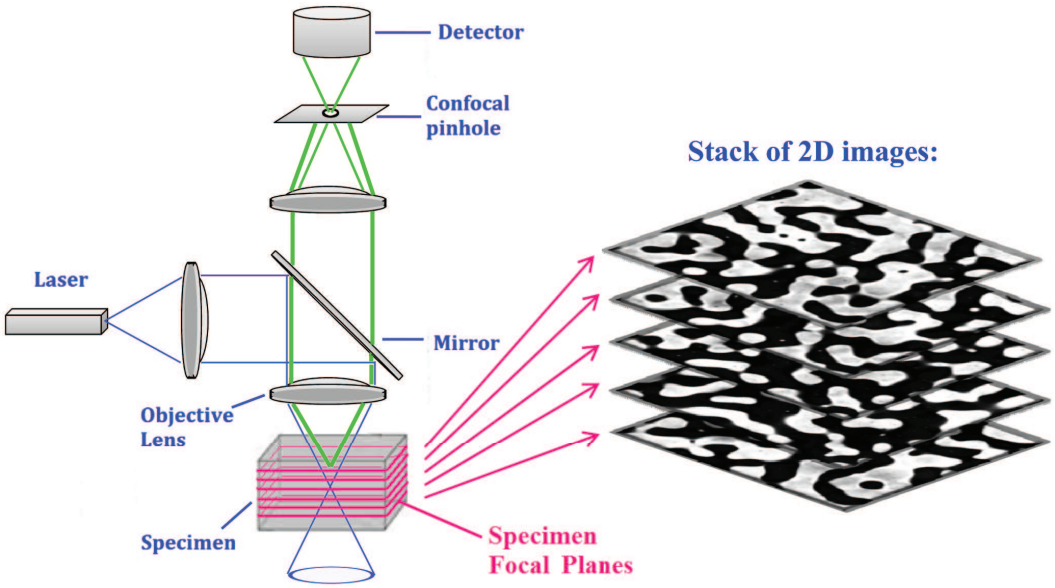

Figure 3.1: Schematic of LSCM and stack of 2D images obtained at different focal planes into the specimen.

during the late stage of spinodal decomposition of binary mixtures of deuterated polybutadiene/polybutadiene [64, 34, 35] and of poly(styrene-ran-butadiene)/polybutadiene [56, 65, 33, 35]. In the present work we extensively used LSCM to visualize immiscible blends with cocontinuous morphologies at different coarsening stages.

3.2.2 Interfacial curvature measurements

Jinnai and coworkers developed two methods to quantify the curvature between the two phases by applying differential geometry to the 3D reconstructed images: (i) using a parallel surface method, they measured the area-average of the mean (H) and Gaussian (K) curvatures [33], and (ii) using a sectioning and fitting (SF) method, they were able to measure the local values of H and K [34]. In this chapter we present a methodology to characterize the interface between the two phases of an immiscible polymer blend made of fluorescently labeled polystyrene (FLPS) and styrene-ran-acrylonitrile copolymer (SAN). We analyzed confocal images following the approach of Jinnai and coworkers to study the local shape of interfaces in spinodal decomposed systems[34, 35].

Unlike the parallel surface method, used by Jinnai et al. [34] and Voorhees and coworkers [54] a simplified method to calculate the local mean and Gaussian curvatures base on surface patch parameterization is introduced here. LSCM is used to study for the first time the local shape of interfaces formed in immiscible polymer blends after mechanical mixing. The time evolution of the local shape and topology of such interfaces are analyzed for both a symmetric (50/50 w/w) and a non symmetric (35/65 w/w) FLPS/SAN blend. From the interfacial metrics two different coarsening regimes were identified for the symmetric blend. For the non-symmetric blend a transition from cocontinuous to matrix-droplet morphologies (pinch-off) was observed and quantified with the geometry and topology of the interface.

3.3 Experimental methods

3.3.1 Materials.

As mentioned before, the use of LSCM for 3D image reconstruction is restricted to transparent and fluorescent samples. For that reason a model system was chosen for this study, namely the transparent blend made of a fluorescently-labeled polystyrene (FLPS) and styrene-ran-acrylonitrile copolymer (SAN). Specifically, the polymers used in this part of the thesis are FLPS120K and SAN20, because their closeness in viscoelastic propeties (see Figures 2.4 and 6.1) make them ideal to form cocontinuous structures during mixing [68]. The synthesis and key properties of these polymers are described in Chapter 2 (see Table 2.2). The interfacial tension between FLPS120K and SAN20, measured by the breaking thread method and a rheological method (see Appendix C), is 0.86 ± 0.14.

3.3.2 Blend preparation and annealing

Figure 3.2 shows an schematic of the blending and annealing processes. FLPS/SAN blends were prepared in a recirculating, conical twin-screw extruder (DACA Instruments) at 100 rpm and at a temperature of 180 °C for 10 minutes with N_2 purge. The blend composition was 50/50 and 35/65 (w/w) FLPS/SAN. After mixing, the blends were extruded out of the mixer and were cut into small pellets of about 3.5 mm diameter

and 2 mm long. The pellets were placed between two glass slides with a ring spacer of about 1 mm thick. The samples were annealed under N_2 at 200 °C. The annealing process was performed in a hot press, by just touching the glass slides with the press plates, but without applying any pressure. These samples were taken out of the press after different times and plunged into water to freeze the morphology.

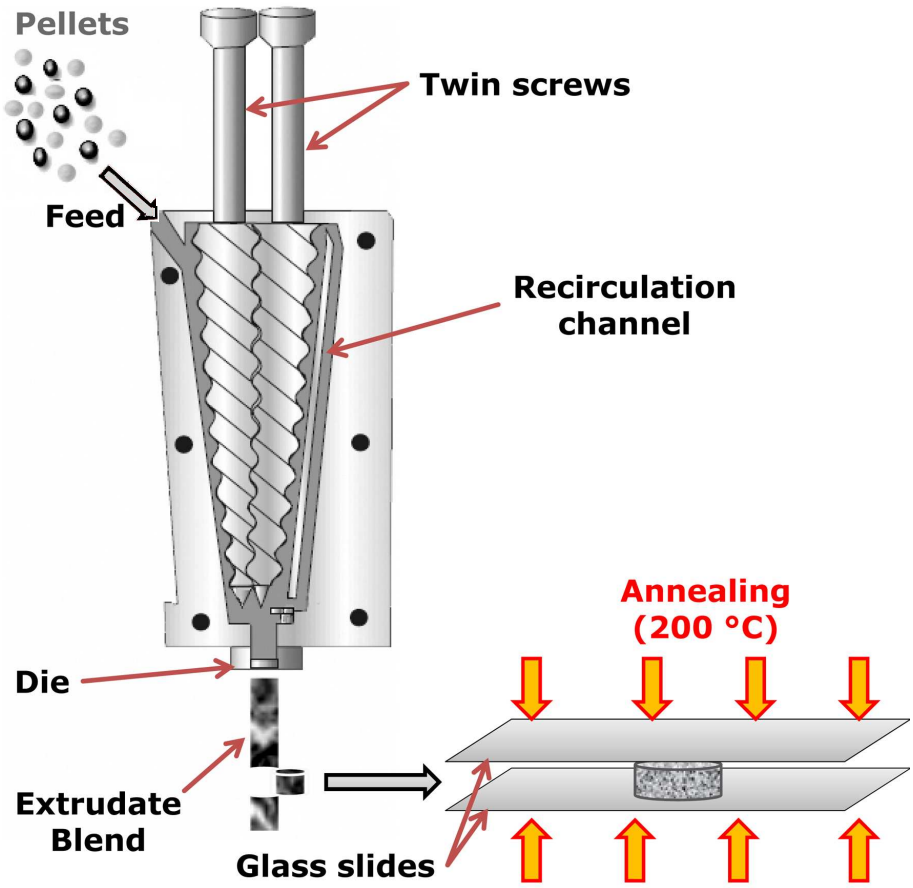

Figure 3.2: Schematic of the blending and annealing processes. The diagram of DACA MicroCompounder is shown on the left. After mixing, the blends were annealed at 200 $^{\circ}C$ in between two glass slides to generate a flat surface.

Laser scanning confocal microscopy (LSCM). The annealed samples were observed in a LSCM (Olympus FluoView 1000) at room temperature with an incident laser beam of wavelength of 405 nm. Two oil-immersed 40× or 20× objectives (LCPlanFl,

Olympus) with numerical apertures (NA) of 0.6 and 0.4, respectively, were used. The 40× and 20× objectives were used to visualize features smaller and bigger than about 30 μm, respectively. The acquisition wavelength was set by selecting a barrier filter (461 nm) to detect only fluorescence from the anthracene attached to the polystyrene. Hence, the FLPS phase was identified as the bright phase under the LSCM (see Figure 3.3). The laser beam was scanned in the lateral (x-y) plane generating 2D optically sliced images comprised of 512 x 512 pixels with an excellent depth resolution [‡] [69]. The objective was moved up the z-axis after each lateral plane scanning to obtain a series of 2D images with an increment $\Delta z \simeq 0.5\mu$m. About 100 2D image slices per sample were recorded at a distance of 20 to 120 μm away from the cover slip to avoid wall effects on the growth of the blend microstructure.

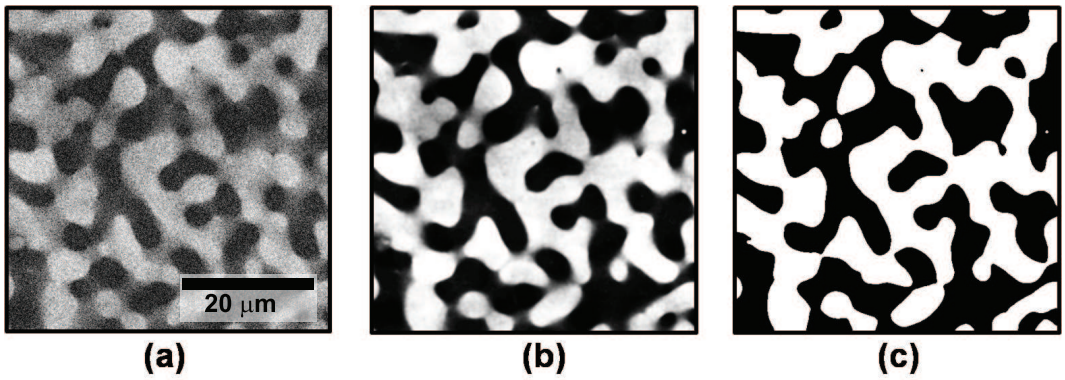

Figure 3.3: LSCM micrograph of FLPS/SAN: (a) before image processing, (b) after deconvolution, and (c) after thresholding. The bright and dark zones represent the FLPS and SAN phases, respectively.

[‡]The lateral (x-y) resolution can be calculated with the expression: $r_{lateral} = 0.61 * \lambda_{exc}/NA$, where λ_{exc} is the excitation wavelength and NA is the numerical aperture of the objective (see ref 69). Therefore, $r_{lateral}$ is 412 and 618 nm for the 40X and 20X objectives, respectively. These values are comparable with the z-resolution which is typically 500 nm for LSCM.

3.4 Image analysis

3.4.1 3D reconstruction

The 2D sliced images collected with LSCM were processed to reduce image degradation produced by noise and blurring. Out-of-focus blur was reduced by applying a deconvolution technique using the software Huygens (Scientific Volume Imaging - `http://www.svi.nl/`, accesed in October 28^{th}, 2009), which utilizes a model of blur based on the concept of three dimensional point spread function [70]. Noise was removed from the deconvoluted images by applying a series of image filters available in the software Adobe® Photoshop® [71]. The images were finally thresholded into binary images. Figure 3.3 shows the improvement of an image taken from the LSCM (Figure 3.3(a)), after deconvolution (Figure 3.3(b)) and after thresholding (Figure 3.3(c)). The thresholding criterion was that the ratio of area between the two phases (in the 2D images) equals the volume ratio. The series of thresholded images were stacked into a single file to create a 3D image. A non structuring meshing method based on the marching cubes algorithm [72] was applied on the 3D image to generate a triangular mesh representation of the interface. Figure 3.4(a) displays the interface between the two phases rendered using this method. Figure 3.4(b) shows a detail of the interface where the triangular mesh is evident. The number of triangles per image is of the order of 10^7. We used an IBM System x3950 to perform the rendering process. Figure 3.4(c) displays a *solid model* of the microstructure.

3.4.2 Surface geometry

Differential geometry applied on the triangular meshes was used to calculate the geometrical parameters of the interfaces, i.e. the specific interfacial area and the local curvature. The interfacial area (Q) per unit volume was obtained simply by adding the areas of all the triangles (A_i) forming the mesh and dividing the sum by the total volume of the sample (V), i.e.

$$Q = \frac{1}{V} \sum_{i=1}^{N} A_i, \tag{3.1}$$

where N is the total number of triangles.

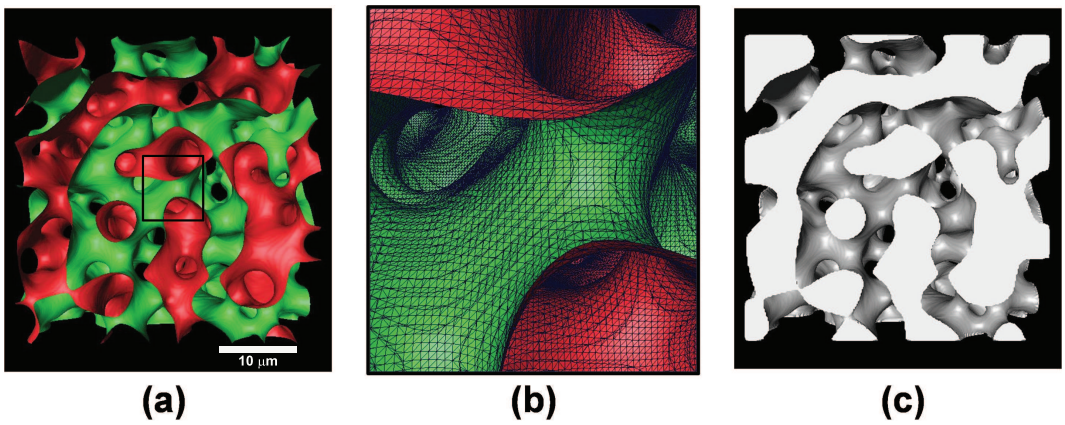

Figure 3.4: Rendered 3D microstructure for FLPS/SAN blend: (a) Interface between blend phases (red and green facing towards the FLPS and SAN phases, respectively), (b) detail of the interface (from the black square in the center of (a)) showing the triangular mesh, and (c) solid model of the microstructure (the solid and the transparent parts represent the FLPS and SAN domains, respectively).

Figure 3.5 illustrates the method used to determine curvature. The vector $\mathbf{v}_p$ is tangent to surface $\mathbf{M}$ at the point of interest (POI). The normal curvature $\kappa(\mathbf{v}_p)$ is a real number that measures how $\mathbf{M}$ bends in the direction $\mathbf{v}_p$. In other words, $\kappa(\mathbf{v}_p)$ is the curvature of the plane curve formed by the intersection of $\mathbf{M}$ with the plane passing through $\mathbf{v}_p$ meeting $\mathbf{M}$ perpendicularly. The so-called principal curvatures, i.e. κ_1 and κ_2, are the maximum and minimum values among all the normal curvatures [73]. Figure 3.6 shows a schematic of the principal curvatures of four surfaces. Note that the sign of each curvature depends on the direction the surface curves along the path given by the corresponding tangent vector, i.e. it is positive if the path is concave from one side, negative if it is convex and zero if it is straight.

The shape of the surface $\mathbf{M}$ can be locally determined by the values of the principal curvatures on the point of interest (POI) or, alternatively, by the values of the mean (H) and Gaussian (K) curvatures, defined as:

$$H = \frac{\kappa_1 + \kappa_2}{2} \tag{3.2}$$

and

$$K = \kappa_1 \cdot \kappa_2. \tag{3.3}$$

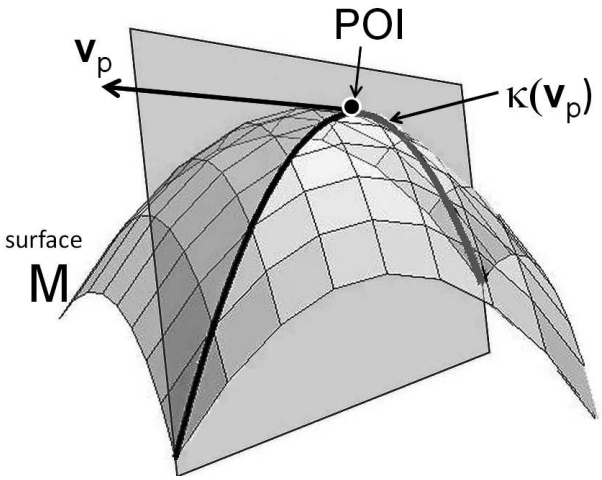

Figure 3.5: Schematic of a normal curvature of a surface M. The dark curve is generated from the intersection of surface $\mathbf{M}$ and a normal plane containing the tangent vector $\mathbf{v}_p$ at the point of interest (POI). The curvature of such a curve (normal curvature), $\kappa(\mathbf{v}_p)$, measures how $\mathbf{M}$ bends in the direction of $\mathbf{v}_p$.

The sign of the Gaussian curvature permits us distinguish four type of points on a surface: hyperbolic if $K < 0$ (i.e. κ_1 and κ_2 have opposite signs, see Figure 3.6(a)), elliptic if $K > 0$ (i.e. κ_1 and κ_2 have the same sign, see 3.6(b)), parabolic if $K = 0$, but $H \neq 0$ (i.e. exactly κ_1 or κ_2 is zero, see 3.6(c)), and planar if $K = 0$ and $H = 0$ (i.e. $\kappa_1 = \kappa_2 = 0$, see Figure 3.6(d)). Therefore, the complex interfacial shapes created in immiscible polymer blends can be quantified with the probability densities of the mean and Gaussian curvatures (defined below).

On the other hand, the quantification of the mean curvature is fundamental in the study of evolving interfaces. It is well known that there exists a jump in normal stress across any interface, given by [74]

$$\mathbf{n} \cdot \sigma_{\mathbf{1}} \cdot \mathbf{n} \; - \; \mathbf{n} \cdot \sigma_{\mathbf{2}} \cdot \mathbf{n} = \Gamma(\nabla \cdot \mathbf{n}), \tag{3.4}$$

were σ_1 and σ_2 are the stress tensors in either side of the interface, $\mathbf{n}$ is the unit vector normal to the interface and Γ is the interfacial tension. Note that the quantity $\Gamma(\nabla \cdot \mathbf{n})$ is the curvature force per unit area and $\nabla \cdot \mathbf{n}$ is twice the mean curvature of the surface. Hence, the tendency to minimize the curvature follows the necessity to minimize the difference in normal stress across the interface. In particular, static surfaces with gravity

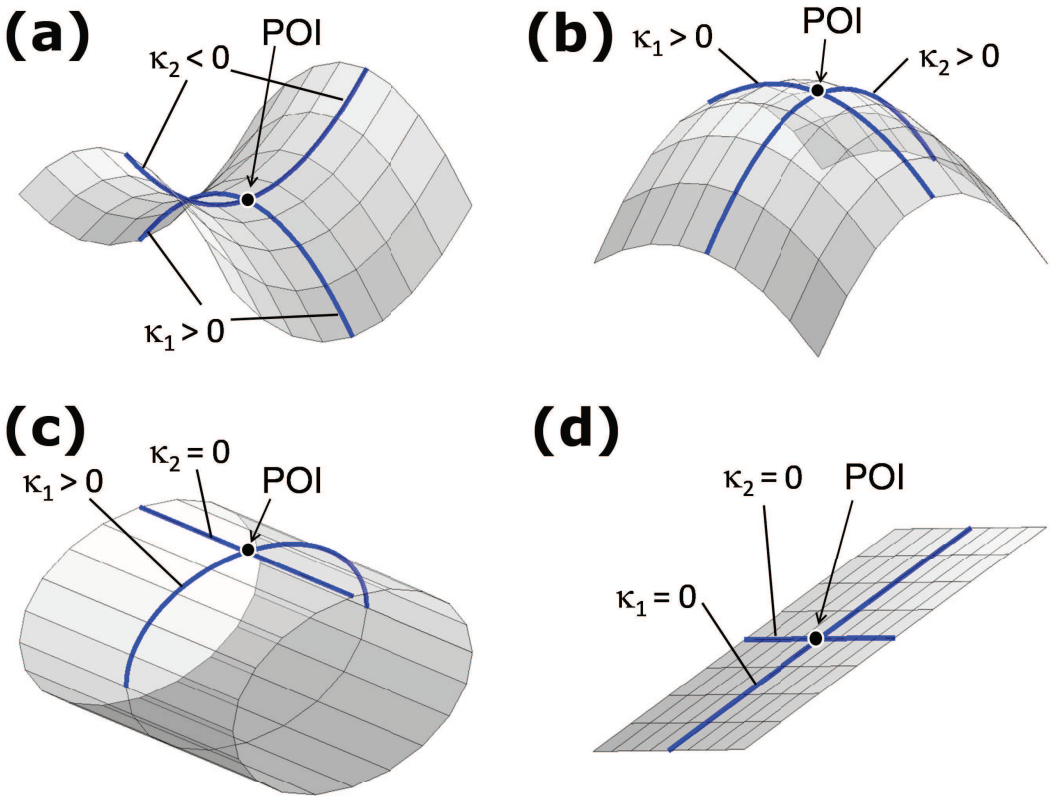

Figure 3.6: Principal curvatures of four different surfaces: (a) hyperbolic, (b) elliptic, (c) parabolic, and (d) planar.

absent have constant mean curvature, so that a minimal surface (defined as a surface where the mean curvature is zero everywhere) is a special and the most stable case of a static surface [50].

3.4.3 Surface topology

Additionally, the topology of surfaces is related to the area integral of the Gauss curvature, also known as the integral curvature, by the Gauss-Bonnet theorem [73]:

$$\begin{aligned} \iint_{Surf} K da &= 2\pi\chi \\ &= 4\pi(1-g), \end{aligned} \tag{3.5}$$

where χ and g are the Euler-Poincaré characteristic and the genus, respectively. These quantities are topological invariants of the surface, i.e. they depend only on the topology of the surface and not on its shape. For instance, the genus represents the number of holes or handles in the surface, provided the surface is closed. A sphere and any other polyhedron have no holes and thus $g = 0$. A torus and a coffee-cup have one handle and both will have a genus of one. Attaching handles (or digging holes) one by one results in an increase of g by 1. Infinitely-connected interfaces such as those found in bicontinuous structures will have a genus equal to infinity. Consequently, the importance of the Gaussian curvature in the characterization of the interface is paramount.

3.4.4 The coordinate transformation method

A variety of methods have been developed to calculate the mean (H) and Gaussian (K) curvature from 3D images. Jinnai, et al. [35], and Krammer et al. [54] used the parallel surface method to calculate the curvatures of spinodally decomposed systems and metal alloys, respectively. Stokely and Wu [75] described five different methods based on surface patch parametrization. One of these methods, which was proposed by Sander and Zuker [76], is the coordinate transformation (CT) method. This method was used here and roughly consists in transforming the coordinates of all surface patch points (x, y, z) into $(u, v, h(u, v))$. The surface patches are approximated using the quadratic

form:

$$\begin{aligned} S(u,v) &= (u,v,h(u,v)) \\ &= (u,v,au^2+2buv+cv^2). \end{aligned} \tag{3.6}$$

The usefulness of the local parameterization of the surface is evident in the calculation of H and K. According to differential geometry the coefficients of the first and second fundamental forms of a regular patch described parametrically by $S(u,v)$ are readily obtained with [73]:

$$E = \frac{\partial \mathbf{S}}{\partial u}\cdot\frac{\partial \mathbf{S}}{\partial u},\;\; F = \frac{\partial \mathbf{S}}{\partial u}\cdot\frac{\partial \mathbf{S}}{\partial v},\;\; G = \frac{\partial \mathbf{S}}{\partial v}\cdot\frac{\partial \mathbf{S}}{\partial v}, \tag{3.7}$$

$$e = \frac{\partial^2 \mathbf{S}}{\partial u^2}\cdot\frac{\frac{\partial \mathbf{S}}{\partial u}\times\frac{\partial \mathbf{S}}{\partial v}}{|\frac{\partial \mathbf{S}}{\partial u}\times\frac{\partial \mathbf{S}}{\partial v}|},\;\; f = \frac{\partial^2 \mathbf{S}}{\partial u\partial v}\cdot\frac{\frac{\partial \mathbf{S}}{\partial u}\times\frac{\partial \mathbf{S}}{\partial v}}{|\frac{\partial \mathbf{S}}{\partial u}\times\frac{\partial \mathbf{S}}{\partial v}|},\;\; g = \frac{\partial^2 \mathbf{S}}{\partial v^2}\cdot\frac{\frac{\partial \mathbf{S}}{\partial u}\times\frac{\partial \mathbf{S}}{\partial v}}{|\frac{\partial \mathbf{S}}{\partial u}\times\frac{\partial \mathbf{S}}{\partial v}|}; \tag{3.8}$$

and H and K are simply:

$$H = \frac{1}{2}\frac{Eg-2Ff+Ge}{EG-F^2}, \tag{3.9}$$

$$K = \frac{eg-f^2}{EG-F^2}. \tag{3.10}$$

Thus, considering the quadratic form, given by equation (3.6), at the inspection point $(u,v)=(0,0)$ we obtain: $E=1$, $F=0$, $G=1$, $e=2a$, $f=2b$, and $g=2c$; and the curvature values are given by

$$H = a+c, \tag{3.11}$$

$$K = 4(ac-b^2). \tag{3.12}$$

Curvature values were calculated in each triangle by defining surface patches consisting of the triangle of interest (TOI) and the twelve triangles sharing a common edge and/or a common vertex with it. Such a patch was fitted to the quadratic form (Eqn. (3.6)) and the curvatures of the TOI were calculated with equations (3.11) and (3.12). The values of the calculated curvatures were averaged with the curvature values of nearest (first-order) neighbor triangles. This last step was applied to obtain a smooth curvature distribution through the surface. Figure 3.7 shows the detail of a triangular mesh with the mean curvature of each triangle represented by a color scale map.

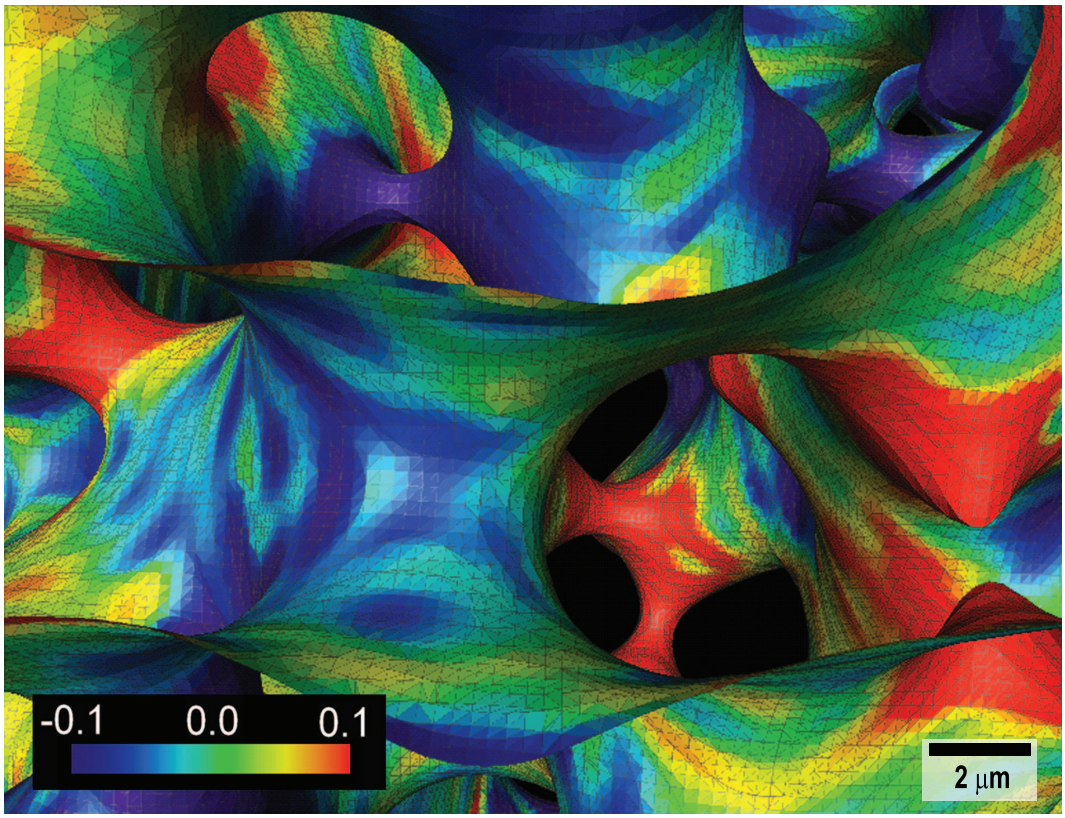

Figure 3.7: Detail of the triangular mesh with color scale map representing the mean curvature for the 50/50 FLPS/SAN blend interface. The value of the curvature (in μm^{-1}) on each triangle is given by the color scale bar.

A number of methods to compute local curvatures of surface patches have been reported [34, 75]. Nishikawa et al. [34] used the SF method, where two set of curvilinear coordinates, (u,v), have to be defined at each point of interest (POI). Curvilinear coordinates are defined by two sectioning planes. The two curves formed by the intersection of the sectioning planes and the surface have to be fitted with a parametric equation, then the coefficients of the first and second fundamental forms (Eqns. (3.7) and (3.8)) are calculated for each curve. H and K are finally found as the solution of a system of simultaneous linear equations. We chose the CT method, over other methods, because of its simplicity of implementation (i.e. it is easier to code and efficient enough to run on a personal computer). In Appendix A, the accuracy of the CT method was tested using a model bicontinuous interface (the gyroid surface), for which the local curvature can be analytically computed.

3.5 Results and discussion

3.5.1 Symmetric blends

Figures 3.8(a-e) show 3D-reconstructed images of the microstructure of the 50/50 (w/w) FLPS/SAN blend for annealing times of 5, 10, 20, 40, and 105 min, respectively. The solid part and the empty space represent the FLPS and the SAN phases, respectively. Two facts are evident just by visual inspection of these images: One is the coarsening over time and second is that cocontinuity of the microstructure is maintained over the coarsening process. Note that micrographs in Figure 3.8(a-c) have the same X-Y-Z dimensions and the growth of pore size is obvious. Micrographs in Figure 3.8(d-e) seem to have similar pore size but the magnification is different, hence the coarsening is also evident. This difference in magnification was chosen to show enough of the microstructure in the late-coarsened structures. In order to quantify the increase in length scale, the reciprocal specific surface area ($1/Q$) is plotted as a function of time (t) (Figure 3.9). A linear growth is observed at early stages of coarsening ($t < 40min$) as described by Siggia which considers a capillary flow driven by interfacial tension, $\lambda \propto (\Gamma/\eta)t$, where λ is the characteristic length and η is the viscosity [14]. After 40 min the coarsening deviates from the linear behavior which could indicate a second process involved in the structure evolution. This behavior was also observed by Pyun et al. [53]

in blends made of polystyrene/high density polyethylene.

Two additional features can be inferred from the reconstructed images: the predominant hyperbolic nature of the interface and the self-similar growth of the global structure. These facts can be confirmed from the statistical analysis of the curvature distributions. Following the approach proposed by Jinnai et al. [35], the probability densities of the mean curvature, $P_H(H)$, and the Gaussian curvature $P_K(K)$ are defined as:

$$P_H(H) = \frac{\sum_{i=1}^{N} A[i|H - \Delta H/2 \leq H_i < H + \Delta H/2]}{\Delta H \sum_{i=1}^{N} A_i} \tag{3.13}$$

and

$$P_K(K) = \frac{\sum_{i=1}^{N} A[i|K - \Delta K/2 \leq K_i < K + \Delta K/2]}{\Delta K \sum_{i=1}^{N} A_i}, \tag{3.14}$$

where H_i and K_i are the mean and Gaussian curvatures and A_i is the surface area of the *i-th* triangle. The terms $A[i|H - \Delta H/2 \leq H_i < H + \Delta H/2]$ and $A[i|K - \Delta K/2 \leq K_i < K + \Delta K/2]$ accounts for the surface area of the triangles that satisfy the conditions: $H - \Delta H/2 \leq H_i < H + \Delta H/2$ and $K - \Delta K/2 \leq K_i < K + \Delta K/2$, respectively. ΔH and ΔK are the class intervals of H and K, respectively. The terms in the denominator are included to satisfy the normalization conditions, i.e. $\sum_H P_H(H)\Delta H = 1$ and $\sum_K P_K(K)\Delta K = 1$.

Figures 3.10(a-b) show the time evolution of P_H and P_K. Note that the curvature is defined as positive when the sampled surface patch is convex towards the FLPS phase. Several characteristics of the surface evolution are elucidated from these plots:

1. P_H is symmetric and centered in zero at every time (Figure 3.10(a)). Hence, the area averaged mean curvature ($< H >$) is zero, which indicates that the evolution of the interface progresses along a path of minimal energy,

2. The full width at half maximum (FWHM) of the distribution of P_H and P_K decreases with time, and the maximum value of the probabilities (close to H or K equal to zero) increases. This result confirms the fact that the way the surface evolves towards a more stable state is by minimizing its curvature, and

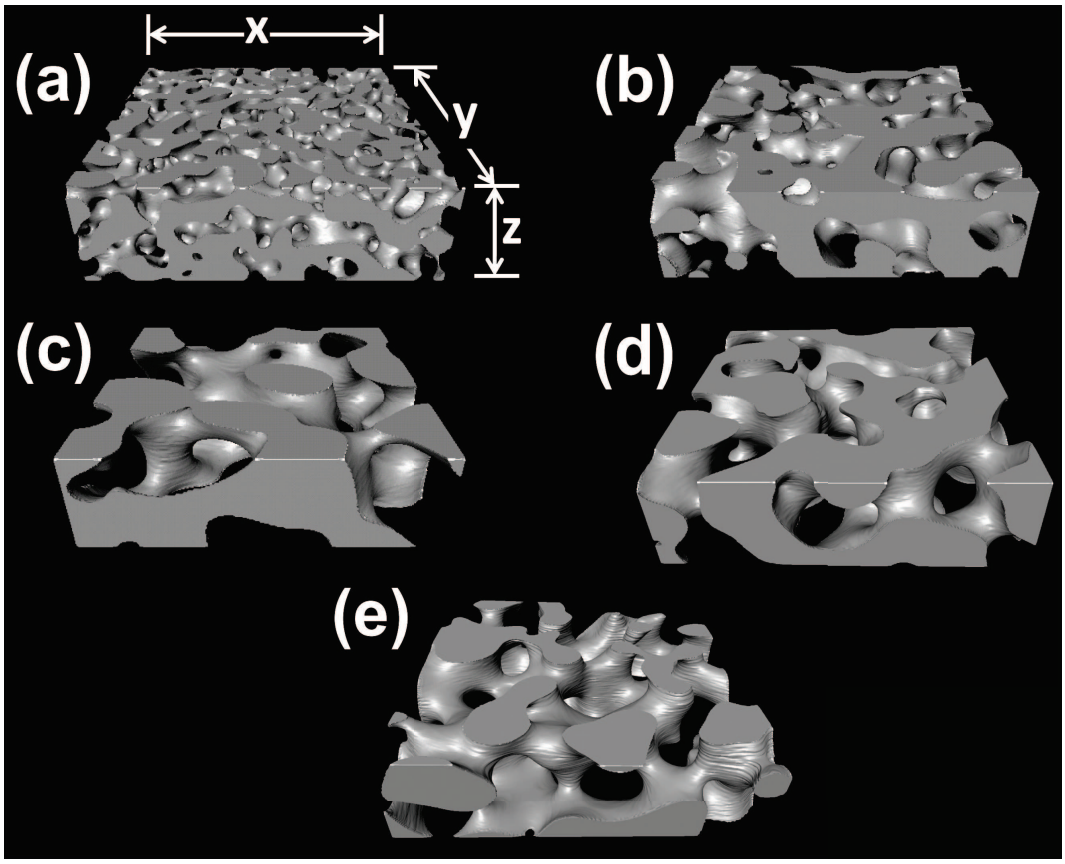

Figure 3.8: 3D rendered micrographs of 50/50 FLPS/SAN blend annealed for (a)5, (b)10, (c)20, (d)40, and (e)105 min.The X-Y-Z dimensions are: (a)-(c) 160×160×45 μm^3, (d) 320×320×90 μm^3, and (e) 500×500×140 μm^3.

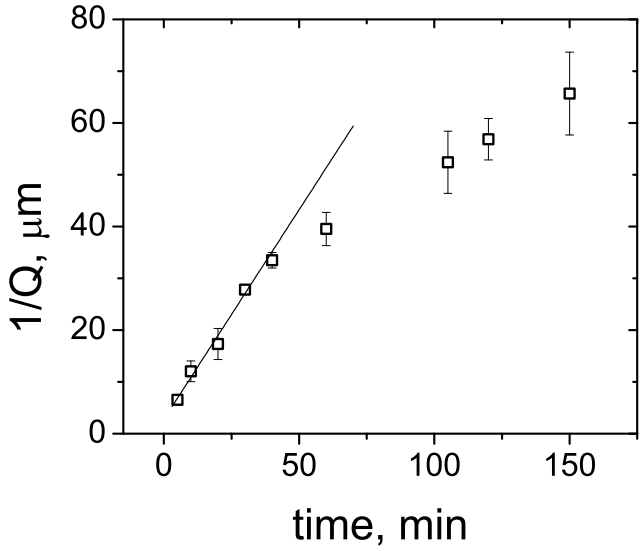

Figure 3.9: Inverse of interfacial area per unit volume ($1/Q$) vs annealing time of 50/50 FLPS/SAN blends measured from LSCM images. The straight line indicates linear growth of 1/Q up to about 40 min. The error bars indicate the standard deviation calculated from measurements of five different samples.

3. The distribution of P_K (Figure 3.10(b)) highlights the fact that the Gaussian curvature is largely negative at any time during the coarsening process. This proves that the surface is predominantly hyperbolic during the whole coarsening process, as observed in the 3D reconstructed images (Figure 3.8).

Jinnai and coworkers observed similar characteristics in the microstructure evolution of partially miscible polymer blends during the late stage of spinodal decomposition (SD) [35, 64, 65, 34]. This is surprising since the formation mechanism of the microstructure of SD mixtures (i.e. continuous growth of the amplitude of unstable concentration fluctuations [77, 78]) is different to that of mechanically mixed immiscible blends (i.e. stretching and folding of the domains due to the complex nature of the flow field in the mixer [79, 80, 46]). To our knowledge analysis of curvatures has not been performed before for immiscible blends prepared by mechanical mixing. However these kind of blends are very important since most polymer pairs are immiscible [2]. Therefore, the recognition of this similarity allows us to use the theory developed for SD systems in

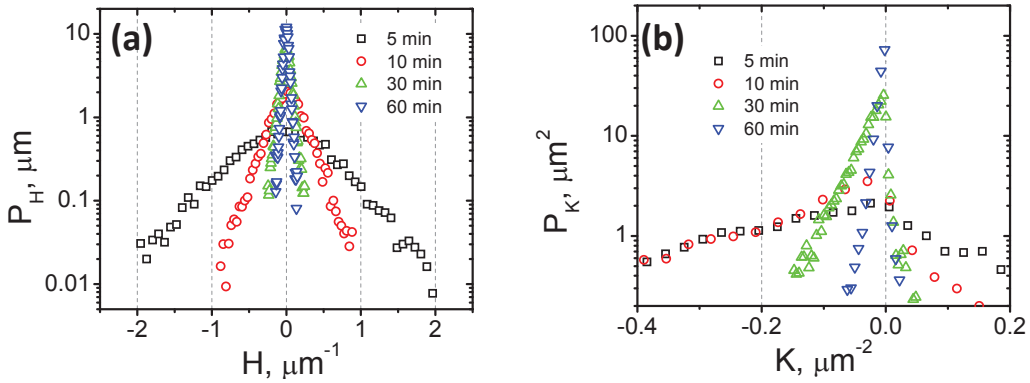

Figure 3.10: Probability densities of (a) the mean and (b) the Gaussian curvatures of 50/50 FLPS/SAN blend interface at different annealing times.

the study of structural evolution of immiscible polymer blends.

Visual inspection of Figure 3.8(c-d) suggest that the structure evolves with dynamic self-similarity, i.e. structures formed at various times are statistically identical while the characteristic length of the periodic structure increases. To verify this, $1/Q$ and $1/Q^2$ were used to normalize the mean and Gaussian curvature distributions, respectively. Figure 3.11(a-b) show the scaled probability densities corresponding to the data from Figure 3.10(a-b). Note that all the curves lie on a single master curve indicating that the local shape of the interface evolves with dynamic self-similarity until an annealing time of 60 min. This is again in accordance to the observed results from spinodally-decomposed systems [35]. However for longer annealing times ($t > 60min$), the dynamic scaling law does not hold any more (see Figure 3.11(c-d)). This coincides with the departure from the linear growth with time of the characteristic length, $1/Q$, observed in Figure 3.9. This behavior was not observed in the spinodally decomposed blends studied by Jinnai and coworkers [35, 64, 34], perhaps, because the time was not long enough for their system to reach this late stage. On the other hand, this decrease in growth rate has been recently observed for 50/50 immiscible blends made of polyethylene/polystyrene [53] and polypropylene/polystyrene [81]. We found that this departure from linear growth of 1/Q is related to the change in the local shape distribution, as discussed in Chapter 4.

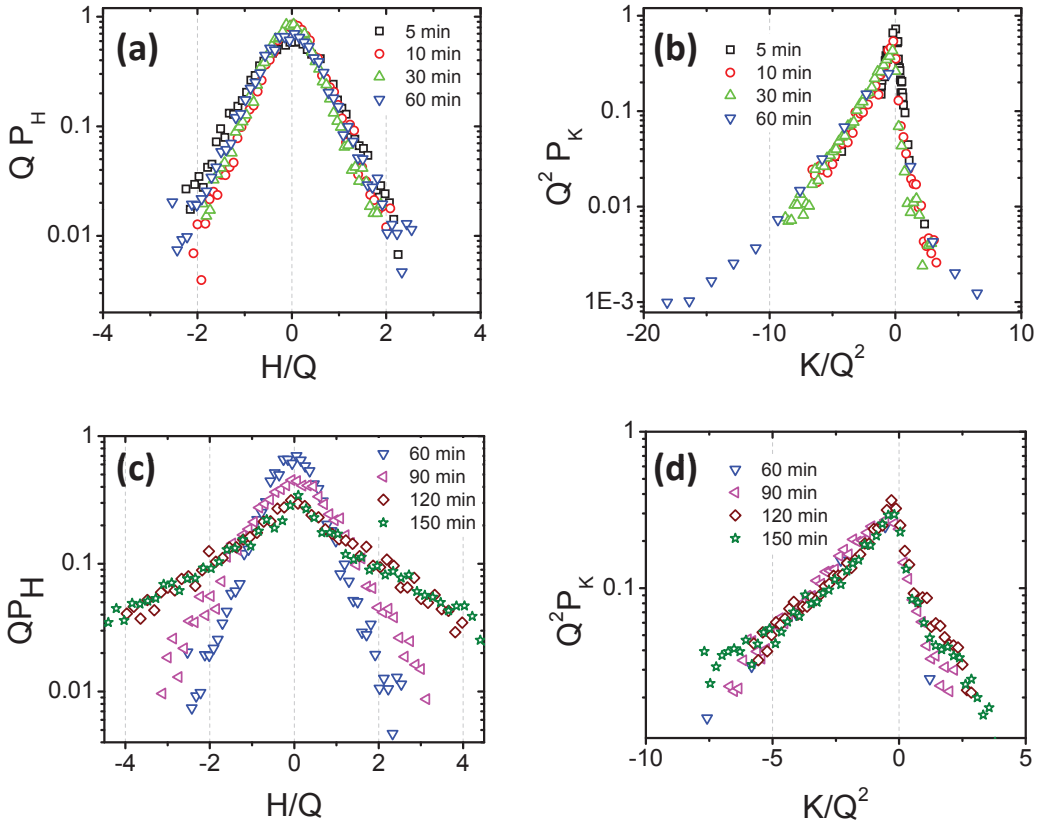

Figure 3.11: Scaled probability densities of the mean ((a) and (c)) and the Gaussian ((b) and (d)) curvatures of 50/50 FLPS/SAN blend interface, at early ((a) and (b)) and late ((c) and (d)) times of annealing.

3.5.2 Non-symmetric blends

The initial morphology of the 36/65 (w/w) FLPS/SAN mixture is shown in Figure 3.12(a). Note that the morphology is cocontinuous but the FLPS domains are more elongated than those observed in the symmetric blend, as expected due to the fact that it is the minor phase.

Interestingly the P_H-distribution is symmetric, but centered around a positive value of H (see Figure 3.13(a)). This result indicates that the interface is globally more curved towards the polystyrene phase, another consequence of the non-symmetric composition. The initial P_K distribution shows similar shape as that corresponding to the 50/50 blend

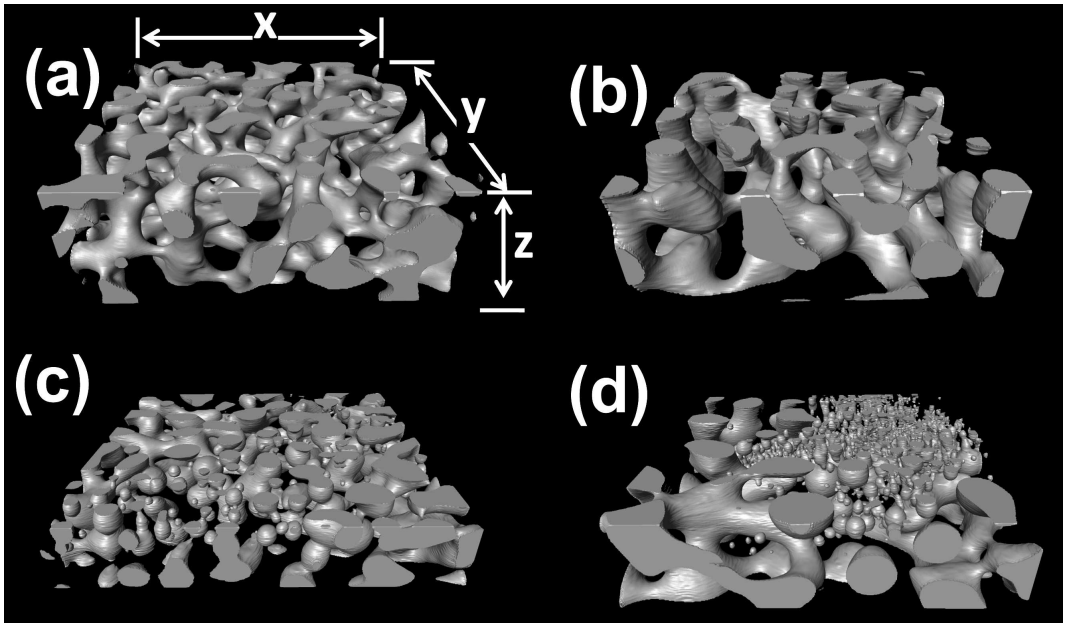

Figure 3.12: 3D rendered micrographs of 35/65 FLPS/SAN blend annealed for (a)5, (b)10, (c)40, and (d)120 min.The X-Y-Z dimensions are: (a)-(b) 80×80×30 μm^3, (c)-(d) 260×260×65 μm^3.

(see Figure 3.13(b)), i.e. mostly populated in the $K < 0$ region, confirming that the interface is for the most part hyperbolic.

The morphology evolution of the blends with composition 36/65 (w/w) FLPS/SAN was significantly different from that observed on the 50/50 blends. Note, in Figure 3.12, that at 40 min and 120 min the microstructure is composed of a mixture of interconnected domains and polystyrene droplets. The droplet formation is a consequence of the break-up of the FLPS elongated domains (pinch-off) which starts at about 20 min of annealing.

The breakup process did not occur uniformly throughout the samples. Figure 3.14 shows the composite microstructure of the blend annealed for 20 min. Zones with high population of droplets are observed coexisting within zones of cocontinuous structure. These droplet-zones are observed throughout the blend and are roughly circular. The formation of these regions and the reason why the pinch-off is not uniform in the blend is not clear. Our hypothesis is that the pinch-off occurs in a nucleation and growth type of process. After a droplet is formed, by local pinch-off, its presence influences the flow

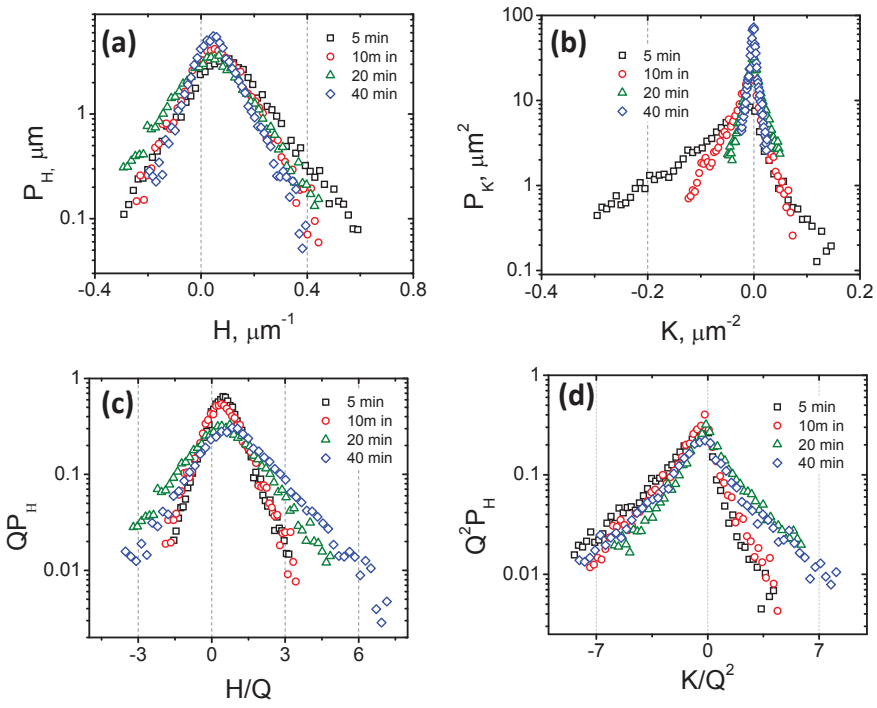

Figure 3.13: Probability densities ((a) and (b)) and scaled probability densities ((c) and (d)) of the mean ((a) and (c)) and the Gaussian ((b) and (d))curvatures of 35/65 FLPS/SAN blend interface at different annealing times.

around it, promoting the break-up of the surrounding interconnected domains. This could explain the circular shape of the droplet regions. In this case the growth is not self-similar, which was verified with the time evolution P_H and P_K (described below).

The characteristic length of the sample, represented by $1/Q$, grows with time as shown in Figure 3.15. However the measurement of Q after the onset of the pinch-off is complicated for two reasons: one is the non-uniformity of the microstructure and second is that there is a considerable population of very small droplets with sizes, smaller than the lateral resolution of LSCM, i.e. 500 nm [43]. Thus in the 3D-reconstruction and surface area quantification, the smallest droplets are not considered, and the error is hard to estimate. To minimize the error due to the non-uniformity, 3D-images from

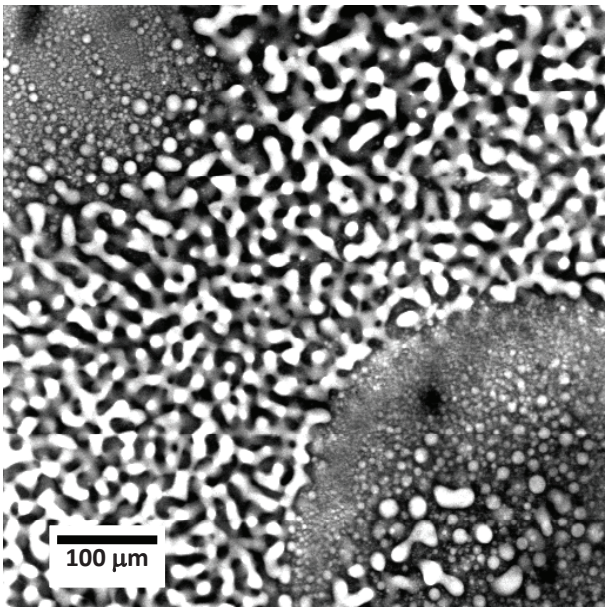

Figure 3.14: LSCM micrograph of 35/65 FLPA/SAN blend after 20 min of annealing, showing the composite microstructure generated after local pinch-off.

5 different zones in each sample were analyzed. The large error bars after 20 min (in Figure 3.15) reflect the discrepancy between the measurements of the different zones.

Evolution of the local shape of the interface can be inferred from the time evolution of P_H and P_K (Figure 3.13(a-b)). Note that some of the features observed in the corresponding distributions for the 50/50 blend are also present in the 35/65 blend. These are: (1) the distributions of P_H and P_K narrow with time, and the curvature values tend to decrease, indicating that the interface evolves through a path of decreasing free energy, (2) the Gaussian curvature is mostly negative at $t < 20min$, indicating that at early times of annealing, the interface is hyperbolic almost everywhere. However some differences are manifest.

Figure 3.13(a) shows that distributions of H are not centered around zero. For the early times ($t < 20min$) this shift is because the elongated domains (of FLPS) have more triangles with positive values of H. At later times ($t > 20min$) the shift is more pronounced (i.e. H is globally more positive) because of the formation of droplets which have positive mean curvature. Due to the growing population of spherical (or ellipsoidal) droplets after the onset of pinch-off ($t > 20min$), the P_K distribution shifts

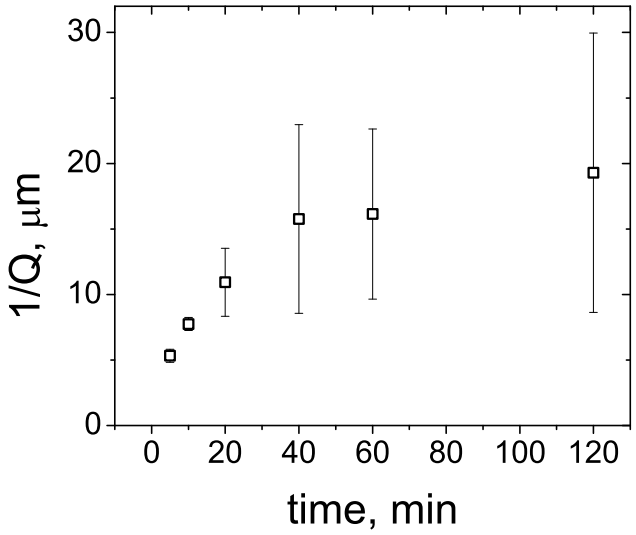

Figure 3.15: Inverse of interfacial area per unit volume ($1/Q$) vs annealing time of 35/65 FLPS/SAN blends measured from LSCM images. The error bars indicate the standard deviation calculated from measurements of five different samples.

toward positive values of K.

As mentioned before, the microstructure growth of the 36/65 blend is not uniform and consequently is non self similar. This was verified from the analysis of the time evolution of the scaled probability densities. Figures 3.13(c-d) show that only the scaled P_H and P_K curves corresponding to the early times ($t < 10$) superimpose, but the dynamic scaling law fails at times longer than 20 min, which coincides with the onset of pinch-off processes. This supports the fact that the microstructure grows in a self similar fashion before the polystyrene elongated domains start to break up.

3.5.3 Surface topology

Using equation (3.5) it is possible estimate the value of the Euler-Poincaré characteristic and the surface genus from each 3D image as

$$\begin{aligned} \chi &= \frac{1}{2\pi}\sum_{i=1}^{N} K_i A_i \\ &= 2(1-g), \end{aligned} \tag{3.15}$$

where A_i and K_i are the surface area and Gaussian curvature of the i-th triangle, respectively, and N is the total number of triangles.

Fialkowski et al. [82] proposed the scaling law: $-\chi \propto \Lambda^{-d}$, where Λ is the characteristic length and d is the dimensionality of the system. This follows from the Gauss-Bonnet theorem (Eqn. (3.5)) and assuming the scaling laws: $K \propto \Lambda^{-d+1}$ and $Q \propto \Lambda^{-1}$ [82]. Considering , for our system, $\Lambda \propto Q^{-1} \propto t$ and $d = 3$, then, according to Fialkowski et al. [82]: $K \propto t^{-2}$ and $-\chi \propto t^{-3}$. However, our experimental results are in disagreement with their predictions. Figure 3.16 shows the area-average Gaussian curvature, $< K(t) >$, for the 50/50 blend and the genus per mm^3, $g(t)/V$, for the 50/50 and 35/65 blends. Note that g and $-\chi$ scale equally with time, but the genus gives a clearer picture of the connectivity of the cocontinuous structures. In the early stage of coarsening ($t < 60min$) the exponent of the scaling laws for both, $- < K >$ and $-\chi$ is $\approx -5/3$ (-1.64 ± 0.03 for $- < K >$ and -1.7 ± 0.05 for $-\chi$), in contrast to -2 for K and -3 for χ predicted by Fialkowski et al [82].

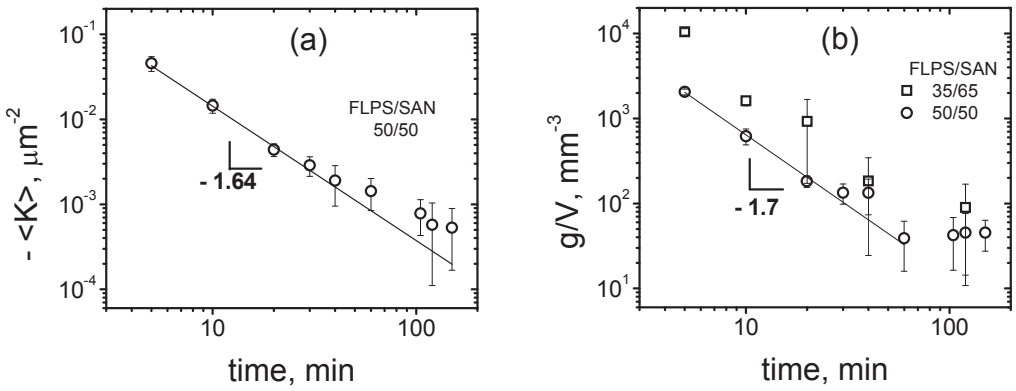

Figure 3.16: (a) Area-average Gaussian curvature and (b) Genus per unit volume for the FLPS/SAN blend as a function of annealing time. Error bars represent the standard deviation calculated from measurements of 5 different samples.

The decrease of g/V with time in the symmetric blend (shown in Figure 3.16(b)) arises from the growth of the global microstructure of the blend. Recalling that the value of the genus represents the number of holes in a surface [73], then for a given volume, the number of holes in the cocontinuous interface will decrease as the microstructure coarsens. This can be confirmed by observing Figure 3.8(a)-(c), where equal volumes

of the 50/50 blend annealed for three different times show a decrease in the number of interconnected channels. This decrease follows the power law: $g/V \propto t^{-1.7}$ during the early coarsening ($t < 60min$) when the microstructure growth is self-similar (see Figure 3.16(b)). After 60 min, when the coarsening slows down, g/V stops decreasing. This coincides with the failure of the dynamic scaling law (Figure 3.11) and the departure from the linear growth of $1/Q$ (Figure 3.9).

For the case of the non-symmetric blend, the decrease of g/V has two causes: the growth of the interconnected structures and the formation of the isolated droplets, for which genus is equal to zero. However due to the high uncertainty in the measurement of the curvatures and interfacial areas (as discussed above) the calculation of the genus is very imprecise as evidenced by the large error bars in the plot (Figure 3.16(b)).

Considering the power laws describing the early evolution of $1/Q$ and g/V, namely $1/Q \propto t$ and $g/V \propto t^{-1.7}$, respectively, we defined a scaled genus that is independent of the size of the sample as

$$G = g/V \cdot (1/Q)^{1.7}. \tag{3.16}$$

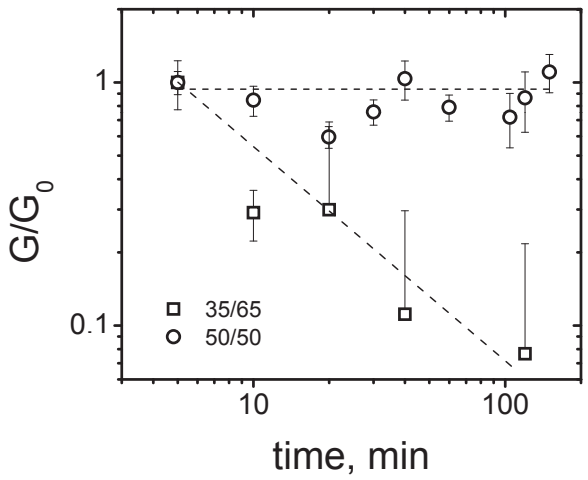

Figure 3.17: Scaled genus, $G = g/V \cdot (1/Q)^{1.7}$, normalized with $G_0 = G(t = 5min)$ for the FLPS/SAN blends as a function of annealing time.

Figure 3.17 shows a plot of G/G_0 versus time where G_0 is the value of G at 5

minutes. The error bars in the plot were calculated using the general rule [83]:

$$\Delta(G) = \sqrt{\left(\frac{\partial G}{\partial(g/V)}\right) \cdot \Delta(g/V)^2 + \left(\frac{\partial G}{\partial(1/Q)}\right) \cdot \Delta(1/Q)^2}, \tag{3.17}$$

where $\Delta(1/Q)$ and $\Delta(g/V)$ are the measured errors of the variables $1/Q$ and g/V, respectively, and $\Delta(G)$ is the composite error of G. If G is given by Eqn. (3.16), Eqn. (3.17) becomes:

$$\Delta(G) = G \cdot \sqrt{\left(\frac{\Delta(g/V)}{g/V}\right)^2 + \left(\frac{1.7 \cdot \Delta(1/Q)}{1/Q}\right)^2}. \tag{3.18}$$

For the 50/50 blend the value of G is rather constant throughout the whole coarsening process. This fact evinces that, taking sections of the sample with size proportional to the annealing time, the number of holes in the interface is the same at either time. In other words, the topology of the cocontinuous interface remains constant regardless the change in size of the microstructure. For the 35/65 blend, both g/V and G decrease with time indicating an effective change in the blend topology as a result of the loss of connectivity due to droplet formation.

3.6 Conclusions

The time evolution of cocontinuous structures formed via mechanical mixing of two immiscible polymers was studied using laser scanning confocal microscopy (LSCM). 3D images were reconstructed from stacks of two dimensional (2D) images captured at different focal depth in the sample via LSCM. The interface between the two phases, represented with a triangular mesh, was obtained after thresholding the 2D images and applying the marching cubes algorithm [72] on the 3D stacks.

Both the mean and Gaussian curvatures were computed using differential geometry. To do this, a simplified method proposed by Sander and Sucker [76], called the coordinate transformation (CT) method, was applied for the first time on the differential analysis of 3D images obtained from phase separated systems. The CT method involves the generation of quadratic parametric equations (Eqn. (3.6)) representing the interface, which were then combined with the coefficients of the first and second fundamental forms (Eqns. (3.7) and (3.8)) to compute the curvature values at each triangle

in the mesh. This method is more accurate than the SF method used by Jinnai and coworkers [34] (see Appendix A) and is easier to implement.

Probability densities of the mean and the Gaussian curvatures of the interface have been obtained for both a symmetric (50/50 w/w FLPS/SAN) and a non-symmetric (35/65 w/w FLPS/SAN) blends. In both cases we found that a large portion of the interface formed after mechanical mixing consists of saddle-shaped surfaces, evidenced by the dominant population of negative values of the Gaussian curvature. The shape of the interface of these blends is remarkably similar to those formed by a different mechanism, namely spinodal decomposition, as reported previously[34].

Two regimes of coarsening were observed in the symmetric blends: In the early stage self-similar evolution of the interface is characterized by the scaling of the probability densities of the curvatures at various times with a time-dependent characteristic length ($1/Q$). This confirms the validity of the dynamic scaling law. In this regime $1/Q$ grows linearly with time. In the late stage, a slowing down of the coarsening is accompanied by the failure of the dynamic scaling. This behavior was recently reported by Pyun et al. for 50/50 PE/PS blends [53] and by Omonov et al. for PP/PS blends [81], but is not well understood yet. However, as will be discussed in Chapter 4, we claim that the decrease in the rate of coarsening is directly related with the decrease in the interfacial curvature with time.

For the non-symmetric blends a different mode of coarsening was found. Due to the more elongated FLPS domains and the non-symmetric volume ratio, break-up of the FLPS threads (pinch-off) is induced. However, pinch-off was not uniform through the samples. Instead, circular domains with droplet-matrix morphologies were observed within cocontinuous domains (see 3.14).

Besides geometry, topology of immiscible blend microstructures was studied for the first time via time evolution of a topological invariant, namely the genus. We defined a *scaled* genus, G, that is independent of the sample volume. A constant value of G, observed in the symmetric blends, attested that the topology is unchanged throughout the whole coarsening process. While for the non-symmetric blends the value of G decreases monotonically with time, reflecting a loss in connectivity due to the pinch-off process.

Chapter 4

The Role of Interfacial Curvature in the Coarsening Dynamics of Cocontinuous Blends

4.1 Introduction

It is well known that properties of microstructured polymer blends heavily depend on the morphology, i.e. size and shape of the microdomains [5, 1]. In the case of isotropic cocontinuous two-phase morphologies, the two components contribute simultaneously to the properties of the blend in all directions. Additionally the amount and shape of interface between the phases contribute considerably to certain blend properties, such as the elastic modulus [84] and tensile properties [85, 46].

Cocontinuous morphologies can be formed by mechanical mixing two immiscible polymers [1, 6, 46] or by spinodal decomposition of partially miscible systems [1, 86, 87, 56]. In either case, a highly curved interface is formed, leading to a thermodynamically unstable system. The energy stored at the interface drives the growth of the characteristic size (λ) of the microstructure during annealing (coarsening). This change in λ could dramatically affect the properties of these materials when they are post processed. Therefore, understanding the growth mechanism is crucial for an adequate design and control of the microstructure and properties of these materials.

A number of mechanisms of coarsening have been proposed in previous studies [17, 40, 14]. Three of them are summarized next:

1. McMaster observed a linear growth with time for spinodally decomposed blends made of styrene-acrylonitrile copolymer and polymethyl methacrylate [40]. He used Tomotika's model [88] for the breakup of cylindrical threads surrounded by a second fluid under the action of the interfacial tension and viscous forces to explain the breakup of the interconnected domains. Assuming that the sinusoidal disturbances occurring on the thread interface grow exponentially with time, the time dependence of the dominant instability with initial amplitude, α_0, is

$$\alpha = \alpha_0 e^{qt} \tag{4.1}$$

where the growth rate of the dominant disturbance is given by

$$q = \frac{\Gamma\Omega}{2a\eta_m} \tag{4.2}$$

where η_m is the matrix viscosity, a is the filament radius, and Ω is Tomotika's function,[88] which is a function of the viscosity ratio and the dominant wavelength. Then the initial growth rate of the disturbances is:

$$\left.\frac{d\alpha}{dt}\right|_{t=0} = c'\frac{\Gamma}{\eta_m} \tag{4.3}$$

with

$$c' = \frac{\alpha_0}{2a}\Omega \tag{4.4}$$

Assuming that the growth of interconnected channels is governed by the breakup of elongated domains, McMaster equated the rate of coarsening with the rate of growth of the dominant disturbances (eqn 4.3). Thus, he obtained the linear growth law experimentally observed.

We disagree with McMaster approach for two reasons. First, from Tomotika's analysis, the condition for the dominant disturbance to growth is that its wavelength is at least ten times a . Thus, in interconnected structures, the breakup

process described by Tomotika can occur only when the dominant wavelength is shorter than the range of connectivity. However, we (see Fig. 4.1) and other authors[17, 53] have observed that the length of interconnecting channels in cocontinuous morphologies are of the order their radius, a. Therefore, the growth of the disturbances are very unlikely to occur. The second reason is that, even though eqn 4.3 depicts a linear growth, it is only valid for the start up of the process of growth of sinusoidal disturbances on a cylindrical thread with *constant* radius. In fact the function Ω is a complex function of Bessel functions which naturally arise from the cylindrical shape of the thread. Interconnections in cocontinuous blends are hyperbolic (saddle shaped), not cylindrical (see Fig. 4.1b).

2. Using scaling arguments, Siggia [14] predicted the same linear growth law as McMaster [40] for the late stage of spinodal decomposition in systems with volume fractions above the percolation threshold. In his analysis Siggia assumed that the capillary flow within the interconnected channels was responsible for the global coarsening. Considering Poiseuille flow, the average velocity (v) is given by

$$v = \frac{a^2}{8\eta}\frac{\Delta P}{\lambda} \tag{4.5}$$

where a is the radius of the channels, λ is the characteristic size of the microstructure, η is the fluid viscosity and $\Delta P/\lambda$ is the pressure gradient which drives the flow. Considering that the pressure difference is determined by the interfacial tension and the mean curvature, H, according to the Young Laplace equation ($\Delta P = 2\Gamma H$), Siggia obtained

$$\lambda = c_1\frac{\Gamma}{\eta}t \tag{4.6}$$

after assuming (1) only one characteristic length (i.e. $a \approx \lambda \approx H^{-1}$) and (2) only one velocity, $v = d\lambda/dt$. Assumption (1) is not accurate, since, as is evidenced in Fig. 4.1, the radius of the channels are in general smaller than the characteristic length, λ. Moreover, as shown in Fig. 3.7, the interfacial curvature is not uniform along the channels, and as demonstrated below, the average value of H^{-1} is not equal to the characteristic length, λ.

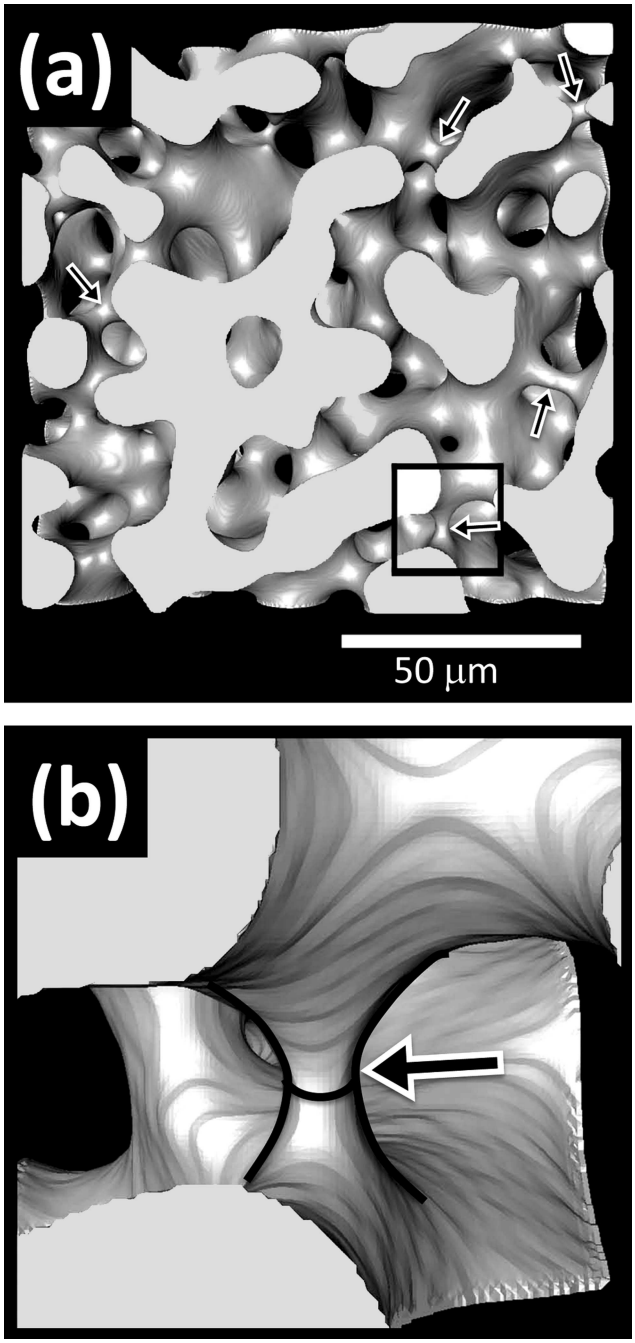

Figure 4.1: 3D image of a 50/50 blend of fluorescently labeled polystyrene (FLPS) and styrene-acrylonitrile copolymer (SAN20) after 20 min of annealing. The FLPS phase is represented by the solid parts and the SAN20 phase by the transparent parts. The arrows in (a) point to the thinnest interconnections. In (b) a detail from the black square in the lower-left part in (a) shows the saddle shape of thin interconnections.

3. Veenstra et al. reported linear growth with time for a series of immiscible blends with different interfacial tension and viscosity.[17] They suggested that the coarsening process is due to the breakup and retraction of interconnected elongated domains forming the cocontinuous structures. The processes of breakup [88] and retraction [89] of isolated polymer fibers in a polymer matrix are interfacial tension driven and opposed only by viscous forces. Therefore, their rates are proportional to the ratio between interfacial tension (Γ) and effective viscosity (η_e) [88, 89]. Hence, the rate of coarsening is proportional to Γ/η_e, which is the same result obtained by McMaster [40] and Siggia [14] for spinodally decomposed blends.

The linear growth predicted by the mechanisms described above has been experimentally observed on several immiscible polymer blends[17, 19], biopolymer blends [90, 18, 91] and spinodally decomposed systems [87, 56, 78]. However, a transition to a regime of slower coarsening at very late times was reported in a number of studies.[53, 81, 45] Pyun et al. [53] studied the coarsening of 50/50 polyethylene/polystyrene blends with a 2D technique (SEM) and two 3D techniques (X-ray microtomography and mercury porosimetry). They observed an initial linear growth followed by a second, slower coarsening rate at longer annealing times. Given that the varying rate was reproduced by the three techniques, they concluded that the phenomenon was real. Omonov et al., [81] and Lopez-Barron and Macosko [45] observed the same behavior in 50/50 blends of polystyrene/polypropylene and polystyrene/styrene-acrylonitrile copolymer, respectively.

The transition to a second regime of coarsening is not explained by the linear models described above [17, 40, 14]. We believe that the main reason is that those theories do not take into account the changing curved nature of the interface. Given that the driving force for the coarsening process originates from the excess free energy of the interface, which is proportional to its curvature, then it is important to include this parameter in the analysis.

Scholten et al. [18] considered the elastic bending coefficients to derive an expression for the hydrodynamic flow within inteconnected channels. In the present study we compared, for the first time, experimental data of 50/50 blends with predictions from Scholten et al. expression. Blends made of fluorescently labeled polystyrene (FLPS) and styrene-acrylonitrile copolymers (SAN) with three different acrylonitrile content,

and different interfacial tension, were analysed. From the fitting of the experimental data with the Scholten et al. expression, the elastic bending coefficients were calculated for the three systems. However, this expression was found to be inadequate to fit all the coarsening data in the time range studied.

On the other hand, we follow a different approach to develop a new model for the hydrodynamic flow considering the effect of the interface curvature directly in the Young-Laplace equation. From the resulting expression (eqn 4.27), we obtained a linear growth regime in the limit $t \to 0$, and a slowing down of the coarsening at long times. Both regimes were observed experimentally and fit with the new expression. The crossover between both regimes occured at a value of capillary number, which is common for all the systems, and was predicted by our model.

4.2 Theoretical background

4.2.1 The role of the curvature

It is well known that the driving force for the coarsening of structures with curved interfaces is minimization of the excess free energy localized at the interface. Consider a curved interface undergoing a displacement in the direction $\hat{n}$, normal to itself, which in turn causes a change in interfacial area, δA (see Fig. 4.2). The change in excess Helmholtz free energy, F^{surf}, due to this process (assuming constant temperature and number of moles) is given as [92]

$$\delta F^{surf} = \Gamma \delta A \tag{4.7}$$

Let $A(= xy)$ be the initial interfacial area of the reference surface depicted in Fig. 4.2. A displacement of the surface, δn, generates an increase in area given by

$$\delta A = (x + \delta x)(y + \delta y) - xy \tag{4.8}$$

Neglecting second order differential quantities, eqn 4.8 can be approximated with

$$\delta A = x\delta y + y\delta x \tag{4.9}$$

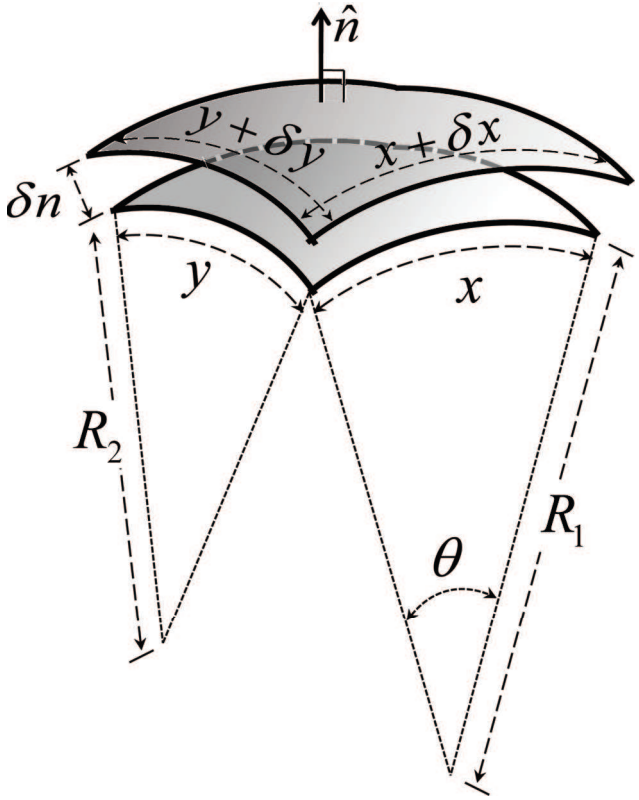

Figure 4.2: Schematic of the evolution of a reference surface with area: A=xy in the normal direction $\hat{n}$.

For a small length, x is related to the angle θ by $x = R_1\theta$ and, similarly, $x + \delta x = (R_1 + \delta n)\theta$. Therefore, we can write

$$\frac{x}{R_1} = \frac{x + \delta x}{R_1 + \delta n} \tag{4.10}$$

Likewise

$$\frac{y}{R_2} = \frac{y + \delta y}{R_2 + \delta n} \tag{4.11}$$

Combining eqns 4.9, 4.10 and 4.11, we obtain $\delta A = 2HA\delta n$, where H ($\equiv \frac{1}{2}\left(\frac{1}{R_1} + \frac{1}{R_2}\right)$) is the mean curvature. Thus, eqn 4.7 can be expressed as

$$\delta F^{surf} = 2H\Gamma A\delta n \tag{4.12}$$

Clearly, the amount of excess free energy is proportional to both the interfacial area and the interface curvature. Therefore, a decrease of these two quantities will provoke a decrease in the coarsening driving force, which in turn could qualitatively explain the slowing down of the coarsening at late times.

4.2.2 Contribution of bending rigidity to interfacial tension

Recognizing that the interfaces of the interconnected domains are not flat but curved, Scholten et al .[18] proposed a generalization to the Siggia's analysis, considering the bending energy as a contribution to the interfacial energy. Using the Helfrich's elastic model [93], in which an interfacial excess free energy is represented as a quadratic expansion of curvature around a flat surface with interfacial tension Γ_0, the expression for the curvature dependent interfacial tension is given by

$$\Gamma = \Gamma_0 + 2E_B(H - H_0)^2 + E_T K \tag{4.13}$$

where E_B and E_T are the elastic bending and torsion (Gaussian) moduli and H_0 is the spontaneous mean curvature. Assuming $H = 1/\lambda$ and neglecting both H_0 and E_T, Scholten et al. obtained the next expression for the interfacial tension

$$\Gamma = \Gamma_0 + \frac{2E_B}{\lambda^2} \tag{4.14}$$

Combining eqns 4.6 and 4.14 gives

$$\frac{d\lambda}{dt} \approx \frac{\Gamma_0}{\eta} + \frac{2E_B}{\eta}\lambda^{-2} \tag{4.15}$$

The first term of the right hand side on eqn 4.15 depicts the effect on the coarsening rate of the (shape independent) stretching contribution to the interfacial energy. The second term represents the (curvature dependent) bending contribution. Solving eqn 4.15 for λ gives

$$\lambda - R_c \arctan\left(\frac{\lambda}{R_c}\right) \approx \frac{\Gamma_0}{\eta}t \tag{4.16}$$

where

$$R_c = \sqrt{2E_B/\Gamma_0} \tag{4.17}$$

is the crossover length scale where the stretching and the bending terms are equal. Recognizing that the function $\arctan(x)$ can be approximated by $x - x^3$ for $x \ll 1$, and by $\pi/2$ for $x \gg 1$, Scholten et al. [18] obtained two regimes of coarsening, namely

$$\lambda \propto \left(\frac{2E_B}{\eta}\right)^{1/3} t^{1/3}, \quad for\ \frac{\lambda}{R_c} \ll 1 \tag{4.18}$$

$$\lambda \propto \frac{\Gamma_0}{\eta}t, \quad for\ \frac{\lambda}{R_c} \gg 1 \tag{4.19}$$

Therefore at length scales where the bending contribution dominates ($\lambda \ll R_c$), i.e. where the local curvature is high enough to have a significant contribution, the coarsening exponent is 1/3; while at larger length scales ($\lambda \gg R_c$) where the interface is flatter and the stretching term dominates, the exponent is 1, equivalent to the obtained by Siggia.[14] The crossover between the two regimes is marked by $\lambda \sim R_c$.

4.2.3 Contribution of interface curvature to hydrodynamic flow

Here, we proposed a new approach to include the contribution of the interfacial curvature in the hydrodynamic flow within the interconnections in cocontinuous structures. As mentioned above, Siggia deduced the linear growth law after assuming $\lambda = H^{-1}$ [14]. However, as stated before, this assumption is not accurate, since the local radius of

curvature of the interconnecting channels is not necessarily equal to the characteristic size of the microstructure (see Fig. 4.1). Actually, as shown below (see Fig. 4.6), λ and the inverse global curvature have comparable numerical values and evolve similarly at early times, but quite differently at late times. Therefore, Siggia's assumption is not longer valid in this late stage. Thus, including the effect of H in the pressure gradient, eqn 4.5 becomes

$$\frac{d\lambda}{dt} \sim \frac{\Gamma}{\eta}\lambda H \tag{4.20}$$

which, after integrating, leads to

$$\lambda \sim \exp\left[\frac{\Gamma}{\eta}\int H dt\right] \tag{4.21}$$

Recently, we showed that for symmetric immiscible polymer blends, the probability distribution of the mean curvature is symmetric and centered in zero [45]. Therefore, the average mean curvature is zero at any time. However, the interface is locally curved. To account for the intensity of the interface curvature we used the *curvedness*, $\mathscr{C}$, which depicts how gently or strongly a surface bends. The curvedness is mathematically described as [94]

$$\mathscr{C} = \sqrt{\frac{\kappa_1^2 + \kappa_2^2}{2}} \tag{4.22}$$

where κ_1 and κ_2 are the principal curvatures, which can be calculated from the mean (H) and the Gaussian (K) curvatures[†] with

$$\begin{aligned} \kappa_1 &= H + \sqrt{H^2 - K} \\ \kappa_2 &= H - \sqrt{H^2 - K} \end{aligned} \tag{4.23}$$

H and K are computed with the coordinate transformation (CT) method, described in Chapter 3. Using equations 4.22 and 4.23, it can be readily demonstrated that the curvedness is related to the mean and Gaussian curvature as

$$\mathscr{C}^2 = 2\,|H|^2 - K \tag{4.24}$$

[†]These curvatures are defined as $H \equiv \frac{\kappa_1+\kappa_2}{2}$ and $K \equiv \kappa_1 \cdot \kappa_2$

Recognizing this proportionality between the curvedness and the magnitude of the mean curvature, we can substitute the area average curvedness, $\mathscr{C}_A$, by H in eqn 4.21. We defined $\mathscr{C}_A$ as

$$\mathscr{C}_A = \frac{\sum_{i=1}^{N} \mathscr{C}_i A_i}{\sum_{i=1}^{N} A_i} \tag{4.25}$$

where $\mathscr{C}_i$ and A_i are, respectively, the curvedness and area of the triangle i of the triangular mesh forming the interface.[45] Measurement of local curvatures at different annealing times were used to compute $\mathscr{C}_A(t)$, which combined with eqn 4.21 and after integration gives a more accurate expression for the instantaneous characteristic length (eqn 4.27).

4.3 Experimental

4.3.1 Materials

Fluorescently labeled polystyrene (FLPS) and three styrene-acrylonitrile copolymers with different acrylonitrile (AN) content were prepared by free radical polymerization at 60 °C with azobisisobutyronitrile as initiator. To obtain the contrast enhancement for the microscopy, 1 %w of anthracenyl methyl methacrylate was used in the styrene polymerization. Details of the materials synthesis and characterization are described in Chapter 2. Relevant properties of the materials are summarized in Table 4.1.

Table 4.1: General characteristics of the materials.

Material	M_w, kg/mol	M_n, kg/mol	$\eta_0(at 200°C)$, Pa-s	AN-content, %mol
FLPS	122	71.3	1485	–
SAN10	135	86.9	2110	9.50
SAN20	116	71.2	2376	19.3
SAN30	103	61.8	2510	28.4

4.3.2 Blend preparation and annealing

The materials were melt blended in a 5 cm^3 conical twin screw microcompounder (Daca Instrument) under a constant flow of nitrogen, at 180 °C and 100 rpm for 10 min. Symmetric (50/50 w/w) and non symmetric (25/75 w/w) blends of FLPS with SAN10, SAN20 and SAN30 were prepared. After mixing, the blends were extruded out of the mixer. Extrudates of the non symmetric blends were molded into disks for rheology tests. For the symmetric blends, small pieces of the extrudate were put in between two glass slides and annealed in a Wabash hydraulic press at 200 °C under a flow of nitrogen. In order to avoid any deformation or flow, the press plates just contacted the glass slides, without applying any pressure to the samples. The samples were removed from the press at different annealing times and submerged in water to freeze the morphology.

4.3.3 Imaging and image analysis

The annealed samples were imaged at room temperature using an Olympus Fluo-View 1000 laser scanning confocal microscope (LSCM). A laser with 405 nm wavelength was used to excite the anthracene molecules attached to the polystyrene chains. A barrier filter (461 nm) in front of the photomultiplier was used so that only fluorescent light was detected. An increment of 0.5 μm along the optical axis of the microscope (z-axis) perpendicular to the focal plane (x-y plane) was used to obtain 2D sliced optical images, composed of 512 X 512 pixels. In order to attain good resolution at different length scales, corresponding to different annealing times, three oil immersed objectives were used. The lateral and axial resolutions, r_{xy} and r_z, of the objectives are indicated in Table 4.2. The resolutions are calculated with $r_{xy} = 0.61\lambda_{exc}/NA$ and $r_{xy}/r_z = 3.28n/NA$, where λ_{exc} is the excitation wavelength, n the refractive index of the object medium (in this case oil with $n = 1.52$) and NA the numerical aperture of the objective lens.[95]

The 2D sliced images obtained by LSCM were enhanced, stacked and 3D reconstructed using a nonstructuring meshing method based on the marching cubes algorithm [72]. A triangular mesh representation of the interface is obtained with this method. Local mean and Gaussian curvatures were calculated by applying the coordinate transformation (CT) method [45, 76] on the 3D images. The CT method involves

the generation of quadratic parametric equations representing the interface, which combined with differential geometry allow us to compute the mean and Gaussian curvature values at each triangle in the mesh (see Fig. 3.7). The interfacial area per unit volume (Q) was calculated by adding up the surface area of all the triangles forming the mesh. About 100 2D slices per 3D image were used for the computation of Q and $\mathscr{C}_A$. The 2D image processing, 3D reconstruction and image analysis are detailed elsewhere [45].

4.3.4 Rheological measurements

Dynamic tests of the materials and the blends with non-symmetric composition were carried out under dry nitrogen atmosphere at 200 °C using a parallel plate ARES rheometer (TA Instruments) in a frequency range of 10^{-1} to 10^{2} rad/sec. Disk shaped samples with 25 mm diameter and 1.5 mm thickness were pressed using a Wabash hydraulic press at 180 °C and subsequently dried at 95 °C under vacuum for 24 hours before the tests. Zero shear viscosity of the materials was obtained by fitting frequency sweep data (Fig. 4.3) with the Cross model [48].

4.3.5 Interfacial tension measurements

Interfacial tension between FLPS and SAN10, SAN20 and SAN30 was measured using two methods, namely, the rheological method (RM) [27, 96], and the breaking thread method (BTM).[97] For the BTM method, 1 mm thick films of FLPS were formed in a Wabash hydraulic press. Fibers of SAN10, SAN20 and SAN30 were drawn from the Daca mixer at 220 °C. The fiber diameters ranged from 50 to 150 μm. The films and

Table 4.2: Optical characteristics of the objectives used in LSCM.

Objective	Magnification	NA	r_{xy}, nm	r_z, nm
1	60X	1.25	198	787
2	40X	0.6	412	3420
3	20X	0.4	612	7690

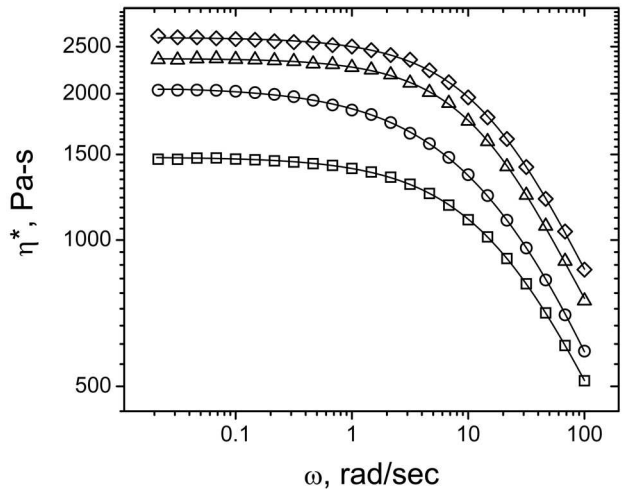

Figure 4.3: Complex viscosity of (□) FLPS, (○) SAN10, (△) SAN 20 and (◇) SAN 30 measured at 200 °C. The solid lines depict Cross model fittings.[48]

fibers were annealed at 90 °C for 48 hr to ensure the release of stresses generated during the pressing and drawing processes. The fibers were put in between two FLPS films. The sandwich sample was put in between a glass slide and a cover slip and placed in a Mettler FP82 Hot Stage which was placed under an optical microscope (Olympus BHS). Then, it was heated to a temperature of 200 °C and the time evolution of the fiber shape was recorded using a CCD camera mounted on the microscope. Details about the calculation of interfacial tension with the two methods are given in Appendix C. The average interfacial tension measured with these two methods is shown in Table 4.3.

4.4 Results and discussion

4.4.1 Initial characteristic size.

The characteristic length of biphasic systems (λ) is related to the interfacial area per unit volume (Q) as $\lambda \propto Q^{-1}$.[‡] The initial morphology is shown in Fig. 4.4 and the measured value of $\lambda|_{t_0=5min}$ is shown in Table 3 for the three blends studied. We allowed the blends to anneal for 5 minutes to eliminate the anisotropy acquired during

[‡]The exact relation is $\lambda = 2\phi(1-\phi)Q^{-1}$ where ϕ is the volume fraction (see page 128 in ref. 78))

Table 4.3: Experimental interfacial tension, initial characteristic size and coarsening parameters for the three blends obtained experimentally at 200°C.

	Blend ID: Polymer1/Polymer2		
Parameter	FLPS/SAN10	FLPS/SAN20	FLPS/SAN30
[a] Γ, mN/m	0.29 ±0.07	0.86 ±0.14	1.11 ±0.20
[b] Γ/η_0, μm/min	9.71	26.73	32.96
[c] $\lambda\|_{t_0=5\ \min}$, μm	1.15 ±0.46	6.56 ±0.87	10.1 ±0.83
[d] R_c,μm	—	36.2	43.9
[d] $E_B \times 10^{-7}$, kT	—	5.2	8.1
[d] $\frac{d\lambda}{dt}\|_{late\ times}$, μm/min	0.161	0.292	0.162
[e] c_1	0.029	0.031	0.036
[e] c_2,μm	0.05	1.1	1.3
[e] $c_3, [units]$	2.7×10^{-1} $[\min^{0.82}/\mu\text{m}]$	4.3×10^{-3} $[\min^{0.42}/\mu\text{m}]$	2.1×10^{-3} $[\min^{0.33}/\mu\text{m}]$
[e] c_4	0.18	0.58	0.67

[a] $\Gamma = \frac{\Gamma_{BTM}+\Gamma_{RM}}{2}$ (see Appendix).

[b] $\eta_0 = \frac{\eta_{0,FLPS}+\eta_{0,SAN}}{2}$ (see Table 1).

[c] initial annealing time, $t_0 = 5min$, to achieve isotropic recovery.

[d] parameters from Scholten's expressions (eqns 4.18 and 4.19).

[e] parameters from new coarsening model (eqns 4.6 and 4.27).

the extrusion process. It is evident that the interfacial tension has a considerable effect on the initial morphology.

Despite several studies conducted to understand the mechanism of formation of cocontinuous blends during mechanical mixing,[46, 80, 98, 99, 100, 101] it is not yet fully understood. However, regardless of the formation mechanism, the main condition to form and to maintain cocontinuous structures is to create stable elongated structures of at least one of the phases [46]. It is well known that low values of Γ/η favor the deformation and hinder the breakup of domains during mixing processes [46, 102]. For the case of droplet-matrix morphologies, this leads to large and elongated droplets. But in cocontinuous structures, low interfacial tension produce smaller characteristic lengths because the thin threads are less likely to breakup due to capillary instabilities. This explains, at least qualitatively, the proportionality between λ_0 and Γ/η shown in Table 4.3.

4.4.2 Coarsening

Fig. 4.4 shows the morphology of the blends after 5 and 20 min of annealing. It is evident that the growth of the microstructure is more pronounced as the interfacial tension is bigger. Figure 4.5 shows the characteristic length as a function of annealing time. A linear growth at early times of annealing followed by a slowing down at late times was observed for all three blends. Lopez-Barron and Macosko showed that the transition to the second regime was also marked by a failure in the dynamic scaling of the curvature distributions [45]. The slope of the initial growth is proportional to the ratio Γ/η , which is in accordance to the Siggia's result (eqn 4.6). The onset of the second regime occurred at shorter times for the blend FLPS/SAN30, followed by blend FLPS/SAN20 and lastly blend FLPS/SAN10. As mentioned before, this behavior is not explained by previous models [17, 14, 40], apparently because these models assume that the interconnected domains have cylindrical shape, while they are more saddle shaped with broad curvature distributions.

Fig. 4.6 shows that both Q and $\mathscr{C}_A$ decrease throughout the blend annealing, which make the driving force weaken during the process (see eqn 4.12). As we stated before, this explains the abatement of the rate of coarsening observed in the blends studied in the present work as well as in other systems [53, 81]. Apparently, the late coarsening leads

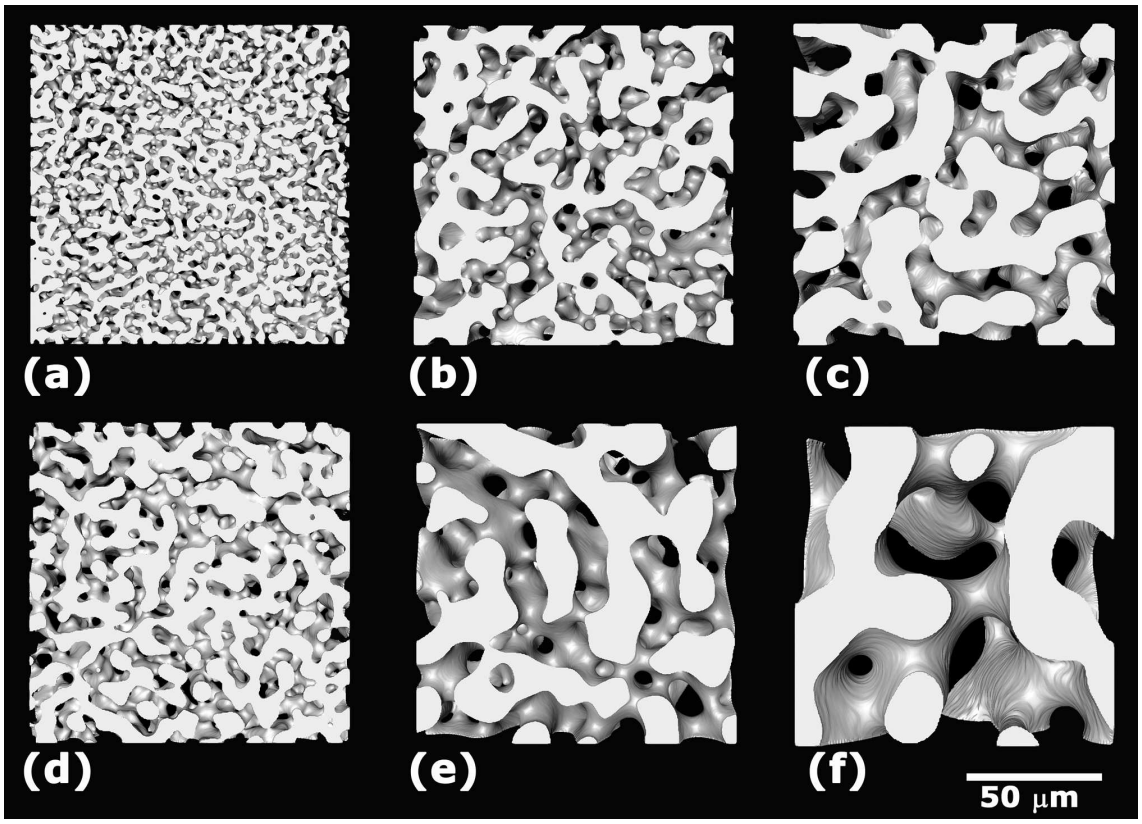

Figure 4.4: 3D rendered micrographs of 50/50 (a,d) FLPS/SAN10, (b,e) FLPS/SAN20 and (c,f) FLPS/SAN30 blends annealed for 5 (upper row) and 20 min (lower row). The FLPS phase is represented by the solid parts and the SAN phases by the transparent parts. The scale bar is common for all the micrographs.

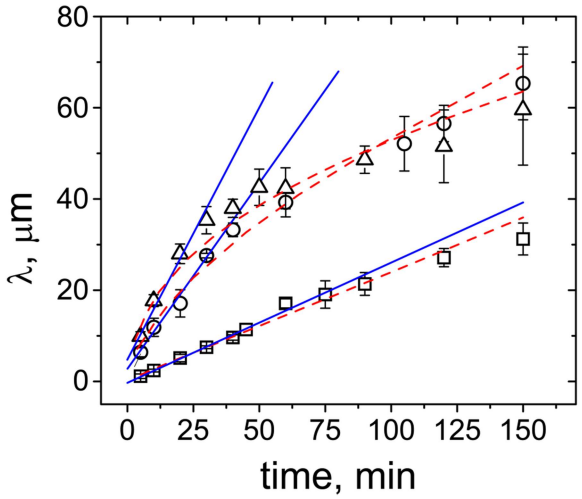

Figure 4.5: $\lambda(= Q^{-1})$ vs. annealing time of 50/50 (□) FLPS/SAN10, (○) FLPS/SAN20 and (△) FLPS/SAN30 blends measured from LSCM images. Straight (solid) and curved (dashed) lines are fit with eqns 4.6 and 4.27, respectively. The error bars indicate the standard deviation calculated from measurements of five different samples.

to an asymptotic constant value (not reached in the experimental time studied in this work) of interfacial area and curvature which would correspond to an state of minimal interfacial energy (i.e. $F^{surf} \to 0$), as a consequence of having $H = 0$ everywhere, as is the case of the Gyroid surface [45, 39].

4.4.3 Assessment of Scholten's expression

Fig. 4.7 shows the time evolution of λ fit with eqns 4.18 and 4.19. Data from the early coarsening were fit with a power law with exponent 1/3 and late coarsening with exponent 1. Data from the early coarsening of blend FLPS/SAN10 could not be fit with the exponent 1/3. For the other two blends the crossover length scale (R_c) was measured as the intersection between the two fitting curves. Using eqn 4.17 and the measured interfacial tension the bending elasticity was calculated and shown in Table 3. These data indicate that both, R_c and E_B are increasing functions of the AN-content of the SAN in the blend. Scholten et al.[90] showed that for phase separated biopolymer mixtures $E_B \sim 500\ k_bT$ and $R_c \sim 1\ \mu m$. Unfortunately data for bending elasticity of the interface between polystyrene and SAN is not available and its measurement is

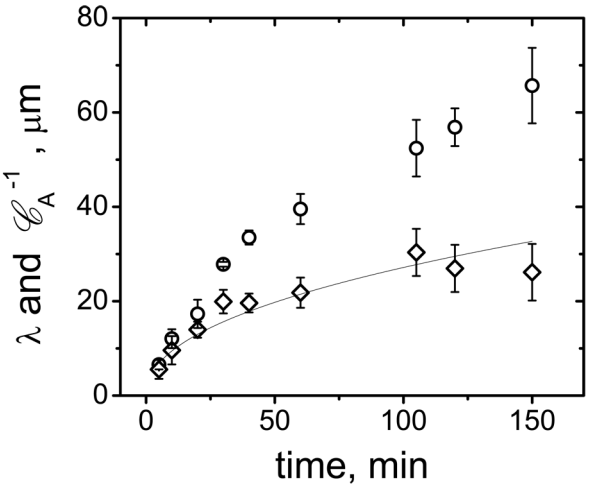

Figure 4.6: Time evolution of (□) the carateristic size, $\lambda = Q^{-1}$, and (○) reciprocal average curvedness, $\mathscr{C}_A^{-1}$, of 50/50 FLPS/SAN20 blend. The solid line depicts the power law fitting: $\mathscr{C}_A \propto t^{-0.42}$. The error bars indicate the standard deviation calculated from measurements of five different samples.

beyond the scope of this work.

A disconcerting result is that the rate of coarsening at late times, $\frac{d\lambda}{dt}\big|_{late\ times}$ (see Table 3), which according to eqn 4.19 should be proportional to Γ_0/η (also shown in Table 3), does not follow this tendency. This observation and the fact that early coarsening data for the blend FLPS/SAN10 could not be fit with the 1/3 exponent make us think that the Scholten et al. model is not adequate to explain the coarsening behavior of immiscible polymer blends.

4.4.4 Comparison of new coarsening model with experiments

In order to assess the new expression for the instantaneous characteristic size (eqn 4.21), the time evolution of $\mathscr{C}_A$ was fit with the power law

$$\mathscr{C}_A = mt^n \tag{4.26}$$

with exponents -0.82, -0.42, and -0.33 for the blends FLPS/SAN10, FLPS/SAN20 and FLPS/SAN30, respectively. Fig. 4.6 shows both λ and $\mathscr{C}_A^{-1}$ for the blend FLPS/SAN20. Both quantities grow linearly at the early stage of coarsening, and their evolution start

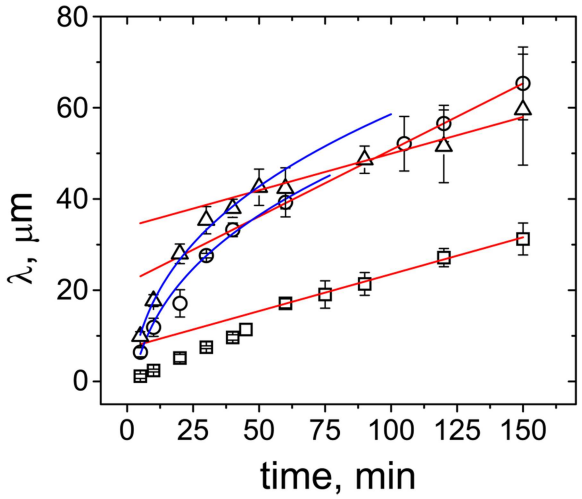

Figure 4.7: $\lambda(= Q^{-1})$ vs. annealing time of 50/50 (□) FLPS/SAN10, (○) FLPS/SAN20 and (△) FLPS/SAN30 blends measured from LSCM images. Curved and straight lines are fit with eqns 4.18 and 4.19, respectively. The error bars indicate the standard deviation calculated from measurements of five different samples.

slowing down at about the same time but at different rates. The solid line depicts the fit obtained with eqn 4.26. Fig. 4.5 shows the early regime fitted with the linear relation given by eqn 4.6, and both early and late regimes with the expression

$$\lambda = c_2 \exp\left[c_3 \frac{\Gamma}{\eta} t^{c_4}\right] \tag{4.27}$$

which was obtained by substituting H (in eqn 4.21) for $\mathscr{C}_A$ (from eqn 4.26). The value of the constants c_1 (eqn 4.6), c_2, c_3 and c_4 are shown in Table 3.

The initial growth was fit with very similar values of c_1 (0.032 ± 0.004) for all the blends. This is in agreement with the values used by Veenstra et al. [17], who fit experimental data for a series of symmetric and non-symmetric blends, using c_1 =0.07 and .03, respectively.

Note that the constant c_2 in eqn 4.27 correspond to an initial value of characteristic length (i.e. $c_2 = \lambda(t = 0) = \lambda_0$). It is difficult to assign physical meaning to constants c_3 and c_4, however they are related to the parameters in eqn 4.26 as $c_3 = m(1 + n)^{-1}$, and $c_4 = 1 + n$. Generating a power series expansion for eqn 4.27 about the initial

characteristic time defined as $\tau_0 = \frac{\eta}{\Gamma}\lambda_0$, we obtain

$$\lambda = \lambda_0 M_0 \left[1 + M_1(t-\tau_0) + M_2(t-\tau_0)^2 + \mathcal{O}\left((t-\tau_0)^3\right)\right] \tag{4.28}$$

with

$$\begin{aligned} M_0 &= \exp\left[c_3 \left(\frac{\Gamma}{\eta}\right)^{-n} \lambda_0^{1+n}\right] \\ M_1 &= m\left(\frac{\Gamma}{\eta}\right)^{1-n} \lambda_0^n \\ M_2 &= \frac{m}{2}\left(\frac{\Gamma}{\eta}\right)^{2-n} \lambda_0^{n-1}\left[m\left(\frac{\Gamma}{\eta}\right)^{-n} \lambda_0^{1+n} + n\right] \end{aligned} \tag{4.29}$$

Note that $M_0 \sim 1$,therefore $\lambda \to \lambda_0$ when $t \to \tau$. The series 4.28 is not defined for $t < \tau$. For short times (but $t > \tau$) only the term containing M_1 in the series contributes, giving the linear relation observed experimentally at early times of annealing. From scaling analysis of the series, it is plain that $M_2 < 0$. Hence for $t \gg \tau$, the term containing M_2 will be responsible for the damping of the coarsening function (eqns 4.27 or 4.28).

To account for the relation between the viscous forces and interfacial energy, including the curvature contribution in the latter, we propose the following form of Capillary number:

$$Ca = \frac{\eta \frac{d\ln\lambda}{dt}}{\Gamma \mathscr{C}_A} \tag{4.30}$$

Fig. 4.8 show the time evolution of Ca, which decreases at the same rate for the three blends due to the reduction of the characteristic velocity with time. A transition to the second regime with smaller rate occurs at a critical value of capillary number, $Ca = 32.5 \pm 1.5 \times 10^{-4}$, for the three blends. The reduction of rate is due to the reduction of interfacial energy, which in turn is due to the decrease in surface curvature, with respect to the viscous force which opposes the coarsening. This transition occurred at t=33.7, 24.3, and 18.6 min for the blends FLPS/SAN10, FLPS/SAN20, FLPS/SAN30, respectively. These values are close to the crossover time between the early (eqn 4.6) and late stages (eqn 4.27), which are, respectively 28.5, 21.3 and 16 min (see Fig. 4.5).

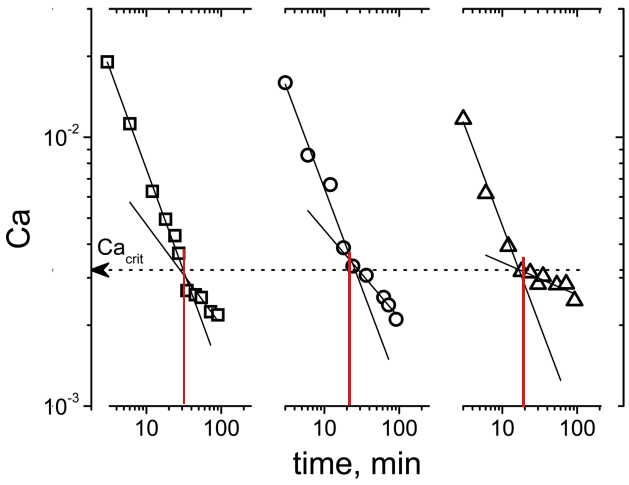

Figure 4.8: Capillary number vs. annealing time of 50/50 (□) FLPS/SAN10, (○) FLPS/SAN20 and (△) FLPS/SAN30. The dotted line indicates the critical value of Ca.

4.5 Conclusions

We studied the time evolution of cocontinuous morphologies (size and shape) in 50/50 w/w FLPS/SAN blends, with different interfacial tensions, via 3D LSCM coupled with differential geometry. A linear growth was observed at early times of annealing, followed by a second regime of slower coarsening at late times. Only the first regime can be explained by the classical analysis by Siggia [14]. A generalized expression proposed by Scholten et al. [18] was used for the first time to fit experimental data of evolving cocontinuous structures. From this analysis it was found that both the characteristic length at the crossover between the two regimes and the elastic bending energy increase with the AN-content of the SAN in the blend. However, the Scholten el al. expression was inadequate to fit the early coarsening data for the low interfacial tension blend (FLPS/SAN10). Moreover, it was impossible to fit the data from the whole time range with a single set of parameters for the three blends. We proposed a new model for the coarsening which considers the effect of the local curvature on the hydrodynamic flow. With this model we were able to describe both early (linear) and late (decreasing) coarsening regimes for all three blends with a single set of parameters. From our analysis we corroborated that the decrease in rate of coarsening is due to a continuous reduction

of the global curvature of the interface. We found that the crossover between the two regimes occurs at a single value of capillary number ($Ca \sim 0.003$), which in turn, was predicted by our model.

Chapter 5

Effect of Block Copolymer on the Coarsening of Cocontinuous Blends*

5.1 Introduction

Blending of immiscible polymers is an important route to high performance materials, often with synergistic improvements in properties [5]. When the blend composition is close to 50/50, cocontinuous morphologies can form with advantageous properties such as enhanced processability and mechanical properties [46], static charge dissipation † and controlled moisture adsorption [13]. Cocontinuous blends tend to be less stable than blends with dispersed droplets, however, and coarsen rapidly and continuously during annealing [46]. A few studies, mostly with blends of polystyrene (PS) and polyethylene (PE), have shown that block copolymers can slow coarsening. Mekhilef et al. [103]

*Reproduced with permission from "Annealing of Cocontinuous Polymer Blends: Effect of Block Copolymer Molecular Weight and Architecture" Bell, J.R.; Chang, K.; Lopez-Barron, C.R.; Macosko, C.W.; Morse, D.C., submitted for publication. Unpublished work copyright 2009 American Chemical Society.

†(a) Lubrizol, Stat-Rite Conductive Polymers, The Lubrizol Corporation Technical Publication. Copyright 2007. Accessed at `http://www.lubrizol.com/EngineeredPolymers/` on Sept 25th, 2009.
(b) Conductive Thermoplastics, RTP Company Technical Publication. Copyright 2005. Accessed at `http://www.rtpcompany.com/`on Sept 25th, 2009.

found that the addition of styrene-(hydrogenated butadiene)-styrene (SEBS) triblock copolymer slowed the coarsening of cocontinuous morphologies in 50/50 PS/PE blends. In a more quantitative study, Veenstra et al. [17] found that 5% SEBS slowed coarsening three fold. Yuan and Favis [21] reported that adding 0.5% of a PS-b-PE diblock copolymer suppressed coarsening nearly completely while 7.5% SEBS was required to achieve similar stability. Galloway et al. [20] studied the effect of molecular weight and concentration of symmetric PS-b-PE bcps and found that as little as 0.1% of bcp with an optimum molecular weight could completely suppress coarsening after an initial reduction in interfacial area.

Here we extend the experimental work of Galloway et al. and provide a more detailed discussion of our theoretical interpretation of the results. We experimentally explore the role of block asymmetry, molecular weight and concentration in stabilization of cocontinuous morphology for another two polymer pairs with lower interfacial tension, PS/polymethylmethacrylate (PMMA) and PS/styrene-ran-acrylonitrile copolymer (SAN).

We note that an extremely low interfacial tension, and a correspondingly low rate of coarsening, could be obtained with symmetric copolymers at concentrations above the copolymer critical micelle concentration in either of two ways. Some systems of nearly symmetric copolymers of intermediate molecular weight can reach a very low equilibrium interfacial tension, in which the interfacial layer of adsorbed copolymer remains in equilibrium with a reservoir of micelles. Alternatively, in systems of longer copolymers, the interfacial coverage can be compressed above the equilibrium saturation coverage by the decrease in interfacial area during coarsening, thus driving the interfacial tension to zero, if copolymers are unable to desorb from the interface and reform micelles as interfacial area decreases. We discuss the expected implications of both of these scenarios, as well as a third in which, for sufficiently small copolymers, no micelles may form. We conclude that our results contain examples whose behavior is consistent with each of these three scenarios. In cases in which the evidence suggests that the interface remains in equilibrium with a reservoir of micelles, we infer values for interfacial tension from the observed rates of coarsening, and compare these results to an equilibrium theory for the dependence of equilibrium interfacial tension upon copolymer asymmetry [41], with encouraging results.

5.2 Experimental methods

5.2.1 Materials

Table 5.1 shows the properties of the blend components for these experiments. PS and high density PE (HDPE, Dow 4452N) were supplied by the Dow Chemical Company. Their low shear rate viscosities, at 0.1 rad/s and 170 °C, were nearly equal, 3200 and 3300 Pas, respectively. Viscosities were measured using a parallel plate rheometer (ARES, TA Instruments) in dynamic frequency. Symmetric (by weight) PS-PE diblock copolymers (PS-b-PE) with varying molecular weights, as well as two asymmetric 40 kg/mol (40k) PS-b-PE, were used. PS-b-PE was prepared by first synthesizing PS-b-PBD (polybutadiene) by anionic polymerization followed by selective hydrogenation. Details of the anionic polymerization, catalytic hydrogenation and characterization of the copolymers are described elsewhere [104, 105]. Molecular weight and polydispersity of the polymers (shown in Table 5.1) were measured by gel permeation chromatography (GPC) using polystyrene standards. The χN_{core} values shown in Table 5.1 were calculated using $\chi = 0.07$ for PS/PE (reference volume = 100 Å^3 [104]. N_{core} is equal to $(1 - f_{PS})M_n/M_0$, where f_{PS} is the volume fraction of the polystyrene block and M_0 is the average molecular weight of the monomers. f_{PS} values were measured by nuclear magnetic resonance.

PS (Dow 685D) and PMMA (Arkema V825N) are commercially available. Their low shear rate viscosities, at 0.1 rad/s and 220 °C, were both 11,000 Pa·s. The 42k, 74k, 100k, and 260k PS-b-PMMA were supplied by Polymer Source; information on their synthesis is given by Varshney and coworkers [106, 107]. The 900k PS-b-PMMA was supplied by Polymer Standard Services. The 160k PS-b-PMMA was synthesized at the University of Minnesota [108]. The anionic polymerization was done in THF at -78 °C. After styrene was polymerized via sec-butyllithium, and the living chains were end-capped with diphenylethylene right before the addition of MMA. The polymerization was terminated with degassed methanol. The χN_{core} values (shown in Table 5.1) were calculated using $\chi = 0.035$ for PS/PMMA (reference volume = 178 Å^3) [109].

Table 5.1: Material properties.

Material	M_n kg/mol	M_w/M_n	[a] f_{PS}	[b] χN_{core}	
PS	61	< 1.1	$--$	$--$	
HDPE (Dow 4452N)	18	5	$--$	$--$	
6k PS-b-PE	3-3	< 1.1	0.45	[c] 4	
20-20k PS-b-PE	20-20	< 1.1	0.45	[c] 25	
28-10k PS-b-PE	28.5-10.5	< 1.1	0.69	[c] 13	
33-5k PS-b-PE	33-5	< 1.1	0.84	[c] 6	
100k PS-b-PE	50-50	< 1.1	0.45	[c] 65	
200k PS-b-PE	100-100	< 1.1	0.45	[c] 130	
PS (Dow 685D)	150	1.8	$--$	$--$	
PMMA (Arkema V825N)	52	1.9	$--$	$--$	
FLPS	72	1.7	$--$	$--$	
SAN	71	1.6	$--$	$--$	
42k PS-b-PMMA	21-21	1.1	0.54	[d] 7	[e] 0.05
74k PS-b-PMMA	37-37	1.1	0.54	$--$	[e] 0.09
100k PS-b-PMMA	50.6-47.6	1.1	0.55	[d] 17	[e] 0.12
160k PS-b-PMMA	80-80	1.1	0.54	[d] 27	$--$
260k PS-b-PMMA	130-133	1.1	0.53	[d] 44	[e] 0.3
900k PS-b-PMMA	450-450	1.1	0.54	$--$	[e] 1.0

[a] volume fraction of the PS block.

[b] N_{core} is the total number of repeat units in the smaller block.

[c] using $\chi = 0.07$ (PS/PE) [104].

[d] using $\chi = 0.035$ (PS/PMMA) [109].

[e] using $\chi = 2.4 \cdot 10 - 4$ (PS/SAN), calculated from the measured interfacial tension (Appendix C).

Fluorescently labeled polystyrene (FLPS) and styrene-ran-acrylonitrile copolymer (SAN) was synthesized using free radical polymerization at 60 °C in toluene with azo-bisisobutyronitrile as initiator [45]. 1% of a fluorescent monomer (anthracenylmethyl methacrylate) was used in the FLPS polymerization. The acrylonitrile content in SAN, measured by elemental analysis, was 19.3 mol%. The low shear rate viscosities of FLPS and SAN, at 0.01 rad/s and 200 °C, were 1500 and 2400 Pa·s, respectively. The value of χ was estimated to be about $2.6 \cdot 10^{-4}$, from the FLPS/SAN interfacial tension, $\Gamma = 0.86$ mN/m [‡], and the Helfand and Tagami equation [110] $\Gamma = kTb\rho_0\sqrt{6\chi}$, where b is the statistical segment length and ρ_0 is the monomer number density. For polystyrene, b and ρ_0 are estimated to be 0.59 nm and $5.4 \cdot 10^{-3}$ Å^{-3}, respectively [111]. For SAN the same values were used as no data were available in the literature. The density of PS is estimated to be 0.933 g/cm^3 based on the value at 140 °C reported by Fetters et al. [111], and the thermal expansion coefficients [112]. The density of SAN with ∼20 mol% AN is 0.936 g/cm^3 [113].

5.2.2 Blend preparation

PS/PE and PS/PMMA blends were prepared by mixing the components in a HAAKE batch mixer (HBI System 90 or Polylab OS, Thermo Electron Co.) using a 25 ml mixing bowl equipped with roller blades. To prevent thermal degradation, antioxidant (Irganox 1010, Ciba) was added at 0.2 wt%. The materials were dried under vacuum overnight. The dried materials, 20 g total, were added in one step, and mixed at 50 rpm (average shear rate = 25 s^{-1}) [114] for 10 min at a temperature of 170 °C for PS/PE or 220 °C for PS/PMMA. The blends were then immediately removed from the mixer and plunged into a liquid nitrogen bath to quench the morphology. For PS/PE the blend composition was held constant at 50 wt% PS, while for PS/PMMA blends PS was 45 wt% to ensure the blend morphology was cocontinuous [22].

50/50 FLPS/SAN blends were prepared in a recirculating, conical twin-screw extruder (Microcompounder, DACA Instruments) at 180 °C under nitrogen purge. Blending was performed at a screw speed of 100 rpm for 10 min. After the mixing, the blends were extruded out of the mixer, quenched with water then cut into small pellets.

[‡]Interfacial tension was measure with two methods, namely the breaking thread method and the rheological method (see Appendix C).

5.2.3 Annealing

After quenching the PS/PE blends, several pieces, ∼2 mm thick, were annealed under quiescent conditions in the environmental chamber of our rheometer (ARES, TA Instruments). Samples were annealed for various time intervals at 170 °C under a nitrogen atmosphere then quenched using liquid nitrogen. PS/PMMA blends were annealed in a hydraulic press (Wabash). Small blend chunks were placed between Teflon sheets in a 25 mm diameter by 1 mm thick mold and then placed between the two heated metal platens. No pressure was applied. Samples were annealed for various time intervals at 220 °C. After annealing, cold water was flushed through the press platens to rapidly cool the samples below the glass transition temperatures of PS and PMMA; the cooling time (∼1.25 min to ∼100 C) was taken into consideration for annealing time determinations.

Pellets of FLPS/SAN blends were put in between two glass slides[§] separated by 2 mm thick steel washers and then annealed in a Wabash hydraulic press at 200 °C for different time intervals. No pressure was applied in the sample to avoid any sample deformation. After annealing, the samples were plunged into water to stop the coarsening.

5.2.4 Microscopy and image analysis

PS/PE samples were cryo-microtomed (Reichert UltraCut S Ultramicrotome) at -120 °C using a glass knife. Contrast between the phases was achieved by immersing each sample in toluene for 2 min to selectively remove the PS at the surface. PS/PMMA samples were microtomed at room temperature. Contrast between the phases was achieved by immersing each sample in cyclohexane at 40 °C for 4 min to selectively remove the PS at the surface. Care was taken to ensure that the extraction was deep enough to show the surface morphology, but shallow enough as to not expose other features of the sample interior [115]. Samples were then coated with 50 Åof platinum and imaged at 5 kV using scanning electron microscopy (SEM, JEOL 6500).

Since the size scale of the domains and depth of field in the micrographs made it difficult to accurately detect the interfaces using automated methods, the interfaces were manually traced for this analysis. The traced images were then scanned and each phase

[§]The annealing was carried out on glass slides to obtain flat surfaces, desirable for the confocal microscopy (LSCM) technique.

was filled in using graphic software (CorelDRAW^{TM}). An analysis algorithm [115] was then used to determine the interface perimeter per unit area (Q) for each micrograph. For each set of conditions, 5 to 15 images were analyzed to determine the average Q. Assuming that the samples are isotropic, characteristic length for the cocontinuous morphologies is obtained by taking $1/Q$. It has been shown that phase size calculated using this 2D technique agrees with 3D results obtained using mercury porosimetry and X-ray microtomography as long as the phase size does not become too large [22, 53]. Stereological corrections [52] may be used to correct errors in the large size region (see Appendix B).

FLPS/SAN samples annealed on glass slides were imaged, without further treatment, using laser scanning confocal microscopy (LSCM). For each sample a stack of about 100 2D images at different focal depths (z-position) was obtained. 3D images were rendered from the stacks, obtaining a triangular mesh depicting the blend interface. Details of the microscopy method and the image analysis can be found in Chapter 3 [45]. The value of Q, in this case, was obtained by adding the surface area of all the triangles in the mesh and dividing by the volume of the sample, which was obtained by adding the volume of all the voxels forming the 3D image.

5.3 Results and discussion

5.3.1 Effect of block copolymer architecture

Figure 5.1 shows SEM micrographs of non-annealed and annealed 50/50 PS/PE blends without copolymer and with several different 40k PS-b-PE copolymers of different compositions. All micrographs on the left represent blends quenched immediately after mixing, and all micrographs on the right represent blends annealed for 15 min. at 170 °C. Note the scale bars differ for Figures 5.1a and 5.1b. Figure 5.2 plots the characteristic length, $1/Q$, for these blends, showing the effect of bcp symmetry on suppression of coarsening. Even the most asymmetric copolymer, 33-5k, reduces the coarsening rate, but much less so than the more symmetric ones.

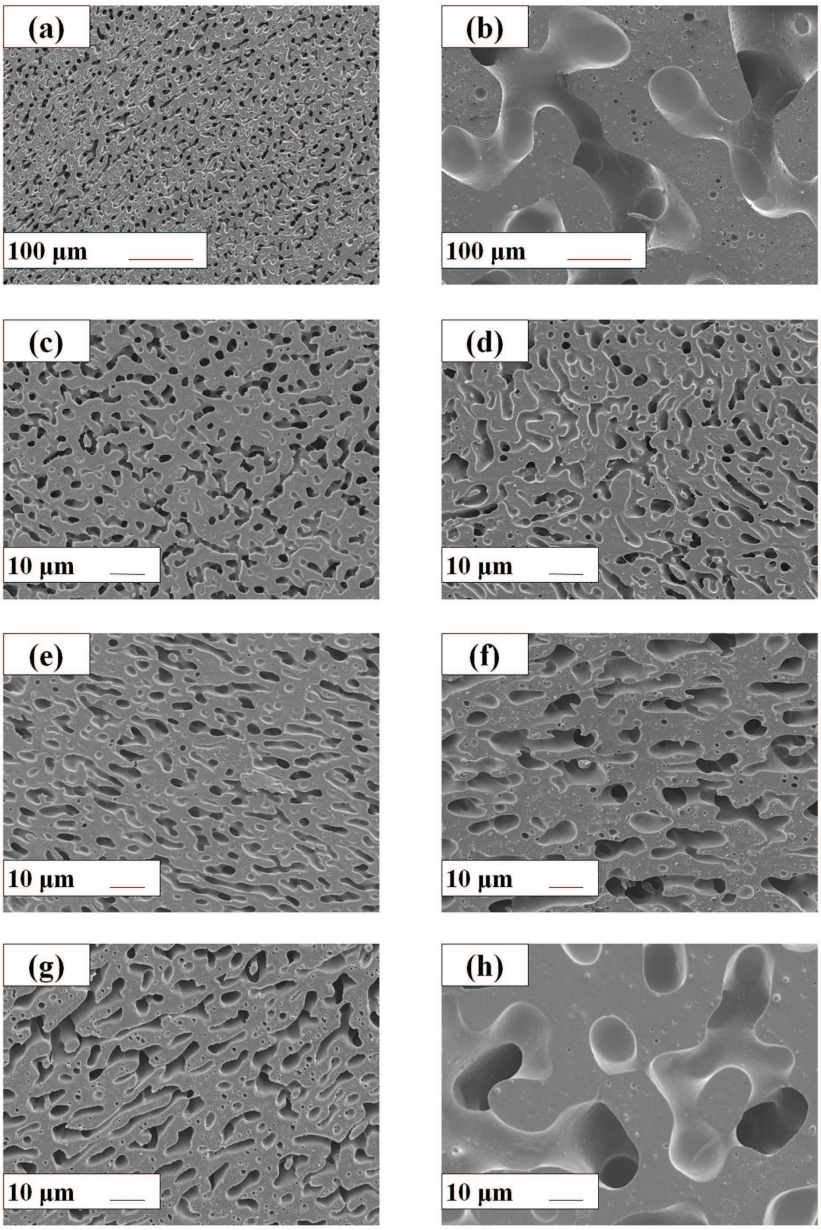

Figure 5.1: SEM micrographs of 50/50 PS/PE polymer blends with 1% 40k PS-b-PE, with various block architectures, annealed at 170 °C for (left column) 0 and (right column) 15 min. (a) and (b) have no bcp, (c) and (d) have 20-20k, (e) and (f) have 28.5-10.5k, and (g) and (h) have 33-5k.

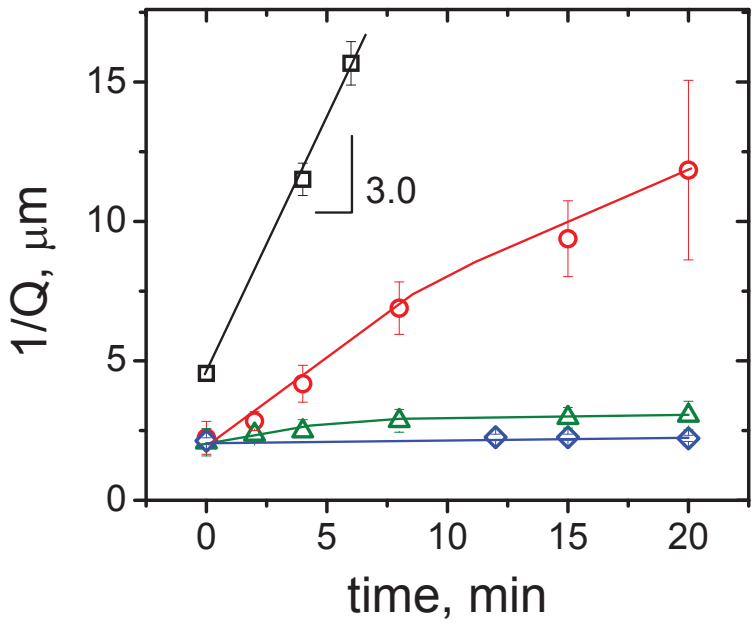

Figure 5.2: Plot of $1/Q$ vs annealing time at 170 °C for 50/50 PS/PE blends. Blends with (□) no bcp, (red ○) 1 wt% 33-5k PS-b-PE, (green △) 1% 28-10k PS-b-PE, and (blue ◇) 1% 20-20k PS-PE. Lines are to guide the eye and error bars represent standard deviation.

Table 5.2: Normalized interfacial coverage, characteristic size and interfacial tension.

Bcp	$^{d}\Sigma/\Sigma_{max}$		$^{a}1/Q_0$	$^{b}1/Q$	^{c} Normalized $c_1\Gamma$	
	after Mixing	^{e}after Annealing	μm	μm	initial	final
PS-b-PE (none)	$--$	$--$	4.6	43.8	1.00	$--$
0.1% 40k (20-20)	0.3	1.0	6.4	20.4	0.80	0.05±0.01
0.3% 40k (20-20)	0.6	1.3	3.7	8.4	0.42	0.00±0.01
1% 40k (20-20)	1.1	1.2	2.1	2.2	0.00	0.00±0.01
1% 40k (28.5-10.5)	$\sim$1	1.3	2.1	3.0	0.01	0.01±0.03
1% 40k (33-5)	$\sim$1	6.2	2.2	11.8	0.16	0.13±0.11
1% 6k	12.0	92	6.6	32.8	0.37	0.37±0.05
1% 100k	1.8	3.2	6.4	11.6	0.24	0.01±0.02
1% 200k	1.0	3.0	6.1	19.0	0.29	0.11±0.08
PS-b-PMMA (none)	$--$	$--$	2.5	13.2	1.00	$--$
0.1% 100k	0.2	1.0	3.2	10.3	0.75	0.08±0.03
0.3% 100k	0.4	1.8	2.6	8.0	0.38	0.04±0.01
1% 100k	1.1	1.8	2.2	3.6	0.13	0.01±0.01
3% 100k	1.3	1.7	0.8	1.2	0.01	0.01±0.00

Continued on Next Page...

Table 5.2 – Continued

1% 42k	1.6 g	1.8	[f]1.8	1.9	0.02	0.02±0.00
1% 160k	0.7	1.8	2.1	4.0	0.23	0.06±0.01
1% 260k	0.9 g	1.7	[f]3.2	4.7	0.18	0.08±0.01
FLPS-b-SAN (none)	−−	−−	[f]6.56	17.32	1.00	−−
0.1% 100k	[g]0.3	0.8	[f]5.8	11.46	0.22	0.04±0.02
0.5% 100k	[g]0.9	2.1	[f]3.42	5.50	0.11	0.04±0.02
1% 100k	[g]1.2	2.4	[f]2.31	3.28	0.05	0.04±0.01
5% 100k	[g]1.6	4.3	[f]0.62	0.94	0.02	0.01±0.00
1% 42k	[g]4.0	18.1	[f]4.46	8.42	0.34	0.17±0.04
1% 74k	[g]1.6	5.0	[f]2.62	3.25	0.15	0.09±0.02
1% 260	[g]0.9	1.1	[f]3.4	3.74	0.02	0.01±0.00
1% 900k	[g]0.6	1.2	[f]5.25	6.77	0.15	0.02±0.02

[a] Initial characteristic length.

[b] Characteristic size after 20 min. annealing.

[c] $c_1\Gamma$ was normalized using $c_1\Gamma$ for the blend with no bcp.

[d] Assumes all bcp is at the interface.

[e] Σ was calculated based on the specific interfacial area after 60 min or average area if coarsening arrested.

[f] Characteristic size after 5 min. annealing

[g] Calculated after 5 min. of annealing.

5.3.2 Effect of block copolymer molecular weight

Figure 5.3 shows the effect of annealing on 50/50 FLPS/SAN blends with and without 100k PS-b-PMMA. Micrographs on the left and right show blends after 5 min and 60 min of annealing, respectively. Figure 5.4 shows the effect of the bcp molecular weight on $1/Q$ for the PS/PE (Figure 5.4a), PS/PMMA (Figure 5.4b) and FLPS/SAN (Figure 5.4c) blends. For the three systems, the block copolymer which proved to be the most effective in slowing the coarsening were 40k PS-b-PE for PS/PE, 42k PS-b-PMMA for PS/PMMA and for FLPS/SAN 100 and 260k PS-b-PMMA.

5.3.3 Effect of block copolymer concentration

Figure 5.5 shows the effect of annealing on 45/55 PS/PMMA blends with varying concentrations of 100k PS-b-PMMA. All micrographs on the left represent blends annealed for 5 min. at 220 °C and all micrographs on the right represent blends annealed for 60 min. Figure 5.6 gives plots of $1/Q$ vs. annealing time for PS/PE, PS/PMMA and FLPS/SAN blends with varying concentrations of a copolymer that was effective at slowing coarsening. The plot in Figure 5.6a shows 50/50 PS/PE blends with 20-20k PS-b-PE, which was reported by Galloway et al. [20] The concentrations are 0.1, 0.3, and 1% PS-b-PE. The plot in Figure 5.6b shows 45/55 PS/PMMA blends with 100k PS-b-PMMA; concentrations are 0.1, 0.3, 1, and 3% PS-b-PMMA. The plot in Figure 5.6c shows 50/50 FLPS/SAN blends with 100k PS-b-PMMA with concentrations 0.1, 0.5, 1 and 5% PS-b-PMMA. In the three plots an initial rapid coarsening is observed, followed by very slow or negligible coarsening for bcp concentrations <1%.

The coverage in number of bcp molecules per interfacial area, Σ, is a useful parameter for understanding the plateaus in Figure 5.6. Σ was estimated by:

$$\Sigma = \frac{w_{bcp}\rho_{bcp}N_{av}}{QM_n} \tag{5.1}$$

where w_{bcp} is the weight fraction of bcp in the blend, ρ_{bcp} is the density of the bcp (0.855 g/cm^3 for PS-b-PE and estimated to be 1.0 g/cm^3 for PS-b-PMMA [111]), N_{av} is Avogadros number, and M_n is the number average molecular weight of the bcp. Equation 5.1 is based on the assumption that all the bcp added to the blends resides at the interface. The quantity Σ in Equation 5.1 is thus an apparent interfacial coverage

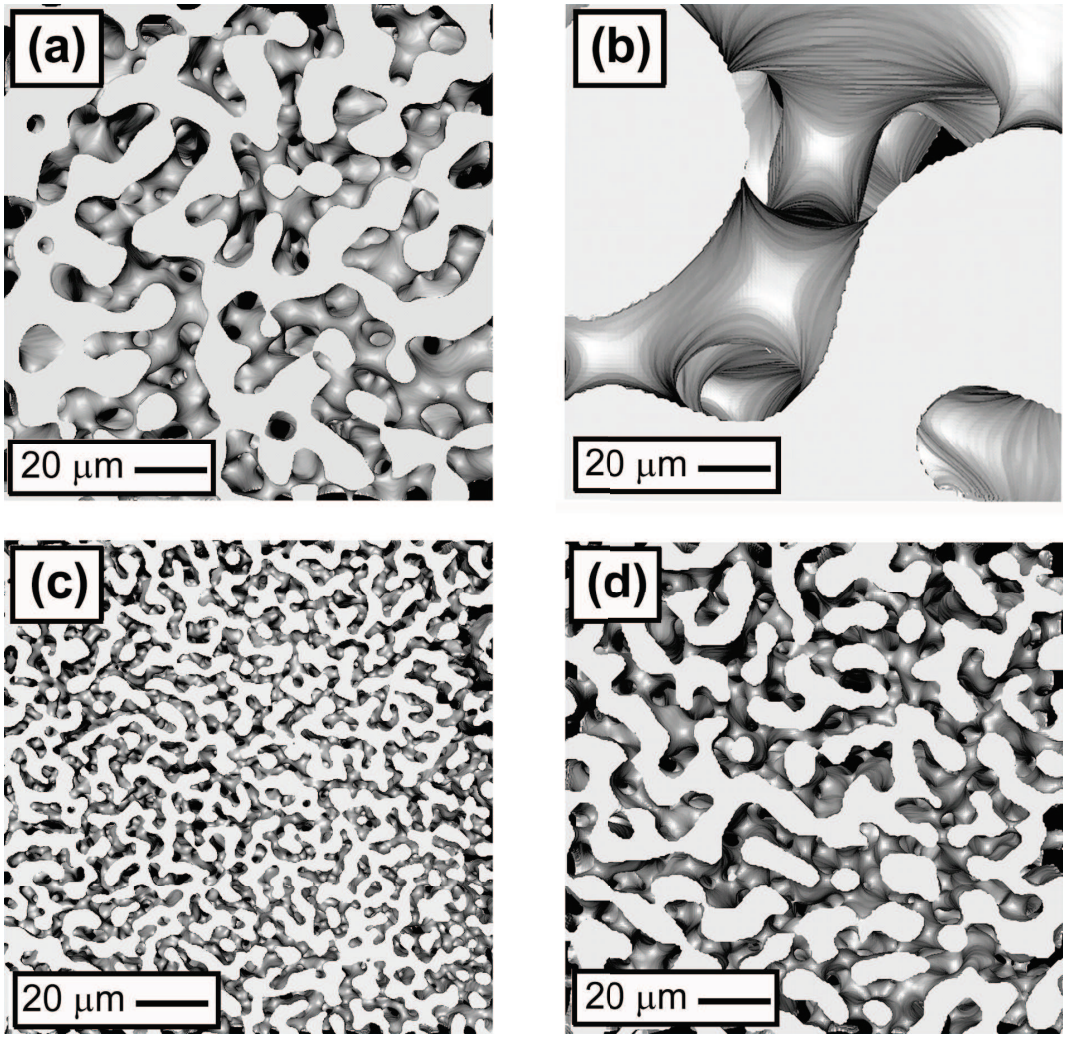

Figure 5.3: 3D rendered LSCM micrographs of 50/50 FLPS/SAN blends without bcp (a and b) and with 1% 100k PS-b-PMMA (c and d) prepared by mixing at 100 rpm for 10 min. at 180 °C. Micrographs on the left represent blends annealed for 5 min. after mixing, while micrographs on the right represent blends annealed for 60 min. at 200 ° C.

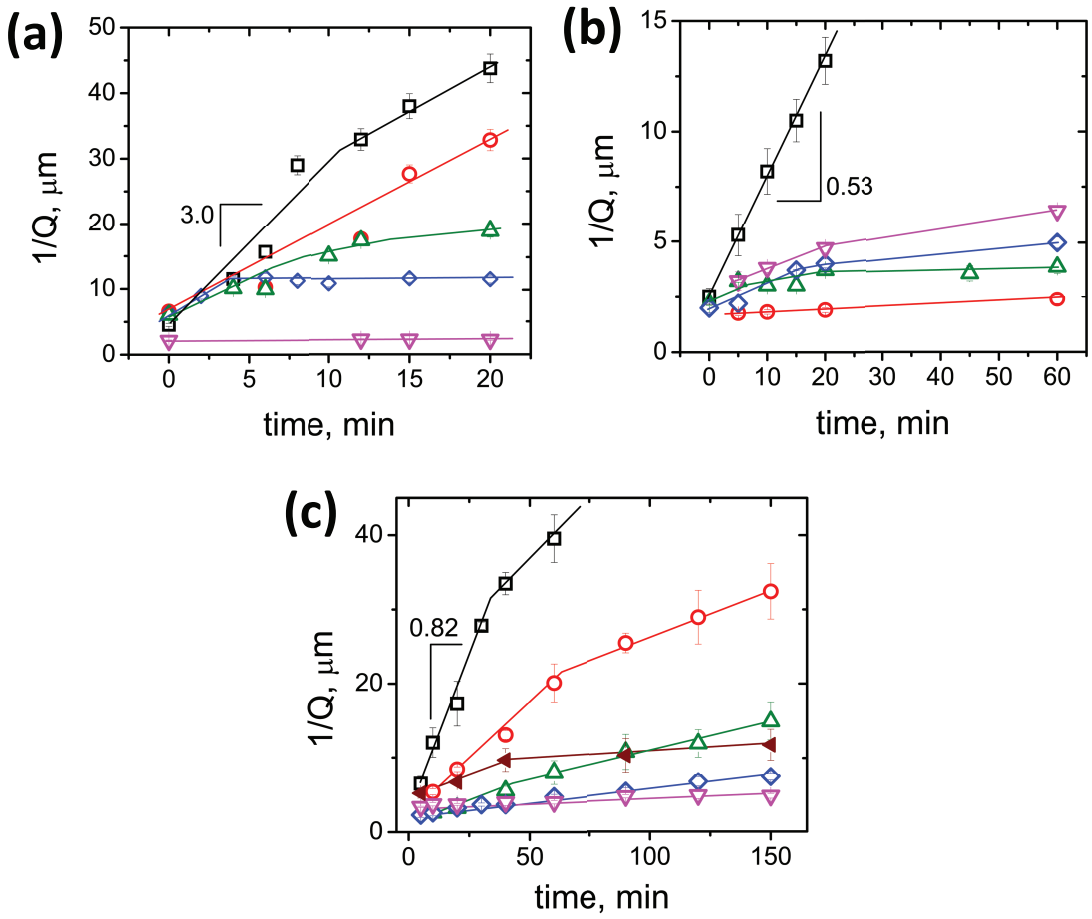

Figure 5.4: Plot of $1/Q$ vs. annealing time for (a) 50/50 PS/PE, (b) 45/55 PS/PMMA and (c) FLPS/SAN blends: In (a): blends with (□) no bcp, (red ○) 1% 6k PS-b-PE, (green △) 1% 200k PS-b-PE, (blue ◇) 1% 100k PS-b-PE, and (pink ▽) 1% 20-20k PS-b-PE [20]. In (b): blends with (□) no bcp, (pink ▽) 1% 260k PS-b-PMMA, (blue ◇) 1% 160k PS-b-PMMA, (green △) 1% 100k PS-b-PMMA, and (red ○) 1% 42k PS-b-PMMA. In (c): blends with (□) no bcp, (red ○) 1% 42k PS-b-PMMA, (green △) 1% 74k PS-b-PMMA, (blue ◇) 1% 100k PS-b-PMMA, (pink ▽) 1% 260k PS-b-PMMA, and (wine ◄)1% 900k PS-b-PMMA Lines are to guide the eye and error bars represent standard deviation.

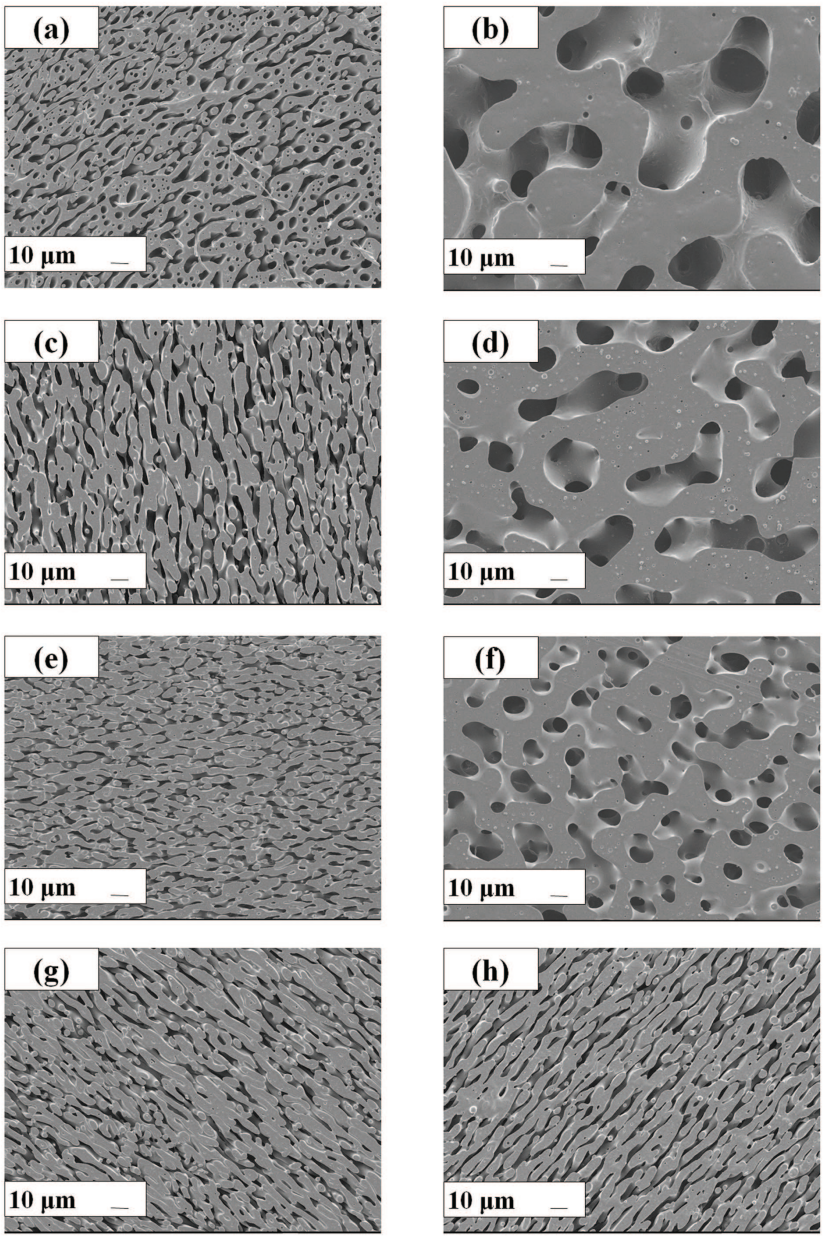

Figure 5.5: SEM micrographs of 45/55 PS/PMMA blends, with various amounts of 100k PS-b-PMMA, annealed at 220 °C for (left column) 5 min. And (right column). (a) and (b) have no bcp, (c) and (d) have 0.1%, (e) and (f) have 0.3%, and (g) and (h) have 1% PS-b-PMMA.

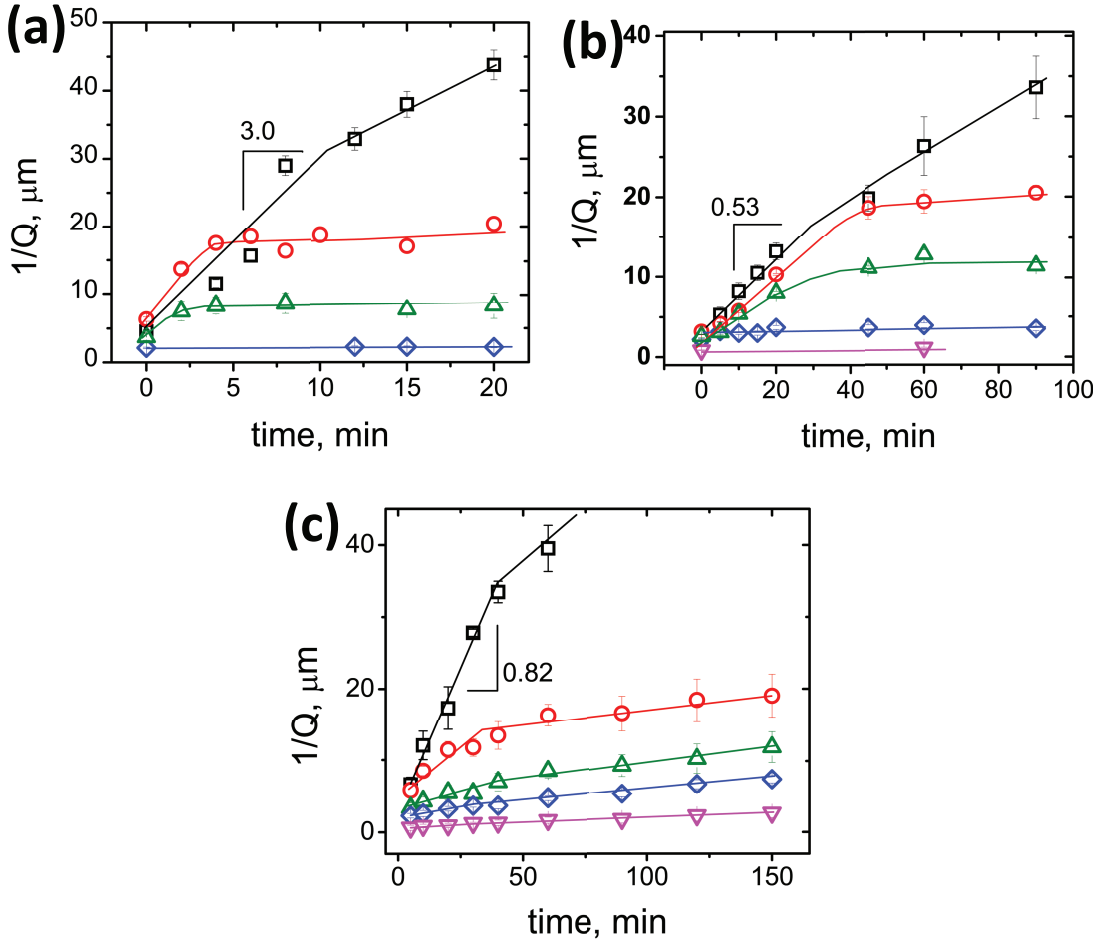

Figure 5.6: Plots of $1/Q$ vs. annealing time for (a)50/50 PS/PE [reference Galloway et al. 2005], (b) 45/55 PS/PMMA , and (c) 50/50 FLPS/SAN blends. In (a): blends with (□) no bcp, (red ○) 0.1% 20-20k PS-b-PE, (green △) 0.3% 20-20k PS-b-PE, and (blue ◇) 1% 20-20k PS-b-PE. In (b): blends with (□) no bcp, (red ○) 0.1% 100k PS-b-PMMA, (green △) 0.3% 100k PS-b-PMMA, (blue ◇) 1% 100k PS-b-PMMA, and (pink ▽) 3% 100k PS-b-PMMA. In (c) : blends with (□) no bcp, (red ○) 0.1% 100k PS-b-PMMA, (green △) 0.5% 100k PS-b-PMMA, (blue ◇) 1% 100k PS-b-PMMA , and (pink ▽) 5% 100k PS-b-PMMA. Lines are to guide the eye and error bars represent standard deviation. Note the difference in the time scales.

that we expect to be equal to or greater than the actual number of chains per area adsorbed to the interfaces. The maximum interfacial coverage Σ_{max} has been estimated by approximating the coverage of a saturated monolayer by the area per chain in the lamellar structure of the pure bcp. Lyu et al. reported $\Sigma_{max} = 0.25$ chains/nm^2 for the 20-20k PS-b-PE [104]. Using the scaling relation, $\Sigma_{max} \sim M_n^{-1/3}$, Σ_{max} is estimated to be 0.47 chains/nm^2, 0.18 chains/nm^2, and 0.15 chains/nm^2 for the 6k, 100k, and 200k PS-b-PE, respectively. For the 42k, 74k, 160k, 260k and 900k PS-b-PMMA, Σ_{max} is estimated to be 0.159, 0.132, 0.102, 0.087 and 0.057 chains/nm^2, respectively, using $\Sigma_{max} = 0.119$ chains/nm^2 for the 100k PS-b-PMMA [116] and the same scaling relation. Table 5.2 shows Σ/Σ_{max} for the blends after mixing and after 60 min or from the average value of $1/Q$ when coarsening arrested.

The interfacial coverage results in Table 5.2 give insight into the plateaus in Figure 5.6. At 0.1% 40k PS-b-PE and 0.1% 100k PS-b-PMMA coarsening stops just at complete coverage, $\Sigma/\Sigma_{max} = 1$. For the higher concentrations of 40k PS-b-PE $\Sigma/\Sigma_{max} = 1.21.3$, which may also represent coarsening to just full saturation within the accuracy of this calculation. However, this concentration >1 also could indicate that some of the bcp is in micelles, perhaps formed during mixing. The fact that after mixing the 1% sample is already slightly above interface saturation supports micelle formation during mixing. All the compatibilized PS/PMMA blends, except the 0.1% 100k PS-b-PMMA, coarsen to $\Sigma/\Sigma_{max} = 1.8$ and some start at $\Sigma/\Sigma_{max} > 1$, again indicating micelle formation during mixing. The PS/PE blend compatibilized with 6k PS-b-PE has very high Σ/Σ_{max} values, pointing to relatively high solubility of bcp in the homopolymer. The same behavior was observed in the FLPS/SAN blend compatibilized with 42k PS-b-PMMA.

5.3.4 Theoretical considerations

The coarsening that we observe in these experiments is driven by interfacial tension. Several authors have predicted that the characteristic length scale, $1/Q$, of a cocontinuous structure should increase linearly with time (see section 4.1) [17, 14, 40]

$$\frac{dQ^{-1}}{dt} = c_1 \frac{\Gamma}{\eta} \tag{5.2}$$

where Γ is interfacial tension and η is polymer viscosity. Here c_1 is a dimensionless number that may depend upon the volume fractions of the two phases, the ratio of

their viscosities, and details of the interfacial geometry. This prediction follows from a simple balance of viscous stresses against capillary forces across curved interfaces [14]. If the structure coarsens in a self-similar manner (i.e., if the only change in statistical geometry induced by coarsening is a change in characteristic length), and the interfacial tension remains constant, then c_1 should be independent of time, and should depend only upon volume fraction and viscosity ratio. This prediction is roughly consistent with the nearly linear increase of $1/Q$ with time that we, and others [17, 14, 40, 19], observed for immiscible blends in the absence of copolymer. Our observation of a decrease in dQ/dt at long times in the absence of block copolymer may indicate, however, that the coarsening is not perfectly self-similar over the time scale of the experiments (see Figures 5.4 and 5.6), as discussed in Chapters 3 and 4 and in Ref. 45.

In the presence of a copolymer some of the systems that we have studied exhibit an initial linear increase of $1/Q$ with time, followed by a dramatic decrease (or complete suppression) in the rate of coarsening. We assume that this dramatic decrease is the result of a decrease in interfacial tension caused by an increase in the interfacial concentration of adsorbed copolymer: as the system coarsens, the decrease in interfacial area tends to increase the concentration of adsorbed copolymer per unit area, and thus decrease the interfacial tension. If this process drives the interfacial tension to zero, the driving force for coarsening is removed, and coarsening ceases.

In its simplest form, the above argument assumes that any change in interfacial concentration during coarsening is solely a result of change in interfacial areas, but that no copolymer is transported to or from the interface during coarsening. This will be the case, however, only if there are significant kinetic or transport limitations to the adsorption or desorption of copolymer to or from the interface. In the absence of such limitations, coarsening would tend to force copolymer to desorb from the interface as the interfacial area decreased.

The opposite point of view would be to assume instead that there are no significant kinetic or transport limitations, and that the interface thus remains in diffusional equilibrium with a reservoir of dissolved copolymer and (generally) micelles. In this case, coarsening would tend to force copolymer to desorb in order to maintain a nearly constant interfacial concentration.

Before considering kinetic limitations in more detail, we discuss the expected behavior of the interfacial tension in true thermal equilibrium, along the lines of Refs. 41, 117 and 118. In equilibrium, the interfacial tension of a macroscopic interface decreases with increasing concentration of dissolved copolymer until the critical micelle concentration (CMC) is reached in one of the two coexisting phases. For concreteness, consider a mixture of A and B copolymers in which the relevant CMC (i.e., the one that occurs at lower surfactant chemical potential) is that of the A phase. Once the concentration in the A phase exceeds this CMC, micelles form, and the equilibrium interfacial tension saturates to a value that is almost independent of concentration, which we will refer to as Γ_{cmc}. As discussed in Ref. 41, Γ_{cmc} is closely related to the difference between the free energy per interfacial area in the micellar state and that in a flat macroscopic interface. This free energy difference, and thus the equilibrium interfacial tension, depends strongly upon the composition of the copolymer and the structure of the micelles that it forms. Within a series of AB diblock copolymers of varying composition f_A, for a given pair of homopolymers, Γ_{cmc} is expected to reach an almost vanishing minimum value at a value of f_A that corresponds to the *balance point* at which an interfacial monolayer of copolymer has a vanishing spontaneous curvature. In the idealized case of an interface between two homopolymers with the same molar volumes and the same statistical segment lengths, this balance point is $f_A = 0.5$.

We suspect that the most important kinetic limitation in this experiment is a limitation on the rates at which micelles can dissolve and reform. The rates at which micelles can dissolve into unimers, or form from a solution of dissolved unimers, can be described by an activated state theory analogous to the theory of homogeneous nucleation, as discussed by Semenov [117]. He found that the magnitude of the barrier to micelle formation depends primarily upon the product χN_{core}, and increases as $N_{core}^{4/3}$ with increasing core chain length. The predicted barrier becomes prohibitively large ($\gg$ 10 kT) for χN_{core} greater than a critical value of order 10. The implication is that only modestly segregated micelles can dissolve and reform rapidly enough to maintain equilibrium between an ensemble of micelles and a macroscopic interface.

Semenov's predictions are consistent with the results of our own work on measurements of interfacial tension in the presence of a block copolymer additive [118]. We found that very low equilibrium interfacial tensions were achievable reasonably rapidly with

a series of low molecular weight diblock copolymers, for which χN_{core} approximately, but that transport of copolymer to the interface was several orders of magnitude slower for a symmetric copolymer with $\chi N_{core} = 25$, making it impossible for us to equilibrate systems containing the higher molecular weight copolymer. We attributed the slow transport of the longer copolymer to slow micelle dissolution.

The experiments presented here are sensitive to limitations on transport of copolymer to the interface only during the initial mixing process. The subsequent coarsening process is instead sensitive to the rate at which copolymer can be driven off the interface and reform into micelles. During coarsening, at concentrations above the CMC of the A homopolymer, a nonzero, nearly constant equilibrium tension Γ_{cmc} can be maintained if copolymer can continuously desorb from the interface and reform into micelles: for the interface to stay in equilibrium with its surroundings at concentrations above the CMC, a constant concentration of dissolved free copolymers equal to the CMC must be maintained in the A phase, as well as a constant interfacial concentration. In equilibrium, any material that is driven off the interface must thus form micelles. Conversely, if micelles cannot form at the CMC chemical potential over experimentally relevant time scales, then upon coarsening the chemical potential within the interface can be driven above that of an equilibrated micellar solution, and so the interfacial tension Γ can be driven below Γ_{cmc}, potentially to zero.

The above discussion suggests three possible scenarios: (1) For sufficiently short copolymers, micelles may not form in equilibrium. (2) For somewhat longer copolymers, micelles may form, but micelle dissolution and creation may remain rapid. (3) For even longer copolymers, micelles will form, but micelle dissolution and creation can become very slow at the CMC. Which scenario will occur is controlled primarily by the value of the product χN_{core}, which controls both the thermodynamic and kinetic stability of a micelle. Each of these scenarios is discussed below in more detail:

- Case (1): Sufficiently short copolymers do not form micelles. Diblocks with a B minority block that remain disordered in the limit of a pure copolymer melt, rather than forming an ordered phase, will generally also not form micelles in a dilute solution of copolymer in a A homopolymer matrix. In this case, we expect the equilibrium interfacial tension to decrease somewhat with increasing concentration of dissolved copolymer, but to remain nonzero at all concentrations.

Also, because transport is not limited by slow micelle creation and dissolution, we expect copolymer to able to desorb as the interfacial area decreases, and thereby maintain the nonzero equilibrium interfacial tension of an interface in equilibrium with a solution of molecularly dissolved copolymer. In this case, we thus expect *continuous coarsening at a nearly constant rate somewhat lower than that observed in the absence of copolymer.* We also expect that the apparent interfacial coverage could greatly exceed unity, i.e. $\Sigma/\Sigma_{max} \gg 1$.

- Case (2): For somewhat higher molecular weight copolymers, there will exist a range of parameters in which micelles form, but micelle dissolution and formation may remain facile. Semenov's theoretical estimates [117], and our experience with interfacial tension measurements [118], suggests this will occur in (roughly) the range $\chi N_{core} = 10 - 20$. In this case, at concentrations above the CMC, the interface can remain in equilibrium, and so will maintain a nearly constant equilibrium interfacial tension Γ_{cmc}. Coarsening should proceed at a nearly constant rate that is independent of concentration above the CMC, but that depends upon the composition of the copolymer. Because Γ_{cmc} becomes very small for nearly balanced copolymers, this rate of coarsening may be very slow (perhaps immeasurably so) for such copolymers. In this case, we also expect that the interfacial tension should reach Γ_{cmc} during the mixing process, since transport to the surface is also not limited by slow micelle dissolution. We do not expect diffusion limitations to be important while the system is being subjected to intense mixing. We thus expect to observe a *nearly constant rate of coarsening starting from immediately after mixing ceases, but at a rate much lower than case (1)* and even near zero for nearly balanced copolymers.

- Case (3): For sufficiently strongly segregated micelles ($\chi N_{core} \gg 20$), rates of spontaneous micelle dissolution and reformation will become negligible at the equilibrium CMC. During mixing, this could limit the amount of copolymer delivered to the surface, and thus could result in a subsaturated interface with $\Gamma > \Gamma_{cmc}$ when mixing ceases. These samples will then coarsen until the interface saturates (as discussed above). During coarsening, copolymer will be stuck in the interface allowing the interfacial tension to be driven to zero by the coarsening process. This

scenario could thus lead to a *measurable initial rate of coarsening*, even for nearly balanced copolymers, followed by a *dramatic decrease in the rate of coarsening* as the interfacial tension approaches zero.

5.3.5 Experimental results versus theory

There is some evidence for all three of the above scenarios in the coarsening experiments with PS/PE, PS/PMMA and FLPS/SAN systems. We first consider the data for PS/PE systems.

The behavior of the 6k symmetric copolymer (Figure 5.4a) copolymer appears to be consistent with that expected in scenario (1): This system coarsens continuously at a rate slightly less than that of the system with no copolymer. At $\chi N_{core} = 4$ this symmetric copolymer is actually disordered and thus not expected to form micelles.

In the PS/PE systems, all of the 40k copolymers (Figure 5.2) exhibit behavior that appears to be consistent with scenario (2). All three systems exhibit a coarsening rate that is much lower than that obtained in the absence of copolymer. The rate of coarsening is easily measurable only for the 33k-5k copolymer, which is the most asymmetric of the three copolymers, for which we expect the highest value of Γ_{cmc}. We show below that the rates of coarsening for these systems are consistent with the values of Γ_{cmc} predicted from equilibrium SCFT. One potential problem with this interpretation is the fact that our estimate of a value of $\chi N_{core} = 25$ for the 40k symmetric copolymer, using literature values for χ, is similar to our estimate of the same quantity for the PI/PDMS copolymer that was found to exhibit very slow transport to the interface in Ref. 118. Our proposed interpretation thus requires us to assume either that limitations on micelle dissolution and formation have a significant effect on this experiment only at somewhat higher values of χN_{core} than those at which they dramatically suppress transport in a macroscopic interfacial tension measurement, or that there is a significant uncertainty in the literature value of χ in one of these systems.

The behavior of the 100k and 200k symmetric PS-b-PE copolymer (Figure 5.4a) appear to be consistent with the predictions of scenario (3): Both exhibit initial coarsening followed by a saturation of the characteristic length $1/Q$.

Next, we consider our results for symmetric PS/PMMA polymers, shown in Figure 5.4b. All four symmetric PS/PMMA copolymers (42k, 100k, 160k, and 260k) yielded

slow coarsening. The simplest explanation of this, by analogy with the explanation given above for the PS/PE systems, is that all of these systems are exhibiting scenario (2), micellization with facile micelle creation and dissolution. Our estimates of $6 < \chi N_{core} < 25$ for the 42k, 100, and 160k polymers are all less than or equal to our estimate for the symmetric 40k PS-b-PE polymer, which exhibited similar behavior. Our estimate of $\chi N_{core} = 44$ for the 260k PS/PMMA copolymer is, however, significantly higher than that of the 40k PS-b-PE copolymer, forcing us to (again) revise upward our estimate of the range of values of χN_{core} over which scenario (2) can be obtained.

Finally, three of the block copolymers used in the PS/PMMA blend (42k, 100k and 266k PS-b-PMMA) and two more (74k and 900kPS-b-PMMA) were used to compatibilize the FLPS/SAN blend. Remarkably, the most effective molecular weight for the latter system was the 260k PS-b-PMMA (Figure 5.4c), in contrast to 42K PS-b-PMMA for the PS/PMMA system. Another big discrepancy between the PS/PS-b-PMMA/SAN system and the other two systems previously discussed, is that scenario (2) occurs at around $\chi N_{core} = 0.3$, which is about two orders of magnitude smaller than the values corresponding to the PS/PE and PS/PMMA blends. This can be understood if we consider that mixtures of PMMA and SAN can be miscible. Fowler et al. [119], reported negative χ values and observed miscibility in blends of PMMA and SAN with AN-content between approximately 9 and 33 %w. The compatibility between the SAN and PMMA blocks favors the presence of the copolymer in the SAN phase. Once there, the equilibrium between micelle formation and dissolution will be governed by the interaction between the core block (i.e. the PS-block) and the SAN matrix; i.e. by $\chi_{PS/SAN}$. Due to the chemical similarity between PS and SAN, the value of $\chi_{PS/SAN}$ is very small ($2.4 \cdot 10^{-4}$), which explains why very high molecular weights are required for micelle formation. Hence, the onset of scenarios (2) and (3) are shifted to much smaller values of χN_{core}.

It is evident that the miscibility between SAN and PMMA complicates the analysis and is not considered in the Semenov's predictions. The analysis of A/B/A-b-C systems is beyond the scope of this paper. Nevertheless, the observed behavior in the FLPS/SAN system can be rationalized with the three scenarios: (1) with 42K and 74k PS-b-PMMA, (2) with 100k and 260k PS-b-PMMA and (3) with 900k PS-b-PMMA.

The block copolymers used for the concentration study (Figures 5.5 and 5.6) are all

expected to follow scenario (2), i.e. coarsen until their concentration in the interface is in equilibrium with their micelles. At equilibrium they all should coarsen at the same rate, independent of the concentration. The normalized interfacial tension results in Table 5.2 for those systems are in reasonable agreement, supporting scenario (2).

Taken as a whole, the data remains broadly consistent with our proposed interpretation (assuming that our estimates of χ are sufficiently accurate) if we assume that the crossover between scenarios (2) and (3) occurs somewhere near $\chi N_{core} = 50$, based on the fact that the two PS/PE systems for which χN_{core} exceeds this value exhibited the behavior predicted for scenario (3) and the PS/PMMA with 260k block copolymer does not fit scenario (2). The FLPS/SAN system also exhibited this behavior but at much lower values of χN_{core} due to the low values of $\chi_{PS/SAN}$.

5.3.6 Comparison to equilibrium SCFT

The above discussion suggests that the interfaces in the PS/PE blends with 40 k PS-b-PE copolymer are probably in equilibrium with a reservoir of micelles. To test this idea, we have attempted to compare the values of normalized interfacial tension Γ/Γ_{max} that we inferred for the three different 40k copolymers to values predicted by equilibrium self consistent mean field theory (SCFT).

Our analysis of these systems makes use of an approximation for Γ_{cmc} that was introduced in Eq. (21) of Ref. 41, in which Γ_{cmc} is expressed as a function of the elastic parameters of a saturated monolayer. All of our calculations use a interaction parameter of $\chi = 0.07$, and an average statistical segment length of b=6 Ådefined for a reference volume of v=135 Å^3. All SCF calculations have used monodisperse PE polymer with $N = 642$ (corresponding to the experimental value M_n=18 kg/mol and ρ=0.78 g/cm^3 for PE), and a monodisperse PS homopolymer with N=586 (corresponding to M_n=61 kg/mol and ρ=0.97 g/cm^3 for PS). To calculate Γ_{cmc} as a function of copolymer composition for several hypothetical series of copolymers we keep the core block size fixed and vary the corona block size. The three curves shown in Figure 5.7 are the results of a series of SCFT calculations of the Helfrich elastic parameters as functions of copolymer composition, in which the size of the PE block was taken to be equal to the size of the minority block of each 40k PS-b-PE copolymer. The single solid dot on each of the three curves marks the experimental value of f_{PE}, and is thus the predicted value for

one of the three systems. Each of the three curves has a balance point at which Γ_{cmc} vanishes, which is the composition at which the spontaneous curvature vanishes for a copolymer with the specified core block size. The composition of the balance point is approximately $f_{PE} = 0.45$ for all three block sizes. Note that the 20-20k ($f = 0.55$) and 28.5-10.5k (f=0.31) bcps fall on either side of the balance point, but remain close enough to the balance point to yield very low predicted values of $\Gamma_{cmc}/\Gamma_0 = 0.03 - 0.04$. The experimental values of Γ_{cmc}/Γ_0, shown as open squares in Figure 5.7, are even lower. The predicted value of $\Gamma_{cmc}/\Gamma_0 = 0.23$ for the 33-5k bcp is also slightly higher than the observed value of 0.16. We conclude that the data is broadly consistent with these predictions. 20-20k ($f_{PE} = 0.55$) and 28.5-10.5k ($f_{PE} = 0.31$) bcp fall on either side of the balance point, but are still close enough to produce appreciable reductions in Γ (see Table 5.2). The 33-5k bcp falls farther away from the balance point, but also shows some reduction in Γ. his would suggest that the shape of the quadratic is fairly broad for this system. Qualitatively, the theory appears to agree favorably with PS/PE experimental results.

5.4 Conclusions

The coarsening during annealing of cocontinuous polymer blends was measured via SEM and LSCM with image analysis. For all three systems studied here, i.e. PS/PE and PS/PMMA and FLPS/SAN, symmetric diblock copolymers of intermediate molecular weight were found to be most effective at stopping coarsening. The results were consistent with the theory proposed here in which three scenarios are expected, namely (1) poor compatibilization with short block copolymers due to its rapid desorption from the decreasing interfacial area during coarsening, (2) good compatibilization with intermediate size copolymers due to establishment of an equilibrium between desorption and micelle formation, and (3) initial fast coarsening followed by an abrupt stop of coarsening with sufficiently large copolymers, due to an incapacity of these to be transported to the interface and to desorb from it. Scenario (3) can also lead to good compatibilization if mixing can drive enough block copolymer into the blend interface.

The coarsening rate of cocontinuous blends can be used to quantify reduction of interfacial tension due to the addition of block copolymer. This is a difficult property

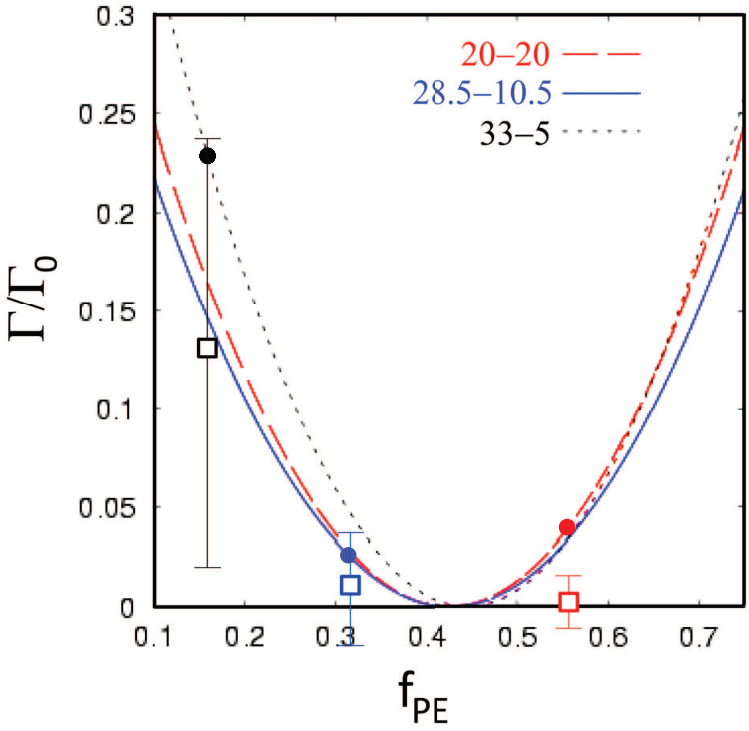

Figure 5.7: Interfacial tension reduction vs. volume fraction of PE block in PS-b-PE in the PS/PE system. Lines are calculated from ref 41. Small circles mark experimental f_{PE}. Open squares are data from Table 5.2 for the three 40k block copolymers with different symmetry.

to measure by the usual pendant or spinning drop methods since it can take many hours for block copolymers to diffuse the typical distances required to reach equilibrium in these samples [120]. The interfacial tension reduction determined from coarsening measurements are consistent with values calculated by SCFT. In addition to being a class of multiphase polymer materials of practical importance, cocontinuous blends provide valuable insight into the thermodynamics and dynamics of block copolymers.

Chapter 6

Rheology of Non-compatibilized Blends during Coarsening

6.1 Introduction

Due to the interdependence between microstructure and viscoelastic properties the flow behavior of incompatible polymer blends is rather complex. Flow fields applied during rheological characterization may alter the blend morphology, whereas the microstructure affects the rheology. The parameters governing the microstructure stability as well as the rheology-morphology interplay include the blend composition, the component viscoelastic properties, the viscosity ratio, and the interfacial tension [96, 1]. Veenstra et al. studied the effect of interfacial tension, viscosity and physical cross-links in the coarsening of thermoplastic blends with cocontinuous morphologies [17]. Yuan and Favis [19] observed that the the stability of cocontinuous structures is independent of the viscosity ratio but highly dependent on the component viscosities. To our knowledge, no study on the component properties-morphology-rheology of cocontinuous blends has been reported. This study is aimed to analyse these relations, paying particular attention to the interfacial tension and viscosity ratio.

In general, rheological behavior of immiscible blends is characterized by an extra-contribution to the elastic modulus at low frequencies, corresponding to long-time relaxation processes, which is due to the presence of the interface [27, 24, 96, 121]. This increase in elasticity is manifested as a shoulder in the plot of G' vs frequency for blends

with disperse morphologies and as a power law for blends with cocontinuous structures [24].

The flow behaviour of immiscible liquids was studied for the first time by Taylor [122], who extended the Einstein's work on relative viscosity of suspension spheres [123, 124, 125] to emulsions of Newtonian drops in Newtonian liquids. Taylor's pioneering work was further extended by Oldroyd and by Choi-Schowalter, who derived expression for the linear viscoelasticity of dilute [126, 127] and semidilute emulsions [128] of Newtonian liquids, respectively. These expressions were refined to account for the viscoelasticity of the components [129, 27]. These studies resulted in models for the viscoelastic response of blends with matrix-droplets microstructure. In particular, Palierne's model has successfully been applied to describe the rheological response of different blend systems [130, 131, 132]. It was also shown by Friedrich et al. [131] that particle-size distributions can be derived from measured blend data if the interfacial tension is known. A detailed analysis of Paliernes model for the case of complex interfacial stress states is given by Jacobs et al. [133].

Doi and Otha proposed a model to describe the rheological behavior of two phase systems with Newtonian components, mixed in a nearly equal ratio [28]. Lee and Park extended this model to account for a wider range of component properties [134]. In these models the morphology of a blend is described by two characteristic quantities: a scalar Q which represents the specific interfacial area and a tensor q_{ij} which is a measure of the interface anisotropy. These models are not restricted to a particular type of morphology, but they consider systems with complex interfaces formed due to coagulation, rupture, and deformation of droplets. Hence, in principle they should be able to describe the rheological response of cocontinuous blends. Vinckier and Laun [32] found good agreement between predictions of the DoiOhta theory for the elastic modulus of immiscible blends and experimental data of a 40/60 polymethyl methacrylate/α-methyl styrene-ran-acrylonitrile copolymer blend. According to Doi-Ohta's theory the extra stress due to the presence of interface in two phase systems is proportinal to q which, along with Q, can be implicitly computed via semiphenomenological equations. However this parameter has never been measured experimentally, perhaps because of the lack of data of local normal vector of the interface n (see Eqn 6.5), which is not accessible from 2D images of the microstructure but it is from 3D images.

In the present study morphology of FLPS/SAN blends with different viscosity ratio and interfacial tension were fully characterized using rheology and 3D imaging coupled with differential geometry. The coordinate transformation method (developed in chapter 3) was used to obtain the specific interfacial area and local curvatures of the blends during coarsening. For all the blends, the characteristic length grew linearly with time at early times of annealing. At late times, a decrease in the rate of coarsening was observed. The rate of coarsening was observed to be proportional to the ratio between the interfacial tension and the blend viscosity. This is in accordance with classical theories of spinodally separating systems [14]. The rheological response of the blends were tested before and during the coarsening process. It was found that the interfacial tension has a bigger effect than the viscosity ratio on both the initial extra contribution to the elastic modulus and its decrease rate during coarsening. A simplification of the Doi-Ohta model [28] was proposed based on the fact that the measured degree of anisotropy is negligible, compared to the specific interfacial area. A power law like relation between the elastic modulus and the annealing time (with exponent -1) was obtained with this approximation. Experimental data show two regimes of decrease of elastic modulus described by power laws, with exponent values smaller than the predicted by the approximation. Further research is required to understand this discrepancy.

6.2 Experimental

6.2.1 Materials

The synthesis and characterization of the polymers used in this study is described in Chapter 2. Three polystyrenes with different molecular weight and three styrene-ran-acrylonitrile copolymers with different AN content were used here. Table 2.2 shows the key properties of the blend components for these experiments. As mentioned before the synthesis of these polymers was carefully designed to prepare blends with different values of viscosity ratio and interfacial tension. The rheological measurement methods for the components were described previously (see section 2.3). Figure 6.1 show the complex and elastic moduli as well as $\tan\delta$ as a function of frequency for the components measured at 200 $^{\circ}C$. The complex viscosity versus frequency is shown in Figure 2.4. It should be noted that the viscoalestic properties of the three SAN copolymers are

very similar to those of FLPS120K, but significantly diferent to those of FLPS40K and FLPS200K. The viscosity ratios between the blend components ($p = \eta_{0,FLPS}/\eta_{0,SAN}$) are show in Table 6.1. Zero shear viscosities (η_0) were obtained by fitting complex viscosity data with the Cross model (see Figure 2.4).

Table 6.1: Key characteristics of blends.

Blend	p	$^a\eta_{comp}$	$^b\Gamma$ mN/m	Γ/η_{comp} $\mu m/min$
PS40K/SAN10	0.044	443	- -	39.2
PS40K/SAN30	0.037	483	- -	138
PS120K/SAN10	0.704	1770	0.29 ± 0.07	9.84
PS120K/SAN20	0.625	1878	0.86 ± 0.14	27.5
PS120K/SAN30	0.592	1931	1.11 ± 0.20	34.5
PS200K/SAN10	3.24	3798	- -	4.58
PS200K/SAN30	2.72	4143	- -	16.1

$^a\eta_{comp} = \sqrt{\eta_{FLPS} \times \eta_{SAN}}$.

$^b\Gamma = \frac{\Gamma_{BTM}+\Gamma_{RM}}{2}$ (see Appendix C).

6.2.2 Blend preparation, annealing and 3D imaging

Blends were prepared in batches of 5 g using a DACA microcompounder (DACA Instruments) at 180 $°C$ for 10 min. A schematic of the blending and annealing processes is shown in Figure 3.2 (Chapter 3). The blends listed in Table 6.1 were prepared with a composition 50/50 w/w and annealed for different times in a hot press at 200 $°C$, as described in section 3.3. The annealed blends were imaged using a laser scanning confocal microscope (Olympus Fluo-view 1000) with the operating conditions described in Chapter 4. The confocal images were deconvoluted, binarized and reconstructed into 3D images following the processes detailed in Chapter 3. The CT method, developed in section 3.4, was used here to calculate the local curvatures and the specific interfacial

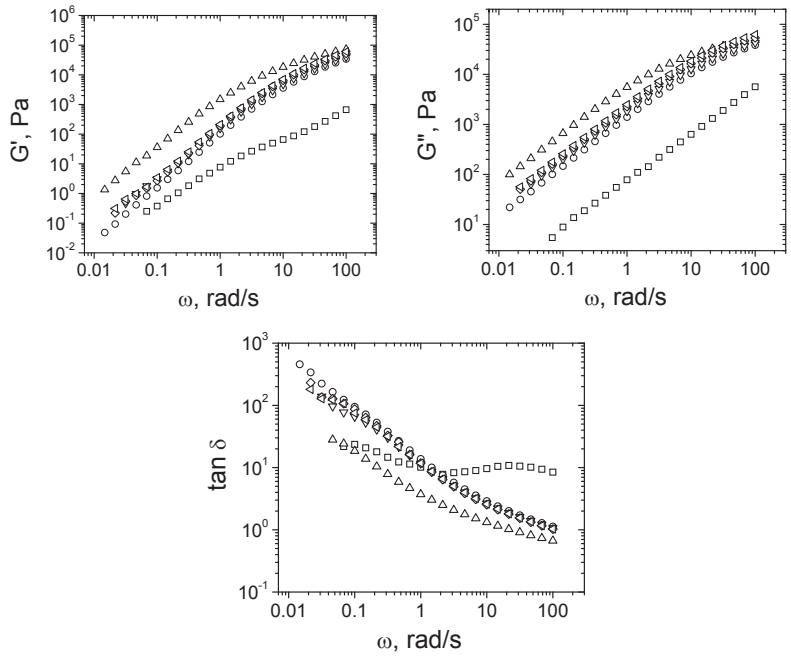

Figure 6.1: Dynamic moduli and tan δ versus frequency for FLPS40K ($\square$), FLPS120K ($\bigcirc$), FLPS200K ($\triangle$), SAN10 ($\bigtriangledown$), SAN20 ($\diamond$) and SAN30 ($\triangleleft$), measured at 200 $^{\circ}C$ and strain = 20 %.

area of the blends interface.

6.2.3 Rheological characterization of blends

Samples of the non annealed blends were molded into 25 mm disks and dried at 90 $^{\circ}C$ under vacuum for at least 24 hrs before rheology. Rheological measurements were performed on a strain-controlled rheometer (TA Instruments Rheometrics series ARES) with parallel plate geometry (25 mm diameter). Dynamic frequency sweeps at 200 $^{\circ}C$ were carried out over a range of 100-0.02 rad/s with strains of 20 %. Dynamic time sweeps were performed at 200 $^{\circ}C$ at a frequency of 0.1 rad/s with strains of 20 %. All measurements were carried out under nitrogen purge to minimize sample degradation.

6.2.4 Interfacial tension

Interfacial tension between the blend components (Γ) was measured using two methods, namely the rheological method (RM) and the breaking thread method (BTM). These methods are described in detail in the Appendix C. The average of Γ values obtained using the two methods is shown in Table 6.1. Note that only one of the polystyrenes (FLPS120K) was used in these measurements. Nevertheless, given that the molecular weight of the polymers used in this study are way above the entanglement molecular weight value (i.e. $M_{e,PS} = 13kg/mol$[135] and $M_{e,SAN} = 9.8kg/mol$ [136]), it is expected that Γ does not depend on molecular weight of either of the polymers [137, 138, 139, 135] but only on the AN-content in the SAN copolymer.

6.3 Results and discussion

6.3.1 Rheology of blends before coarsening

Correction of frequency sweeps

The results of dynamic frequency sweeps for the FLPS120K/SAN20 blend are shown in Figure 6.2. Besides the typical power law behavior in G' at low frequencies [24], a reduction in the elasticity of the blend (evidenced by a decrease in G' and an increase in $\tan\delta$) is observed after sequential time sweeps. The decrease in G' is, as discussed below, due to a decrease in the interfacial area (i.e. coarsening) occurring in the rheometer during the test. Therefore, there exist an inherent error in the frequency sweep tests of these evolving structures, since each sweep takes about one hour to completion.

Figure 6.3 shows the microstructure of the blend at different times of annealing along with the $G'(\omega)$ plot indicating the time of measurement for three data points. Note that the last data point (at $\omega = 0.215$ rad/sec) is recorded after about one hour of starting the experiment. During that time the characteristic size of the blend microstructure became about 6 times bigger than the initial size (see Figure 6.3c). That is to say, the interfacial area of the final microstructure is one sixth of the initial one *.

Several authors have reported the power law in the low frequency regime [140, 141,

*The relation between interfacial area, Q, and characteristic length, λ, is $\lambda = 2\phi(1-\phi)Q^{-1}$ where ϕ is the volume fraction (see page 128 in ref. 78)

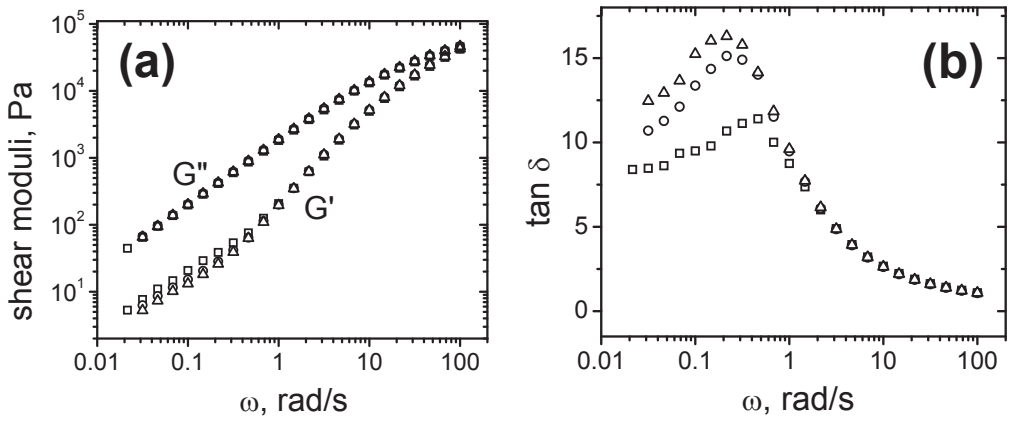

Figure 6.2: Frequency sweeps for 50/50 FLPS120k/SAN20 blend performed sequentially: (□) after loading the sample (+10 min), (○) after first sweep (+65 min) and (△) after second sweep (+105 min)

121, 142, 24]. However in none of these studies the error due to coarsening during the test is corrected or even mentioned. We addressed this error by running a series of time sweeps at different frequencies (see Figure 6.4). G' data from the time sweeps corresponding to 5 min were used to rectify the frequency sweep plots. Figure 6.3 shows both the corrected and non-corrected elastic modulus for the FLPS120K/SAN20 blend. This procedure was used to correct the frequency data for all seven blends analysed in the present study. The corrected plots correspond to frequency sweeps measured on blends annealed for 5 minutes throughout the frequency range.

Effect of interfacial tension, viscosity and viscosity ratio on the viscoelasticity of blends

Figures 6.5 and 6.6 show arrays of plots with the dynamic moduli and tan δ, respectively, for all the blends. Note that both arrays are arranged is such a way that interfacial tension varies horizontally and viscosity ratio vertically (see Table 6.1). In order to compare the viscoelastic response of the blend with that of the components, the average properties of the component properties (G'_{comp},G''_{comp} and tan δ_{comp}) were computed and included in Figures 6.5 and 6.6. Several mixing rules have been proposed in literature

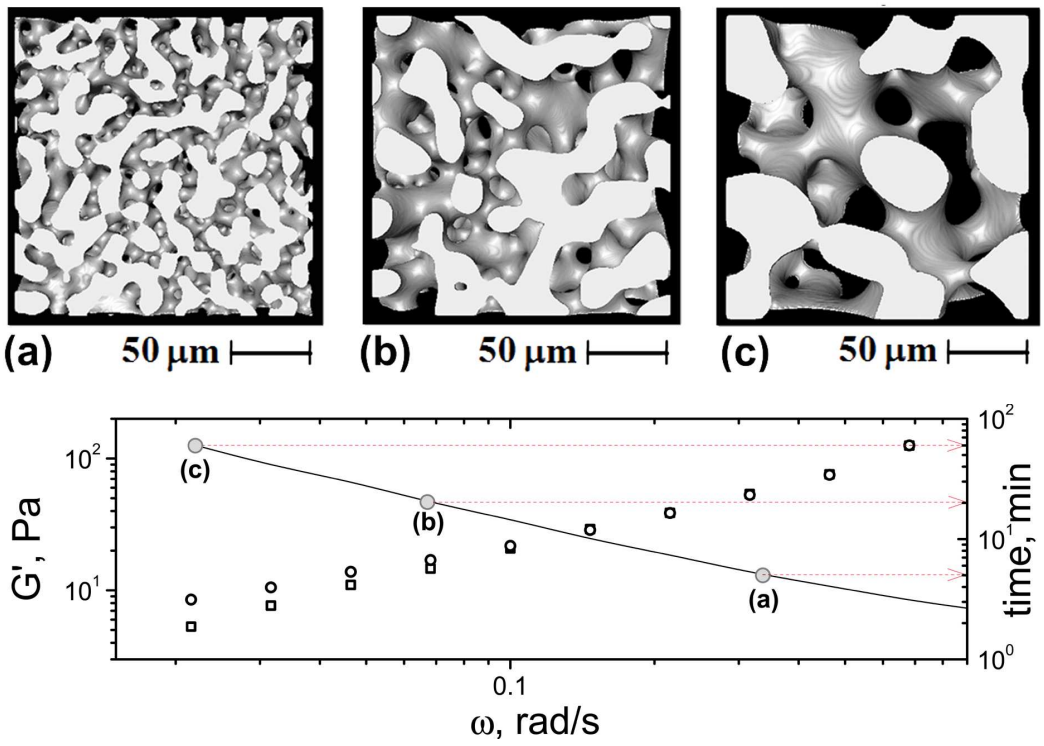

Figure 6.3: Upper row: 3D reconstructed images of 50/50 FLPS/SAN20 blend microstructure quiescently annealed for (a) 5, (b) 20 and (c) 60 minutes. Lower row: (□) non-corrected and (○) corrected elastic modulus for the same blend. The solid line indicates the time for data collection and the points marked with letters indicate the times of occurrence for the three morphologies shown in the upper row.

[134, 143], but most of them are valid only for low concentration of one of the components and assume a droplet-matrix structure. Here we chose to use the geometrical mean, given by $G'_{comp} = \sqrt{G'_{FLPS} \times G'_{SAN}}$ and similar formulas for G''_{comp} and $\tan\delta_{comp}$. The justification to use this simple mean is that the resulting values match quite well with the viscoelastic properties of the blends in the region of high frequency, where the properties should not be affected by the structure of the blend.

Several remarks arise from the analysis of Figures 6.5 and 6.6. First, no effect was observed in G'', compared to G''_{comp}, Second, an increase in G' and a decrease in $\tan\delta$

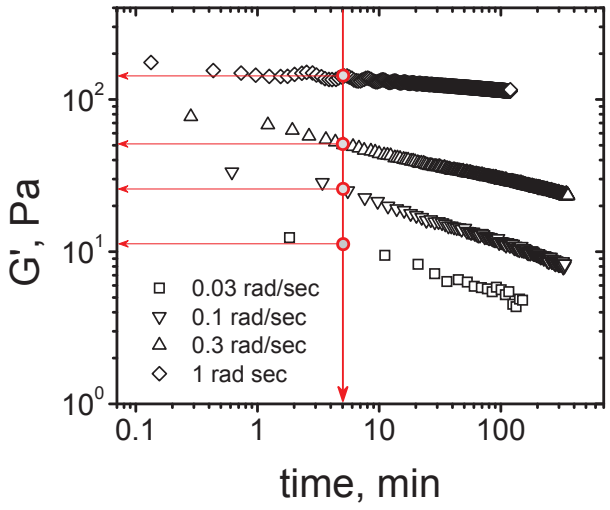

Figure 6.4: Dynamic time sweeps performed at different frequencies at 200 $^{\circ}C$ with a strain = 20%. Data taken at 5 min where used to correct dynamic frequency sweeps.

with respect to the components is observed for all the blends. This increase in the elastic character of the blend was characterized by a power law-like relation, $G' \propto \omega^a$, at low frequencies. Vinckier and Laun [24] explained this behavior by comparing cocontinous morphologies with network structures [121]. In network structures, the number of crosslinks per unit volume governs the elastic behavior. By analogy, they assumed that the number of "interconnections" per unit volume is more important than the diameter of the filaments. However we [45] demonstrated that these two quantities (i.e. characteristeic length, λ, and genus per unit volume, g/V) are indeed related (see Chapter 3). Similarly, Weiss et al. [142] attributed the power law behavior to the presence of domains with different characteristic lengths, which generates relaxation processes with different characteristic times. We believe that the extra elastic stress is due to an extra interfacial energy which is a function of interfacial area and interfacial curvature (see Chapter 4). We have shown that there is a distribution in interfacial curvatures in the cocontinuous blends [45] which is responsible for the power law distribution of relaxation times.

Only a subtle difference between the viscoelastic response of blends with different

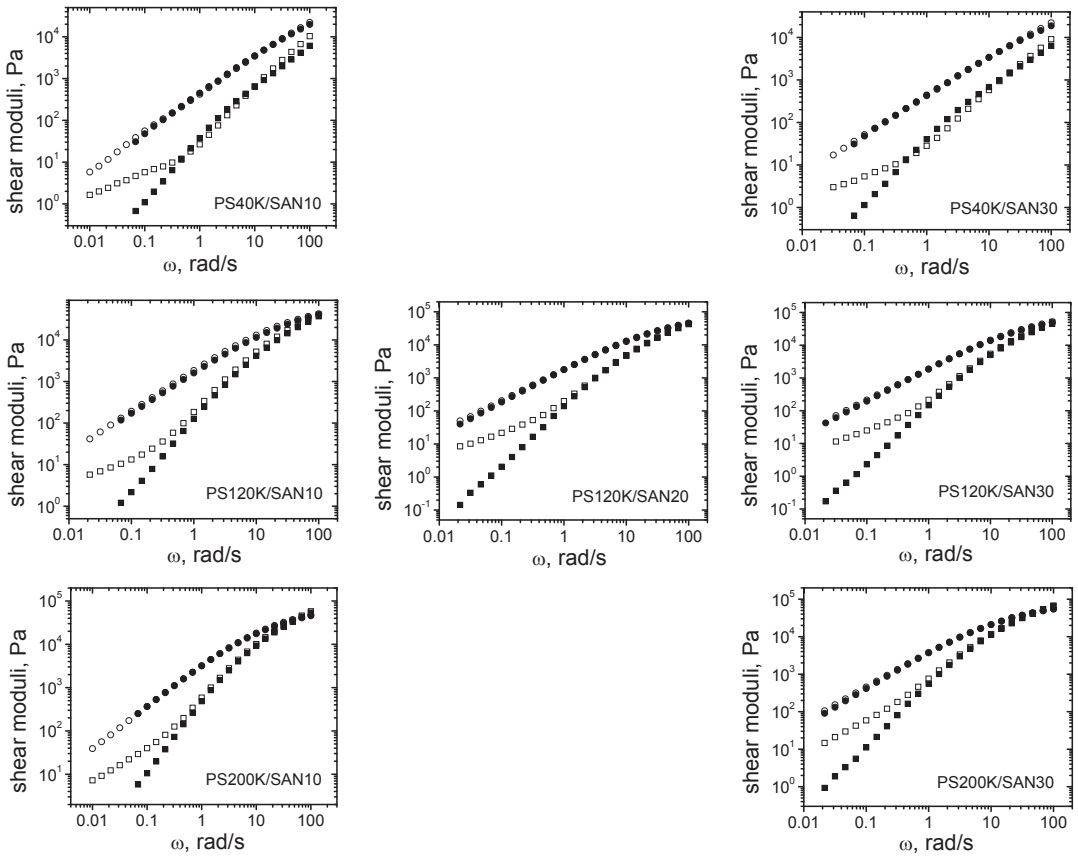

Figure 6.5: $G'(\omega)$ (squares) and $G''(\omega)$ (circles) for 50/50 blends (open symbols) measured at 200 $^{\circ}C$ and strain=20 %. Filled symbols correspond to geometric mean of data for the components.

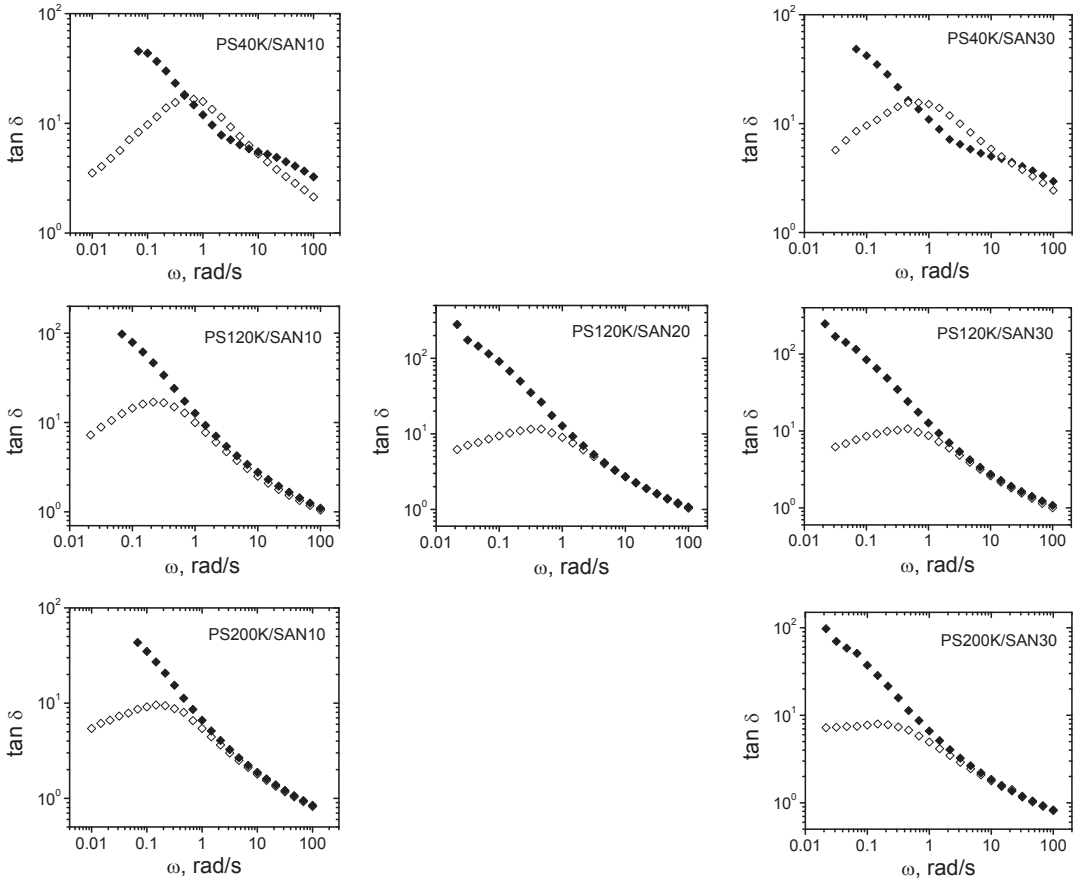

Figure 6.6: $\tan\delta(\omega)$ for 50/50 blends (open symbols) measured at 200 $^{\circ}C$ and strain=20 %. Filled symbols correspond to geometric mean of data for the components.

viscosity ratio (p) is observed in Figures 6.5 and 6.6. No difference was observed between blends with different interfacial tension. To make these differences clearer, G'/G'_{comp} as a function of frequency is plotted in Figure 6.7. It is remarkable that the effect of interfacial tension is almost null. The power law exponent, b, shown in the plots is bigger for the low p blends. This exponent is related to the exponent a as $b = a - 2$. Hence, the values of alpha for the blends with low (blends with PS40K), intermediate (blends with PS120K) and high (blends with PS200K) viscosity ratio are 1.07, 1.075 and 1.25, respectively. This is in discordance to Weiss et al [142], who suggested that $a < 1$. It should be noted that the variations of p is accompanied by a variation in the average viscosity (η_{comp}). The combined effect of p and η_{comp} is difficult to decouple without further experiments.

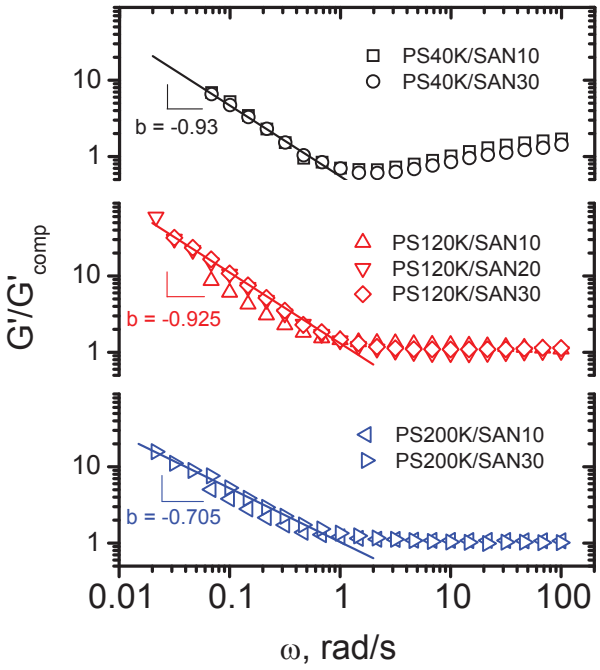

Figure 6.7: Ratio between G' and G'_{comp} for all the blends, measured at 200 $^{\circ}C$ and strain = 20 %.

Cole-Cole plots

The empirical Cole-Cole model was first introduced in the context of dielectric relaxation spectrum [144], and subsequently applied to the dielectric spectrum of polymeric materials by Havriliak and Negami [145]. These authors realized that the molecular mechanisms underlying dielectric relaxation and stress relaxation were identical. Specifically, the same molecular motions that generate a frequency dependence for the dielectric spectrum are also responsible for the relaxation of orientation in polymer liquids. With these ideas in mind Haviliak y Nagami extended the Cole-Cole type spectrum to the linear viscoelastic mechanical properties of polymer melts. Specifically, the dynamic compliance and the dynamic viscosity functions.

Plots of the imaginary dynamic viscosity versus the real dynamic viscosity, has the advantage that the explicit frequency dependence is eliminated. For linear backbone flexible polymers with a monomodal molecular weight distribution (MWD), Cole-Cole plots yield an arc of a circle [146]. Generally the broader the MWD, the shallower the arc. For monodisperse polymers, with approximately a single relaxation time, a semicircle is generated. Miscible blends of two polymers show well defined semicircles in Cole-Cole plots [147], whereas immiscible blends show drift from the semicircle. The shape of the drift is an indication of the type of morphology [148, 140, 147].

Figure 6.8 shows the Cole-Cole plot (normalized with the zero shear viscosity) for the blends and their components. In all cases, semicircles appear in the left hand side, wich correspond to the relaxation spectrum of chain orientation of the components. Additional to the semicircle, a tail appears in the right hand side. These tail was observed previously in a symmetric blend made of polymethyl methacrylate (PMMA)/poly(styrene-co-maleic anhydride) (SMA) with cocontinuous morphology [147] and is just another representation of the power law behaviour observed in G' versus ω plots (Figure 6.5). However, there is not a clear difference between the shape of the tails of the plots in Figure 6.8, ergo, we conclude that Cole-Cole plots are not suitable to study differences in blend morphology due to differences in Γ or p.

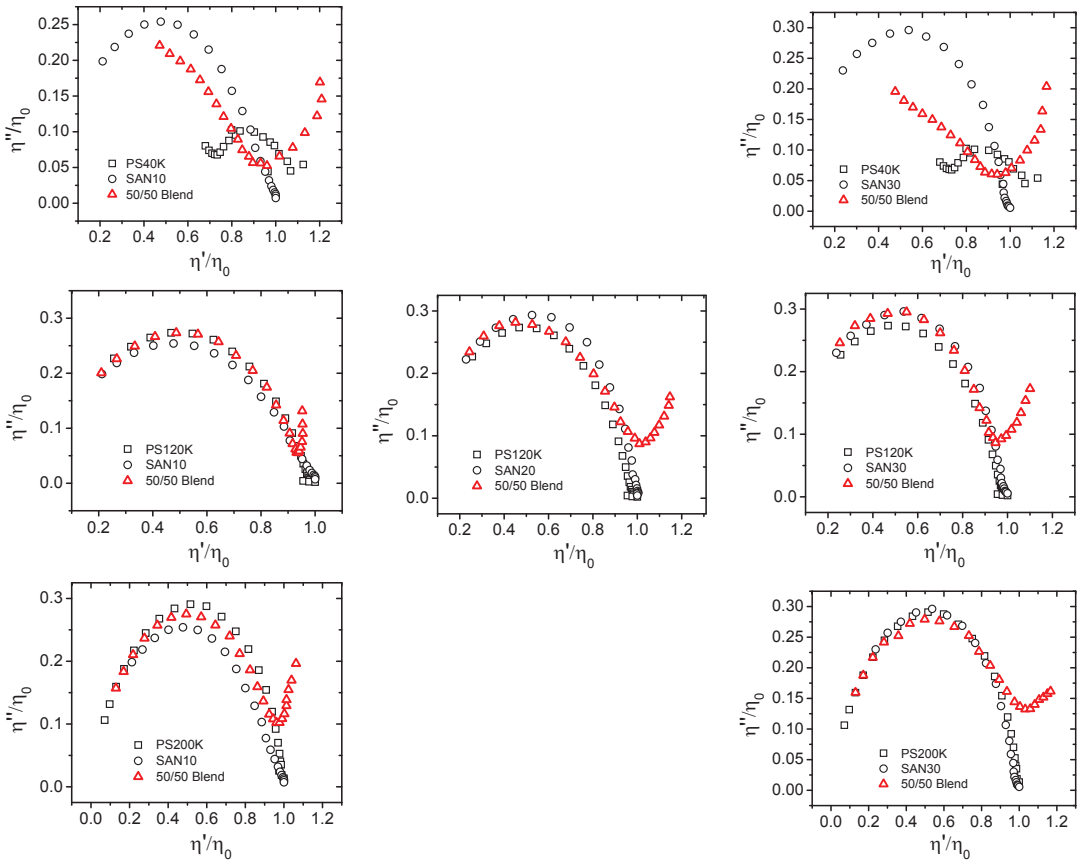

Figure 6.8: Cole-Cole plots of 50/50 blends and their components at 200 $^{\circ}C$.

van Gurp-Palmen Plots

van Gurp and Palmen proposed to use a plot of the loss angle, δ, versus the logarithm of the absolute value of the complex modulus, $|G^*|$ to test the validity of time-Temperature superposition (tTs) [149]. If data obtained at several temperatures all superimpose in the same curve on such a plot, this indicates that tTs is valid without a vertical shift. Besides testing tTs, the van Gurp-Palmen (vGP) plot has been used to evaluate polydispersity, tacticity and chemical composition of linear polymers as well as to clasify topology of branched chain polymers [150, 151, 152]. Delgadillo-Velazquez et al. used vGP plots to infer miscibility of polyolefin blends [153]. Li et al. characterized the rheological behavior of phase separated PMMA/SMA blend with droplet-matrix and cocontinuous morphologies [147]. They were able to discriminate between both types of morphology by comparing the shape of the vGP plots in the low $|G^*|$ region. In the present work we observed characteristics in the vGP plot for the cocontinuos blends similar to those reported by Li et al. [147].

Figure 6.9 shows the plots of δ versus $|G^*|$ for all the blends and their components. For all the components, the vGP plot show a plateau at $\delta = 90°$ and low $|G^*|$ values, which is what has been reported for homogeneous linear polymers [150, 152, 147]. On the other hand, for all the blends the δ vs $|G^*|$ plots shift to smaller phase angle values in the low $|G^*|$ region, indicating the increased elasticity observed at low frequencies in the $G'(\omega)$ and $\tan\delta(\omega)$ (see Figures 6.5 and 6.6). The same way as in the $G'(\omega)$ and $\tan\delta(\omega)$ only a subtle difference can be noted between the plots in Figure 6.9, indicating a that the shift from $\delta = 90°$ decreases as the viscosity ratio increases. No effect was observed in the vGP plot due to interfacial tension.

Relaxation spectra

In the previous sections the frequency dependence of G', $\tan\delta$, as well as the Cole-Cole and vGP plots for all blends suggested that there exist an extra elastic stress, characterized by a power law in the low frequency region. It was suggested that the origins of the power law behavior is a distribution of relaxation times associated to the distribution of local interface curvatures. Therefore, it is very interesting to examine the relaxation spectra of the blends.

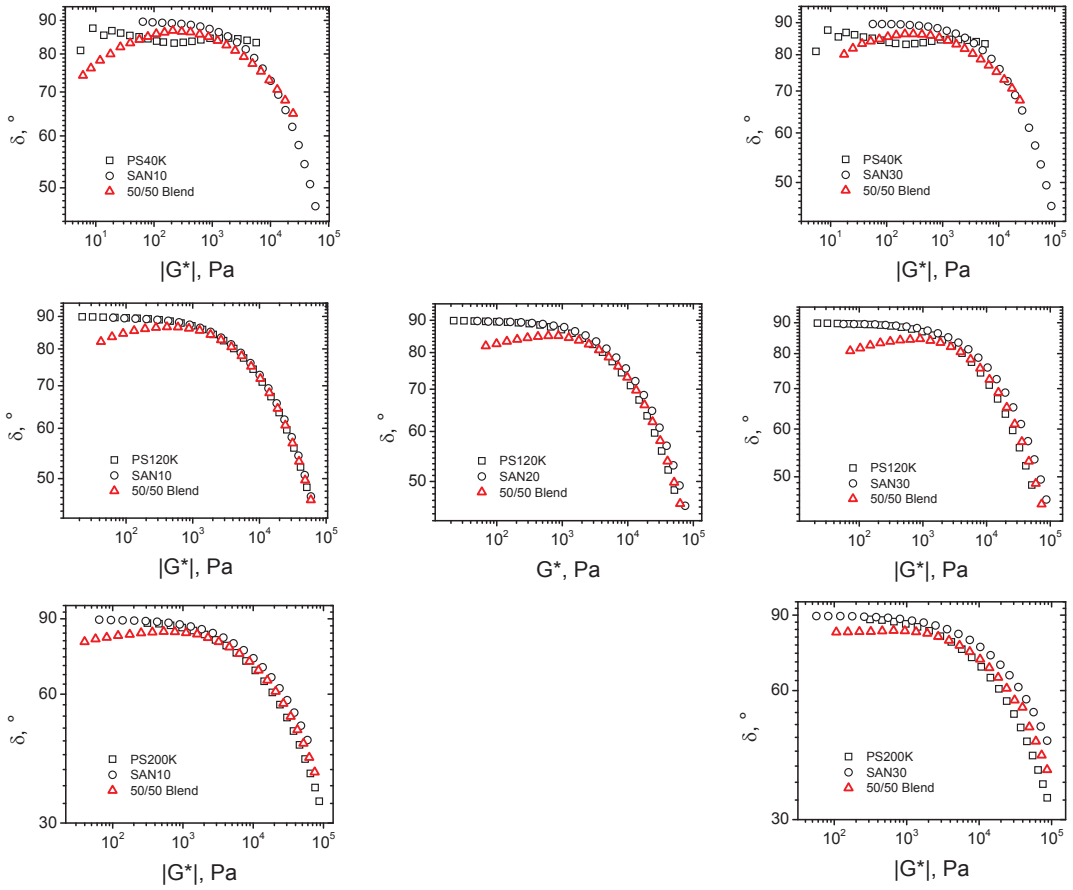

Figure 6.9: van Gurp -Palmen plots of 50/50 blends and their components at 200 $^{\circ}C$.

Figure 6.10 gives the relaxation spectra, $H(\tau)$, for all the blends and their components. The relaxation spectra was calculated using the $G'(\omega)$ data from Figure 6.5 and the second order approximation proposed by Tschoegl [154], namely

$$H(\tau) = G' \left[\frac{d \log G'}{d \log \omega} - \frac{1}{2} \left(\frac{d \log G'}{d \log \omega} \right)^2 - \frac{1}{4.606} \frac{d^2 \log G'}{d (\log \omega)^2} \right]_{\tau = \sqrt{2}/\omega} \tag{6.1}$$

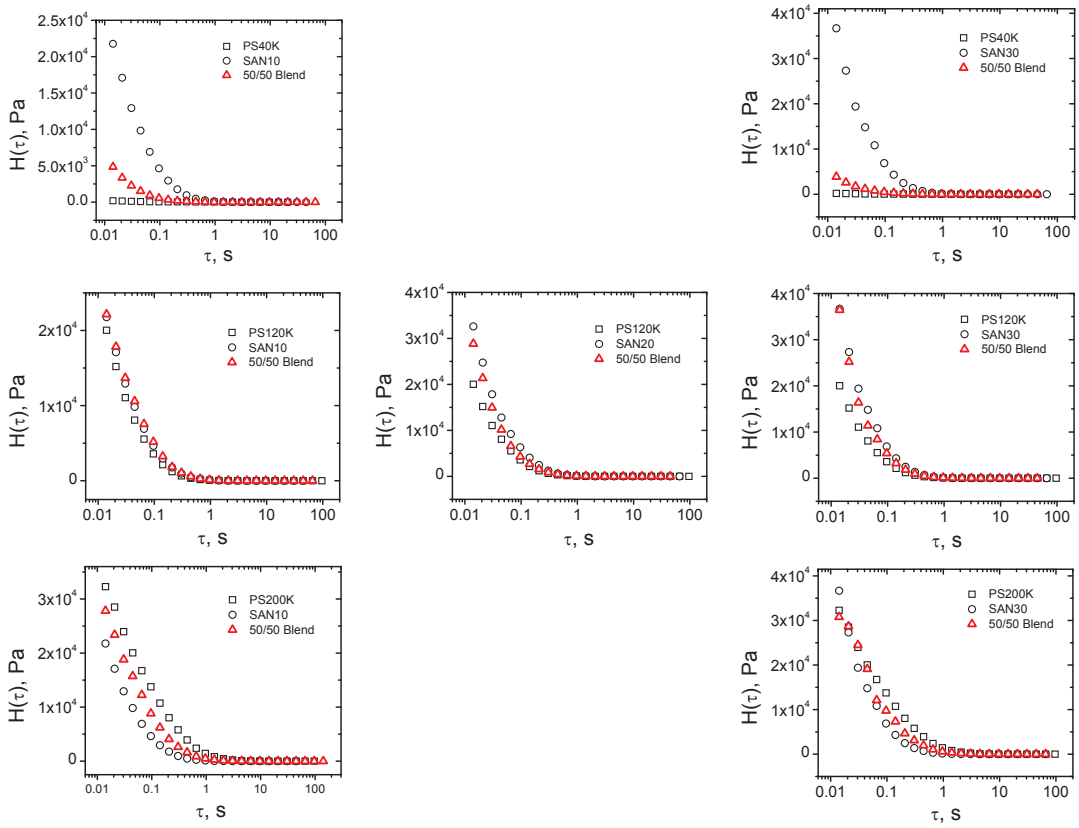

Figure 6.10: Relaxation spectra for 50/50 blends and their components at 200 $^{\circ}C$.

The right hand side of the spectra in Figure 6.10 depicts the contribution of the blend components, while the left hand side contains the portion of the spectra corresponding to the relaxation of the blend interface. However, the sensitivity of $H(\tau)$ plot to these relaxations is very weak and hence the difference between the blend and their components is imperceptible.

To separate the relaxation times of the interface from the contribution of the components we used the method proposed by Gramespacher and Meissner [155], consisting on plotting the weighted relaxation spectrum $\tau \cdot H(\tau)$ versus τ. The use of the first moment of the spectrum magnifies the contribution of slow processes. Hence, interfacial relaxations become more evident. The weighted spectra for all the blends and their components are shown in Figure 6.11. The peak appearing in the right hand side of the weighted spectra of the blends corresponds to the contribution of the component polymers. The tail developed in the long tau region correspond to the relaxation of the interface. Li et al. reported similar behavior for PMMA/SMA blends with cocontinuous morphologies [147]. They argued that the tail corresponds to slow relaxations of interpenetrating networks (IPN) forming the cocontinuous structure. We believe that the relaxations depicted by the tail are due to a spectrum of relaxation times corresponding to a distribution of local shapes (characterized by the local curvature).

In order to make clearer the difference between the spectra of the blends and those of their components, we constructed plots of the weighted spectra normalized with the values of $\tau H(\tau)$ and τ corresponding to the peak (i.e. $(\tau H(\tau))_{peak}$ and τ_{peak}). The normalized plots of the blends and their components (shown in Figure 6.12) superimpose on each other in the region of short relaxations. Thus, the difference in the long relaxations between blends and components is enhanced. Following this idea, we subtracted the normalized values of $\tau H(\tau)$ of the components from that of the blends in order to completely get rid of the contribution of the components. Thus, the increment in normalized weighted spectra, defined as

$$\Delta\left[\tau \cdot H/\left(\tau \cdot H\right)_{peak}\right] = \left[\frac{\tau \cdot H(\tau)}{\left(\tau \cdot H(\tau)\right)_{peak}}\right]_{blend} - \left[\frac{\tau \cdot H(\tau)}{\left(\tau \cdot H(\tau)\right)_{peak}}\right]_{componets} \tag{6.2}$$

are shown in Figure 6.13. The trends observed in this plot are in accordance to those observed in Figure 6.7, namely, a more pronounced deviation from the component behavior in the blends with low viscosity ratio and an almost null effect of the interfacial tension.

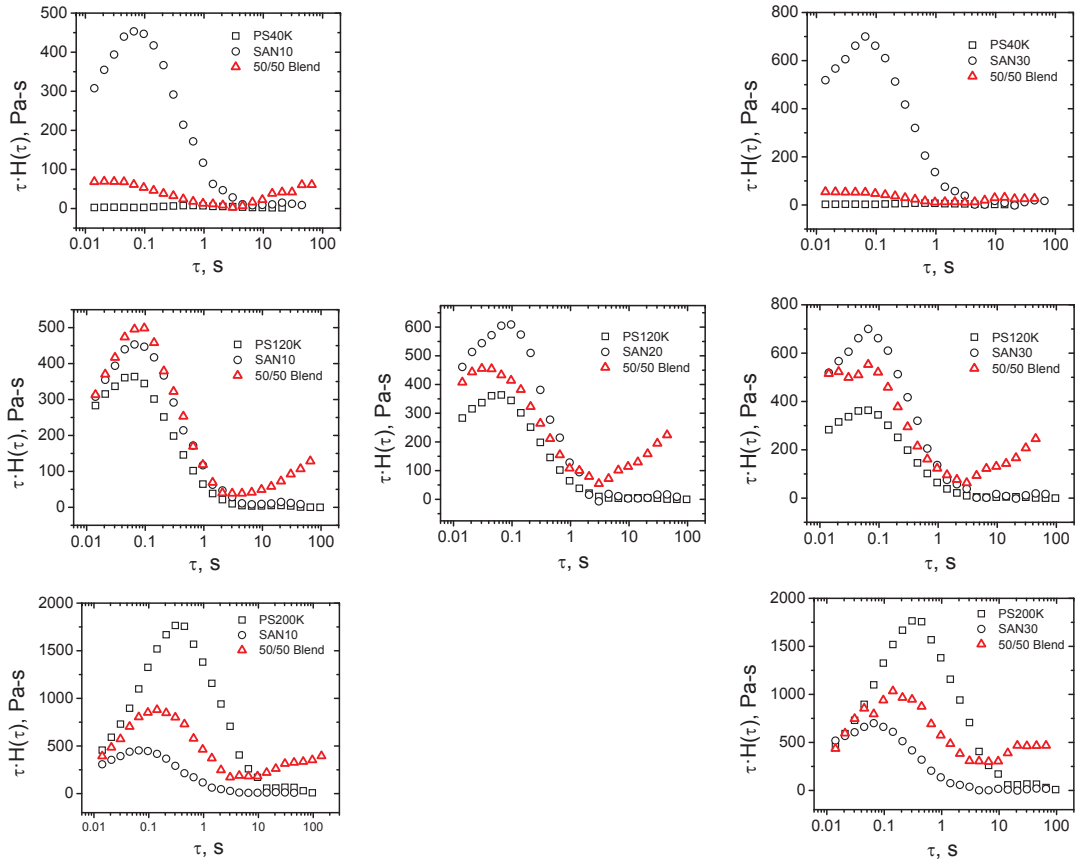

Figure 6.11: Weighted relaxation spectra for 50/50 blends and their components at 200 $^{\circ}C$.

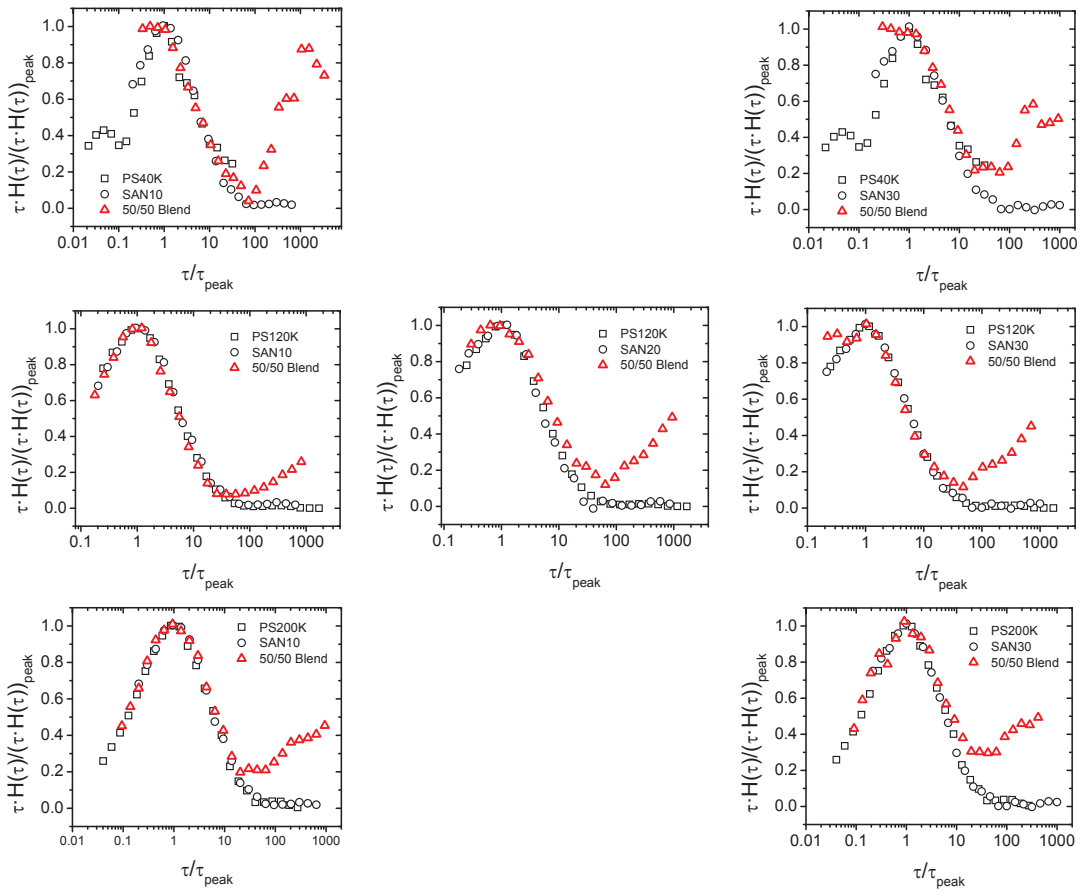

Figure 6.12: Normalized weighted relaxation spectra for 50/50 blends and their components at 200 $^{\circ}C$.

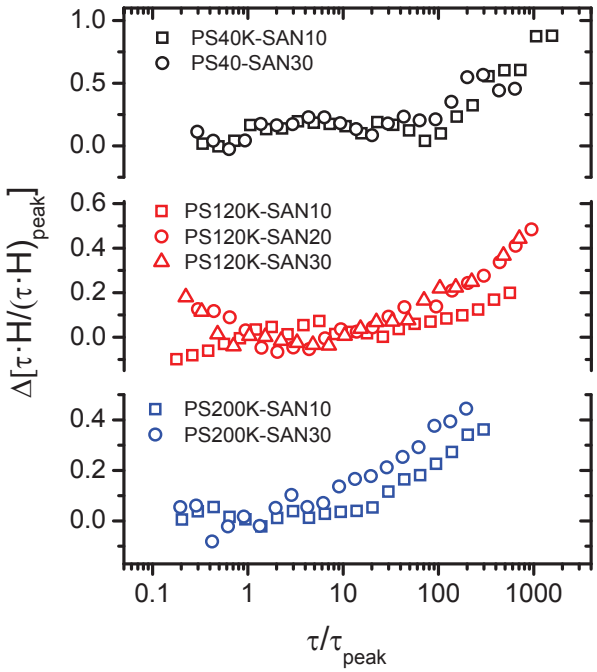

Figure 6.13: Increment in normalized weighted spectra (as defined in eqn 6.2) for 50/50 blends at 200 $^{\circ}C$.

6.3.2 Coarsening of blends

One of the main disadvantages of blends with cocontinuous morphologies is their instability when they are above the glass transition (or melting) temperature of their components. It is known that the stability of those type of morphologies is governed by the ratio between interfacial tension, Γ, and viscosity, η (see Chapter 3) [40, 14, 17]. In this section, the relation between Γ/η and the rate of coarsening, $d\lambda/dt$, of our blends is investigated.

Figure 6.14 shows the time evolution of the characteristic length of all the blends during annealing at 200 $^{\circ}C$. It should be noted that the annealing was done in a quiescent mode as described in section 3.3. For all the blends, a linear growth of λ was observed at early times followed by a gradual decrease in $d\lambda/dt$. This decrease is more abrupt for the blends with higher Γ/η (i.e. those containing SAN30). The slowing down

of the coarsening was addressed in Chapter 4.

The slope of the solid lines in Figure 6.14 give the initial rate of coarsening, $d\lambda/dt$ ($t \to 0$). The values of $d\lambda/dt$ are plotted in Figure 6.15. In general, the expected trend in this parameter was observed, i.e. $d\lambda/dt$ increase with Γ and decreased with η_{blend}. The effect of the viscosity ratio is not evident, since its variation is coupled with that of the blend viscosity (see Table 6.1). The inset in Figure 6.15 shows the rate of coarsening as a function of Γ/η. All data lie around the solid line, which depicts linear relation between $d\lambda/dt$ and Γ/η. This is in accordance to the coarsening linear law proposed by Siggia for the late stages of spinodal decomposition [14] and observed in various systems with cocontinuous morphologies [40, 17, 19, 53].

6.3.3 Rheology of blends during coarsening

To investigate the rheological behavior of the blends during coarsening, isothermal time sweeps at 200 °C were performed on the blends and their components. A fixed frequency of 0.1 rad/sec and a strain of 20 % were used in all the tests. Time sweeps for the blend components show fairly constant values of G' for at least 150 min (see Figure 6.16). This indicates that the all materials are thermally stable during the tests.

The elastic modulus of the blends, G'_{blend}, can be decomposed in two components, one due to the components contribution, G'_{comp}, and other due to interface relaxation, G'_{inter} [134]. Given the stability of the components (Figure 6.16) G'_{comp} is considered to be constant throughout the time sweep test, whereas G'_{inter} varies during the test due to morphological evolution, i.e. coarsening. The interface contribution, given by

$$G'_{int} = G'_{blend} - G'_{comp} \tag{6.3}$$

is shown in Figure 6.17. The same as in section 6.3.1, G'_{comp} was computed as the geometric mean of the G' values of the components.

The rheological behavior during the time sweeps of all the blends was very much alike, namely, a rapid initial decrease in G' followed by a gradual slowing down of the decay rate with an apparent tendency to reach a plateau at very long times. Similar results were reported by Vinckier and Laun [24, 32] for a blend made of poly(alpha methylstyrene-co-acrylonitrile)/ polymethyl methacrylate and recently by Niu et al.

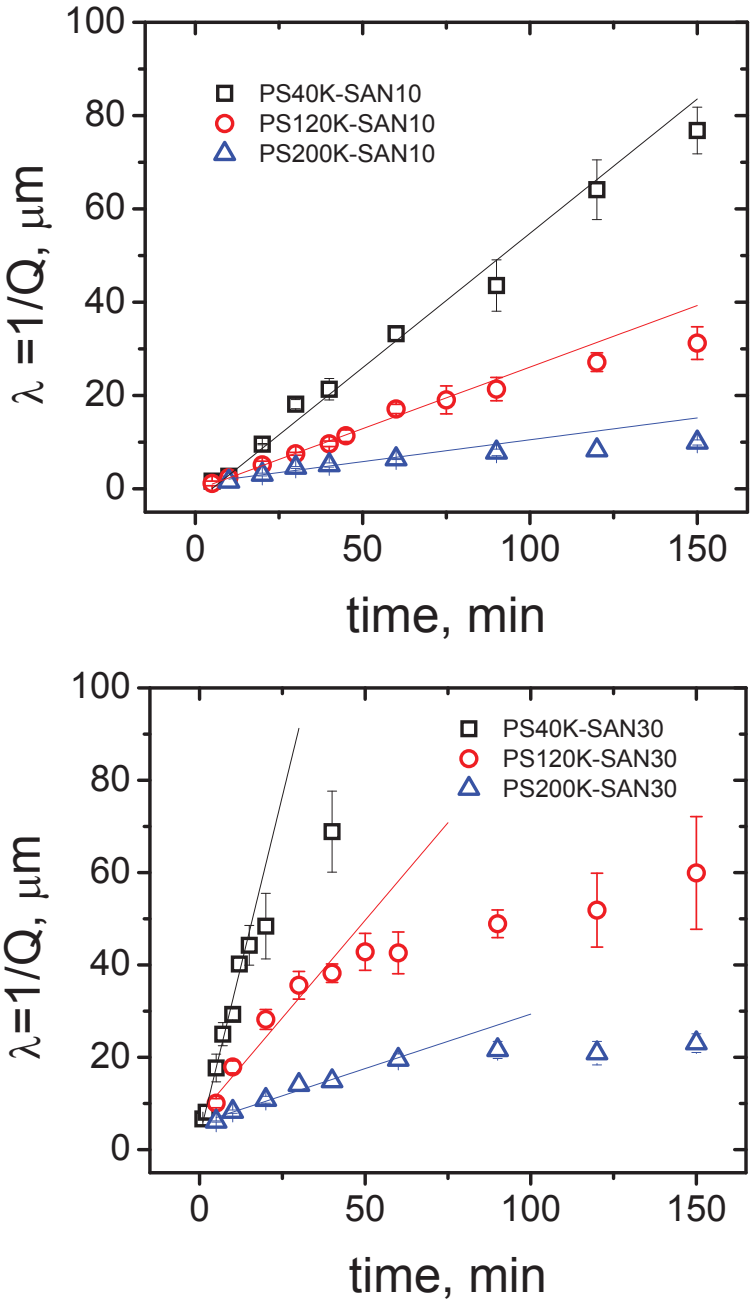

Figure 6.14: Characteristic size of 50/50 blends versus annealing time at 200 $^{\circ}C$.

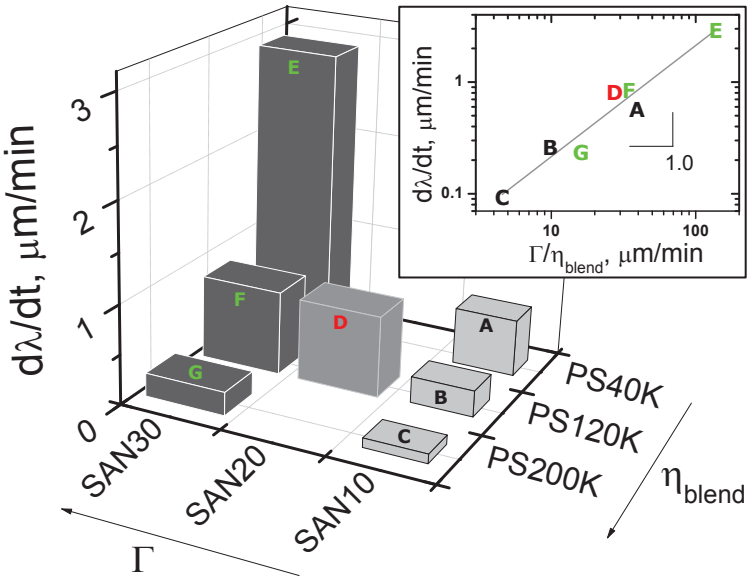

Figure 6.15: Initial rate of coarsening of 50/50 blends (slopes of lines in Figure 6.14) as a function of Γ and η_{blend}. The inset illustrate the linear relation between rate of coarsening and Γ/η_{blend}.

for polyolefin blends [156]. Polios et al. [121] compared cocontinuous structures with interpenetrated networks (IPN). They attributed the decrease in G' to a loss of interconnection due to break up of the network structure. A different hypothesis proposed by Doi and Ohta [28] considers that the extra-contribution to the stress tensor (and hence to the elastic modulus [134]) is due to interfacial relaxation whose intensity depends on the size and shape of the blend interface. The evolution of the latter is responsible for the decrease in G'.

Doi and Ohta theory

Doi and Ohta [28] proposed a model for the rheology of two phase liquids of Newtonian liquids with equal viscosity (η_0). This theory considers systems with complex interfaces whose stress is given by [157, 158]

$$\sigma_{ij} = \eta_0(\kappa_{ij} + \kappa_{ji}) - \Gamma q_{ij} - p\delta_{ij} \tag{6.4}$$

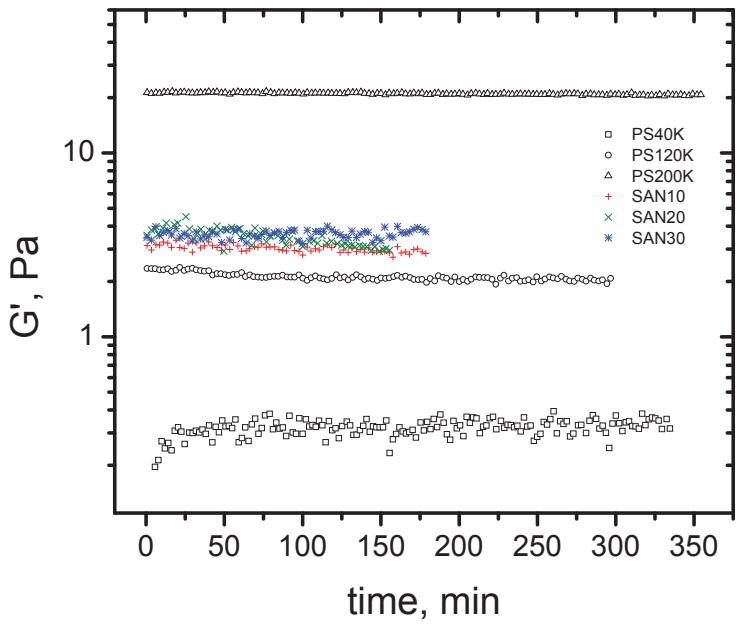

Figure 6.16: Dynamic elastic modulus as a function of time for the blend components measured at 200 °C with a fixed frequency of 0.1 rad/sec and 20 % strain.

were $\kappa_{ij} = \partial v_i / \partial r_j$ is the macroscopic volumetric gradient, δ_{ij} is the Kroeneker delta and q_{ij} is the interface tensor, which is a measure of the *anisotropy* of the interface. This vector is given by [158]

$$q_{ij} = \frac{1}{V} \int dS \left(n_i n_j - \tfrac{1}{3} \delta_{ij} \right) \tag{6.5}$$

where V is the total volume, dS an interface element, and n_i denotes the i-th component of the unit vector normal to the interface. The integral is over the the whole interface S contained in the volume V. Eqn 6.4 implies that the mere presence of an interface generates an extra stress, whose value is proportional to both the interfacial tension and the interface anisotropy

$$\sigma_{ij,int} = -\Gamma q_{ij} \tag{6.6}$$

The time evolution of both q_{ij} and the interfacial area per unit volume, Q (=

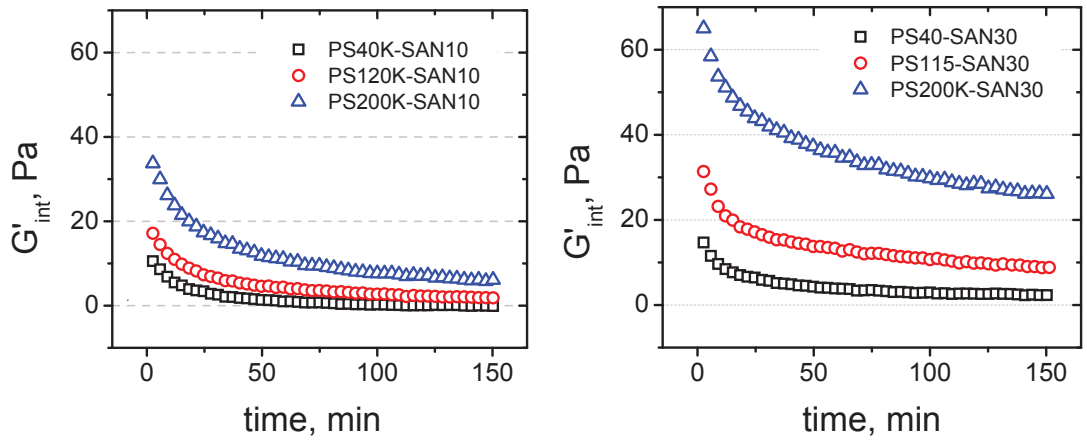

Figure 6.17: Interface contribution to the elastic modulus as a function of time for 50/50 blends measured at 200 °C with a fixed frequency of 0.1 rad/sec and 20 % strain.

$\frac{1}{V}\int dS$), are coupled and given by semiphenomenological kinetic equations. These equation are based on the assumption that the interface evolution is governed by two factors: the external flow (which orients the interface to an anisotropic state) and a relaxation process (driven by interfacial tension). These factors are accounted separately

$$\frac{dQ}{dt} = \left.\frac{dQ}{dt}\right|_{flow} + \left.\frac{dQ}{dt}\right|_{relax} \tag{6.7a}$$

$$\frac{dq_{ij}}{dt} = \left.\frac{dq_{ij}}{dt}\right|_{flow} + \left.\frac{dq_{ij}}{dt}\right|_{relax} \tag{6.7b}$$

The terms in the right hand side of eqns. 6.7a and 6.7b were derived by Doi and Ohta [28]

$$\left.\frac{dQ}{dt}\right|_{flow} = -\kappa_{ij}q_{ij} \tag{6.8}$$

$$\left.\frac{dq_{ij}}{dt}\right|_{flow} = -q_{ik}\kappa_{kj} - q_{jk}\kappa_{ki} + \tfrac{2}{3}\delta_{ij}\kappa_{lm}q_{lm} \tag{6.9}$$

$$-\tfrac{1}{3}Q(\kappa_{ij} + \kappa_{ji}) + Q^{-1}q_{lm}\kappa_{lm}q_{ij}$$

$$\left.\frac{dQ}{dt}\right|_{relax} = -\alpha\beta\frac{\Gamma}{\eta_0}Q^2 \tag{6.10}$$

$$\left.\frac{dq_{ij}}{dt}\right|_{relax} = -\alpha\frac{\Gamma}{\eta_0}q_{ij} \tag{6.11}$$

where α and β are positive numbers that may depend on the volume fraction. It is plain that setting $\Gamma = 0$ the time evolution of the shape and size of the interface will be entirely determined by the macroscopic velocity field, $\mathbf{v}(\mathbf{r}, t) = \kappa(t) \cdot \mathbf{r}$ (i.e. by the flow terms in equations 6.8 and 6.9). Contrarily, for quiescent conditions, i.e. for $\kappa_{ij} = 0$, only the terms in eqns 6.10 and 6.11 will contribute to the time evolution of q_{ij} and Q. At this point some remarks are pertinent

- The rates of size relaxation (decrease of amount of interface), r_{size}, and shape relaxation (decrease in anisotropy), r_{shape}, are in general determined by η_0, Γ, and the configuration of the interface, which is characterized by q_{ij} and Q. Doi and Ohta [28] considered the simplest approximation, to wit, they disregard the dependence of r_{size} and r_{shape} on q_{ij}. Using dimensional analysis they obtained

$$r_{size} = \alpha\beta\frac{\Gamma}{\eta_0}Q \tag{6.12a}$$

$$r_{shape} = \alpha(1-\beta)\frac{\Gamma}{\eta_0}Q \tag{6.12b}$$

  Note that the quantity $\beta/(1-\beta)$ gives the ratio between the speeds of size relaxation and shape relaxation. Alternatively β represents the speed of the size relaxation relative to the total relaxation speed. If we could measure the time evolution of q_{ij} and Q, we may calculate α and β.

- Equation 6.10 is based in the assumption that the size relaxation is associated to a single relaxation time, that is, the morphology is characterized by a single length

scale. It has been demonstrated that this assumption is correct for complex interfaces created during spinodal decomposition [87, 78] and melt mixing of immiscible polymers with symmetric volume fractions [45]. Indeed the physics behind Siggia's theory of phase separation [14] is the same as that of equation 6.10. The well known result from Siggia's analysis, i.e. the linear growth of characteristic length, follows as well from this equation.

- Q and q_{ij} are the isotropic and deviatoric parts of the area tensor, A_{ij}, defined by Wetzel and Tucker [159]. The area tensor describes the local morphology of two phase mixtures through volume average size and orientation and is defined as

$$A_{ij} = \frac{1}{V}\int dS\,(n_i n_j) = q_{ij} + \frac{1}{3}Q\delta_{ij} \tag{6.13}$$

  with $\mathrm{tr}A_{ij} = Q$, and hence $\mathrm{tr}q_{ij} = 0$. These descriptors (whether A_{ij} or $\{Q, q_{ij}\}$) apply indistinctly to disperse and cocontinuous morphologies. Wetzel and Tucker [159] gave exact relations to compute A_{ij} for ellipsoids and Vinckier et al. [160] reported relations to obtain qij for cylinder with spherical ends. Given that the interface in cocontinuous morphologies cannot be described analytically, relations for A_{ij} or q_{ij} are not obtainable, although, as shown below, they can be computed if local information of the interface geometry is available.

- Doi and Ohta model predictions have been compared to data of blends mostly with disperse morphologies [161, 29, 162, 163, 164, 165]. To our knowledge, in only one study, reported by Vinckier and Laun [32], data of blends with cocontinuous morphologies are compared with predictions from the model.

Measurement of q_{ij} from 3D images.

Despite the relevance of the surface descriptors (q_{ij} or A_{ij}), direct measurement of these quantities has been limited to a few studies. Almusallam et al. [163] measured the changes in q_{ij} during breakup and retraction of highly elongated droplets. Takahashi and coworkers [166, 165] evaluated the change in the length of semiaxes for rod-like and spheroidal droplets to obtain the components of the anisotropy tensor during droplet retraction after shearing. These studies used 2D microscopy with image analysis, which

is adequate for axisymmetric geometries, but not for intricate 3D interfaces where the normal vector field is neither available from 2D cuts of the microstructure nor obtainable analytically.

To our knowledge the vector q_{ij} has never been computed for cocontinuous structures, due, perhaps, to the lack of 3D information of the interface location. Given the location of three vertices, $\mathbf{V}_1$, $\mathbf{V}_2$ and $\mathbf{V}_3$, forming three edges of a triangle, we can take two of the edges and calculate the cross product between them (See Figure 6.18). The resulting directional vector will be the normal

$$\mathbf{n} = \frac{(\mathbf{V}_1 - \mathbf{V}_2) \times (\mathbf{V}_1 - \mathbf{V}_3)}{|(\mathbf{V}_1 - \mathbf{V}_2) \times (\mathbf{V}_1 - \mathbf{V}_3)|} \tag{6.14}$$

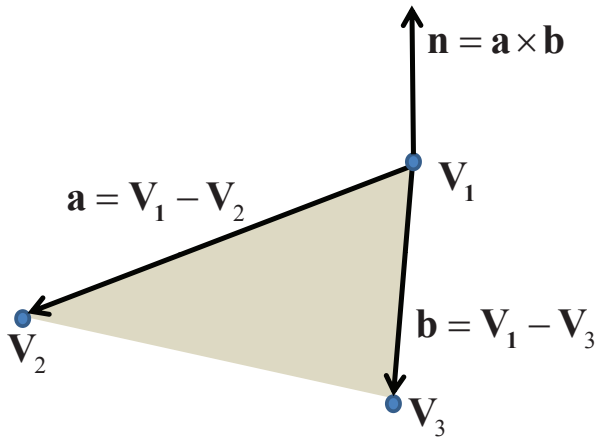

Figure 6.18: Schematic of the calculation of the normal vector of a plane defined by three vertices of a triangle.

As mentioned above, the 3D reconstruction of the confocal micrographs generates a triangular mesh describing the interface [45] (see Chapter 3). Hence, the calculation of the normal vector for each one of the triangles of the mesh is straightforward using eqn 6.14. Figure 6.19 shows a detail of the normal vector field on the obtained with this method.

Once computed the normal vector field, q_{ij} and Q can be calculated with

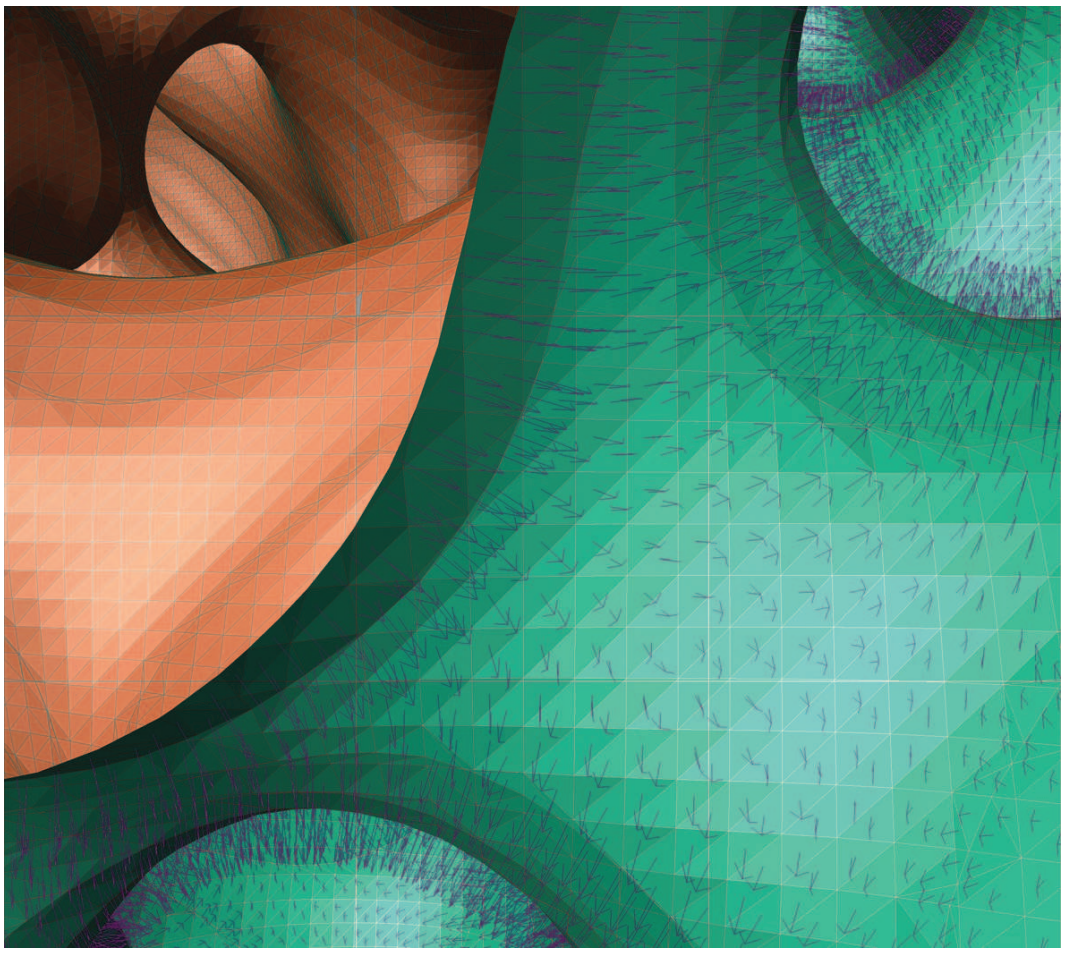

Figure 6.19: Detail of 3D reconstructed interface of a cocontinuous blends with the normal vector field represented with arrows.

$$q_{ij} = \frac{1}{V}\sum_{k=1}^{N} A_k \left(n_{i,k}n_{j,k} - \tfrac{1}{3}\delta_{ij}\right) \quad (6.15)$$

$$Q = \frac{1}{V}\sum_{k=1}^{N} A_k \quad (6.16)$$

where A_k, $n_{i,k}$ and $n_{j,k}$ are the interfacial area and the normal vector components of the k-th triangle. The total number of triangles is denoted with N.

All the dynamic tests in this study were performed using a strain of 20 %. To assess the increased anisotropy due to the shear deformation during the tests, a single strain step ($\gamma = 20\%$) was performed at 200 °C in the rotational rheometer with parallel plate geometry using a 1 mm thick sample disc. The morphology was frozen by dunking the sample into cold water just after the stain step. The image in Figure 6.20 displays the morphology (near the edge of the disc) of PS120K-SAN10 blend after 10 min of quiescent annealing followed by the strain step described above. A very subtle alignment of the microstructure (indicated with the red lines) can be noted due to the shear flow imposed during the strain step. No alignment was observed in the non sheared samples (see Figure 6.3).

The calculated values of the components of q_{ij} are of the order of $10^{-5}\mu m^{-1}$ for all the quiescently annealed samples, regardless the annealing time. The minute value of q_{ij} indicates that the morphology is globally isotropic. For the strained sample q_{ij} ($\sim 10^{-4}\mu m^{-1}$) was bigger than that of the non strained samples, although it is still very small compared to the value of Q (≈ 0.4). The degree of anisotropy (defined as q_{ij}/Q [28]) is $\sim 3 \times 10{-}4$. To elucidate the difference in anisotropy between the sheared and non sheared samples, the summands in eqn 6.15 where statistically analysed. To do that the probability densities of the quantities n_i, $n_i n_j$ and $n_i n_i - 1/3$ (with $n = 1, 2, 3$ and $i \neq j$) were defined. The probability density of n_i, $P_{ni}(n_i)$, is given as

$$P_{n_i}(n_i) = \frac{\sum_{k=1}^{N} A\left[k|n_i - \frac{\Delta n_i}{2} \leqslant n_{i,k} < n_i + \frac{\Delta n_i}{2}\right]}{\Delta n_i \sum_{k=1}^{N} A_k} \quad (6.17)$$

where A_k and $n_{i,k}$ are the interfacial area and the i-th component of the normal vector of the k-th triangle, respectively. The terms $A[k|n_i - \Delta n_i/2 \leqslant n_{i,k} < n_i + \Delta n_i/2]$

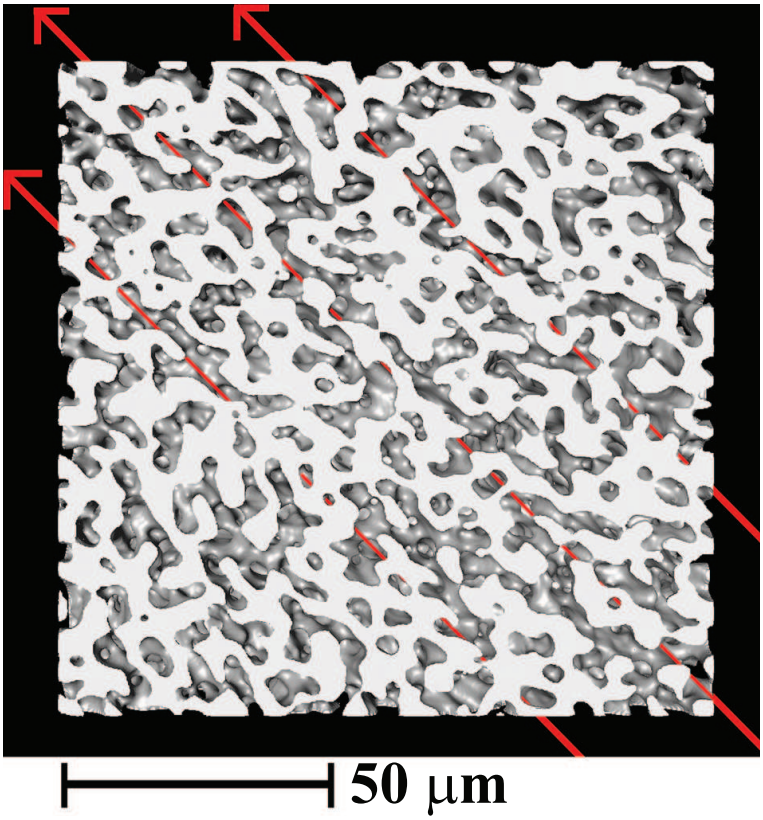

Figure 6.20: 3D image of 50/50 FLPS/SAN20 blend microstructure after 10 min of quiescent annealing followed by a single strain step ($\gamma = 20\%$). The red lines are to direct the eye towards the alignment direction.

gives the surface area of the triangles satisfying: $n_i - \Delta n_i/2 \leqslant n_{i,k} < n_i + \Delta n_i/2$. The denominator is included to satisfy the normalization condition: $\sum P_{n_i} \Delta n_i = 1$. $P_{n_i n_j}$ and $P_{n_i n_i - 1/3}$ were computed with expressions similar to eqn 6.17 (just changing n_i by $n_i n_j$ or $n_i n_i - 1/3$ throughout the equation).

Figures 6.21 show the distributions of n_i, $n_i n_j$ and $n_i n_i - 1/3$ for samples quiescently annealed (non sheared) for 10, 60 and 120 min. It is noteworthy that the three components of the normal vector field show the identical distributions. The same applies to the distributions of $n_i n_i - 1/3$ and $n_i n_j$. This fact and the symmetry of n_i and $n_i n_j$ distributions indicates that, globally, the interface does not have a preferred orientation. Additionally the distributions are independent of the annealing time. These observations support the statement that cocontinuous morphologies are isotropic at any stage of coarsening, which can also be inferred from the symmetry in the mean curvature distribution shown in Figure 3.11 (in section 3.5).

On the other hand, the distributions of n_1, n_2 and n_3 for the sheared sample are clearly different (see Figure 6.22), evidencing that, globally, the normal vector field is not directed equally to all directions. In addition, the asymmetry in the distribution of $n_1 n_2$, $n_1 n_3$, $n_2 n_3$ and the fact that they are all different makes manifest the anisotropy of the morphology.

Simplification of Doi-Ohta model for negligible anisotropy

Despite the obvious difference between the sheared and non sheared samples in the distributions of the normal vector components and their products, the value of q_{ij} is three orders of magnitude smaller than that of Q. Therefore, it can be, as a first approximation, be disregarded from the phenomenological equations for dq_{ij}/dt and dQ/dt (Eqns 6.7 - 6.11). These equation for oscillatory flow (applying a sinusoidal strain $\gamma = \gamma_0 \sin(\omega t)$) are given as [32]

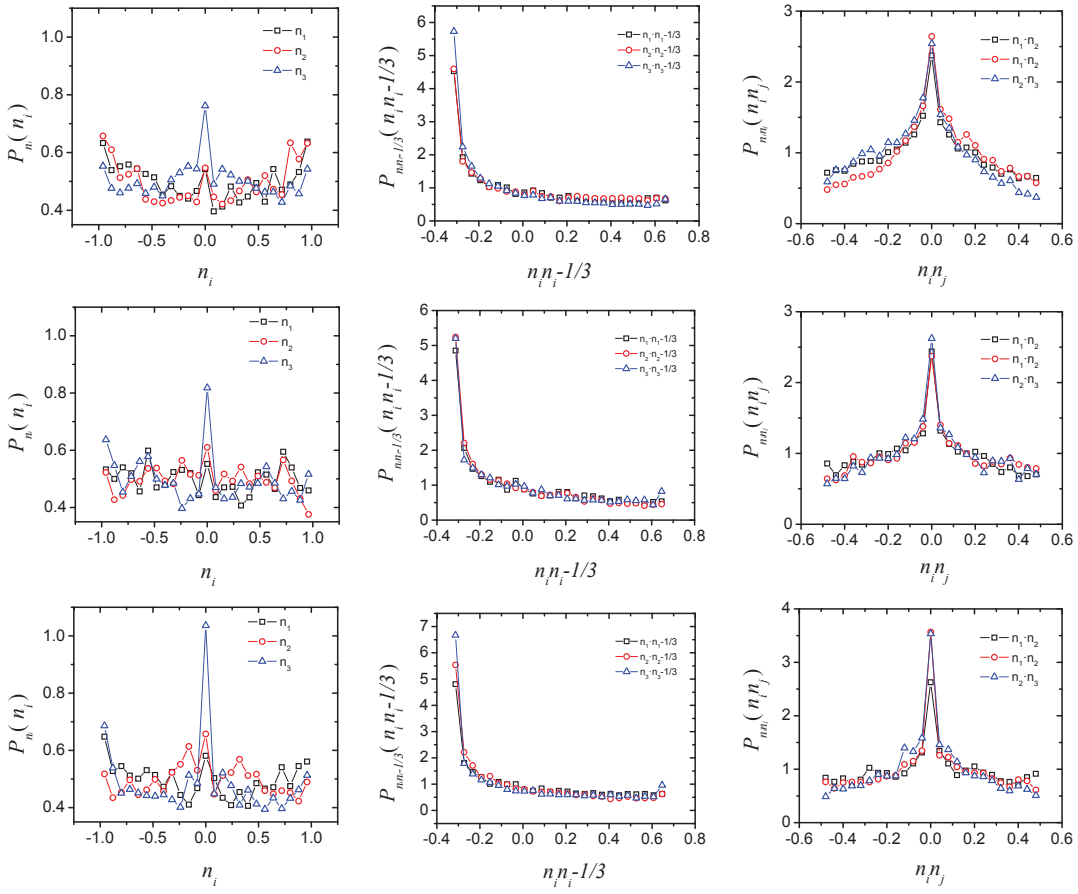

Figure 6.21: Probability densities of (1st column) n_i, (2nd column) $n_i n_i - 1/3$ and (3rd column) $n_i n_j$ $(i = 1, 2, 3; i \neq j)$ for 50/50 blends quiescently annealed at 200 $^\circ C$ for (1st row) 10 min, (2nd row) 60 min and (3rd row) 120 min.

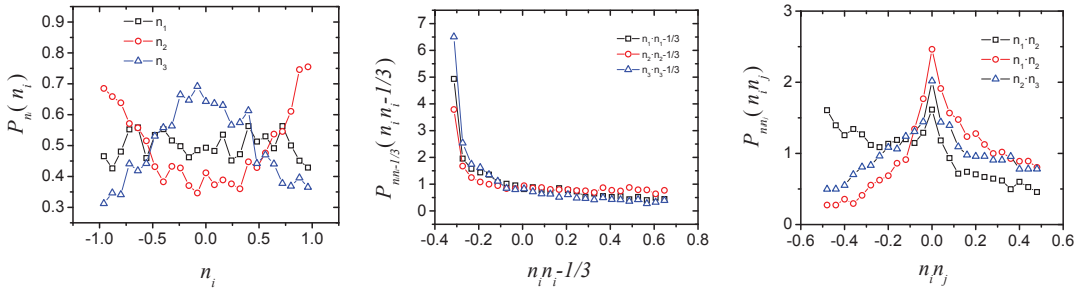

Figure 6.22: Probability densities of (left) n_i, (center) $n_i n_i - 1/3$ and (right) $n_i n_j$ $(i = 1, 2, 3; i \neq j)$ for sheared 50/50 blends quiescently annealed at 200 $^\circ C$ for 10 min and subsequently sheared with $\gamma = 20\%$.

$$\frac{d\tilde{q}_{xy}}{d\mathrm{T}} = \gamma_0 \Omega \cos(\Omega \mathrm{T}) \left(\frac{\tilde{q}_{xy}^2}{\tilde{Q}} - \tilde{q}_{xx} - \frac{\tilde{Q}}{3} \right) - \alpha \tilde{Q} \tilde{q}_{xy} \tag{6.18}$$

$$\frac{d\tilde{q}_{xx}}{d\mathrm{T}} = \gamma_0 \Omega \cos(\Omega \mathrm{T}) \left(\frac{2\tilde{q}_{xy}}{3} + \frac{\tilde{q}_{xx}\tilde{q}_{xy}}{\tilde{Q}} \right) - \alpha \tilde{Q} \tilde{q}_{xx} \tag{6.19}$$

$$\frac{d\tilde{Q}}{d\mathrm{T}} = -\gamma_0 \Omega \cos(\Omega \mathrm{T}) \, \tilde{q}_{xy} - \alpha \beta \tilde{Q}^2 \tag{6.20}$$

where the scaled variables are given by

$$\tilde{q}_{xy} = \frac{q_{xy}}{Q_0}, \;\; \tilde{q}_{xx} = \frac{q_{xx}}{Q_0}, \;\; \tilde{Q} = \frac{Q}{Q_0}, \;\; \mathrm{T} = \frac{\Gamma}{\eta} Q_0 t, \;\; \Omega = \frac{\eta}{\Gamma Q_0} \omega \tag{6.21}$$

with $Q_0 = Q(t = 0)$.

Applying the approximation $\tilde{Q} \gg \tilde{q}_{xy} \sim \tilde{q}_{xx}$ (i.e. $\tilde{q}_{xy} \sim \tilde{q}_{xx} \sim 0$), eqns 6.18 – 6.20 become

$$\frac{d\tilde{q}_{xy}}{d\mathrm{T}} = -\gamma_0 \Omega \cos(\Omega \mathrm{T}) \frac{\tilde{Q}}{3} \tag{6.22}$$

$$\frac{d\tilde{q}_{xx}}{d\mathrm{T}} = 0 \tag{6.23}$$

$$\frac{d\tilde{Q}}{d\mathrm{T}} = -\alpha \beta \tilde{Q}^2 \tag{6.24}$$

Solving eqn 6.24 with the initial condition $\tilde{Q}(\mathrm{T}=0)=1$ we obtain the well known linear law [14]

$$\tilde{Q} = 1 + \alpha\beta\mathrm{T} \tag{6.25}$$

This result implies that the flow does not affect the interfacial area, which is in accordance to what we observed experimentally ($1/Q = 2.39 \pm 0.3$ for the non sheared sample and 2.5 for the sheared sample). The linear law was fulfilled by all the blends in the early stage of coarsening (see Figure 6.14). The deviation from the linear growth is addressed in Chapter 4 and is due to a decrease in the interfacial energy which is the coarsening driving force.

Using eqn 6.25 to solve eqn 6.22, with the initial condition $\tilde{q}_{xy}(\mathrm{T}=0)=0$, we obtain

$$\tilde{q}_{xy} = -\frac{\gamma_0\Omega}{3}\int_0^T \frac{\cos(\Omega\mathrm{T})}{1+\alpha\beta\mathrm{T}}d\mathrm{T} \tag{6.26}$$

This expression can be integrated by parts *to generate an asymptotic expansion. Below are shown the first two leading terms:

$$\tilde{q}_{xy} = -\frac{\gamma_0}{3}\left[\frac{\sin(\Omega\mathrm{T})}{1+\alpha\beta\mathrm{T}} - \frac{\alpha\beta}{\Omega}\frac{\cos(\Omega\mathrm{T})}{(1+\alpha\beta\mathrm{T})^2} + \mathcal{O}\left((1+\alpha\beta\mathrm{T})^{-3}\right)\right] \tag{6.27}$$

Scaling analysis

According to the scaling analysis by Siggia [14] and experimental evidence (see Ref. [17] and Table 4.3 in Chapter 4), $\alpha\beta \sim 0.1$. For the systems studied here, $\Gamma \sim 10^{-3}$ N/m, $\eta \sim 10^3$ Pa·s (see Table 6.1) and $Q_0 \sim 10^6$ m^{-1}. Hence $\alpha\beta Q_0\Gamma/\eta \sim 0.1$ s^{-1} and $Q_0\eta/\Gamma \sim 1$ s.

Let us consider the frequency used in the time sweep tests, i.e. $\omega = 0.1$ s^{-1}. For this particular case $\Omega/\alpha\beta \sim 1$ and, therefore, eqn 6.27 can be written as

$$\tilde{q}_{xy}(\Omega = 0.1) \sim -\frac{\gamma_0}{3}S(\Omega\mathrm{T}) \tag{6.28}$$

*Integrating the $\cos(\Omega\mathrm{T})$ part and differentiating the $(1+\alpha\beta\mathrm{T})^{-1}$ part gives the leading term, i.e. $\sin(\Omega\mathrm{T})(1+\alpha\beta\mathrm{T})^{-1}$. Repeating the procedure generates the higher order terms.

where $S(\Omega T)$ is defined as

$$S(\Omega T) \equiv \frac{\sin(\Omega T)}{1+\Omega T} - \frac{\cos(\Omega T)}{(1+\Omega T)^2} \tag{6.29}$$

Figure 6.23 shows the plots of the functions $S(\Omega T)$ and $\sin(\Omega T)$, showing that both functions have the same periodicity and they are in phase[†]. This indicates that the applied strain and and the extra stress (defined in eqn 6.6) are in phase, which in turn signifies that the nature of the extra stress is purely elastic. This is in agreement with the experimental fact that only the elastic modulus is affected by the presence of interface, while the loss modulus is unaltered (see Figure 6.5).

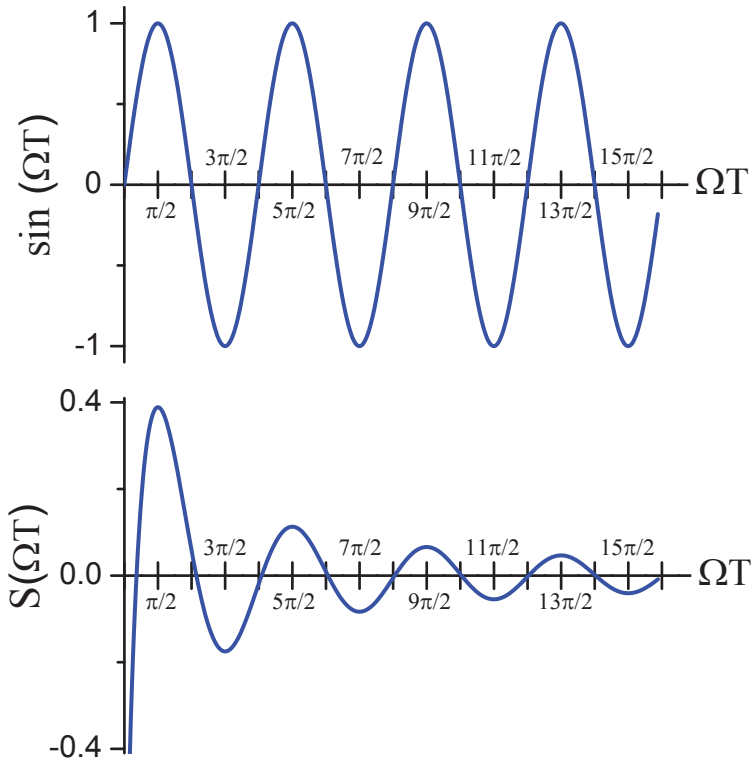

Figure 6.23: Plots of the functions $\sin(\Omega t)$ and $S(\Omega t)$.

[†]To prove this , note that the derivative of the function $S(x)$ is given as $dS/dx = 2\cos(x)(1+x)^{-3} + cos(x)(1+x)^{-1}$. Thus it is plain that the extreme values of both functions ($S(x)$ and $\sin(x)$) occurs at $x|x = \arccos(0)$ i.e. at $x = (2n-1)\pi/2, n = 1, 2, 3, ...$

For limiting case where $\alpha\beta \mathrm{T} \gg 1$, i.e. $t \gg 10s$, we can neglect the second term of function $S(\Omega \mathrm{T})$ (eqn 6.29). It follows that

$$\tilde{q}_{xy}(\Omega \sim 0.1, \mathrm{T} \to \infty) \sim -\frac{\gamma_0}{3}\mathrm{sinc}(\Omega \mathrm{T}) \tag{6.30}$$

where $\mathrm{sinc}(\Omega \mathrm{T})$ is the well known *sine cardinal* function[‡]

$$\mathrm{sinc}(\mathrm{x}) \equiv \frac{\sin(\mathrm{x})}{\mathrm{x}} \tag{6.31}$$

To verify the validity of this approximation, notice that the functions $S(\Omega \mathrm{T})$ and $\mathrm{sinc}(\Omega \mathrm{T})$, as well as the leading term in $S(\Omega \mathrm{T})$, i.e. $\sin(\Omega \mathrm{T})/(1 + \Omega \mathrm{T})$, (all shown in Figure 6.24) converge to the same values at $\Omega \mathrm{T} \gtrsim 10$, which correspond to $t \gtrsim 100$ s. The time scale for the annealing and time sweep experiments were in that range. Hence the approximation is justified.

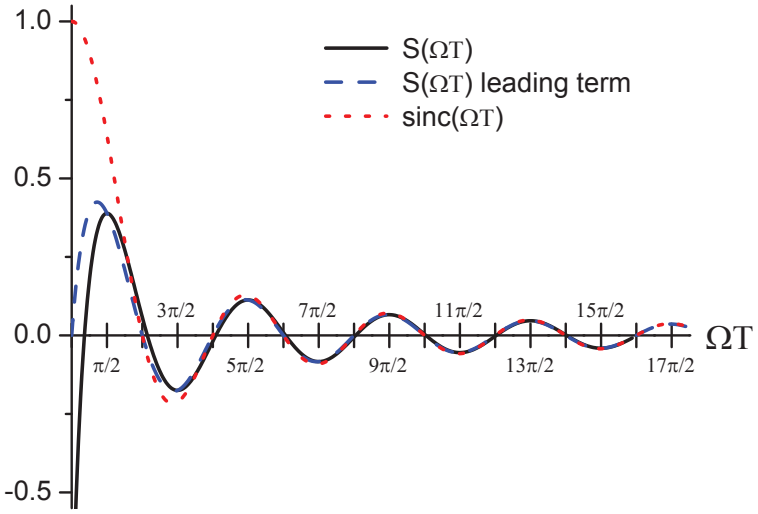

Figure 6.24: Plots of the the functions $S(\Omega \mathrm{t})$ (–), $\sin(\Omega \mathrm{T})/(1+\Omega \mathrm{T})$ (- -) and $\mathrm{sinc}(\Omega \mathrm{T})$ (· · ·).

Eqn 6.30 implies that the amplitude of the extra stress due to the interface , $\sigma_{xy,int}$, is proportional to t^{-1}. It follows that $G' \propto t^{-1}$. The experimental decay of G' follows

[‡]Also known as *sampling function* [167, 168]

two regimes described with power laws (see Figure 6.25) with exponents given in Table 6.2. The absolute value of the exponents are generally lower than 1, except for those corresponding to the late regime of the blends with low Γ (i.e. those containing SAN10). The discrepancy between the exponents indicates that the elastic modulus decrease more slowly than the anisotropy which could be due to a physical effect that escapes our understanding. A more thorough analysis of the evolution of the anisotropy is required to understand this discrepancy. The availability of 3D images along with the method proposed here to compute the normal vector field will help us tu pursue this task in the near future.

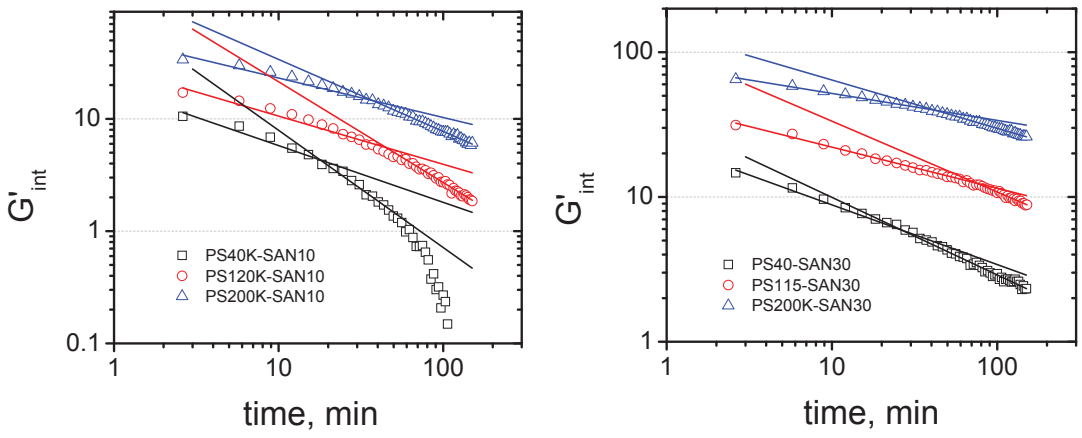

Figure 6.25: Interface contribution to the elastic modulus as a function of time for 50/50 blends measured at 200 °C with a fixed frequency of 0.1 rad/sec and 20 % strain. Same data as in Figure 6.17 but plotted in log-log scale and power law fits included.

Finally, the proportionality between G'_{int} and Γ is confirmed in Figure 6.26. The $G'/G'_{comp}(t)$ plot makes the effect of Γ and clearer that the $G'_{int}(t)$ plot, although G'/G'_{comp} is proportional to G'_{int}. It is evident that G' is generally bigger for the higher Γ blends (those containing SAN30) than for the lower Γ blends (those containing SAN10). Moreover, the $G'/G'_{comp}(t)$ plot levels off to plateau values of 1.4 ± 0.4 for the blends containing SAN10 and 3.0 ± 0.4 for the blends containing SAN20. Remarkably, no effect of p on the elastic modulus was observed, which similar to the effect observed in the non annealed blends (section 6.3.1).

Table 6.2: Experimental power law exponent describing the decrease of elastic modulus ($G'_{int} \propto t^b$) in the early and late stage of dynamic time sweep tests.

Blend	Early stage	Late stage
PS40K/SAN10	-0.51	-1.04
PS40K/SAN30	-0.41	-0.54
PS120K/SAN10	-0.43	-0.90
PS120K/SAN20	-0.26	-0.54
PS120K/SAN30	-0.28	-0.49
PS200K/SAN10	-0.35	-0.64
PS200K/SAN30	-0.18	-0.33

6.4 Conclusions

The effect of interfacial tension and viscosity ratio on the microstructure and viscoelastic response of cocontinuous blends during coarsening was investigated. Data from dynamic frequency sweeps were corrected for the inherent error due to coarsening during the tests. The corrected data were used to construct different plots, namely (1) Cole-Cole plot, (2) van Gurp-Palmen plot as well as (3) non weighted, (4) weighted , and (5) normalized weighted relaxation spectra. The Cole-Cole plot and the non weighted relaxation spectra plots are not sensitive to the difference in interfacial tension and viscosity ratio, while the van Gurp-Palmen plot and the weighted relaxation spectra are. The storage modulus for all the blends follows the typical power law behavior at low frequencies, with exponent dependent on the viscosity ratio but not on the interfacial tension.

At early times, the characteristic length of all the blends grew linearly with time, as predicted by the classical theory of spinodal decomposition developed by Siggia [14]. Also in accordance to Siggia's theory, the rate of coarsening was found to be proportional to the ratio between the interfacial tension and the blend viscosity. At late times, the coarsening starts to slow down, more abruptly for the high interfacial tension blends (i.e. those containing SAN30) than for the blends with low Γ. This decrease in rate of

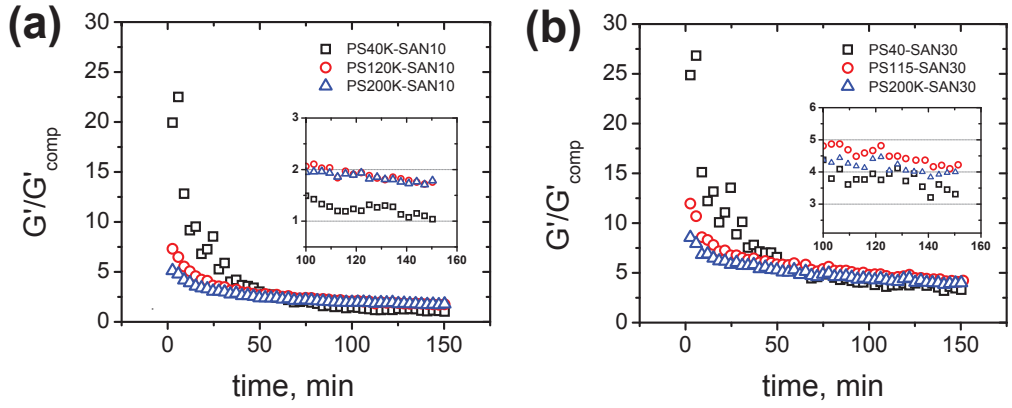

Figure 6.26: Ratio between the elastic modulus of 50/50 blends and their components measured a 200 °C with a fixed frequency of 0.1 rad/sec and 20 % strain.

coarsening, which is due to a gradual reduction in the interfacial energy, was subject of Chapter 4.

Doi-Ohta model [28] considers that the extra stress observed in two phase fluid is due to a relaxation of interface after deforming it into an anisotropic state. We developed a new method to measure the normal vector field of the interface which is used to compute the anisotropy tensor included in the analysis by Doi and Ohta. We proposed a simplification of the Doi-Ohta model based on the fact that the measured maximum anisotropy of the blend during the oscillatory tests is three orders of magnitude lower than the interfacial area per unit volume.

Accompaning the coarsening of the microstructure, a decrease in the extra contribution of the elastic modulus was observed. The simplified (Doi-Ohta) model proposed here predicts a reduction in the elastic modulus described by a power law with exponent -1. On the other hand, experimental results reveal two regimes of decrease in G', both described by power laws with exponents generally lower than 1, except for the case of the low interfacial tension blends (those containing SAN10) during the late stage. Further research is required to understand the discrepancy between the exponents for the other blends and the nature of the two regimes. We believe that the new methodology to compute the anisotropy of complex interfaces will allow us to uncover these unknowns.

Chapter 7

Rheology of Compatibilized Blends during Coarsening

7.1 Introduction

Throughout this thesis it has been emphasized that cocontinous blends are thermodynamically unstable. It has been reiterated, as well, that the nature of the instability lies in the existence of an excess in interfacial energy stored at the interface between the two phases. Such energy, which is proportional to the interfacial tension (Γ), will drive the coarsening of the microstructure. Accordingly, reducing interfacial tension represents a suitable way to hinder the coarsening process. As shown in Chapter 5, a very effective way to reduce interfacial tension in immiscible polymer blends is to add a block copolymer [103, 17, 104, 169, 20, 21].

Besides improving the morphology stabilization, adding a compatibilizer will have an effect on the viscoelastic properties of the blend. In contrast with the abundant literature on the morphology of compatibilized blends, only a limited number of studies were devoted to their rheology. Most of these studies consider systems with droplet-matrix morphologies [30, 170, 171, 172, 173, 174, 175], while very few deal with systems with cocontinuous morphologies [103, 81]. In general, regardless the type of microstruture, the compatibilization enhances the extra-elasticity effect due to the interface of the blend compared to non compatibilized blend. Mekhilef et al. [103] reported that the addition of styrene-ethylene-butadiene-styrene copolymer to a 50/50 polystyrene/polyethylene

blend leads to a significant increase in both the complex viscosity, η^*, and the elastic modulus, G', compared to the compatibilized blend. Additionally, neither η^* nor G' of the modified blends changed with time, which was attributed to a more stable morphology. Omonov et al. [81] showed that rheological measurements of 50/50 polypropilene/polystyrene blends revealed an excess of elasticity in the terminal zone with respect to the neat components. This extra elasticity was more important for blends compatibilized with amino-terminated polystyrene and maleic anhydride grafted polypropylene.

In this study, the effect of PS-b-PMMA copolymer (BC) of varying molecular weight on the rheological response of FLPS/SAN20 blends was investigated in relation with their morphology. Three blend compositions were considered, namely, 20/80, 35/65 and 50/50 w/w. The morphology was characterized using 3D confocal microscopy with image analysis. Neat blends were compared to those containing BC. The effect of annealing on both rheology and morphology was also investigated.

7.2 Experimental

7.2.1 Materials

All the blends used in this study were prepared with FLPS120k and SAN20. The synthesis and characterization of these polymers are detailed in Chapter 2. Their key properties are shown in Table 2.2. These two polymers were chosen for this study due to their closeness in viscosity (the viscosity ratio is 0.625). The interfacial tension between the polymers is 0.86 ± 0.14 (measured with the breaking thread method and the rheological method, see Appendix C). Symmetric block copolymers made of polystyrene and polymetylmethacrylate (PS-b-PMMA) with different molecular weights were supplied by Polymer Source (42k, 74k, 100k, and 260k PS-b-PMMA) and by Polymer Standard Services (900k PS-b-PMMA). They are named in this chapter as BC preceded by their molecular weight. Table 7.1 shows the material's molecular weight and polydispersity.

7.2.2 Blend preparation, annealing and 3D imaging

The materials were mixed using a Daca microcompounder (DACA Instruments) at 180 $^{\circ}C$ under N_2 purge. The blends were prepared with three compositions, namely, 20/80, 35/65 and 50/50 w/w. In these study these blends will be referred as B2080, B3565 and B5050, respectively. B2080 and B3565 were prepared with and without 1% BC100K, while B5050 was prepared without BC, with 1% of all the block copolymers listed in Table 7.1 and with 0.1, 0.5, 1.0 and 5.0 % of BC100K. After 10 minutes of mixing, the blends were extruded out of the mixer and cut into small pellets. The pellets were put in between two glass slides and annealed at 200 $^{\circ}C$ for different times before microscopy. The annealed samples were imaged using a laser scanning confocal microscope (Olympus Fluoview 1000) with two oil-immersed objectives with magnifications of 20× and 40× to observe features bigger and smaller to $\sim 30\mu$m, respectively. An incident laser beam of 405 nm was used to excite the anthracene groups in the FLPS120K and a barrier filter of 461 nm to detect their fluorescent signal. Series of about 100 2D confocal images per sample from different z-positions were obtained, processed and reconstructed into 3D images as described in Chapter 3.

7.2.3 Rheological characterization of blends

Samples of the blends were moulded into 2.5 cm discs and dried at 90 $^{\circ}C$ for 24 hrs. Dynamic frequency and time sweeps were performed on the dried discs at 200 $^{\circ}C$ with a strain of 20% using a strain-controlled rheometer (TA Instruments Rheometrics series ARES) with N_2 purge. For the time sweeps, a frequency of 0.1 rad/s was used. Frequency sweeps were performed over a range of 100 to 0.1 rad/s.

7.3 Results and discussion

7.3.1 Blends morphology

20/80 Blends

Figure 7.1 shows the confocal images of the compatibilized and non compatibilized FLPS/SAN20 20/80 blends after 5 and 40 min of annealing. A droplet-matrix morphology is observed in all four micrographs. The blurriness in the images is due to

the broad distribution in droplet sizes. The size of the bigger droplets is close to the resolution of the confocal micoscope (0.4 μm, see Table 4.2); thus the big population of smaller droplets cannot be resolved and are detected just as blurriness. This fact makes impossible the image threshold processing required for 3D reconstruction.

Measuring the diameter of the well defined droplets (i.e. the bigger ones), we calculated and approximate volume weighted average radius, R_V. The droplet sizes in both blends were stable during annealing. R_V grew from 0.53 μm (at 5 min) to 0.58 μm (at 40 min) for the non compatibilized blend and from 0.1 μm to 0.13 μm for the compatibilized one. Hence, the effect of adding the block copolymer was to reduce the droplet size about five times.

35/65 Blends

Figures 7.2 and 7.3 show 3D reconstructed micrographs of the non compatibilized and compatibilized B3565 blends, respectively, at different annealing times. These blends show an initial cocontinuous structure with an initial size smaller for the compatibilized blends than for the non-compatibilized ones ($\lambda_{B3565w/1\%100KBC}/\lambda_{B3565w/o100KBC} \sim 0.38$). The morphology of the non compatibilized blend remains wholly cocontinuous until $\sim 20min$, after which time, circular regions with droplet-matrix morphologies start to appear throughout the samples (see Figure 7.4a) due to the pinch off of the interconnected domains (see Section 3.5). The same behavior was observed in the compatibilized blend, but the appearance of dispersed domains occurred after ∼40 min of annealing (see Figure 7.4b). Figure 7.3d captured the formation of the first droplets at 40 min of annealing for the compatibilized blends.

Besides the reduction of the initial characteristic size, the BC reduced the rate of coarsening in the *cocontinuous regime* (i.e. before the onset of the pinch off process). The characteristic size as a function of annealing time is shown in Figure 7.5. The size of the compatibilized blend is very stable until the onset of the pinch off, when a sudden increase to sizes comparable to those corresponding to the non compatibilized blends is observed. The big error bars in the composite regime (i.e. after the onset of the pinch off process) in Figure 7.5 reflects to the non-uniformity of the morphology.

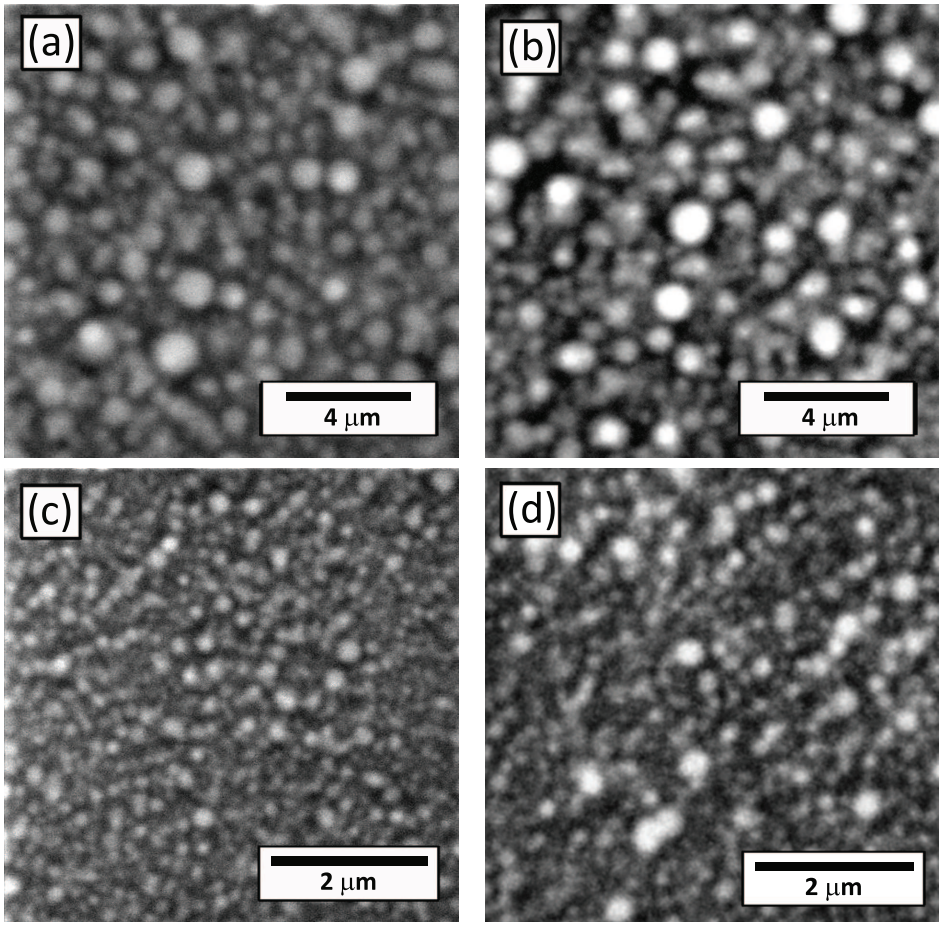

Figure 7.1: Confocal micrographs of 20/80 FLPS/SAN20 blends (a and b) without and (c and d) with 1% 100KBC annealed for (a and c) 5 and (b and d) 40 min at 200 $^{\circ}C$.

Table 7.1: Molecular weight and zero shear viscosity of blend components.

Abbreviation	M_n kg/mol	M_w/M_n	$^a\eta_0$ (at 200 $^\circ C$) Pa-s
FLPS	71.3	1.7	1485
SAN	71.2	1.9	2376
42KBC	21-21	1.1	- -
74KBC	37-37	1.1	- -
100KBC	50.6-47.6	1.1	- -
260KBC	130-133	1.1	- -
900KBC	450-450	1.1	- -

[a] see section 2.3.

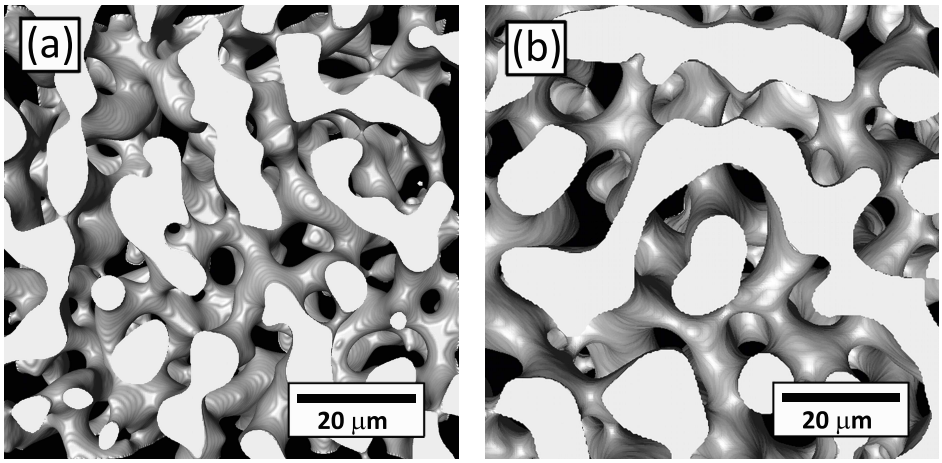

Figure 7.2: 3D images of non compatibilized 35/65 FLPS/SAN20 blends annealed for 5 and 10 min at 200 $^\circ C$.

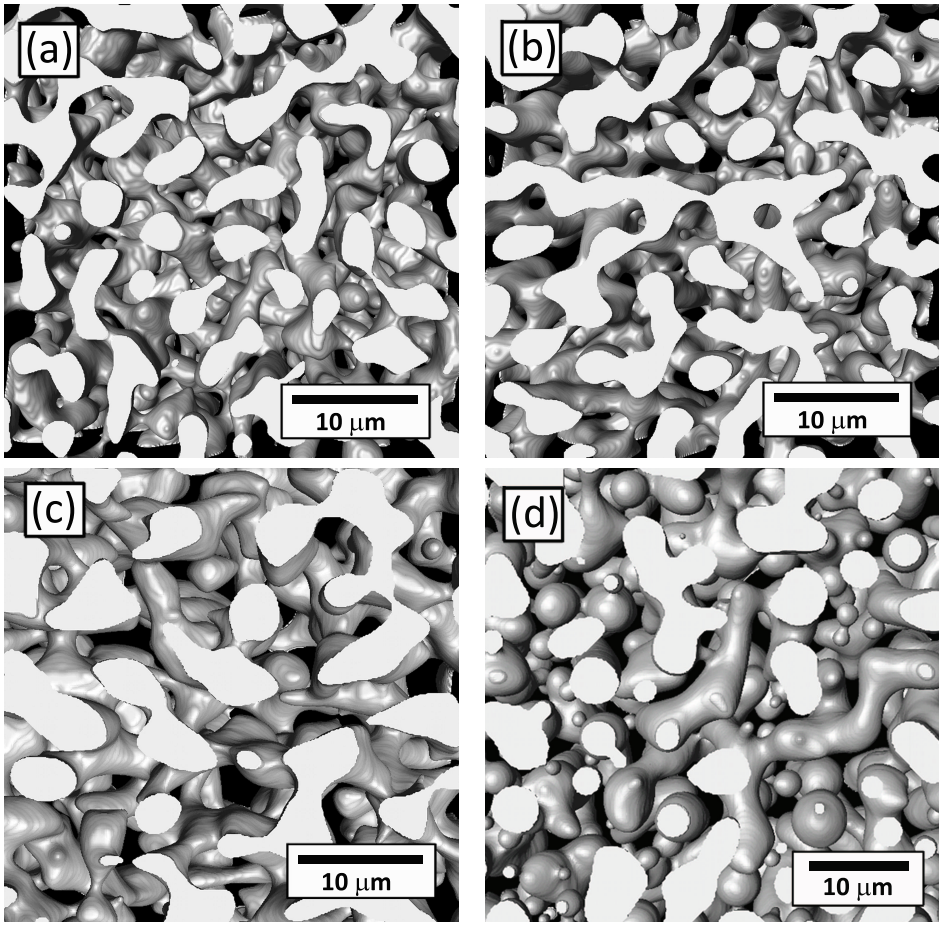

Figure 7.3: 3D images of 35/65 FLPS/SAN20 blends compatibilized with 1% 100KBC annealed for (a) 5, (b) 10, (c) 20 and (d) 40 min at 200 $^{\circ}C$.

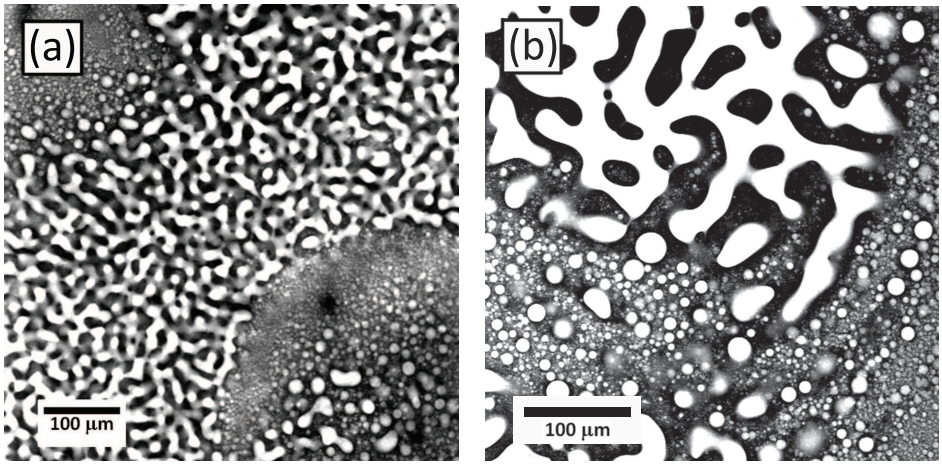

Figure 7.4: Composite microstructure of 35/65 blends after annealing at 200 $^{\circ}C$. (a) shows the morphology of the blends without BC after 20 min of annealing and (b) the morphology of the blend with 1% 100KBC after 60 min of annealing.

50/50 Blends

The morphology during annealing of the non-compatibilized B5050 blends was discussed in Chapter 5. In short, it was found that:

- all blends showed cocontinuous morphologies at all times of annealing,
- the effect of BC was to reduce the initial characteristic size and the rate of coarsening,
- the efficiency in the reduction of coarsening is dependent on the BC molecular weight, following the next order: 260KBC>100KBC>900KBC>74KBC>42KBC. These observations were explained in terms of equilibriums between micelles dissolution and formation and between adsorption and desorption of BC from the interface (see section 5.3.2).
- The compatibilization efficiency was also dependent on the amount of BC added. The higher the BC concentration, the lower the rate of coarsening and initial characteristic size (see section 5.3.3).

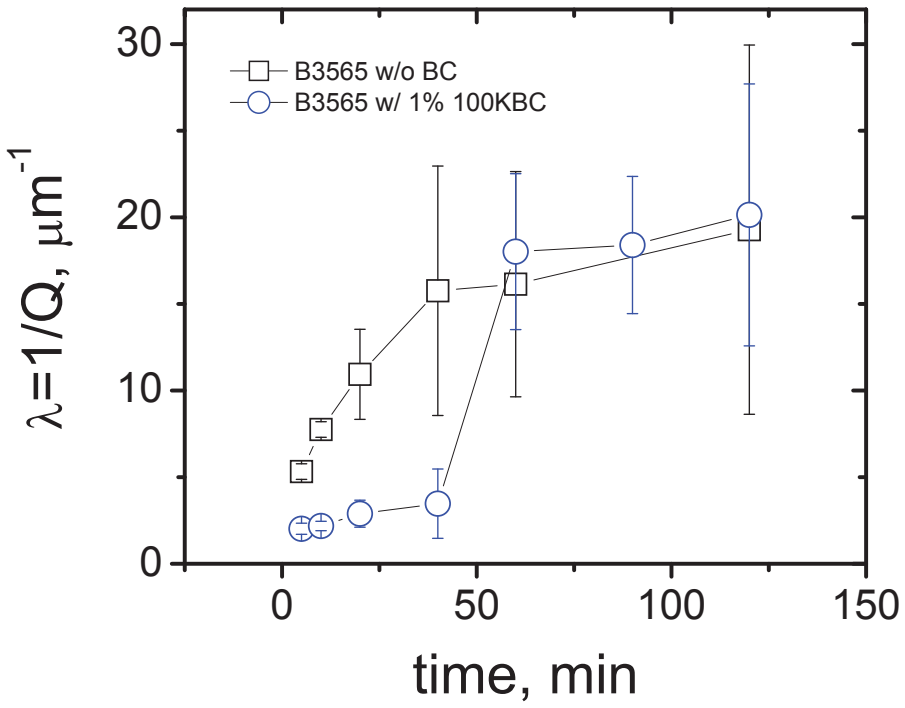

Figure 7.5: Characteristic length versus annealing time of 35/65 FLPS120K/SAN20 blend, with and without BC, measured from 3D images.a The error bars indicate the standard deviation calculated from measurements of five different samples..

On the other hand, in Chapter 3, it was demonstrated that distributions of the mean (H) and Gaussian (K) curvatures for the non compatibilized B5050 blends at different times superimpose with each other when they are normalized with the characteristic length. This indicated that the coarsening takes place in a self-similar manner. Additionally, the symmetry around zero of the mean curvature distribution and the dominant population of negative values of the Gaussian curvature indicate that the interface of these blends are composed mostly of hyperbolic (saddle shaped) patches [45]. The same trends were observed for the 50/50 blends with 1% BC (see Figure 7.6). However for the blends with 5% BC the behavior was markedly different.

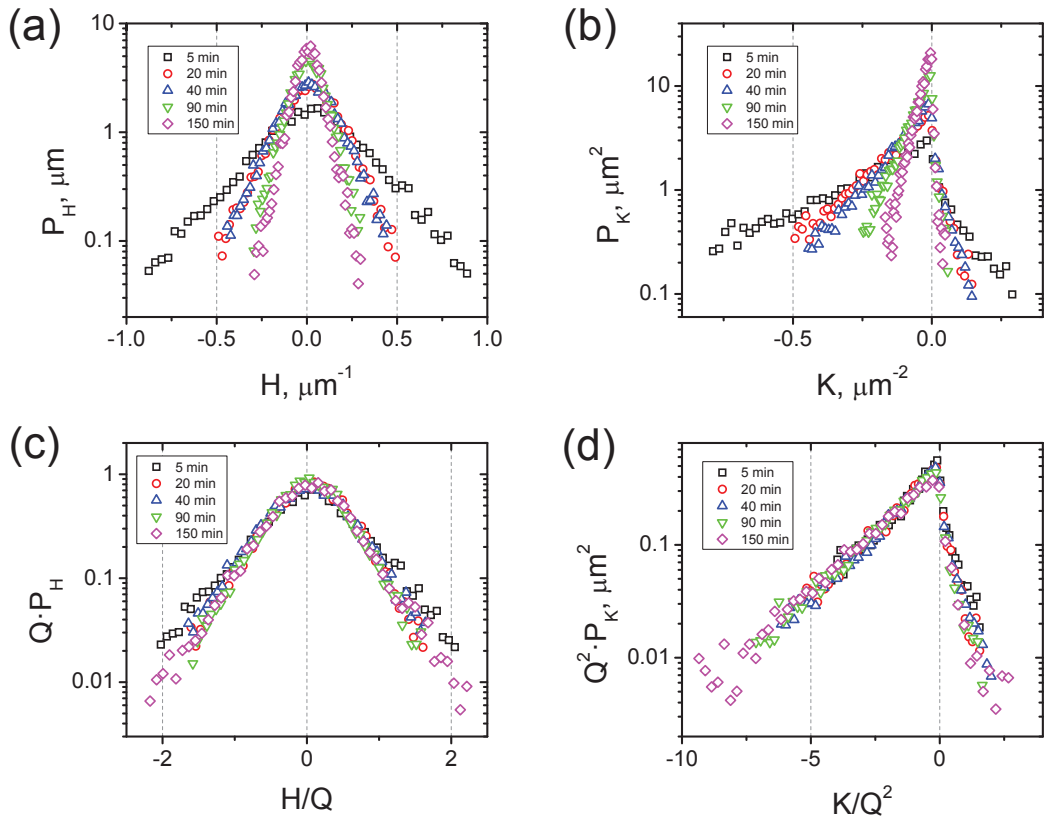

Figure 7.6: Probability densities (a and b) and scaled probability densities (c and d) of the mean (a and c) and the Gaussian (b and d) curvatures of the B5050 with 1% 100KBC at different annealing times.

Figure 7.7 show the distributions of the mean and Gaussian curvatures for the 50/50 blend with 5% BC at different annealing times. The mean curvature distribution at 5 minutes of annealing is symmetric but centered around a finite positive value of H. The shift of the distribution from the central possition, H=0, increases at longer annealing times. This and the evolution of the K-distribution (Figure 7.7b) (from mostly negative to a symmetric distribution of K values) indicates a change in the local shape of the interphase from mostly hyperbolic (saddle shaped) to elliptic (rounded) shapes.

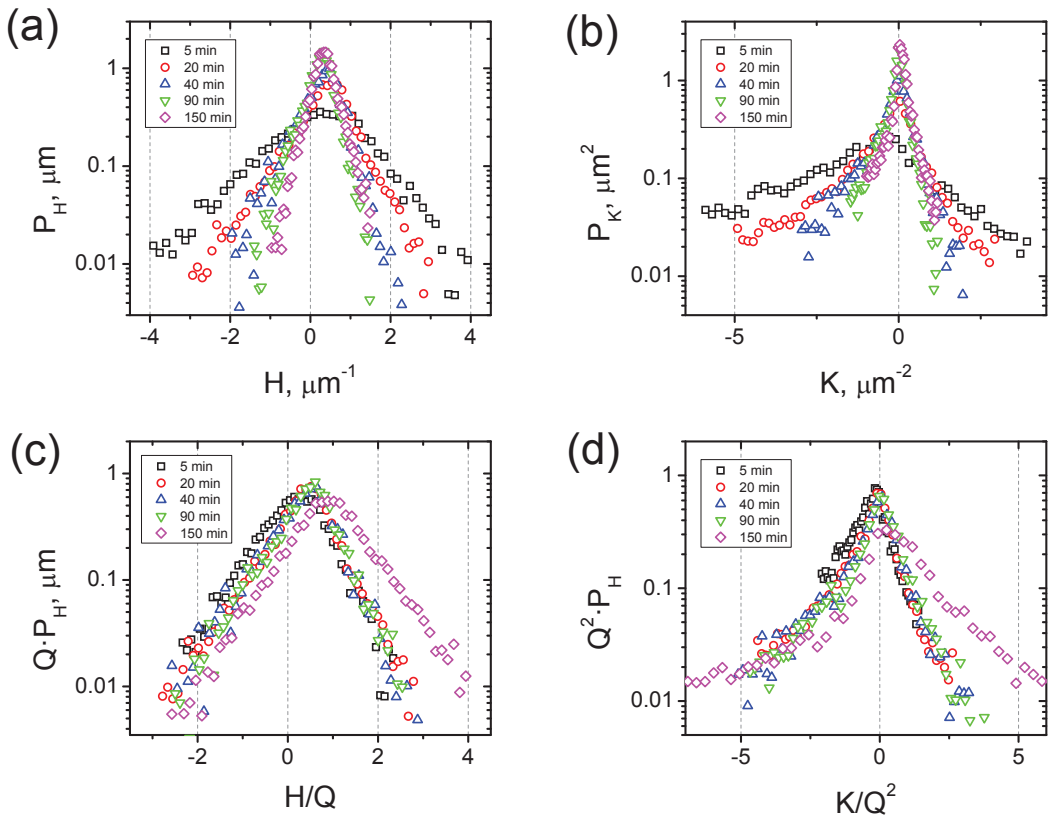

Figure 7.7: Probability densities (a and b) and scaled probability densities (c and d) of the mean (a and c) and the Gaussian (b and d) curvatures of the B5050 with 5% 100KBC at different annealing times.

This transition is evident in the micrographs of the blend at different annealing times, shown in in Figure 7.8. It is plain that, even when the morphology is cocontinous

at any time, the interface evolves toward the formation of more rounded domains to the point that, at 150 min, the morphology is made of interconnected droplets. Evidently, the evolution of the microstructure is not self-similar, which is verified by the non-superimposition of the scaled distributions (Figures 7.7c and 7.7d). As discussed in the next section, the rounded shape of the interface has an effect on the rheology of these blends. However, further research is needed to understand the formation of rounded interface in relation to the high concentrations of BC.

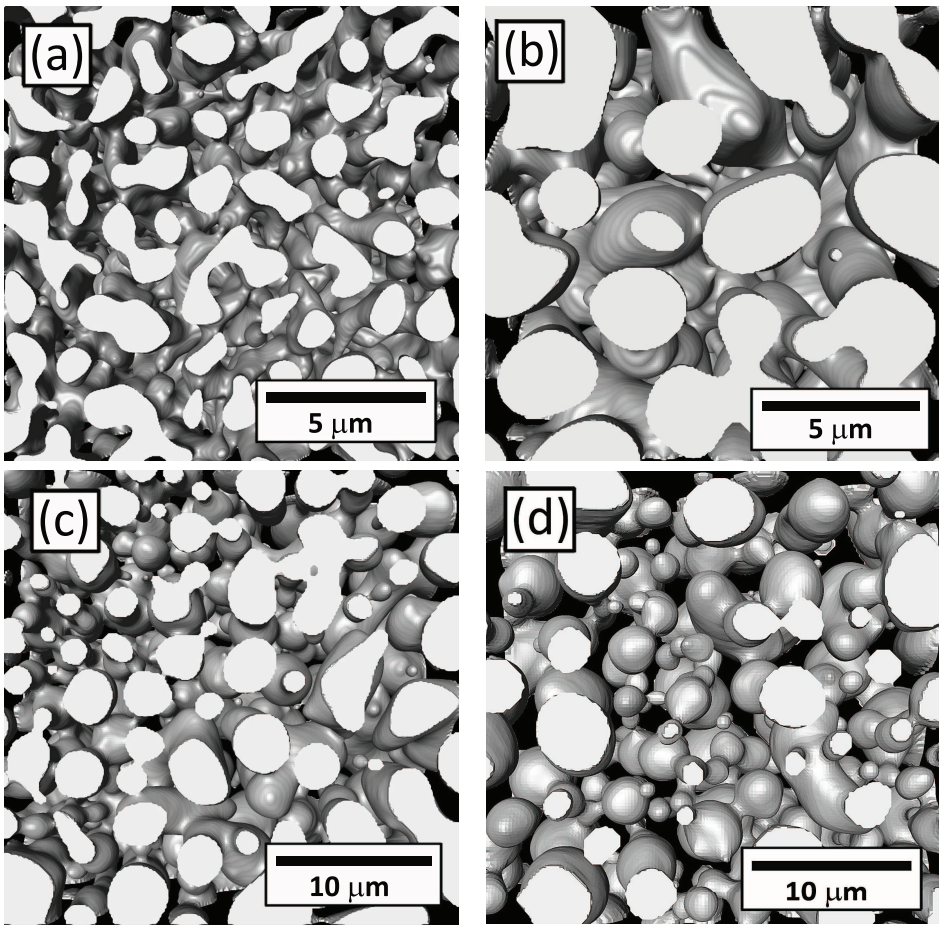

Figure 7.8: 3D images of 50/50 blends with 5% 100KBC annealed at (a) 5, (b) 40, (c) 90 and (d) 150 min.

7.3.2 Rheological characterization

Figure 7.9 shows the corrected data of the dynamic frequency tests for all the compatibilized and non-compatibilized blends. The data were corrected for annealing during the tests following the method described in section 6.3.1. All the blends show an extra-elasticity in the terminal zone with the typical shoulder and power law behavior for the disperse morphologies (B2080 blends) and cocontinuous structures (B5050 blends), respectively [24].

It is worth to notice that B3565 blends display a shoulder instead of a power law behavior at low frequencies even when the morphology of these blends is cocontinuous at the early times of annealing. The amount of extra elasticity observed in this blends is clearly bigger that that for the B2080 or the B5050 blends. The reason for this behavior is not clear, however it could be an effect of the distribution of the local shapes. From the analysis of the curvature distributions, in Chapter 3, it has been proved that the interface in 50/50 blends is dominantly hyperbolic (saddle shaped), while the the interface in the 35/65 blends is a combination of hyperbolic and parabolic (cylindrical shaped) patches, owing to the elongated FLPS domains (see Figures 7.2 and 7.3). Further analysis is required to prove that the difference in local shape is the responsible for the difference in the elastic behavior at low frequencies.

The viscous modulus is less affected by the presence of the interface than the elastic modulus. This effect is more noticeable for the B2080 blends and indiscernible for the B5050 blends. The $\tan\delta(\omega)$ plots confirm that the biggest increase in elasticity is observed in the B3565 blends.

The extra contribution to G' is higher for the compatibilized blends than for the non-compatibilized ones. However, the $G'(\omega)$ plot is very insensitive to this difference. To better understand the rheological differences between the compatibilized and non-compatibilized blends, Cole-Cole plots, van Gurp-Palmen plots and relaxation spectra were constructed from the frequency sweep data.

Cole-Cole plots

The Cole-Cole plots are very useful to investigate rheological behavior in relation with morphology of two phase systems [147] (see section 6.3.1). Some of the rheological

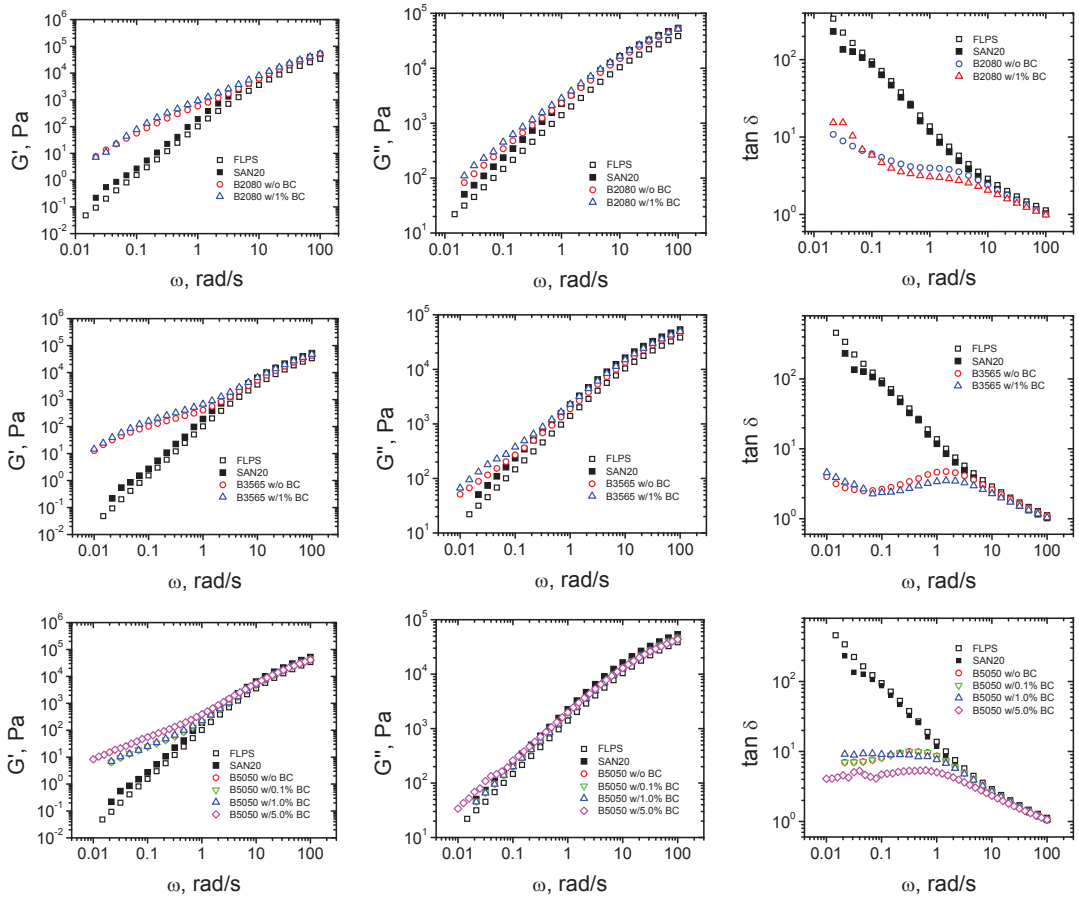

Figure 7.9: Dynamic moduli and $\tan\delta$ of compatibilized and non compatibilized FLPS/SAN20 blends measured at 200 $^{\circ}C$ and strain=20 %.

information derived from this plots include zero shear viscosity, η_0, and characteristic relaxation time, τ [147, 176, 177]. Figure 7.10 illustrate the rheological information obtainable from the Cole-Cole plot with the typical semicircle, characteristic of polymers with monomodal molecular weight distribution.

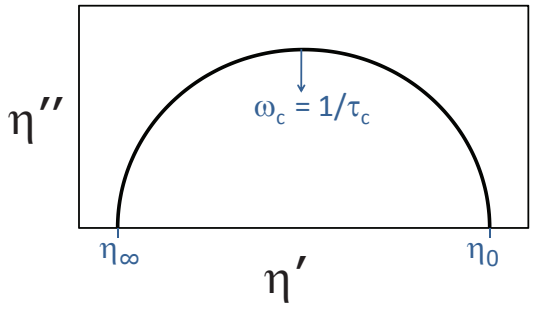

Figure 7.10: Schematic of Cole-Cole plot with rheological parameters.

Figure 7.11 show the Cole-Cole plots for all the blends and their components, computed from the frequency sweep data. The expected semicircle is observed for the blend components. The Cole-Cole plots of the blends display a contribution due to the components (at low values of η') and a contrubution due to the interface (at high values of η').

For the 20/20 blends, an additional peak at high values of η' (Figure 7.11a) depicts the relaxation of the droplets. The peak occurs at different relaxation times for the compatibilized and non-compatibilized blends. This reflects the difference in characteristic size between the two blends. This difference is clearer in the relaxation spectra, as shown later in this section.

The Cole-Cole plot for the 50/50 blends (Figure 7.11c) shows a tail in the high η' region, corresponding to the relaxation of a distribution of sizes forming the cocontinuous structures. Besides the tail, the blend containing 5% BC shows a second maximum, similar to the corresponding to the relaxation of droplets in the 20/80 blends. This additional relaxation is more evident in the relaxation spectra (Figure 7.14c).

Figure 7.11b shows the Cole-Cole plot of the 35/65 blend. The interface contribution is formed by a long tail and a peak at very high values of η'. The interpretation of the

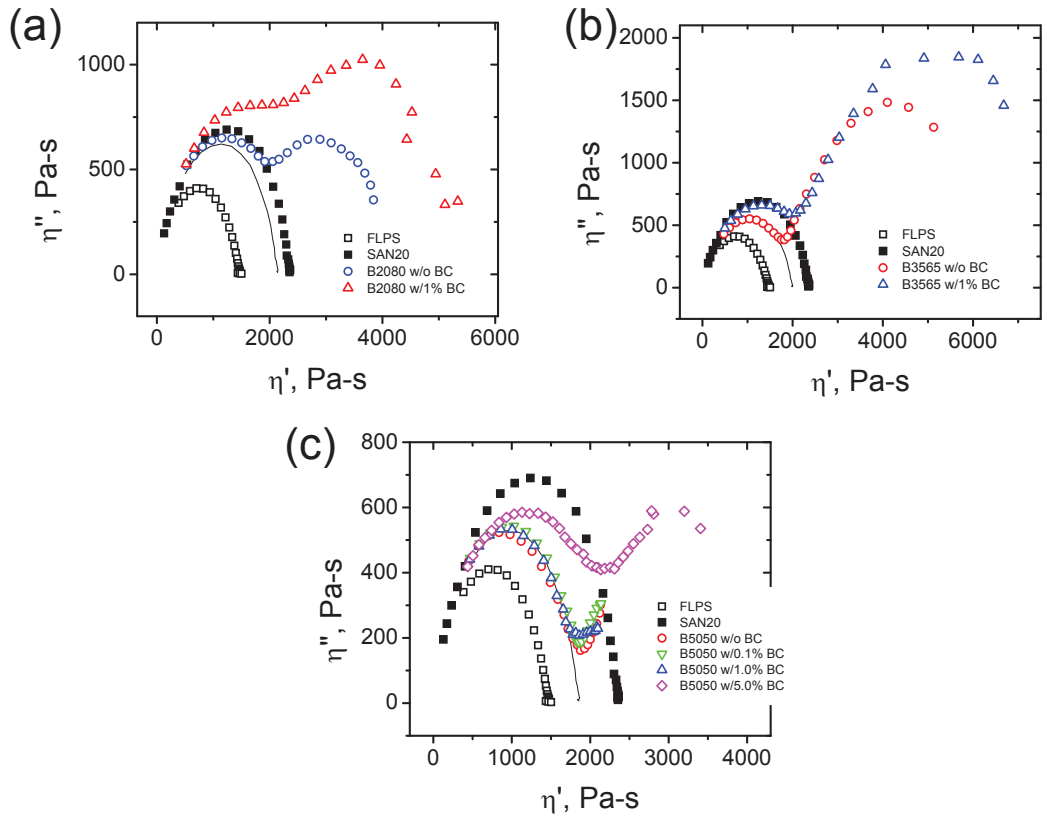

Figure 7.11: Cole-Cole plots of compatibilized and non compatibilized FLPS/SAN20 blends and their components at 200 $^{\circ}C$. The solid line indicates geometrical mean between the component data.

composite shape is not clear, but may be a manifestation of the combination of the two types of shape of the interface (i.e. hyperbolic and parabolic), as discussed above.

Figure 7.12 shows the Cole-Cole plots normalized with the zero shear viscosity for all the blends and their components. It is remarkable that even when the morphologies of both the 35/65 and the 50/50 blends are wholly cocontinuous and their characteristic sizes are comparable, the contribution from the interface, in the high η' region, is three bigger fold than that from the components for the 35/65 blends, whereas the opposite behavior is observed in the 50/50 blends. This indicates that the extra elasticity of cocontinuous blends is dependent on the local shape of the interface, not on the amount of *interconnections* as suggested by Polios et al. [121].

van Gurp-Palmen plots

The van Gurp-Palmen (vGP) plot [149], i.e. a plot of the phase angle, δ, versus the magnitude of the complex modulus, $|G^*|$, has been found to be useful to characterize morphology of phase separated systems. Li et al. [147] found that a valley in the low $|G^*|$ region in the vGP plot indicates the presence of a droplet-matrix morphology, while a maximum indicates a cocotinuous structure.

Figure 7.13 shows the vGP plots for all the blends and their components. The blend components show the vGP plot expected for linear polymers, i.e. a plateau at $\delta = 90°$ in the low $|G^*|$ region [150, 151]. We observed trends in the vGP plots different to those observed by Li and coworkers [147]. For the 20/80 blends, going from high to low values of $|G^*|$, we observed a shoulder followed by an increase in in the $|G^*|$ values (see Figure 7.13a), whereas a valley in the low $|G^*|$ region was observed for the 35/65 blends (Figure 7.13b). For the 50/50 blends, the shape of the vGP plots varied with the BC composition (Figure 7.13c): the non-compatibilized blend (blends with 0% and 0.1 % BC) display similar behavior as that observed by Li et al. (i.e. a peak followed by a downward tendency), the blend with 1% BC displayed a plateau at $\delta \sim 84°$, and the blend with 5% BC exhibited a plateau at $\delta \sim 80°$ followed by a small valley.

By virtue of the discrepancies between Li et al. observations [147] and ours, we conclude that vGP plots are not suitable to distinguish between different type of morphologies.

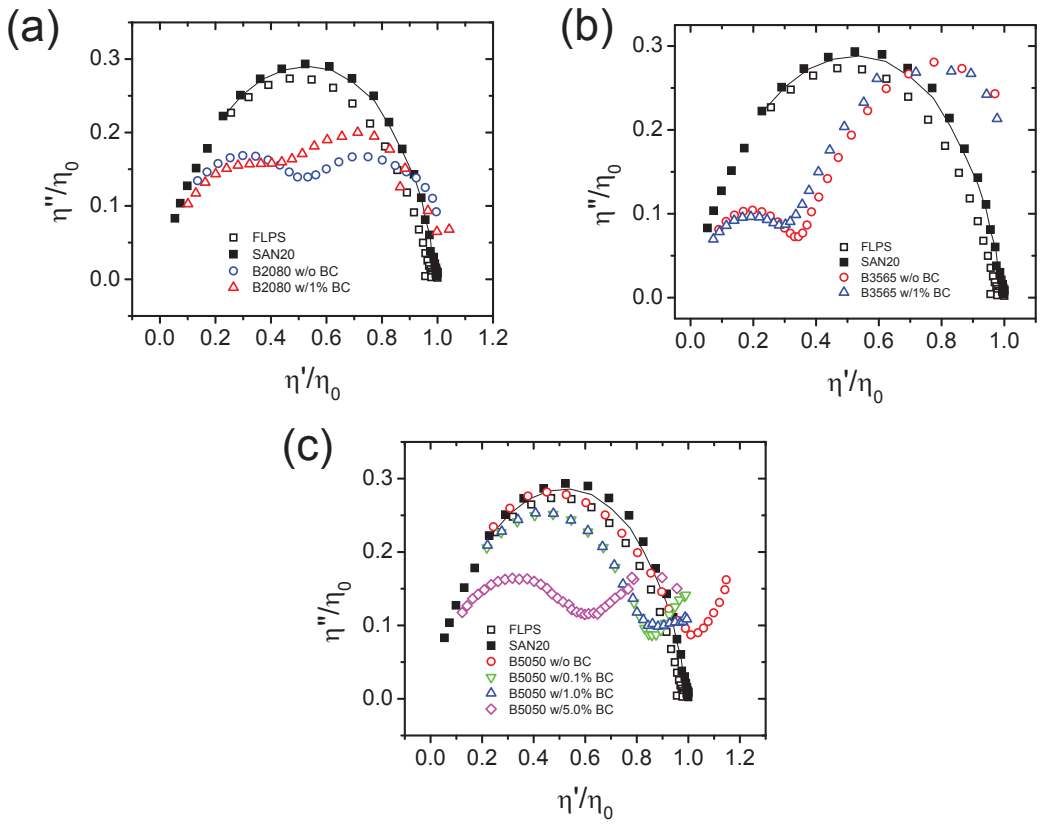

Figure 7.12: Normalized Cole-Cole plots of compatibilized and non compatibilized FLPS/SAN20 blends and their components at 200 $^{\circ}C$. The solid line indicates geometrical mean of the component data. The solid lines indicate the geometrical average between the component data.

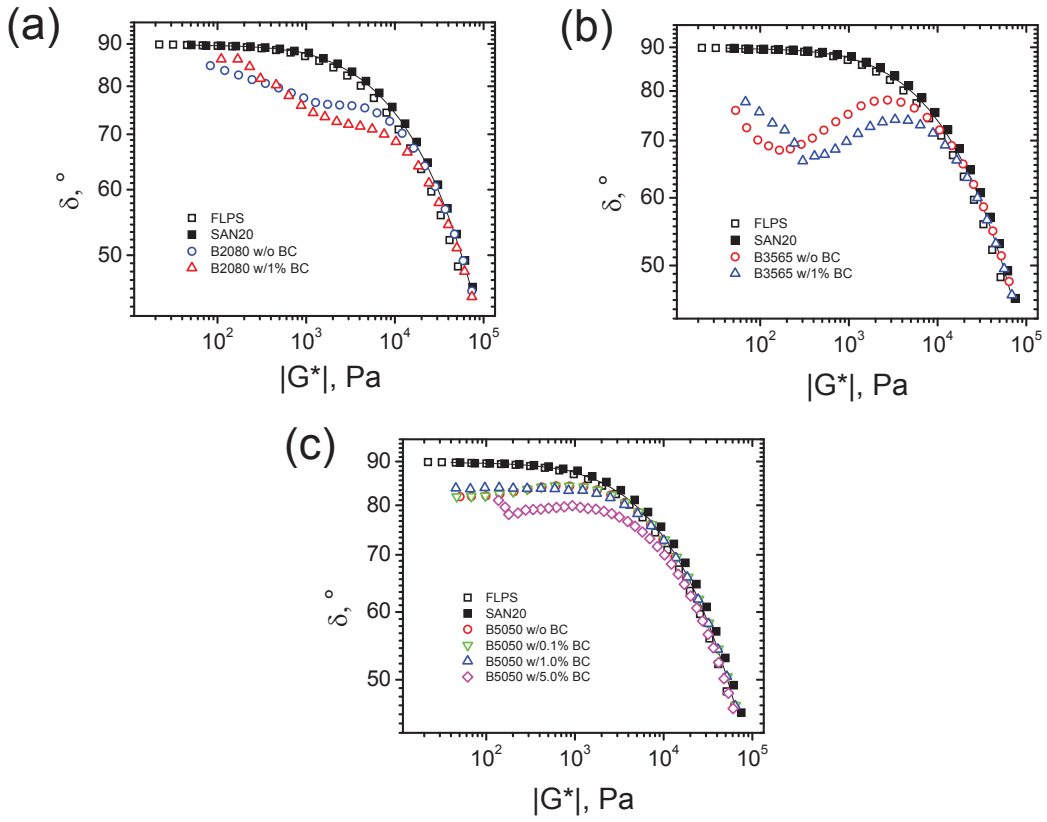

Figure 7.13: van Gurp-Palmen plots of compatibilized and non compatibilized FLPS/SAN20 blends and their components at 200 $°C$. The solid line indicates geometrical mean of the component data. The solid lines indicate the geometrical average between the component data.

Relaxation spectra

A very useful way to measure relaxation times associated to microstrucutre in polymer blends is via the relaxation time spectra [155, 162, 147]. Using the second order approximation proposed by Tschoegl [178] (Eqn. 6.1), relaxation spectra, $H(\tau)$, for all the blends and their components were calculated and shown in Figure 7.14. A peak in the spectra is observed for all the blends at a relaxation time in the range $0.05s < \tau < 0.09s$. This peak is clearly associated to the components. Extra relaxations are observed at larger values of τ.

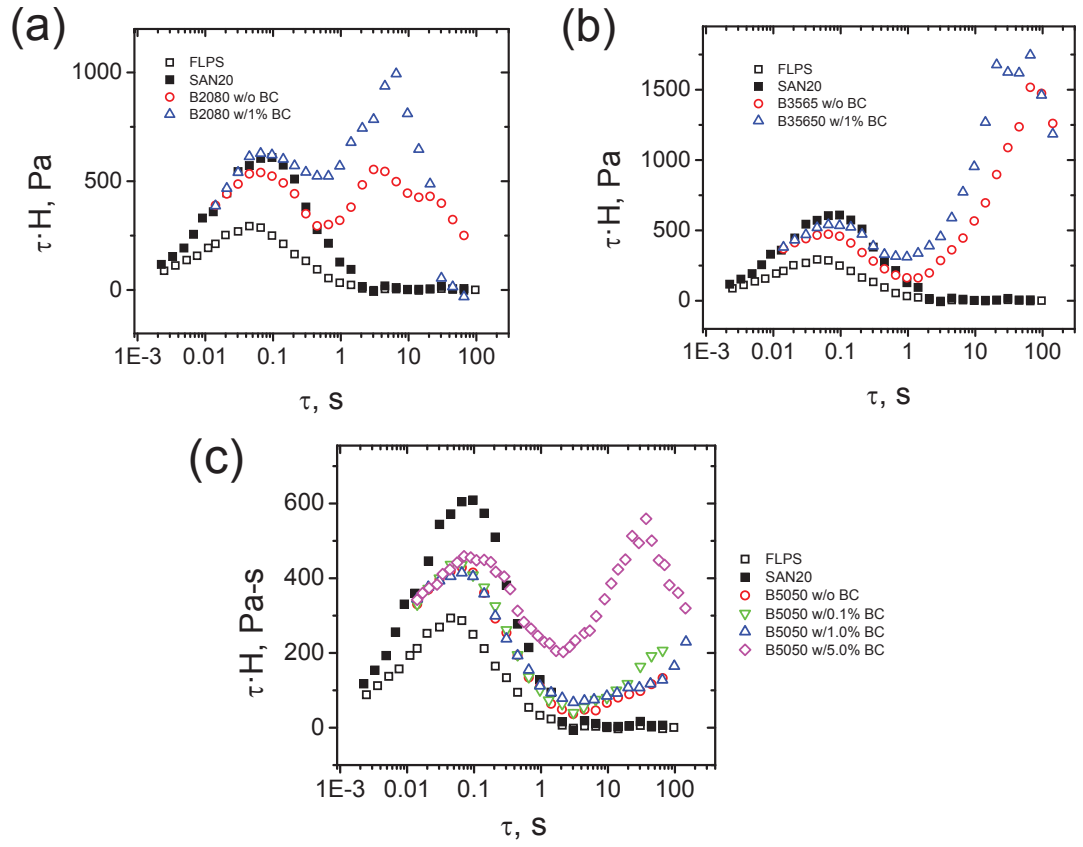

Figure 7.14: Weighted relaxation spectra of compatibilized and non compatibilized FLPS/SAN20 blends and their components at 200 $^{\circ}C$.

20/80 blends without BC display a second peak in the relaxation spectrum (Figure

7.14a) at $\tau \sim 3$ s and a shoulder at around $\tau \sim 20$ s, which indicates a bimodal distribution of droplet sizes. The 20/80 blends with BC exhibit a single peak at $\tau \sim 6$ s, indicating a monomodal distribution of droplet sizes. Hence, besides reducing the droplet size, BC reduces the multimodality of the relaxation spectra.

The relaxation spectra for the 35/65 blends (Figure 7.14b) show a long tail followed by a peak at large values of τ. As discussed in section 7.3.1, the interphase in these blends are composed of parabolic (cylindrical) and hyperbolic (saddle shaped) shapes. The peak in the relaxation spectra may be associated to the relaxation of the cylindrical domains, while the long tail to the distribution of shapes and sizes related to the cocontinuous character of the blends.

The peaks in the 35/65 blends with and without BC occur at $\tau \sim 30$ s and 72 s, respectively. The ratio between these two relaxation times (i.e. $\tau_{B3565w/BC}/\tau_{B3565w/oBC} \sim 0.42$) is close to the ratio between characteristic sizes (i.e. $\lambda_{B3565w/BC}/\lambda_{B3565w/oBC} \sim 0.38$). Graeblin et al. derived the same proportionality between the radius and the characteristic time, $R_V \propto \tau_0$, for droplet relaxation [130, 162] from the Palierne's emulsion model [27].

For the 50/50 blends with BC compositions $< 5\%$ only a tail in the right hand side of the relaxation spectra was observed (see Figure 7.14c). All these blends presented cocontinuous morphologies. Li et al. [147] argued that the relaxations associated to the tails may be attributed to a *network* relaxation of the cocontinuous structures as if they formed interpenetrating networks. We believe that the tail is ascribed to the distribution of local shapes and sizes forming the cocontinuous interface, which relax at different speeds.

An interesting result is the second peak at high values of the relaxation spectra of the 50/50 blend with 5% BC. This can be explained by the rounded interface observed in the micrographs of this blend (Figure 7.8). Our hypothesis is that the rounded domains relax similarly to droplets, producing the peak observed in the right hand side of Figure 7.14c. This supports our hypothesis that the interphase shape plays an important role in the rheological behavior of interconnected morphology.

An alternative procedure to isolate the contribution of the interface is to plot the relaxation spectra normalized with the low τ peak values. Figure 7.15 show the normalized spectra for all the blends and their components. All the curves superimpose

on each other in the low τ/τ_{peak} region, which confirm that the signal in that region corresponds to the components contribution. Additionally, the relation between the signal of the interface and that of the components is more evident in this plot. The tendencies of these relations are the same observed in the normalized Cole-Cole plots (Figure 7.12).

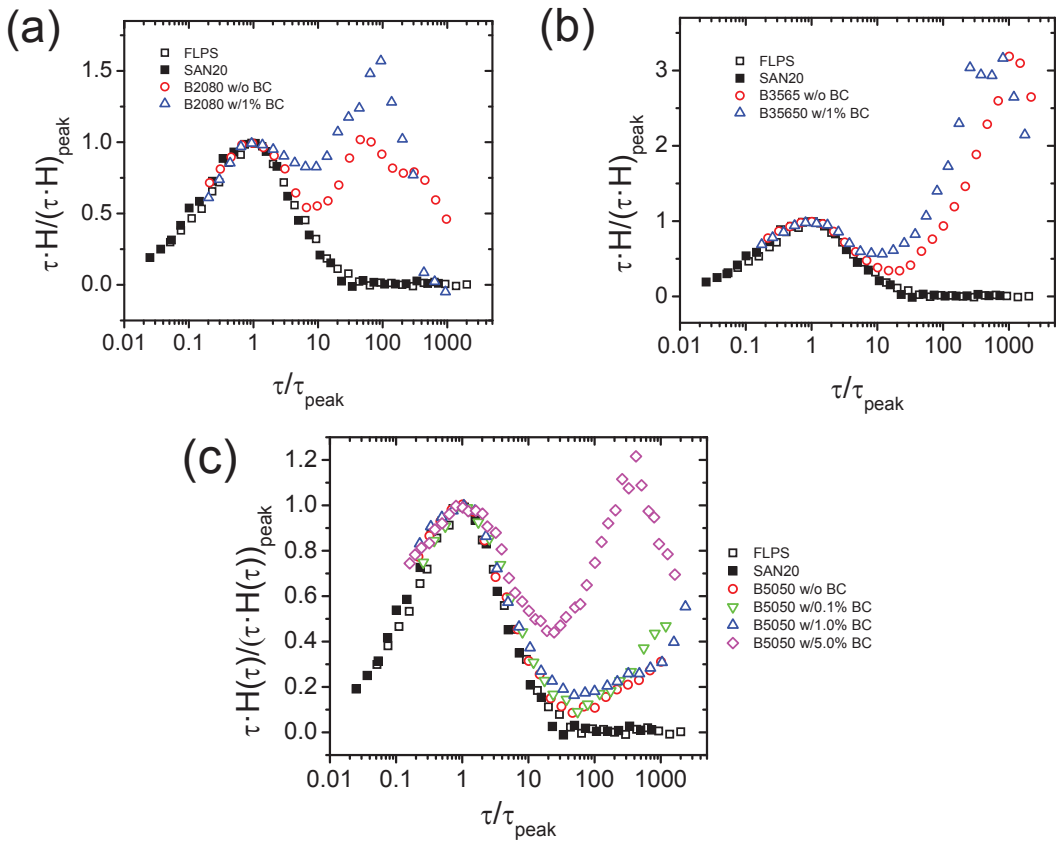

Figure 7.15: Normalized weighted relaxation spectra of compatibilized and non compatibilized FLPS/SAN20 blends and their components at 200 $^{\circ}C$.

7.3.3 Rheological evolution during coarsening

The evolution of the elastic modulus during the coarsening process was monitored by runing dynamic time sweeps at a low frequency ($\omega = 0.1$ rad/s) and a strain in the

linear viscoelastic regime ($\gamma = 20\%$). In section 6.3.3 we demonstrated that this strain does not have an effect on the coarsening of the microstructure.

Figures 7.16, 7.17, 7.18 and 7.19, show the time sweeps for FLPS and SAN20 and blends with different compositions and different amount and molecular weight of BC. The elastic modulus of the blend components remains constant during the tests, evidencing their thermal stability during the tests, whereas the blends show a decrease in G'. The G' value of the blends is bigger than that of the components at any time, and they approach a plateau value at $t \to \infty$. Another fact, common for all the blends, is that the modulus of the blends with BC is higher than that of the ones without BC. This a consequence of the increase in interfacial area, product of the compatibilization.

The evolution of G' of the 20/80 blends (Figure 7.16) indicates an initial growth and a subsequent stabilization of the droplets, evidenced by the plateau. According to Palierne's model, the modulus is determined by the droplet size and the interfacial tension, Γ [27, 130]. In the case of the non compatibilized blend, Γ is constant, hence the evolution of Gp is only due to the coalescence of the droplets.

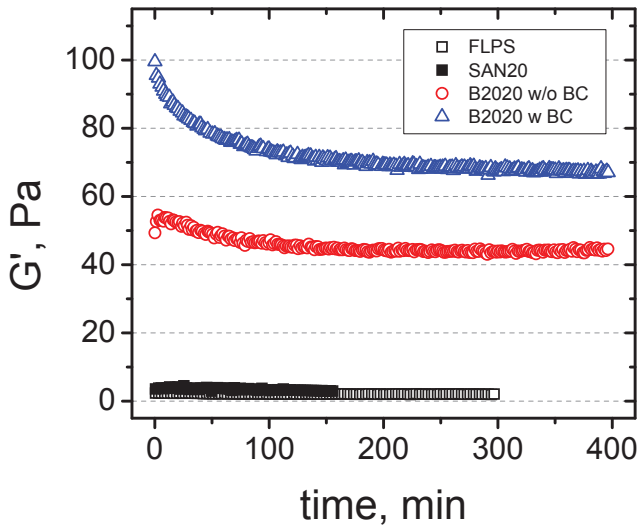

Figure 7.16: Time evolution of elastic modulus of compatibilized and non compatibilized 20/80 FLPS/SAN blends and their components at 200 $°C$. Measurements were carried out at 0.1 rad/s with 20% strain.

For the compatibilized blends, the interface coverage with BC determines the interfacial tension [179]. In turn, this coverage changes during the coarsening process until equilibriums between micelle formation and disolution and BC adsorption and desorption from the interface are reached, as discussed in section 5.3.4. These processes seem to occur during the first 100 minutes of annealing after which time, G' remained constant. Unfortunately the morphology could not be accurately quantified (with the microscopy method used in this work) to confirm these observations.

Blends with composition 35/65 show a remarkably high extra-elasticity compared with blends with 20/80 or 50/50 compositions (see Figure 7.17). Additionally, the reduction of G' with time for these blends is relatively slow. This behavior is difficult to interpret based on the morphological analysis, since, as discussed in section 7.3.1, a topological transformation from purely cocontinuous to composite (cocontinuous with droplets) morphologies is observed during the annealing of these blends. A possible reason for the high elasticity is that the parabolic (cylindrical) domains, forming part of the 35/65 blends, relax slower than droplets or hyperbolic domains. Further analysis is required to test this hypothesis.

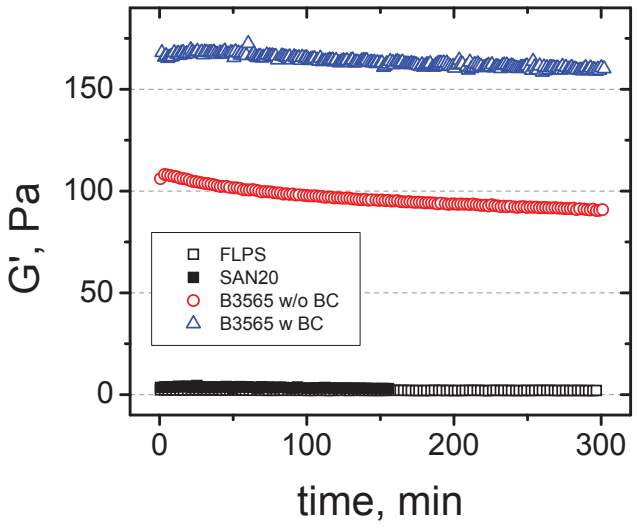

Figure 7.17: Time evolution of elastic modulus of compatibilized and non compatibilized 35/65 FLPS/SAN blends and their components at 200 $^{\circ}C$. Measurements were carried out at 0.1 rad/s with 20% strain.

Even when the initial sizes of the blend with 50/50 composition are comparable to those with 35/65 composition and their morphologies are both cocontinuous, the 50/50 blends presented the least enhancement in elasticity (see Figure 7.9). Additionally, as shown in Figures 7.18a an 7.19a, 50/50 blends are also the least stable, with a very rapid initial decrease in G' followed by a gradual reduction in the rate of decrease.

Figure 7.18a shows the effect of BC molecular weight in the initial elastic modulus and its decrease during annealing. In general, except for the blend with 900KBC, the evolution of the elastic modulus follows the same trend as that of the specific interfacial area (shown in Figure 7.18b), i.e. the higher the molecular weight, the slower the decrease.

The effect of BC concentration on the G' and Q evolutions is shown in Figure 7.19. The decrease of Q and G' show similar tendencies for the blends with BC content $< 5\%$, that is, the higher the BC concentration the higher values of both parameters. The blend with 5% BC shows an increase in G' for the first 90 minutes followed by a continuous decrease, although the interfacial area decreases continuously during the whole annealing process. The increase in G' may be associated to the increase in the population of rounded domains observed in the micrographs (Figure 7.8) and confirmed from the analysis of the curvature distributions in section 7.3.1. Although this hypothesis must be tested with further experiments.

The effect of the BC molecular weight and concentration on Q was addressed in Chapter 5. The results shown above suggest that, overall, G' is directly related to Q. However a model describing this relation is not available yet. In an attempt to relate the blends morphology with their rheological response, a simplification to Doi-Otha's model [28] was developed in section 6.3.3 and compared to non-compatibilized blends. The result from such approximation was a power law relation between the elastic modulus and annealing time given as $G' \propto t^{-1}$. This relation was tested against the data from compatibilized blends.

Figures 7.20 shows the data from Figures 7.18a and 7.19a, plotted in log-log scale. In general, two regimes of G' evolution described by power laws, with exponents given in Table 7.2, were observed. The absolute value of these exponents are way below 1, which indicates that the approximation proposed in Chapter 6.3.3 does not describe the evolution of the elastic modulus for the compatibilized blends.

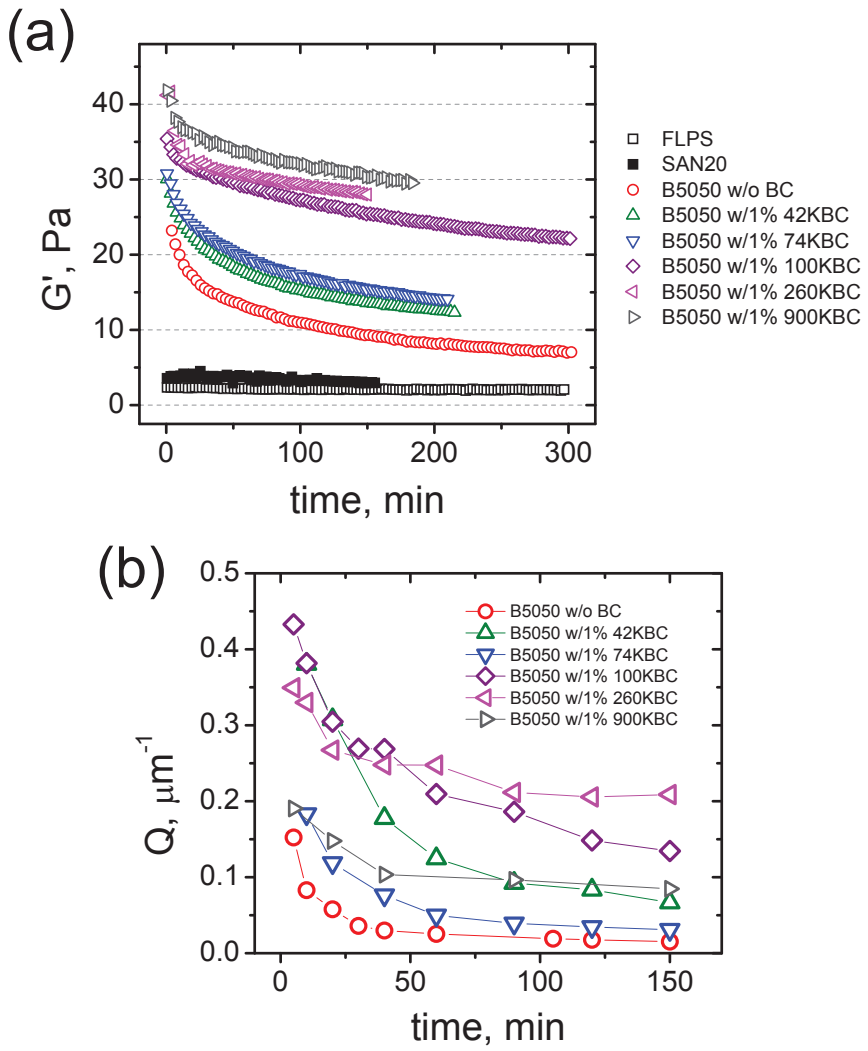

Figure 7.18: Effect of block copolymer molecular weight on the time evolution of elastic modulus of compatibilized 50/50 FLPS/SAN blends at 200 $^{\circ}C$. Measurements were carried out at 0.1 rad/s with 20% strain.

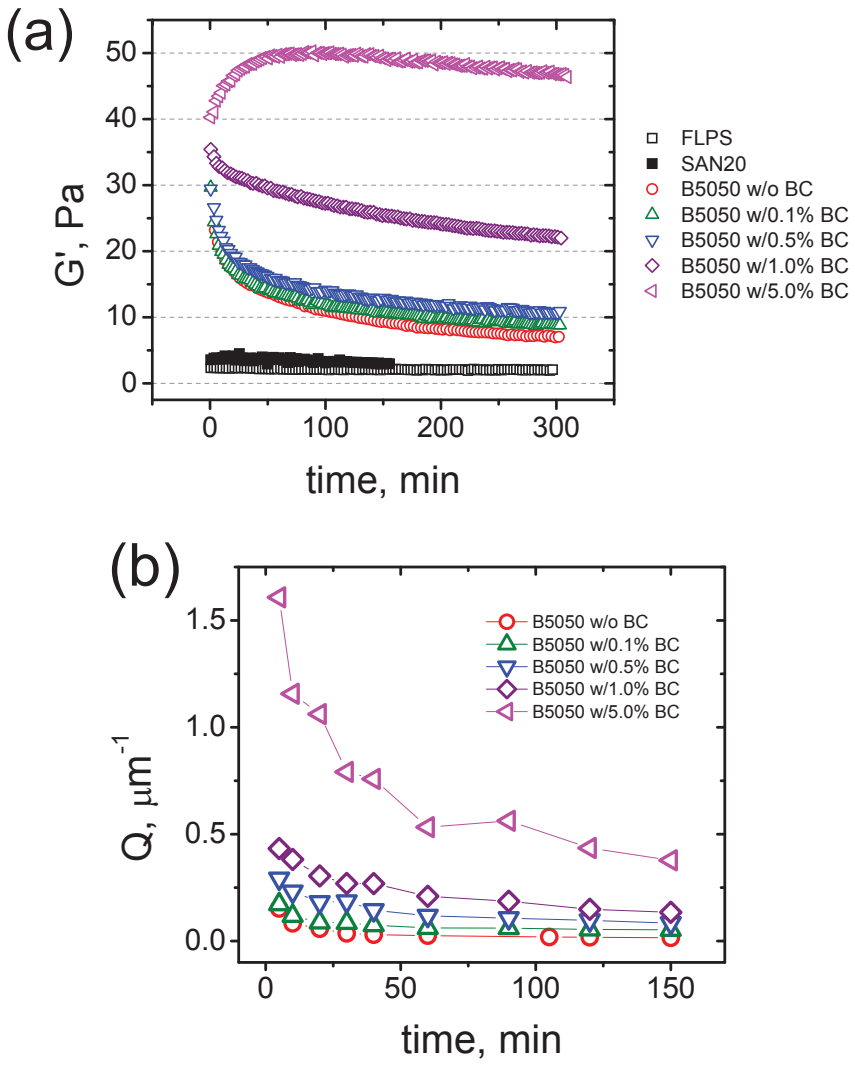

Figure 7.19: Effect of block copolymer concentration on the time evolution of elastic modulus of compatibilized 50/50 FLPS/SAN blends at 200 $^{\circ}C$. Measurements were carried out at 0.1 rad/s with 20% strain.

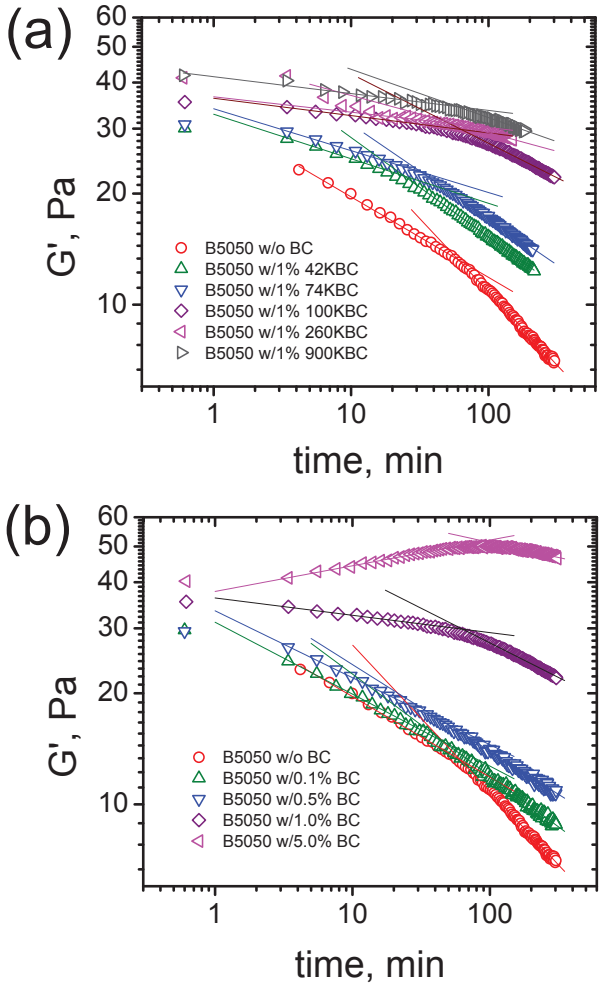

Figure 7.20: Time evolution of elastic modulus of compatibilized and non compatibilized 50/50 FLSP/SAN blends measured at 200 $^{\circ}C$ with 20% strain and 0.1 rad/s. Solid lines indicate power law fits with exponents given in Table 7.2.

Table 7.2: Exponents of power law describing the time evolution of G' for the 50/50 blends plotted in Figure 7.20.

BC	BC composition	Exponent	
	wt%	Early regime	Late regime
No BC	- -	-0.22	-0.40
42KBC	1.0	-0.12	-0.27
74KBC	1.0	-0.11	-0.25
260KBC	1.0	-0.04	-0.1
900KBC	1.0	-0.05	-0.1
100KBC	0.1	-0.19	-0.28
100KBC	0.5	-0.18	-0.23
100KBC	1.0	-0.05	-0.19
100KBC	5.0	0.07	-0.08

7.4 Conclusions

The morphology and rheology of cocontinuous blends is dramaticlly affected by the presence of a compatibilizer. In this study we investigated the effect of block copolymers, with varying molecular weight and composition, on the morphology, stability and viscoelasticity of FLPS120K/SAN20 blends. Three blend compositions were studied, namely, 20/80, 35/65 and 50/50 w/w. The morphologies observed were:

- Droplet-matrix with a bimodal and a monomodal droplet size distribution for the compatibilized and non compatibilized 20/80 blends, respectively.
- Cocontinuous for the 35/65 blends with a transition to a composite microstructure, consisting of droplet-matrix and cocontinuous regions. The onset of the pinch-off process responsible for this transition occurred at ∼20 min for the non-compatibilized blend and at ∼40 min for the compatibilized one.

- Cocontinuous throughout the coarsening process with a continuous increase in the characteristic size for the 50/50 blends.

The droplet size (for the 20/80 blends) or the characteristic size (for both the 35/65 and the 50/50 blends) were reduced by the presence of BC. The morphology was stabilized against coarsening for the 50/50 blends during the whole coarsening process, as well as for the 35/65 blends during the early regime (when the morphology was wholly cocontinuous).

The rheological response and the morphological analysis indicate that compatibilization for the 50/50 blends was more effective for higher BC molecular weights. Likewise, the compatibilization was more effective for higher concentrations of BC. However at high BC concentrations (5%) the interphase curvature was affected by the presence of BC, generating rounded domains that, after coarsening, produced a morphology of interconnected droplets. This had a considerable impact in the viscoelasticity of the blend.

Overall, the presence of BC substantially increased the elastic modulus of the blends. Moreover, increasing the BC molecular weight or concentration, resulted in increased values of Gp. The same trends were observed for the specific interfacial area, which suggest a direct relation between G' and Q. Finding the exact form of such relation is beyond the scope of this work.

Chapter 8

Summary and Overlook

As mentioned in Chapter 1, a big drawback of cocontinuous blends is that the morphology coarsens under conditions normally used in processing operations (i.e. at T>T_g or T_m). This thesis was dedicated to the study of the coarsening process vis 3D imaging analysis and rheology. Some of the most relevant results are summarized below.

2D techniques (such as optical or electronic microscopy) can be used to qualitatively characterization of cocontinuous structures, but are inadequate to wholly quantify the geometry of the interface. For instance, local shape, topology and anisotropy are not obtainable from 2D images. Chapter 3 present a methodology to obtain and analyse 3D images from confocal micrographs of cocontinuous blends made of FLPS and SAN. Triangular meshes representing the blend interface were obtained. The coordinate transformation (CT) method [76] was implemented for the first time to compute *local curvatures* from the 3D meshes. This method was proven to be very accurate, with errors within 6% (see Appendix A). In addition, using the position of the triangle vetices in the meshes, the *normal vector field* of the interface was computed. This is the first time this vector field is computed from 3D micrographs. The normal vector was used to compute the *anisotropy tensor*, which has a big relevance in the measurement of interfacial stresses [28].

The evolution of the characteristic size and local curvatures were monitored during the coarsening of continuous blends. Two regimes of coarsening were identified in the 50/50 blends: an early regime, where the characteristic size increased linearly with time and the interface evolution was self-similar, and a late regime where a failure

of the dynamic scaling failed and a decrease in the rate of coarsening was observed. The behavior in the early regime was in accordance with classical theories of spinodal decomposition [14, 180]. A model based on the evolving local shape of the microstructure was proposed in Chapter 4 to explain the transition to the second regime.

The effect of block copolymers (BC) on the characteristic size and on the stability was studied in Chapter 5. Symmetric PS-b-PMMA block copolymers were found to be very effective in slowing down the coarsening of FLPS/SAN blends. An intermediate molecular weight of BC was optimal for hindering the coarsening. Bell [22] found similar behavior in PS/PE and PS/PMMA blends, compatibilized with PS-b-PE and PS-b-PMMA copolymers, respectively. A theory based on micelle formation/dissolution and BC adsorption/desorption equilibriums [41], was used to explain the results from the three systems.

The blend interface produced an extra contribution to the elastic modulus G'_{int} at low frequencies during oscillatory experiments. The reduction of interface during coarsening was accompanied by a decrease in G'_{int}. In order to relate these two signals, a simplification to Doi-Ohta's model [28], based on the experimental evidence that the degree of anisotropy is negligible during SAOS experiments, was proposed in Chapter 6. The simplification predicted experimental data of low interfacial blends during the late stage of coarsening. Improvements to the model are required to account for both coarsening regimes and different interfacial tensions.

8.1 Future directions

A number challenges are still pending in the area of cocontinuous polymer blends. For instance, even when it was proven throughout this thesis that the analysis of 3D images present numerous advantages over traditional 2D images techniques, the technique used to obtain the raw images (i.e. laser scanning confocal microscopy) suffers from two major drawbacks: (1) it requires transparent blends and (2) at least one of the phases needs to emit a strong fluorescent signal. Blends made of commodity polymers are neither transparent nor fluorescent. Thus, a big amount of work is required to prepare blends with these characteristics. Several alternative techniques to obtain 3D images of polymer blends, with different pros and cons, have been reported in the literature.

Pyun et al. used X-ray microtomography (μ-CT) to image a PS/PMMA cocontinuous blend [53]. μ-CT does does not require fluorescent labels or transparency of the blends, however a big density difference between the phases is needed to obtain images with adequate contrast. That difference is very small for most polymer pairs. Two possible solutions are to extract one of the phases or to use a X-ray source rather powerful (such as that coming from a synchrotron). Further exploration of this technique could help to accelerate the acquisition of 3D images. 3D NMR imaging [62], TEM microtomography [66] and confocal Raman microscopy [181, 182] are other techniques that may be worth to explore.

As discussed in Chapter 5, the BC added to the blends can be located in three different places: disolved in either of the two phases, forming micelles or at the interface between the two phases. The unequivocally identification of that location is a very difficult task. One possible way to address this task, using confocal microscopy, is to attach a florescent label to the BC with emission wavelength different to that for the label attached to the polystyrene. Hence, the location of both, the fluorescent phase and the BC will be identified by changing the filter in front of the detector. Jeon and Macosko [183] visualized fluorescently labelled PS-b-PMMA located at the interface of PMMA droplets surrounded by a PS matrix. They were able to identify BC concentration gradients at the interface, which generate Marangoni stresses. This idea can be extended to cocontinuous morphologies in a 3D mode and, thus, correlate the interfacial concentration gradients with the macroscopic effect of BC on the rheological properties.

The simplification to Doi-Ohta's model [28] proposed in Chapter 6 resulted in a single power law describing the decrease of G' during the coarsenign process. However experimental results showed two regimes of decrease given by two power laws. One idea to improve the model is to explore the effect of the evolving interfacial curvature (which is not consideredby Doi and Ohta [28]) on the rheological response. More experimental and theoretical work is required to assess this effect and to include it in the model.

Finally, the method to compute anisotropy tensors developed in Chapter 6 can be used to measure the anisotropy generated during different types of flow. A simple experiment would be to run extensional tests using the EVF fixture in the Ares rheometer to monitor both the torque and anisotropy during extensional flow. Then using simple

models such as Doi-ohta's, relate extensional rheology and morphology.

Bibliography

[1] C. Harrats, S. Thomas, and G. Groeninckx. *Micro- and nanostructured polymer blends : phase morphology and interfaces*. Taylor Francis, Boca Raton, 2005.

[2] L. M. Robeson. *Polymer blends : a comprehensive review*. Hanser, Munich; Cincinnati, 2007.

[3] L. A. Utracki. *Polymer alloys and blends : thermodynamics and rheology*. Hanser/Oxford University Press, Munich ; New York New York, 1990.

[4] L. A. Utracki. *Commercial polymer blends*. Chapman Hall, London ; New York, 1998.

[5] D. R. Paul and C. B. Bucknall. *Polymer blends*. Wiley, New York, 2000.

[6] C. W. Macosko. *Macromol. Symp.*, 149:171–184, 2000.

[7] C. Harrats. *Multiphase polymer-based materials : an atlas of phase morphology at the nano and micro scale*. CRC Press/Taylor Francis, Boca Raton, FL, 2009.

[8] D. Soane. US Patent 5135627, 1992.

[9] P. Salehi, P. Sarazin, and B. D. Favis. *Biomacromolecules*, 9(4):1131–1138, 2008.

[10] Z. Xiang, P. Sarazin, and B. D. Favis. *Biomacromolecules*, 10(8):2053–2066, 2009.

[11] J. D. De Bruijin, Y. P. Bovell, J. Van Den Brink, and A. Van Blitterswijk. US Patent 6228117 b1, 2001.

[12] N. R. Washburn, C. G. Simon Jr, A. Tona, H. M. Elgendy, A. Karim, and E. J. Amis. *J. Biomed. Mater. Res.*, 60(1):20–29, 2002.

[13] I. M. Hekal. US Patent 5,911,937, 1999.

[14] E. D. Siggia. *Phys. Rev. A*, 20(2):595–605, 1979.

[15] R. C. Willemse. *Polymer*, 40(8):2175–2178, 1998.

[16] R. C. Willemse, E. J. J. Ramaker, J. Van Dam, and A. Posthuma De Boer. *Polym. Eng. Sci.*, 39(9):1717–1725, 1999.

[17] H. Veenstra, J. Van Dam, and A. Posthuma De Boer. *Polymer*, 41(8):3037–3045, 2000.

[18] E. Scholten, L. M. C. Sagis, and E. van der Linden. *Macromolecules*, 38(8):3515–3518, 2005.

[19] Z. Yuan and B. D. Favis. *AIChE J.*, 51(1):271–280, 2005.

[20] J. A. Galloway, H. K. Jeon, J. R. Bell, and C. W. Macosko. *Polymer*, 46(1):183–191, 2005.

[21] Z. Yuan and B. D. Favis. *J. Polym. Sci. B: Polym. Phys.*, 44(4):711–721, 2006.

[22] J. R. Bell. *Cocontinuous Polymer Blends: The Role of Block Copolymer in Blend Morphology Evolution*. Ph.D. Thesis, University of Minnesota, 2007.

[23] D. Graebling, R. Muller, and J. F. Palierne. *Macromolecules*, 26(2):320–329, 1993.

[24] I. Vinckier and H. M. Laun. *Rheologica Acta*, 38(4):274–286, 1999.

[25] C. L. Tucker III and P. Moldenaers. *Annu. Rev. Fluid Mech*, 34:177–210, 2002.

[26] M. Castro, C. Carrot, and F. Prochazka. *Polymer*, 45:4095–4104, 2004.

[27] J. F. Palierne. *Rheol. Acta*, 29(3):204–14, 1990.

[28] M. Doi and T. Ohta. *J. Chem. Phys.*, 95(2):1242–1248, 1991.

[29] G. K. Guenther and D. G. Baird. *J. Rheol.*, 40(1):1–20, 1996.

[30] M. Ansari, A. Haghtalab, and M. Semsarzadeh. *Rheol. Acta*, 45(6):983–993, 2006.

[31] I. Vinckier, P. Moldenaers, and J. Mewis. *J. Rheol.*, 41(3):705–718, 1997.

[32] I. Vinckier and H. M. Laun. *J. Rheol.*, 45(6):1373–1385, 2001.

[33] Y. Nishikawa, H. Jinnai, T. Koga, T. Hashimoto, and S. T. Hyde. *Langmuir*, 14(5):1242–1249, 1998.

[34] Y. Nishikawa, T. Koga, T. Hashimoto, and H. Jinnai. *Langmuir*, 17(11):3254–3265, 2001.

[35] H. Jinnai, Y. Nishikawa, T. Ikehara, and T. Nishi. *Adv. Polym. Sci.*, 170:115–167, 2004.

[36] J. Alkemper and P. W. Voorhees. *Acta Mater.*, 49(5):897–902, 2001.

[37] R. Mendoza, K. Thornton, I. Savin, and P. W. Voorhees. *Acta Mater.*, 54(3):743–750, 2006.

[38] D. Kammer, R. Mendoza, and P. W. Voorhees. *Scr. Mater.*, 55(1):17–22, 2006.

[39] A. H. Schoen. *In Infinite Periodic Minimal Surfaces Without Self-Intersections.* Tech. Note No. D-5541, NASA, Washington, DC, 1970.

[40] L. P. McMaster. *Adv. Chem. Ser.*, 142:43–65, 1975.

[41] K. Chang and D. C. Morse. *Macromolecules*, 39(22):7746–7756, 2006.

[42] K. Chang and D. C. Morse. *Macromolecules*, 39(21):7397–7406, 2006.

[43] C. Sheppard and D. Shotton. *Confocal Laser Scanning Microscopy.* Springer, Oxford; New York, 1997.

[44] J. B. Pawley. *Handbook of Biological Confocal Microscopy.* Springer, New York, 2006.

[45] C. R. Lopez-Barron and C. W. Macosko. *Langmuir*, 25(16):9392–9404, 2009.

[46] P. Potschke and D. R. Paul. *J. Macromol. Sci., Polym. Rev.*, C43(1):87–141, 2003.

[47] B. Moon, T. R. Hoye, and C. W. Macosko. *Polymer*, 43(20):5501–5509, 2002.

[48] C. W. Macosko. *Rheology: Principles, Measurements, and Applications*. VCH, New York, NY, 1993.

[49] J. R. Mohrig. *Techniques in Organic Chemistry : Miniscale, Standard Taper Microscale, and Williamson Microscale*. W.H. Freeman, New York, 2006.

[50] P. G. de Gennes, F. Brochard-Wyart, and D. Quéré. *Capillarity and Wetting Phenomena : Drops, Bubbles, Pearls, Waves*. Springer, New York, 2004.

[51] Samuel A. Safran. *Statistical Thermodynamics of Surfaces, Interfaces, and Membranes*. Addison-Wesley, Reading, MA, 1994.

[52] E. E. Underwood. *Quantitative Stereology*. Addison-Wesley Pub. Co, Reading, MA, 1970.

[53] A. Pyun, J. R. Bell, K. H. Won, B. M. Weon, S. K. Seol, J. H. Je, and C. W. Macosko. *Macromolecules*, 40(6):2029–2035, 2007.

[54] D. Kammer and P. W. Voorhees. *Acta Mater.*, 54(6):1549–1558, 2006.

[55] R. J. Spontak, M. C. Williams, and D. A. Agard. *Polymer*, 29(3):387–395, 1988.

[56] H. Jinnai, Y. Nishikawa, T. Koga, and T. Hashimoto. *Macromolecules*, 28(13):4782–4, 1995.

[57] R. J. Spontak, J. C. Fung, M. B. Braunfeld, J. W. Sedat, D. A. Agard, L. Kane, S. D. Smith, M. M. Satkowski, A. Ashraf, D. A. Hajduk, and S. M. Gruner. *Macromolecules*, 29(13):4494–4507, 1996.

[58] H. Jinnai, Y. Nishikawa, R. J. Spontak, S. D. Smith, D. A. Agard, and T. Hashimoto. *Phys. Rev. Lett.*, 84(3):518–521, 2000.

[59] P. Sengupta and J. W. M. Noordermeer. *Macromol. Rapid Commun.*, 26(7):542–547, 2005.

[60] M. D. Montminy, A. R. Tannenbaum, and C. W. Macosko. *J. Colloid Interface Sci.*, 280(1):202–211, 2004.

[61] A. Momose, A. Fujii, H. Kadowaki, and H. Jinnai. *Macromolecules*, 38(16):7197–7200, 2005.

[62] S. Koizumi, Y. Yamane, S. Kuroki, I. Ando, Y. Nishikawa, and H. Jinnai. *J. Appl. Polym. Sci.*, 103(1):470–475, 2007.

[63] H. Verhoogt, J. Van Dam, A. Posthuma de Boer, A. Draaijer, and P. M. Houpt. *Polymer*, 34(6):1325–1329, 1993.

[64] H. Jinnai, Y. Nishikawa, and T. Hashimoto. *Phys. Rev. E*, 59(3):R2554–R2557, 1999.

[65] H. Jinnai, T. Koga, Y. Nishikawa, T. Hashimoto, and S. T. Hyde. *Phys. Rev. Lett.*, 78(11):2248–2251, 1997.

[66] H. Jinnai, H. Hasegawa, Y. Nishikawa, G. J. A. Sevink, M. B. Braunfeld, D. A. Agard, and R. J. Spontak. *Macromol. Rapid Comm.*, 27(17):1424–1429, 2006.

[67] G. E. Wnek and G. L. Bowlin. Encyclopedia of biomaterials and biomedical engineering, 2008.

[68] A. Onuki. Domain growth and rheology in phase-separating binary mixtures with viscosity difference. *Europhys. Lett.*, 28(3):175–179, 1994.

[69] S. Inoue. *Fundations of Confocal Scanned Imaging in Light Microscopy*, chapter 1, page 1. Handbook of biological confocal microscopy. Springer, New York, 3rd edition, 2006.

[70] John C. Russ. *The Image Processing Handbook*. CRC Press, Boca Raton,FL, 2002.

[71] Jerry Sedgewick. *Scientific Imaging with Photoshop: Methods, Measurement, and Output*. New Riders, Berkeley, CA, 2008.

[72] W. E. Lorensen and H. E. Cline. *Comput. Graph.*, 21(4):163–169, 1987.

[73] A. Gray, E. Abbena, and S. Salamon. *Modern Differential Geometry of Curves and Surfaces with Mathematica*. Chapman & Hall/CRC, Boca Raton, FL, 3rd edition, 2006.

[74] G. K. Batchelor. *An Introduction to Fluid Dynamics*. Cambridge University Press, London, 1967.

[75] E. M. Stokely and S. Y. Wu. *IEEE Trans. Pattern Anal. Mach. Intell.*, 14(8):833–840, 1992.

[76] P. T. Sander and S. W. Zucker. *Proc. 1rst Int. Conf. Comput. Vision (London)*, pages 231–240, 1987.

[77] John W. Cahn and John E. Hilliard. *J. Chem. Phys.*, 28(2):258–267, 1958.

[78] G. R. Strobl. *The Physics of Polymers : Concepts for Understanding their Structures and Behavior*. Springer-Verlag, New York, 1996.

[79] J. M. Ottino. *The Kinematics of Mixing : Stretching, Chaos, and Transport*. Cambridge University Press, Cambridge ; New York, NY, 1989.

[80] C. E. Scott and C. W. Macosko. *Polymer*, 36(3):461–70, 1995.

[81] T. S. Omonov, C. Harrats, G. Groeninckx, and P. Moldenaers. *Polymer,*, 48(18):5289–5302, 2007.

[82] M. Fialkowski, A. Aksimentiev, and R. Holyst. *Phys. Rev. Lett.*, 86(2):240–243, 2001.

[83] J. R. Taylor. *An Introduction to Error Analysis : The Study of Uncertainties in Physical Measurements*. University Science Books, Sausalito, CA, 1997.

[84] C. R. Lopez-Barron and C. W. Macosko. *AIP Conf. Proc.*, 1027:523–525, 2008.

[85] H. Q. Xie, J. Xu, and S. Zhou. *Polymer*, 32(1):95–102, 1991.

[86] H. M. Laun. *Pure Appl. Chem.*, 70(8):1547–1566, 1998.

[87] T. Hashimoto, M. Takenaka, and H. Jinnai. *J. Appl. Crystallogr.*, 24(5):457–466, 1991.

[88] S. Tomotika. *Proc. R. Soc. london, Ser. A*, 150(870):322–337, 1935.

[89] H. A. Stone, B. J. Bentley, and L. G. Leal. *J. Fluid Mech.*, 173:131–58, 1986.

[90] E. Scholten, L. M. C. S., and E. van der Linden. *J. Phys. Chem. B*, 108(32):12164–12169, 2004.

[91] C. Tang, P. Chen, and H. Liu. *Polym. Eng. Sci.*, 48(7):1296–1303, 2008.

[92] C. A. Miller and P. Neogi. *Interfacial Phenomena : Equilibrium and Dynamic Effects*, volume 17. M. Dekker, New York, 1985.

[93] W. Helfrich. *Z. Naturforsch*, 28(11):693–703, 1973.

[94] J. J. Koenderink. *Solid Shape*. MIT Press, Cambridge, Mass., 1990.

[95] S. Inoue. *Fundations of Confocal Scanned Imaging in Light Microscopy*. Handbook of biological confocal microscopy. Springer, New York, 3rd edition, 2006.

[96] R. G. Larson. *The structure and rheology of complex fluids*. Oxford University Press, New York, 1999.

[97] P. H. M. Elemans, J. M. H. Janssen, and H. E. H. Meijer. *J. Rheol.*, 34(8):1311–1325, 1990.

[98] U. Sundararaj and C. W. Macosko. *Polym. Eng. Sci.*, 36(13):1769–1781, 1996.

[99] N. D. B. Lazo and C. E. Scott. *Polymer*, 40(20):5469–5478, 1999.

[100] J. Kyun Lee and C. D. Han. *Polymer*, 41:1799–1815, 2000.

[101] J. A. Galloway. Characterization and compatibilization of cocontinuous polymer blends, 2003. Ph.D. Thesis, University of Minnesota.

[102] D. G. Baird and D. I. Collias. *Polymer Processing : Principles and Design*. Wiley, New York, 1998.

[103] N. Mekhilef, B. D. Favis, and P. J. Carreau. *J. Poly. Sci. B*, 35(2):293–308, 1997.

[104] S. Lyu, T. D. Jones, F. S. Bates, and C. W. Macosko. *Macromolecules*, 35:7845–7855, 2002.

[105] F. S. Bates, J. H. Rosedale, H. E. Bair, and T. P. Russell. *Macromolecules*, 22(6):2557–2564, 1989.

[106] S. K. Varshney, J. P. Hautekeer, R. Fayt, R. Jerome, and P. Teyssie. *Macromolecules*, 23(10):2618–2622, 1990.

[107] P. Teyssie, R. Fayt, J. P. Hautekeer, C. Jacobs, R. Jerome, L. Leemans, and S. K. Varshney. *Makromol. Chem. Macromol. Symp.*, 32:61–73, 1990.

[108] C. W. Macosko, P. Guegan, A. K. Khandpur, A. Nakayama, P. Marechal, and T. Inoue. *Macromolecules*, 29(17):5590–5598, 1996.

[109] T. P. Russell, R. P. Hjelm, and P. A. Seeger. *Macromolecules*, 23(3):890–893, 1990.

[110] E. Helfand and Y. Tagami. *J. Chem. Phys.*, 56(7):3592–3601, 1972.

[111] L. J. Fetters, D. J. Lohse, D. Richter, T. A. Witten, and A. Zirkel. *Macromolecules*, 27(17):4639–4647, 1994.

[112] J. Brandrup, E. H. Immergut, and Eric A. Grulke. *Polymer handbook*. Wiley, New York, 1999.

[113] B. J. Schmitt, R. G. Kirste, and J. Jelenic. *Makromol. Chem.*, 181(8):1655–1672, 1980.

[114] M. Maric and C. W. Macosko. *Polym. Eng. Sci.*, 41(1):118–130, 2001.

[115] J. A. Galloway, M. D. Montminy, and C. W. Macosko. *Polymer*, 43(17):4715–4722, 2002.

[116] T. P. Russell, A. Menelle, W. A. Hamilton, G. S. Smith, S. K. Satija, and C. F. Majkrzak. *Macromolecules*, 24(20):5721–5726, 1991.

[117] A. N. Semenov. *Macromolecules*, 25(19):4967–4977, 1992.

[118] K. Chang, C. W. Macosko, and D. C. Morse. *Macromolecules*, 40(10):3819–3830, 2007.

[119] M. E. Fowler, J. W. Barlow, and D. R. Paul. *Polymer*, 28(7):1177–84, 1987.

[120] D. C. Morse. *Macromolecules*, 40(10):3831–3839, 2007.

[121] I. S. Polios, M. Soliman, C. Lee, S P. Gido, K Schmidt-Rohr, and H. H Winter. *Macromolecules*, 30:4470–4480, 1997.

[122] G. I. Taylor. *Proc. Roy. Soc. (London)*, A138:41–8, 1932.

[123] A. Einstein. *Annalen der Physik*, 19:289–306, 1906.

[124] A. Einstein. *Annalen der Physik*, 34:591–2, 1911.

[125] A. J. Hughes. *Nature*, 173(4414):1089–1090, 1954.

[126] J. G. Oldroyd. *Proc. R. Soc. London, Ser. A*, 218(1132):122–132, 1953.

[127] J. G. Oldroyd. *Proc. R. Soc. London, Ser. A*, 232(1191):567–577, 1955.

[128] S. J. Choi and W. R. Schowalter. *Phys. Fluids*, 18(4):420–427, 1975.

[129] D. Graebling and R. Muller. *J. of Rheol.*, 34(2):193–205, 1990.

[130] D. Graebling, R. Muller, and J. F. Palierne. *Macromolecules*, 26(2):320–329, 1993.

[131] C. Friedrich, W. Gleinser, E. Korat, D. Maier, and J. Weese. *J. Rheol.*, 39(6):1411–1425, 1995.

[132] C. Lacroix, M. Bousmina, P. J. Carreau, B. D. Favis, and A. Michel. *Polymer*, 37(14):2939–2947, 1996.

[133] U. Jacobs, M. Fahrlander, J. Winterhalter, and Chr Friedrich. *J. Rheol.*, 43(6):1495–1509, 1999.

[134] H. M. Lee and O. O. Park. *J. Rheol.*, 38(5):1405–1425, 1994.

[135] G. Biresaw, C. Carriere, and R. Sammler. *Rheol. Acta*, 42(1):142–147, 2003.

[136] E. Kim, E. J. Kramer, P. D. Garrett, R. A. Mendelson, and W. C. Wu. *J. Mat. Sci.*, 30(7):1709–1714, 1995.

[137] S. Wu. *Polymer Interface and Adhesion*. M. Dekker, New York, 1982.

[138] P. C. Ellingson, D. A. Strand, A. Cohen, R. L. Sammler, and C. J. Carriere. *Macromolecules*, 27(6):1643–1647, 1994.

[139] S. H. Anastasiadis, I. Gancarz, and J. T. Koberstein. *Macromolecules*, 21(10):2980–2987, 1988.

[140] A. Ajji, L. Choplin, and R. E. Prud'homme. *J. Polym. Sci. B: Polym. Phys.*, 29(13):1573–8, 1991.

[141] M. Kapnistos, A. Hinrichs, D. Vlassopoulos, S. H. Anastasiadis, A. Stammer, and B. A. Wolf. *Macromolecules*, 29(22):7155–7163, 1996.

[142] C. Weis, J. Leukel, K. Borkenstein, D. Maier, W. Gronski, C. Friedrich, and J. Honerkamp. *Polym. Bull.*, 40:235241, 1998.

[143] C. Lacroix, M. Aressy, and P. J. Carreau. *Rheol. Acta*, 36(4):416–428, 1997.

[144] K. S. Cole and R. H. Cole. *J. Chem. Phys.*, 9:341, 1941.

[145] S. Havriliak and S. Negami. *Polymer*, 8:161–210, 1967.

[146] C. Garcia-Franco and D. W. Mead. *Rheol. Acta*, 38(1):34–47, 1999.

[147] R. Li, W. Yu, and C. Zhou. *J. Macromol. Sci. B*, 45(5):889–898, 2006.

[148] D. Chopra, M. Kontopoulou, D. Vlassopoulos, and S. G. Hatzikiriakos. *Rheol. Acta*, 41(1):10–24, 2002.

[149] M. van Gurp and J. Palmen. *Rheol. Bull.*, 67:5–8, 1998.

[150] S. Trinkle and C. Friedrich. *Rheol. Acta*, 40(4):322–328, 2001.

[151] S. Trinkle, P. Walter, and C. Friedrich. *Rheol. Acta*, 41(1-2):103–113, 2002.

[152] G. Fleury, G. Schlatter, and R. Muller. *Rheol. Acta*, 44(2):174–187, 2004.

[153] O. Delgadillo-Velazquez, S. G. Hatzikiriakos, and M. Sentmanat. *Rheol. Acta*, 47(1):19–31, 2008.

[154] N. W. Tschoegl. *Rheol. Acta*, 10(4):582–594, 1971.

[155] H. Gramespacher and J. Meissner. *J. Rheol.*, 36(6):1127–1141, 1992.

[156] Y. Niu, L. Yang, K. Shimizu, J. A. Pathak, H. Wang, and Z. Wang. *J. Phys. Chem. B*, 113(26):8820–8827, 2009.

[157] S. A. Safran and N. A. Clark. *Physics of complex and supermolecular fluids*. Wiley, New York, 1987.

[158] A. Onuki. *Phys. Rev. A*, 35(12):5149, 1987.

[159] E. D. Wetzel and C. L. Tucker III. *Int. J. Multiphase Flow*, 25:35–61, 1999.

[160] I. Vinckier, P. Moldenaers, and J. Mewis. *J. Rheol.*, 41(3):705–718, 1997.

[161] Y. Takahashi, N. Kurashima, I. Noda, and M. Doi. *J. of Rheol.*, 38(3):699–712, 1994.

[162] I. Vinckier, P. Moldenaers, and J. Mewis. *J. Rheol.*, 40(4):613–631, 1996.

[163] A. S. Almusallam, R. G. Larson, and M. J. Solomon. 2003.

[164] A. S. Almusallam, R. G. Larson, and M. J. Solomon. *J. Rheol.*, 48(2):319–348, 2004.

[165] M. Takahashi and K. Okamoto. *J. Soc. Rheol., Japan*, 35(4):199–205, 2007.

[166] H. Yamane, M. Takahashi, R. Hayashi, K. Okamoto, H. Kashihara, and T. Masuda. *J. Rheol.*, 42(3):567–580, 1998.

[167] M. Abramowitz and I. A. Stegun. *Handbook of mathematical functions with formulas, graphs, and mathematical tables*, volume 55. U. S. Govt. Print. Off., Washington, 1972.

[168] K. Oldham, J. Myland, and J. Spanier. *An Atlas of Functions: with Equator, the Atlas Function Calculator*. Springer, New York, 2008.

[169] S. Lyu. *Macromolecules*, 36(26):10052–10055, 2003.

[170] J. Silva, A. Machado, and J. Maia. *Rheol. Acta*, 46(8):1091–1097, 2007.

[171] J. D. Martin and S. S. Velankar. *J. Rheol.*, 51(4):669–692, 2007.

[172] Y. Huo, G. Groeninckx, and P. Moldenaers. *Rheol. Acta*, 46(4):507–520, 2007.

[173] C. L. DeLeo and S. S. Velankar. *J. Rheol.*, 52(6):1385–1404, 2008.

[174] M. K. Razavi Aghjeh, M. Khodabandelou, and M. Khezrefaridi. *J. Appl. Polym. Sci.*, 114(4):2235–2245, 2009.

[175] J. Li, G. Ma, and J. Sheng. *J. Macromol. Sci. B: Phys.*, 48(5):979–1000, 2009.

[176] G. Marin, J. J. Labaig, and Ph Monge. *Polymer*, 16(3):223–226, 1975.

[177] A. Ajji, L. Choplin, and R. E. Prud'homme. *J. Polym. Sci. B: Polym. Phys.*, 26(11):2279–2289, 1988.

[178] N. W. Tschoegl. *The phenomenological theory of linear viscoelastic behavior : an introduction*. Springer-Verlag, Berlin ; New York, 1989.

[179] S. Velankar, H. Zhou, H. K. Jeon, and C. W. Macosko. *J. Colloid Interface Sci.*, 272(1):172–185, 2004.

[180] T. Hashimoto, M. Itakura, and H. Hasegawa. *J. Chem. Phys.*, 85(10):6118–6128, 1986.

[181] A. Govil, D. M. Pallister, and M. D. Morris. *Appl. Spectr.*, 47:75–79, 1993.

[182] M. Pastorczak, M. Wiatrowski, M. Kozanecki, M. Lodzinski, and J. Ulanski. *J. Mol. Struct.*, 744-747:997–1003, 2005.

[183] Hyun K. Jeon and Christopher W. Macosko. *Polymer*, 44(18):5381–5386, 2003.

[184] S. T. Hyde. *Langmuir*, 13(4):842–851, 1997.

[185] J. C. C. Nitsche. *Lectures on Minimal Surfaces*. Cambridge University Press, Cambridge; New York, 1988.

[186] P. J. F. Gandy and J. Klinowski. *Chem. Phys. Lett.*, 321(5-6):363–371, 2000.

[187] I. S. Barnes. *Austr. Math. Soc. Gazette*, 17:99–105, 1990.

[188] Michael Spivak. *A Comprehensive Introduction to Differential Geometry*, volume 3. Publish or Perish, Inc., Houston, 1999.

[189] S. Passerini, F. Alessandrini, T. Momma, H. Ohta, H. Ito, and T. Osaka. *Electrochem. Solid-State Lett.*, 4(8):A124–A126, 2001.

[190] L. C. Sawyer, D. T. Grubb, and G. F. Meyers. *Polymer microscopy.* Springer, New York, 2008.

[191] J. C. Russ. *Practical stereology.* Plenum Press, New York, 1986.

[192] J. C. Russ. *The image processing handbook.* CRC Press/Taylor Francis, Boca Raton, FL, 2007.

[193] H. E. Exner. *Image Anal. Stereology*, 23:73–82, 2004.

[194] R. T. DeHoff. *Trans. Metal. Soc. AIME*, 239(5):617–621, 1967.

[195] R. E. Miles. *J. Microscopy*, 141:21–27, 1980.

[196] F. Mokhtarian and S. Abbasi. *IEEE Trans. Image Proc.*, 13(5):653–661, 2004.

[197] D. M. Tsai and M. F. Chen. *Patt. Recogn.*, 27(5):699–711, 1994.

[198] F. Mokhtarian and A. Mackworth. *Patt. Anal. Mach. Intell.*, (1):34–43, 1986.

[199] F. Mokhtarian and R. Suomela. *IEEE Trans. Patt. Anal. Mach. Intell.*, 20(12):1376–1381, 1998.

[200] S. A. Saltikov. *Stereometric Metallography.* Metallurgizdat, Moscow, 2nd edition, 1958.

[201] P. Tapadia, S. Ravindranath, and S. Q. Wang. *Phys. Rev. Lett.*, 96(19):196001, 2006.

[202] M. Wilhelm, D. Maring, and H. W. Spiess. *Rheol. Acta*, 37(4):399–405, 1998.

[203] M. Wilhelm, P. Reinheimer, and M. Ortseifer. *Rheol. Acta*, 38(4):349–356, 1999.

[204] K. S. Cho, K. Hyun, K. H. Ahn, and S. J. Lee. *J. Rheol.*, 49(3):747–758, 2005.

[205] R. H. Ewoldt, C. Clasen, A. E. Hosoi, and G. H. McKinley. *Soft Matter*, 3(5):634–643, 2007.

[206] R. H. Ewoldt, A. E. Hosoi, and G. H. McKinley. *J. Rheol.*, 52(6):1427–1458, 2008.

[207] J. M. McMullan and N. J. Wagner. *J. Rheol.*, 53(3):575–588, 2009.

[208] J. Frec, M. C. Heuzey, G. Ausias, and P. J. Carreau. *J. Non-Newtonian Fluid Mech.*, 151(1-3):89–100, 2008.

[209] S. Guido, M. Grosso, and P. L. Maffettone. *Rheol. Acta*, 43(6):575–583, 2004.

[210] Y. Renardy. *Rheol. Acta*, 47(1):89–96, 2008.

[211] Y. Deyrail, M. A. Huneault, and M. Bousmina. *J. Polym. Sci. B: Polym. Phys.*, 47(15):1467–1480, 2009.

[212] M. Grosso and P. L. Maffettone. *J. Non-Newtonian Fluid Mech.*, 143(1):48–58, 2007.

[213] C. Carotenuto, M. Grosso, and P. L. Maffettone. *Macromolecules*, 41(12):4492–4500, 2008.

[214] A. C. Pipkin. *Lectures on viscoelasticity theory*, volume 7. Springer-Verlag, New York, 1986.

[215] M. J. Reimers and J. M. Dealy. *J. Rheol.*, 40(1):167–186, 1996.

[216] C. O. Klein, H. W. Spiess, A. Calin, C. B., and M. Wilhelm. *Macromolecules*, 40(12):4250–4259, 2007.

[217] S. Onogi, T. Masuda, and T. Matsumoto. *J. Rheol.*, 14(2):275–294, 1970.

[218] F. Varnik, L. Bocquet, and J. L. Barrat. *J. Chem. Phys.*, 120(6):2788–2801, 2004.

[219] J.-B. Salmon, S. Manneville, and A. Colin. *Phys. Rev. E*, 68(5):051503, 2003.

[220] F. Rouyer, S. Cohen-Addad, and R. Hohler. *Colloids Surf., A*, 263(1-3):111–116, 2005.

[221] W. M. Holmes, P. T. Callaghan, D. Vlassopoulos, and J. Roovers. *J. of Rheol.*, 48(5):1085–1102, 2004.

[222] O. Radulescu, P. D. Olmsted, J. P. Decruppe, S. Lerouge, J. F. Berret, and G. Porte. *Europhys. Lett.*, 62(2):230–236, 2003.

[223] J.-B. Salmon, A. Colin, S. Manneville, and F. Molino. *Phys. Rev. Lett.*, 90(22):228303, 2003.

Appendix A

Assesment of the Coordinate Transformation Method*

The coordinate transformation method, proposed by Sander and Zuker [76], was implemented and extensively used throughout this thesis to compute the local curvatures of blend interfaces (see section 3.4.4). Following Nishikawa et al.[33, 34], we chose a model bicontinuous structure, namely the gyroid, to test the accuracy of the CT method. The gyroid (or G surface) is an infinitely connected triply periodic minimal surface (TPMS) discovered by Schoen [39]. As with any minimal surface, the gyroid has zero mean curvature at every point. The area-average Gaussian curvature,$< K >$, can be calculated using the homogeneity index, HI, which is a dimensionless number given as [184]

$$\mathrm{HI} \equiv \frac{A^{3/2}}{(-2\pi\chi_V)^{1/2}V}. \tag{A.1}$$

where A is the surface area of the interface with specific (per unit cell) Euler-Poincaré characteristic, χ_V, enclosed within a volume, V. Thus, $< K >$ can be calculated using the Gauss-Bonnet theorem (Eqn. (3.5)) and equation (A.1) as

*Reproduced in part with permission from "Characterizing Interface Shape Evolution in Immiscible Polymer Blends via 3D Image Analysis" Lopez-Barron, C.R.; Macosko, C.W., *Langmuir*, **2009**, 25 (16), 9392–9404. Copyright 2009 American Chemical Society.

$$< K > = \frac{\iint_{Surf} K da}{A} = -\left(\frac{2\pi \cdot \chi_V}{HI \cdot V}\right)^{2/3}. \quad (A.2)$$

For the gyroid, HI = 0.7665 and $\chi_V = -8$ in a unit cell of volume $V = L^3$, where L is the unit cell edge length [184]. Hence, $< K >= -16.3L^{-2}$.

Exact expresions for the coordinates of TPMS can be obtained using the Enneper-Weierstrass representation [185, 186]. However, these expressions are very complex mathematically and actually too hard to handle analytically. For this study we used a trigonometric approximation to the Schoen's gyroid surface, obtained by Barnes [187]:

$$\sin x \cos y + \sin y \cos z + \sin z \cos x = 0 \quad (A.3)$$

This surface, which is not the exact minimal surface, is called a *nodal surface* [187]. Figure A.1 show the computed gyroid-surface with volume $8L^3$. The numerical calculation of the curvatures of a surface, described by $\varphi(\mathbf{r} = (x, y, z)) = 0$, can be performed with the following formulas [188]:

$$H = -\frac{1}{2\sqrt{\varphi_x^2 + \varphi_y^2 + \varphi_z^2}} \frac{B}{A}, \quad (A.4)$$

$$K = \frac{1}{\varphi_x^2 + \varphi_y^2 + \varphi_z^2} \frac{C}{A}, \quad (A.5)$$

where partial derivatives are indicated by the subindices (e.g. $\varphi_x \equiv \partial\varphi/\partial x$). A, B and C are obtained from

$$\det \begin{pmatrix} \varphi_{xx} - \lambda & \varphi_{xy} & \varphi_{xz} & \varphi_x \\ \varphi_{yx} & \varphi_{yy} - \lambda & \varphi_{yz} & \varphi_y \\ \varphi_{zx} & \varphi_{zy} & \varphi_{zz} - \lambda & \varphi_z \\ \varphi_x & \varphi_y & \varphi_z & 0 \end{pmatrix} = A\lambda^2 + B\lambda + C, \quad (A.6)$$

and given by

$$A = -(\varphi_x^2 + \varphi_y^2 + \varphi_z^2), \quad (A.7)$$

$$B = \varphi_x^2(\varphi_{yy} + \varphi_{zz}) + \varphi_y^2(\varphi_{xx} + \varphi_{zz}) + \varphi_z^2(\varphi_{xx} + \varphi_{yy}) \\ -2(\varphi_x\varphi_y\varphi_{xy} + \varphi_x\varphi_z\varphi_{xz} + \varphi_y\varphi_z\varphi_{yz}), \tag{A.8}$$

$$C = \varphi_x^2(\varphi_{yz}^2 - \varphi_{yy}\varphi_{zz}) + \varphi_y^2(\varphi_{xz}^2 - \varphi_{xx}\varphi_{zz}) \\ +\varphi_z^2(\varphi_{xy}^2 - \varphi_{xx}\varphi_{yy}) + 2(\varphi_x\varphi_y(\varphi_{xy}\varphi_{zz} - \varphi_{xz}\varphi_{yz}) \\ +\varphi_x\varphi_z(\varphi_{xz}\varphi_{yy} - \varphi_{xy}\varphi_{yz}) + \varphi_y\varphi_z(\varphi_{yz}\varphi_{xx} - \varphi_{xy}\varphi_{xz})). \tag{A.9}$$

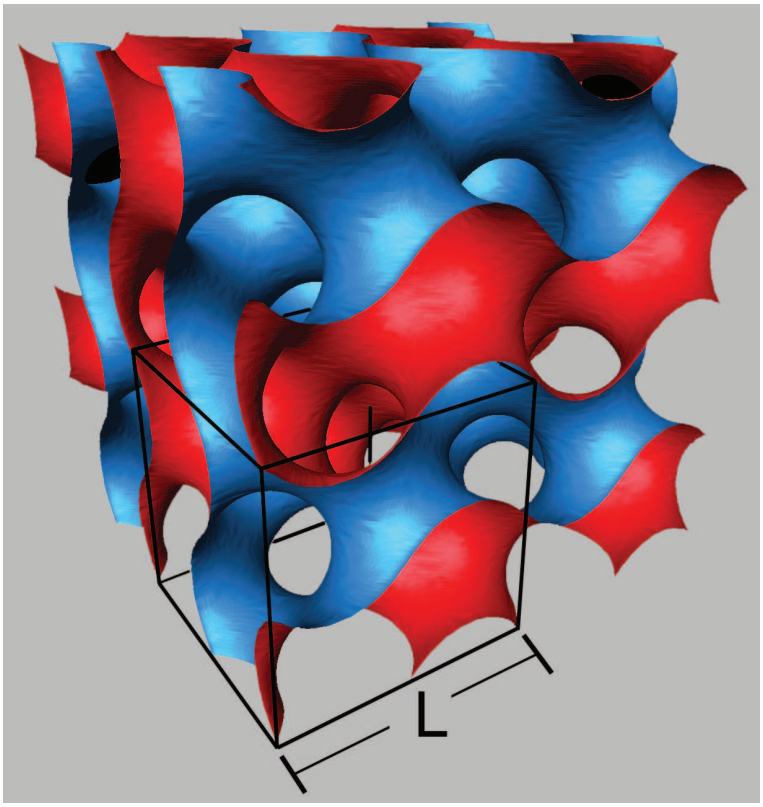

Figure A.1: Gyroid surface containing 8 crystallographic unit cells, approximated as a nodal surface (given by Equation (A.3), with a plotted range: $-2\pi < x, y, z < 2\pi$). The black cubic frame contains a single unit cell.

A gyroid of dimensions $2L \times 2L \times 2L$, i.e. with 8 crystallographic unit cells, was constructed using Equation A.3 and shown in Figure A.1. The roughness of the surface was varied by changing the number of voxels in the rendering process. Figure A.2 show the average area of the triangles in the surface mesh, $< A_{tri} >$, as a function of the

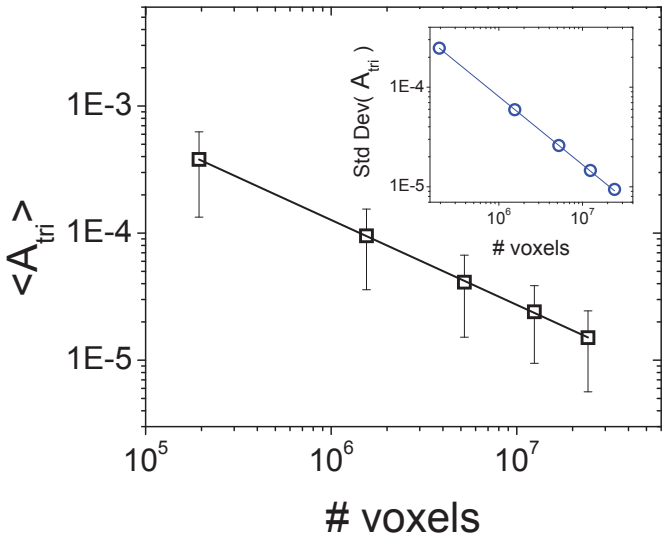

Figure A.2: Area average of the triangles of the mesh describing the gyroid shown in A.1 as a function of number of voxels. The standard deviation is represented by the error bars and also plotted as a function of the number of voxels in the inset graph.

number of voxels. The smaller the area of the triangles, the smoother the interface. To study the effect of roughness on the average curvatures, we used the "roughness index", RI, defined by Nishikawa et al.[33]:

$$RI \equiv \sqrt{A_{tri}} \frac{|<\kappa_1>| + |<\kappa_2>|}{2}, \tag{A.10}$$

which account for the global curvature and the triangle size. Figure A.3 shows the accuracy of the CT method in the computation of the average curvatures. Notice that the discrepancies between the average values of H and K calculated with the CT method and the exact values calculated with equations A.4-A.9 are negligible for all the RI values considered. The only noticeable effect is in the standard deviation, given by the error bars. Bigger deviation is observed for the small values of RI compared to the corresponding deviation of the exact values. This effect is because patches with locally smaller curvature are more frequently produced with larger triangles, corresponding to bigger values of RI, than with smaller triangles. This higher population of "less curved" patches produces narrower distributions. It is important to note that when the values of H are exactly calculated with equations A.4 and A.5 there is a finite standard deviation,

even when $< H > \approx 0$; i.e. H is not zero everywhere. This is because these equations are an approximation, not a true minimal surface. In the same way, the theoretical value of $< K > = -16.3L^{-2}$ is not the same as the one obtained with the approximation ($< K > = -19.6L^{-2}$), although it is very close. The measured errors from the results obtained with the CT method compared to the analytical values, for RI values up to 0.08, are within 2% and 6% for $< H >$ and $< K >$, respectively.

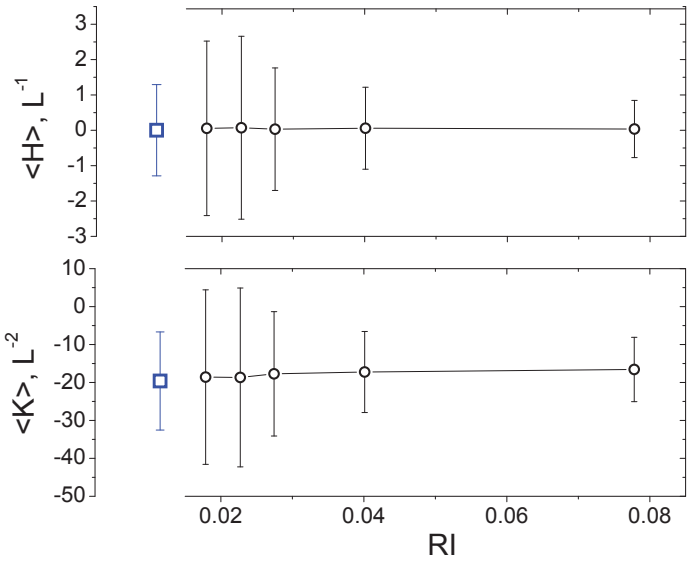

Figure A.3: Area-average mean $< H >$ and Gaussian $< K >$ curvatures as a function of the roughness index, calculated with equation A.4 - A.9 (*blue*□) and with the CT method (○). The error bars represent the standard deviation.

The probability densities of H and K for the gyroid are shown in Figure A.4. Note that these densities are not P_H and P_K (as defined by Equations 3.13 and 3.14), but just the normalized frequency counts. These simplified densities were used in order to compare the distributions obtained from the CT method (with IR=0.04) with those calculated with equations A.4-A.9. With these equations there are no triangle areas to compute P_H and P_K. Note that both distributions are centered in zero but the CT method generates a narrower distribution. Using the SF method, Nishikawa et al.[34] found an even narrower distribution, although they did not compute the analytical distribution to compare it. The analytical K distribution shows a odd peak at $K \approx$

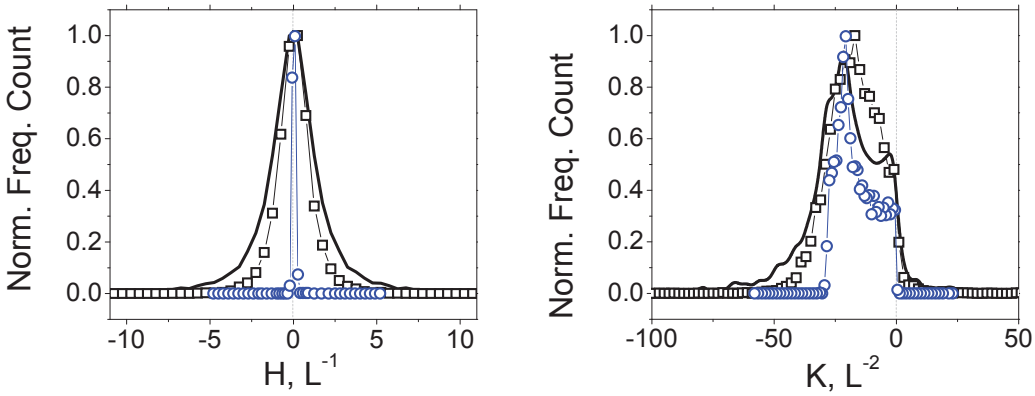

Figure A.4: Normalized frequency count of the mean and Gaussian curvatures calculated with equations A.4-A.9 (–) and measured using the CT method (with RI=0.04) (□); and compared to data obtained by Nishikawa et al.[34] using the SF method (with RI=0.06)(○).

$-21L^{-2}$ which was also observed by Nishikawa et al. at about the same value of K calculated with the SF method [34]. The CT method does not reproduce the shape of the peak but numerically is closest to the analytical distribution. Therefore, we conclude that given that the curvature distributions are well reproduced and the errors from the calculation of the average values are no bigger than 6%, the CT method is very suitable for the quantification of the local shape of bicontinuous structures, and is numerically more accurate than the SFM [34].

Appendix B

Stereological Analysis of Cocontinuous Blends*

B.1 Introduction

Some of the unique properties of cocontinuous polymer blends, that make them ideal for a number of applications, include: synergistic mechanical properties, controlled electrical conductivity, and selective permeability [1, 46, 189, 13]. These properties are strongly dependent of the morphology (i.e. size and shape of the phases). Therefore an accurate characterization of the later is crucial to understand the structure-property relation.

Parameters that have been shown to be important in the characterization of cocontinuous blends are (see Chapter 3):

- Specific interfacial area, S_V.†The reciprocal of S_V is a measure of the characteristic length of the microstructure [78].
- Mean curvature, H. Given that the driving force of the coarsening of cocontinuous structures is the interfacial energy between the phases, which is proportional to

*This article has been submitted for publication to the Journal of Microscopy. Unpublished work copyright 2009 Royal Microscopical Society and Blackwell Publishing.

†In previous Chapters I have used the symbol Q for the specific interfacial area. In this appendix I used S_V to be congruent with notation used in stereology literature [52].

H, then the latter is a measure of the stability of the microstructure [35, 45].

- Gaussian curvature, K. This quantity is particularly useful in characterizing the local shape of surfaces (the sign of K gives the type of local points) and the topology of a surface via the Gauss-Bonnet theorem [73].

- Curvature distributions. From the analysis of the shape of the distribution of local mean and Gaussian curvatures at different annealing times, it has been demonstrated, that cocontinuous structures grow in a self-similar manner [35, 45].

All these parameters can be directly measured from the analysis of 3D images. However, nowadays, 3D imaging techniques are in development and require a considerable amount of work compared to simpler and more mature 2D imaging techniques [190].

For several decades 2D imaging techniques (including optical microscopy, transmission and scanning electron microscopy and atomic force microscopy) have being extensively used to qualify and quantify morphology of polymers blends [1, 190, 2, 7]. Two dimensional images may be representations of two dimensional objects (surface or thin sections of the specimen) or projections of the specimen onto a plane. Using a suitable stereological method, 2D images can give approximate information about the (real) three dimensional microstructure [52, 191].

On the other hand, 3D images contain exact 3D information. However, obtaining 3D images require additional steps such as sophisticated image processing algorithms [192, 71] and 3D-rendering from series of 2D images [72]. In the past decades these processes were considered computationally expensive. Nevertheless, the reduced cost in computing power and the integration of computers with microscopes is driving a strong trend to 3D imaging in many fields [190]. Having said that, it is important to evaluate the pros and cons of 3D and 2D imaging, in order to ascertain whether the analysis of 2D images is enough to calculate the desired geometrical parameters with the required accuracy or more sophisticated methods (e.g. 3D image analysis) are needed. Factors to consider include the computational resources available, the amount of work required for each analysis and the inevitable error generated from the analysis of the 2D images, even after applying stereological corrections [193].

In this work we used 3D confocal microscopy (as described in Chapter 3) to image a fluorescently-labeled polystyrene (FLPS)/styrene-ran-acrylonitrile copolymer (SAN)

blend with cocontinuous morphology. Geometrical parameters obtained from the 3D images were compared to those obtained from the analysis of the 2D sections before 3D reconstruction using a number of fundamental stereological relations. To my knowledge, this is the first time that these types of analyses are carried out in cocontinuous structures. In general, average values of specific surface area and mean curvature were not accurately estimated from the 2D images. Only the volume fraction was estimated within a small error (0.5%). Moreover, the predicted curvature distributions were considerably broader than the real ones.

B.2 Experimental methods

Symmetric (50/50 w/w) and non symmetric (25/75 w/w) blends of FLPS120K/SAN10 were prepared in a twin screw Micro-Compounder (DACA Instruments). Molecular weights of FLPS120K and SAN10 (measured by gel permeation chromatography using polystyrene standards) are 122 kg/mol and 116 kg/mol, respectively. The acrylonitrile content of SAN is 9.5 %mol (measured with CHN analysis performed via combustion at 990 C). The blends were annealed at 200 °C for 30 min (50/50 blend) and 10 min (25/75 blend). After annealing, the blend microstructure was imaged with laser scanning confocal microscopy (LSCM) with a 405 nm excitation laser and a 461 nm wavelength filter for fluorescent light detection. Stacks of 2D images (composed of 512 X 512 pixels) were obtained with a separation of 0.5 μm between each image. The 2D images were deconvoluted and thresholded for a subsequent 3D rendering, which was performed using the marching cubes algorithm [72]. A triangular mesh depicting the blend interface was obtained after the rendering process. Each mesh is made of a number of triangles in the order of 10^7. Synthesis, characterization and blending of the components as well as the methods for image processing and analysis were detailed in Chapter 3.

B.3 Interface characterization

A number of geometrical parameters of the interface were calculated from both the 2D sliced images and the rendered 3D images. They are related via the stereological formulae, summarized in Table B.1. The computation of these parameters is described

below.

Table B.1: Stereological formulae and definitions of 2D and 3D parameters.

Stereological estimators			Definitions	
ID	Formula	Units	Planar curves	Curved surfaces
I	${}^{a}V_V = A_A$	Unitless	$A_A \equiv$Area of intercepted features per unit test area	$V_V \equiv$Volume of features per unit test volume
II	${}^{a}S_V = \frac{4}{\pi} L_A$	μm^{-1}	$L_A \equiv$Length of lineal elements per unit test area	$S_V \equiv$Surface area per unit test volume
III	${}^{b}\bar{H} = \frac{\pi}{4}\bar{\kappa}_c$	μm^{-1}	${}^{d}\bar{\kappa}_c \equiv$Avg. curvature along a curve	${}^{e}\bar{H} \equiv$Avg. mean curvature over a surface
IV	${}^{c}M_V = \frac{4}{\pi} \int\limits_{curve} \kappa_c^2 dl_A$	μm^{-3}	$dl_A \equiv$Element curve length per unit area of the section plane	${}^{f}M_V = M/V \equiv$Integral mixed curvature per unit volume

[a] Underwood (1970) [52]

[b] DeHoff (1967) [194]

[c] Miles (1980) [195]

[d] $\bar{\kappa}_c = \int\limits_{curve} \kappa_c dl \Big/ \int\limits_{curve} dl$, with $L = \int\limits_{curve} dl \equiv$Length of lineal elements.

[e] $\bar{H} = \iint\limits_{surf} H ds \Big/ \iint\limits_{surf} ds$, with $S = \iint\limits_{surf} ds \equiv$Interfacial area

[f] $M = \iint\limits_{surf} m ds \equiv$Integral mixed curvature, with $m = \frac{1}{4}\left(3\kappa_1^2 + 2\kappa_1\kappa_2 + 3\kappa_2^2\right) \equiv$ Mixed curvature.

B.3.1 3D image parameters

Applying the coordinate transformation (CT) method [76] on the triangular meshes, the local mean (H) and Gaussian (K) curvatures were calculated in each triangle. The implementation of the CT method was described in detail in Chapter 3. From the definitions of $H(\equiv \frac{1}{2}(\kappa_1 + \kappa_2)\ )$ and $K(\equiv \kappa_1 \cdot \kappa_2)$, the principal curvatures, κ_1 and κ_2, can be computed with

$$\begin{aligned} \kappa_1 &= H + \sqrt{H^2 - K} \\ \kappa_2 &= H - \sqrt{H^2 - K} \end{aligned} \tag{B.1}$$

The interfacial area between the phases, S, was obtained by adding the area of all the triangles in the mesh. The test volume, V, was obtained by counting the number of voxels forming the 3D image. The interfacial area per unit volume, S_V, is simply equal to S/V and the volume fraction, V_V, is the ratio between the number of voxels corresponding to the FLPS phase and V. The area-average mean curvature, $\bar{H}$, and the integral mixed curvature, M [195], are calculated with

$$\bar{H} = \frac{\sum_{i=1}^{N} H_i s_i}{\sum_{i=1}^{N} s_i} \tag{B.2}$$

$$M = \frac{1}{4} \sum_{i=1}^{N} \left(3\kappa_{1,i}^2 + 2\kappa_{1,i}\kappa_{2,i} + 3\kappa_{2,i}^2\right) \cdot s_i \tag{B.3}$$

where H_i, $\kappa_{1,i}$ and $\kappa_{2,i}$ are the mean and principal curvatures and s_i is the surface area of the i-th triangle.

B.3.2 2D sliced image parameters

The curvature of digital curves can be calculated using a number of approaches [196, 197]. In this work we used the definition of curvature given by Mokhtarian and coworkers [196, 198, 73]

$$\kappa(u,\sigma) = \frac{X_u(u,\sigma)Y_{uu}(u,\sigma) - X_{uu}(u,\sigma)Y_u(u,\sigma)}{(X_u(u,\sigma)^2 + Y_u(u,\sigma)^2)^{\frac{3}{2}}} \tag{B.4}$$

where $X_u(u,\sigma) = x(u) \otimes g_u(u,\sigma)$, $X_{uu}(u,\sigma) = x(u) \otimes g_{uu}(u,\sigma)$ and similar formulas for $Y_u(u,\sigma)$ and $Y_{uu}(u,\sigma)$. The symbol $\otimes$ represents the convolution operator and $g(u,\sigma)$ denotes a Gaussian function with deviation σ. $g_u(u,\sigma)$ and $g_{uu}(u,\sigma)$ are the 1st and 2nd derivatives of $g(u,\sigma)$, respectively.

Following the steps proposed by Mokhtarian and Soumela [199], we used the canny edge detector to extract the edge contours of the 2D sliced images. The boundary was re-sampled and represented by 5000 equally distant points. The curvature in the sampled points was computed using Equation B.4. Hereafter, we will use the notation κ_c to refer to curvature of planar curves in order to distinguish it from the principal curvatures of 3D surfaces defined above (Equation B.1).

The planar area of each phase, A_{FLPS} and A_{SAN}, as well as the length of the phase boundary, L, were measured with ImageJ (available at `http://rsb.info.nih.gov/ij/`). The area fraction, A_A, and the contour length per unit area, L_A, are merely A_{FLPS}/A and L/A , respectively, with $A = A_{FLPS} + A_{SAN}$. Finally, the average curvature, $\bar{\kappa}_c$, is computed with

$$\bar{\kappa}_c = \frac{\sum_{i=1}^{n} \kappa_{c,i} l}{L} \tag{B.5}$$

where l and n are the pixel length and the number of pixels along the phase boundary, respectively.

Besides the global descriptors of the microstructure, given by expressions in Table B.1, other important properties are the distributions of the mean and Gaussian curvatures. In Chapter 3, I showed that the shape of the curvature distributions compared at different annealing times gives a criterion of self-similarity of the interface during coarsening of cocontinuous blends [45]. Therefore, in the context of this Appendix, it is of interest to compare the distribution of the mean curvature obtained from the 3D images with the distribution of the line curvature obtained from the 2D sliced images.

B.4 Results and discussion

Figures B.1 and B.2show binarized LSCM micrographs and 3D rendered images of the 50/50 and 25/75 FLPS/SAN blends, respectively. Note, mainly in the non symmetric

blend, the considerable amount of isolated features observed in the 2D images. Without previous knowledge of the microstructure, these features could be mistaken as droplets. However, as is evident from the 3D images, they are part of the 3D continuous domains. This misinterpretation of the real (3D) microstructure is one of the flaws of 2D imaging techniques.

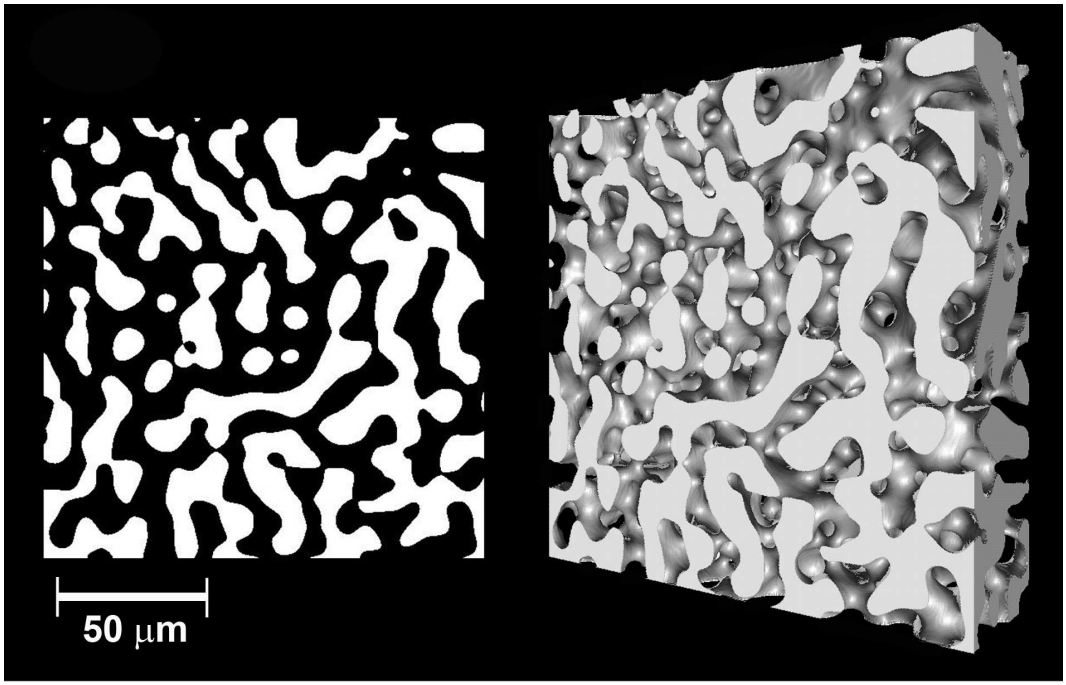

Figure B.1: 2D binarized LSCM micrograph and 3D rendered image of 50/50 FLPS/SAN blend annealed at 200 °C for 30 min.

Figure B.3 shows the distribution of κ_c for both the 50/50 and the 25/75 blends, computed with different number of 2D slices, along with the mean curvature distribution from the 3D images. It is noteworthy that the analysis of a single slice gives the same distribution as that of 50 slices for both blends. The standard deviation of the distribution measured from the 2D images is about 2.35 bigger than that calculated from the 3D images for both blends. This can be explained by the fact that the planar (2D) curves contain information of only one curvature, and the value of the curvature corresponding to the perpendicular plane is not available. To better understand this,

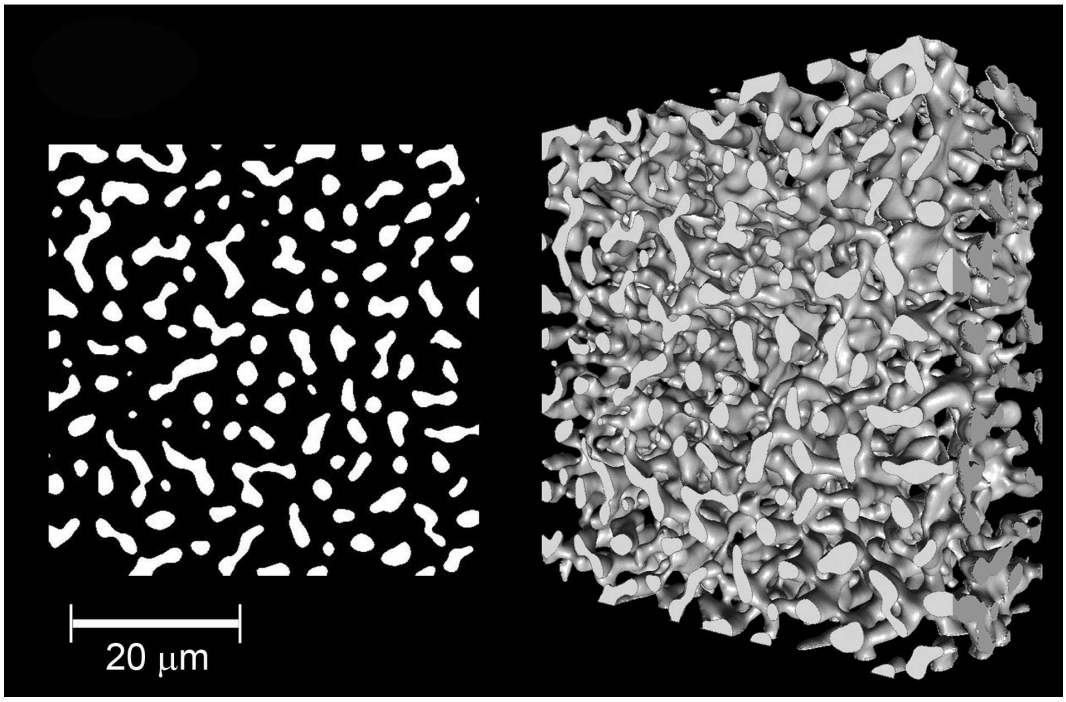

Figure B.2: 2D binarized LSCM micrograph and 3D rendered image of 25/75 FLPS/SAN blend annealed at 200 °C for 10 min.

note that the distribution of Gaussian curvature (shown in Figure B.4) shows a dominant population of hyperbolic (saddle shaped) points, which corresponds to negative values of K [45, 73].[‡]According to the definition of $K(\equiv \kappa_1 \cdot \kappa_2)$, negative values of this parameter indicates that the two curvatures of the curves resulting from the intersection of two perpendicular planes with the surface of interest will be opposite in sign. Hence, the absolute average of these two curvatures will be smaller that the absolute value of either of the two. In the case of 3D images, the curvature of both planes is available, and then the average value (i.e. the mean curvature) can be exactly calculated.

The mean curvature distribution for the symmetric blend is perfectly symmetrical and centered in zero (see Figure B.3a), which is what was expected due to the symmetrical volume ratio. The analysis of the 2D images gives a distribution slightly shifted

[‡]It is worth to mention that K cannot be computed from 2D images.

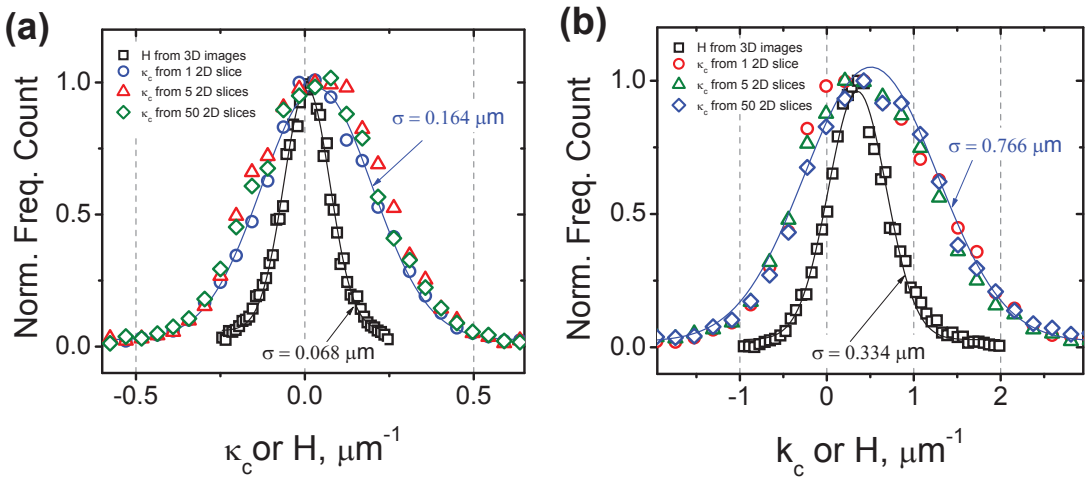

Figure B.3: Normalized frequency counts of the mean curvature calculated from the 3D images, and of the planar curvatures calculated from different number of 2D slices, for (a) the symmetric (50/50) and (b) the non symmetric (25/75) blends. The solid lines depict fits with Gaussian functions with standard deviation (σ) indicated in the plots.

towards positive values of H. For the case of the non-symmetric blend (Figure B.3b)both distributions are symmetrical but shifted towards a positive value of curvature, which is due to the large population of elongated domains with positive curvature. The shifting is greater in the distribution calculated from the 2D slices. From these results we deduce that the mean curvature distributions can be qualitatively predicted from the analysis of the 2D images, but with a substantial error on the width of the distributions.

Figure B.5 and Figure B.6 show A_A, $(4/\pi)L_A^{-1}$, $(\pi/4)\bar{\kappa}_c$ and $(4/\pi)\sum_i \kappa_{c,i}^2 l$ as a function of the total length of phase boundary, L_{Tot}, normalized with the characteristic length of the microstructure (given by S_V^{-1}), for the symmetric and non symmetric blends, respectively. L_{Tot} is defined as

$$L_{Tot} = \sum_{i=1}^{N} L_i \tag{B.6}$$

where L_i is the length of phase boundary of the slice i, and N is the total number of slices. The standard deviation for all the quantities decreases with the number of 2D slices, reaching a negligible value when $L_{Tot} \cdot S_V \geqslant 6000$. This amount of phase

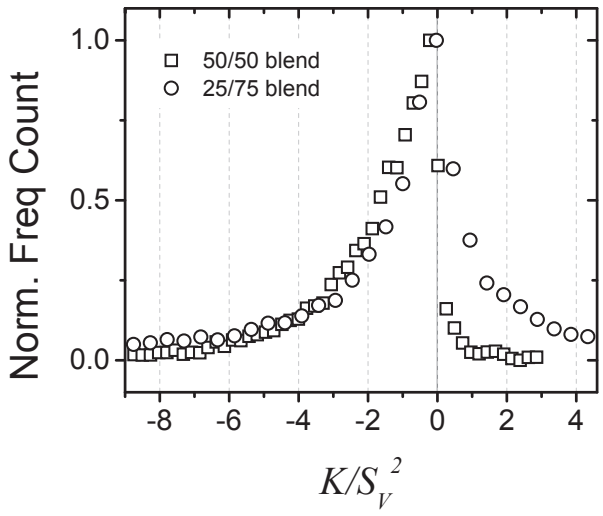

Figure B.4: Normalized frequency counts of the scaled Gaussian curvature calculated from the 3D images for the symmetric (50/50) and non symmetric (25/75) blends.

boundary implied the analysis of at least ten 2D slides for both blends.

In order to test the stereological formulae listed in Table B.1, the values of V_V, S_V^{-1}, $\bar{H}$ and M_V, are included in the plots as indicated in the plot captions (Figures B.5 and B.6). The error from the calculation of A_A compared to the value of V_V is very small for both blends (within 0.5%) while the error of the characteristic length (Formula II in Table B.1) was 8.4% for the symmetric blend and 17.7% for the non-symmetric blend. Pyun et al. [53] measured the characteristic length of a 50/50 polystyrene/polyethylene blend during coarsening from 3D images and 2D cuts. Their results show an error from the 2D images of up 32% without stereological correction. Performing the correction, that error is reduced to 12% which is close to the error obtained in this work.

The average mean curvature, $\bar{H}$, was predicted within a 20% error for the non-symmetric blend but the error was considerable for the symmetric blend (330%). However, considering the standard deviation of the distribution (0.164 μm^{-1}) the calculated value of $(\pi/4)\bar{\kappa}_c$ (0.03) is not very different from the theoretical value of $\bar{H}$ (i.e. $\bar{H} = 0$). In Appendix A I demonstrated that the error generated by the CT method for the computation of $\bar{H}$ is within 2% [45], which is appreciably smaller than the error estimated

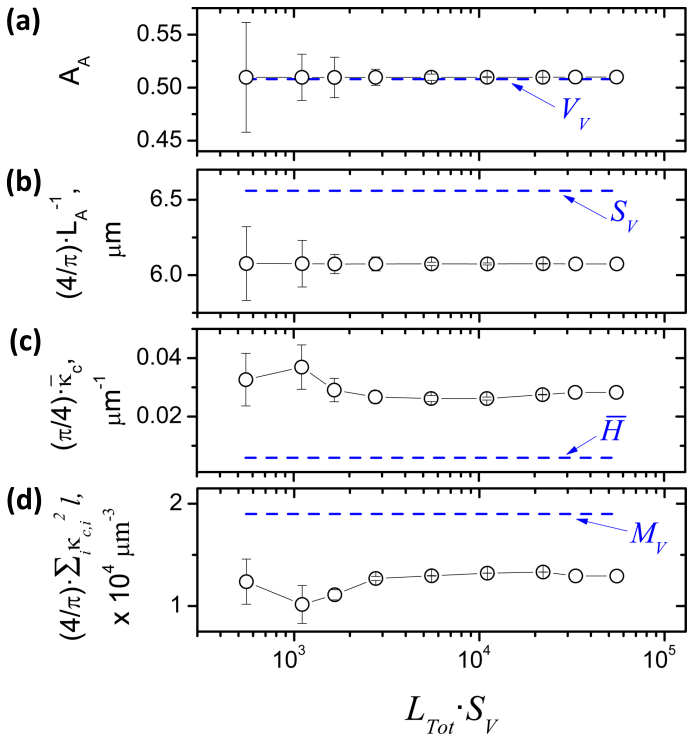

Figure B.5: (a)Area fraction, (b)reciprocal contour length per unit area, (c) average planar curvature and (d) $\sum_i \kappa_{c,i}^2 l$ as a function of normalized contour length, for the 50/50 FLPS/SAN blend. The dashed (blue) lines represent the values of V_V, S_V, $\bar{H}$ and M_V computed from the 3D images.

from the 2D images analysis. Finally the value of $(4/\pi)\int \kappa_c^2 dl_A$, compared to the M_V value obtained from the 3D images show an error within 32% and 19.4% for the symmetric and non-symmetric blends, respectively.

B.5 Conclusions

In the present appendix a series of stereological estimators were tested for the first time in cocontinuous structures. The specific volume (V_V) was estimated with an error of less than 0.5%, while the characteristic length, given by the reciprocal specific interfacial area (S_V^{-1}), gave errors ranging from 8.4% up to 18%. Considering that the characteristic

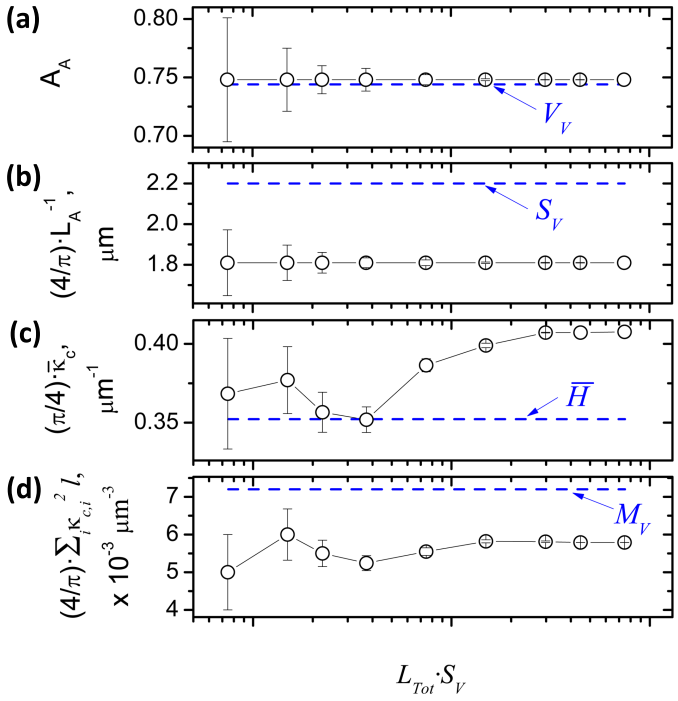

Figure B.6: (a)Area fraction, (b)reciprocal contour length per unit area, (c) average planar curvature and (d) $\sum_i \kappa_{c,i}^2 l$ as a function of normalized contour length, for the 25/75 FLPS/SAN blend. The dashed (blue) lines represent the values of V_V, S_V, $\bar{H}$ and M_V computed from the 3D images.

length is a very important parameter to characterize these microstructures [35, 45], an error of 18% may not be acceptable and could lead to misinterpretations. On the other hand, as mentioned before, the interfacial curvature is directly related to the stability of these structures, hence an accurate estimation of this quantity is crucial in the study of the dynamics of coarsening of these structures. From the present stereological analysis, the estimated average mean curvature and the specific mixed curvature showed errors up to 20% and 32%, respectively. The mean curvature distributions were poorly reproduced when compared to the planar curve curvatures from the 2D slices. The shape of the distribution was qualitatively reproduced for both the symmetric and the non symmetric blends. Nevertheless, the estimated distribution width was substantially bigger than the real one.

The substantial errors in the estimations of characteristic length and curvature need to be taken into account when one has to decide whether use 2D imaging coupled with stereological corrections or 3D imaging. On top of that, the standard deviation of the measurements was negligible only when the total length of boundary (from the 2D images) considered in the analysis is 6000 or more times bigger the characteristic length. For both symmetric and non symmetric blends at least ten 2D slices were needed to account for this amount of phase boundary. Normally, taking 10 images of a single sample is not a practical procedure. Another aspect to be considered is the fact that from 2D images it is difficult to unequivocally identify the type of morphology. From the 2D slices of the 25/75 blend, for instance, it is impossible to distinguish the cocontinuous morphology, but from the 3D images it is evident.

Finally, it is noteworthy that to date, stereological formulae do not include an estimator for the Gaussian curvature, which as mentioned before is extremely useful for the characterization of local points and surface topologies. K is readily obtainable from the analysis of 3D images, as described in Chapter 3.

Appendix C

Measurement of Interfacial tension between FLPS and SAN: Effect of AN content

Two methods were used to measure the blend interfacial tension, namely, the breaking thread method (BTM) and the rheological method (RM). Details on the theoretical development of these methods can be found elsewhere.[88, 96, 27, 97]

The BTM consist on measuring the growth of the capillary instabilities of cylindrical threads of a liquid embedded in a second one.[88] An example is shown in Fig. C.1. The amplitude of these instabilities, α, grow exponentially with a rate q, given by eqn (4.2). Therefore, by plotting $2a\eta_m \ln(\alpha)/\Omega$ versus time, a straight line is generated, whose slope is the interfacial tension. Typical plots for the systems studied here are shown in Fig. C.2. The different slopes evidence the increase in interfacial tension with the AN content in the SAN phase. Values of Γ are shown in Fig. C.5.

The RM consists on fitting the Palierne emulsion model [27] with the rheological experimental data. Palierne model accounts for the linear viscoelastic behavior of spherical viscoelastic inclusions in a viscoelastic matrix. Assuming constant interfacial tension and no interfacial viscosity, the complex modulus of the dispersion, G^*, is given as

$$G^* = G_m^* \left(\frac{1 + \frac{3}{2}\varphi\mathscr{H}}{1 - \varphi\mathscr{H}} \right) \tag{C.1}$$

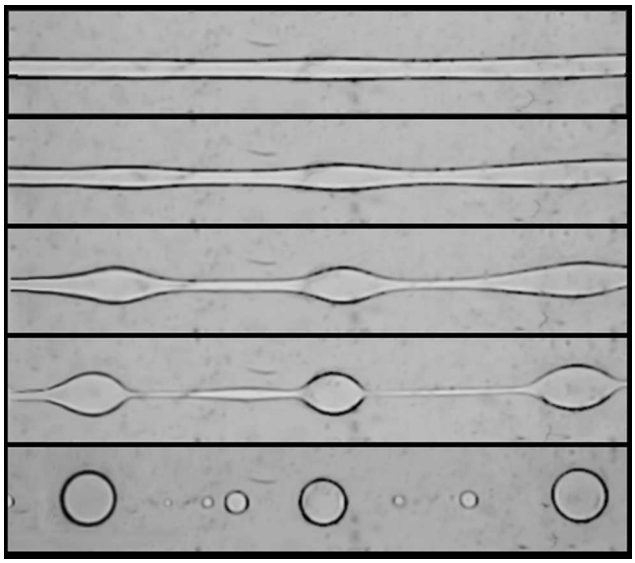

Figure C.1: Optical micrographs showing the breaking thread process of a SAN20 thread, with initial radius 43 μm, embedded in a FLPS matrix. The micrographs were captured, from top to bottom, at 0, 360, 1680, 2520 sec. The temperature was maintained at 200 °C.

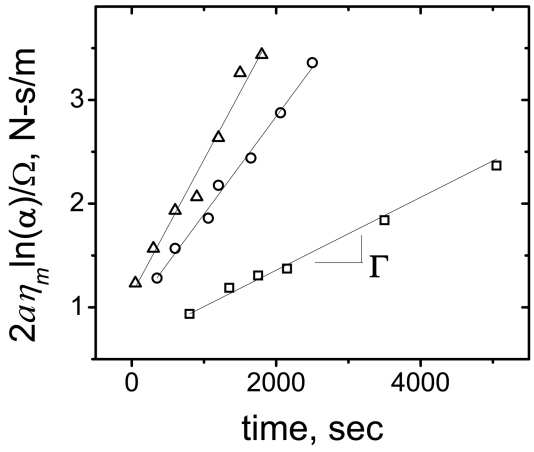

Figure C.2: $2a\eta_m \ln(\alpha)/\Omega$ versus time for the systems: (□) FLPS/SAN10, (○) FLPS/SAN20 and (△) FLPS/SAN30. Solid lines represent linear fits with slope = Γ.

with

$$\mathscr{H} = \frac{2\left(G_d^* - G_m^*\right)\left(19G_d^* + 16G_m^*\right) + 8\Gamma/R_V\left(5G_d^* + 2G_m^*\right)}{\left(2G_d^* + 3G_m^*\right)\left(19G_d^* + 16G_m^*\right) + 40\Gamma/R_V\left(G_d^* + G_m^*\right)} \tag{C.2}$$

where G_m^* and G_d^* are the complex moduli of the matrix and the disperse phases, respectively, ϕ is the volume fraction of the disperse phase, and R_V is the volume average radius of the disperse phase.

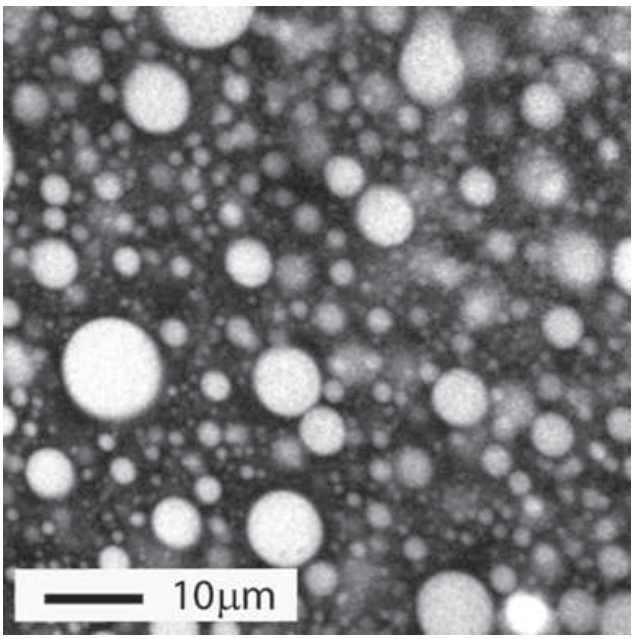

Figure C.3: LSCM micrograph of 25/75 FLPS/SAN20 Blend.

Fig. C.3 show the microstructure of the 25/75 FLPS/SAN20 blend after the frequency sweep test. Evidently, the droplet radii are not uniform. However, using the volume average ($R_V \equiv \left(\sum \varphi_i R_i\right)/\varphi$, where φ_i is the volume fraction of the droplets with radius R_i and $\varphi = \sum \varphi_i$) gives very accurate results because the largest particles represent the most of the volume fraction and their contribution to the elastic modulus of the emulsion is predominant [130, 96]. R_V was determined from the analysis of about 100 micrographs (as the one shown in Fig. C.3) per sample, taken at different depths into the samples, using LSCM. Corrections of the radii were performed using the Schwartz-Saltikov method [200]. The method consists on the classification of the

particle size into 15 size ranges, characterized by their midpoint. The real (volumetric) number of particles of each size range is obtained from the product of a matrix of coefficients and a vector containing the number of particles measured for each size range [200, 52].

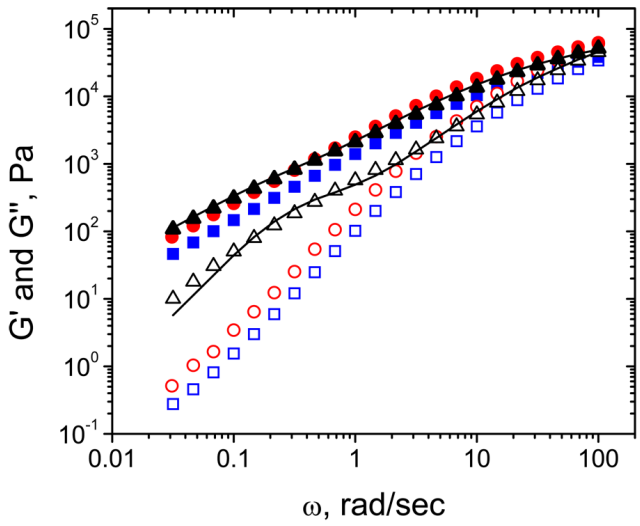

Figure C.4: G' (empty symbols) and G'' (filled symbols) versus frequency for FLPS (squares), SAN30 (circles) and 25/75 FLPS/SAN30 blend (triangles). The solid lines depict the Palierne's model prediction.

Fig. C.4 show the comparison of G' and G'' obtained experimentally and fitting curves obtained with equation C.1 for the blend FLPS/SAN20, using Γ as the fitting parameter. For the three blends, the fitting curves were in good agreement with the experimental data using the values of interfacial tension shown in Fig. C.5.

The interfacial tension measured with the BTM is, for all three systems, bigger than that measured with the RM. A possible reason for this discrepancy is that the annealing treatment of the fibers before the BTM tests was not sufficient to completely release the stresses generated during the drawing process. The remaining extra-stress in the fibers will provoke an acceleration in the growth of the capillary instabilities of the threads, which in turn will make the slopes in Fig. C.2 bigger than the corresponding value for stress-free threads. For the analyses in the present paper we considered the average value of Γ (listed in table 3) between the BTM and the RM.

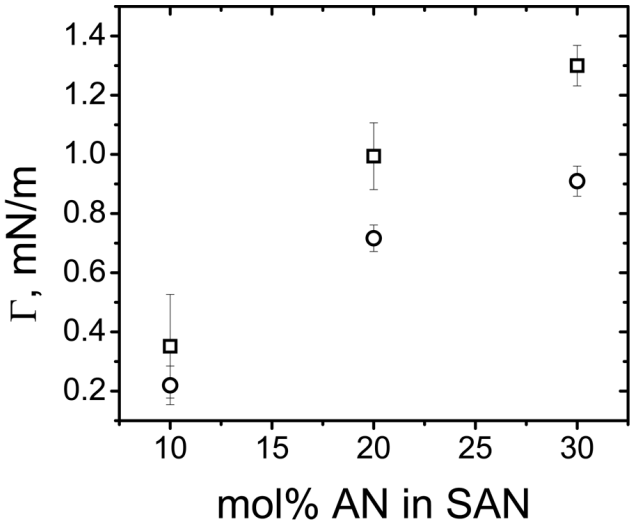

Figure C.5: Interfacial tension between FLPS and SAN as a function of AN content in SAN, measure with (□) the breaking thread method and (○) the rheological method.

Appendix D

Rheological Response under Large Amplitude Oscillatory Measurements (LAOS)

D.1 Introduction

Oscillatory shear measurements represent an effective way to investigate mechanical relaxation of complex fluids. Information of dynamics, molecular weight, and microstructure can be extracted from the analysis of such measurements [96]. By applying amplitudes so small (i.e. SAOS) that the material microstructure is not distorted, a linear response is obtained. That is, the amplitude of the response is directly proportional to the imposed deformation. Under this deformation regime, the time dependent stress is described by a single trigonometric function.

When large amplitude oscillatory shear (LAOS) is applied, the non linear regime is entered, and the material under test may experience structural changes [175, 201]. Additionally, the stress response is no longer described by a single trigonometric function but by a periodic function that can be expressed as a Fourier series [202]. The first harmonic of that series give the linear viscoelastic response and the higher harmonics reflect the non-linearities arising from the large deformations.

Wilhelm and coworkers [202, 203] analyzed the non linear behavior of materials

under the framework of Fourier Transform (FT) rheology. They defined the degree of non linearity as the ratio of the magnitude of the n-th harmonic, $I(n\omega_i)$, with respect to the magnitude of the fundamental frequency, $I(\omega_i)$. Cho et al. [204] avoided FT rheology by decomposing the stress response into elastic and viscous components. Ewoldt et al. (2008) and Yu et al. (2009) further discussed alternative methods to the FT analysis aimed to a more definite way to qualify the steady state stress response, in terms of viscous and elastic non-linearities.

The motivation for this study is the growing interest for undertanding the relation between LAOS response and morphology of complex fluids [205, 206, 207, 208]. Particularly, in polymer blends a number of studies have been devoted to understand drop deformation of dilute emulsion subjected to LAOS measurements [209, 210, 211] or to estimate drop size distribution [212, 213]. However no study on the rheological response of cocontinuous morphologies under LAOS measurements has been published to date.

This appendix is intended to present preliminary results of rheological data of 50/50 FLPS/SAN10 and FLPS/SAN20 blends and their components subjected to LAOS measurements. The objective of these measurements was to explore the non-linearities originating from the blends in contrast to those from their components. The idea is to ascertain if the interface and its evolution has a noticeable effect on the non-linear response of cocontinuous blends. The results are presented as Lissajous–Bowditch curves, at different values of ω and γ_0, and plots of intensity of the third harmonic as a function of ω, γ_0 and annealing time. Non linearities were clearly observed on the components and the blends. Nevertheless, only the blend with higher interfacial tension (FLPS/SAN20) displayed a behavior different from that of the components.

D.2 Experimental methods

D.2.1 Materials

The synthesis and characterization of FLPS120K, SAN10 and SAN20 are described in Chapter 2. Key properties of these polymers are shown in Table 2.2. FLPS/SAN10 and FLPS/SAN20 blends were prepared via melt blending using a Daca microcompounder (DACA Instruments) as described in Chapter 3. Blends with composition 50/50 w/w, with and without 1% 100K PS-b-PMMA block copolymer (BC) were used in this study.

Table 5.1 shows BC properties. Small pieces of the blends were annealed at 200 °C and visualized using laser scanning confocal microscopy.

D.2.2 Rheological measurements

The blends and their components were moulded into discs (25 mm diameter and $\sim$ 1 mm tick) and dried at 90 °C under vacuum for at least 24 hours before the rheological measurements. Oscillatory shear measurements were performed on the blends and their components using the strain controlled rheometer Ares G2 (TA Instruments). This apparatus has the special feature of provide the stress wave form without requiring any modification to the data acquisition system. In addition, the software provided by the rheometer manufacturer computes the ratio between the intensity of the first nine harmonics with the fundamental one, I_n/I_i, $i = 1 \cdots 9$.

Strain sweeps, with strain amplitude ranging from 1 to 1000 %, were performed at six different frequencies on the compatibilized blends. We chose to use the compatibilized blend in these tests due to its stability against coarsening. (see Chapter 5). The strain and stress wave forms as well as the 2nd, 3rd and 5th harmonics for each data were saved for analysis. Time sweeps were carried out on the non compatibilized blends using ten different strain amplitudes ranging from 1 to 1000 % (covering both SAOS and LAOS) and with $\omega = 0.1 rad/s$. The temperature for all the measurements was 200 °C.

D.3 Results

D.3.1 Strain sweeps

Figures D.1–D.5 show the strain sweeps for the three polymers and their blends, respectively. Similar behavior was observed for the blends and the components: Both G' and G'' show a decrease at the onset of the non linear region. This onset is shifted towards smaller values of γ_0 as the frequency is increased. The $\tan\delta$ plots evidence that the onset of the non linear regime is also marked by a decrease in the relative elasticity of the materials.

Two differences between the components and the blends are noticeable in the strain sweep plots: One is the increased elasticity of the blends compared to the components,

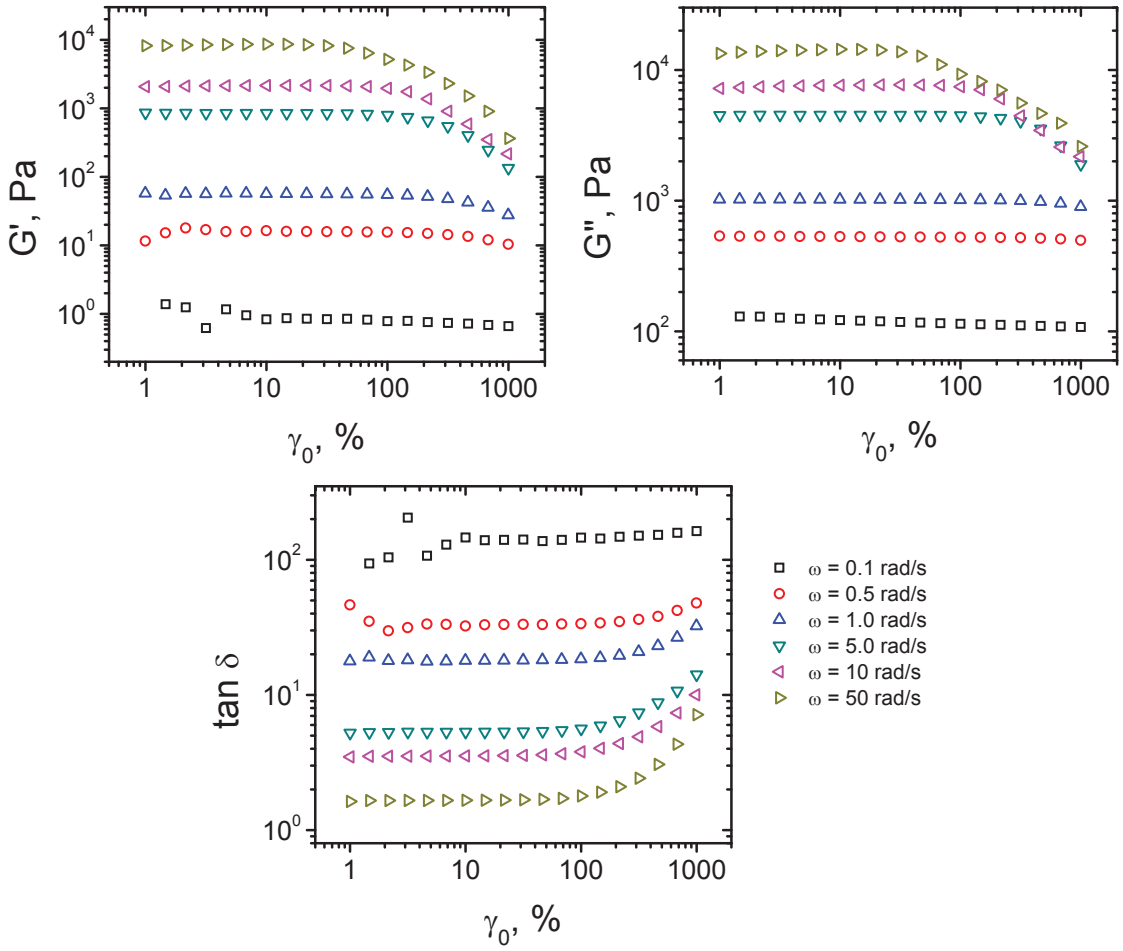

Figure D.1: Dynamic moduli and $\tan\delta$ as a function of strain amplitude for FLPS measured at different frequency values. The symbol descriptions are common for all three plots.

at low frequencies. This is not surprising since it is the same behavior observed in the frequency sweeps given in Chapter 6 (Figure 6.5). The second difference is that at $\omega \leq 0.5$ rad/sec, the non linear regime is not reached for the components in the strain range considered here. In the case of the blend, the elastic modulus start to decrease before reaching the maximum strain. This could be reflecting the non linearity, coming from the interface.

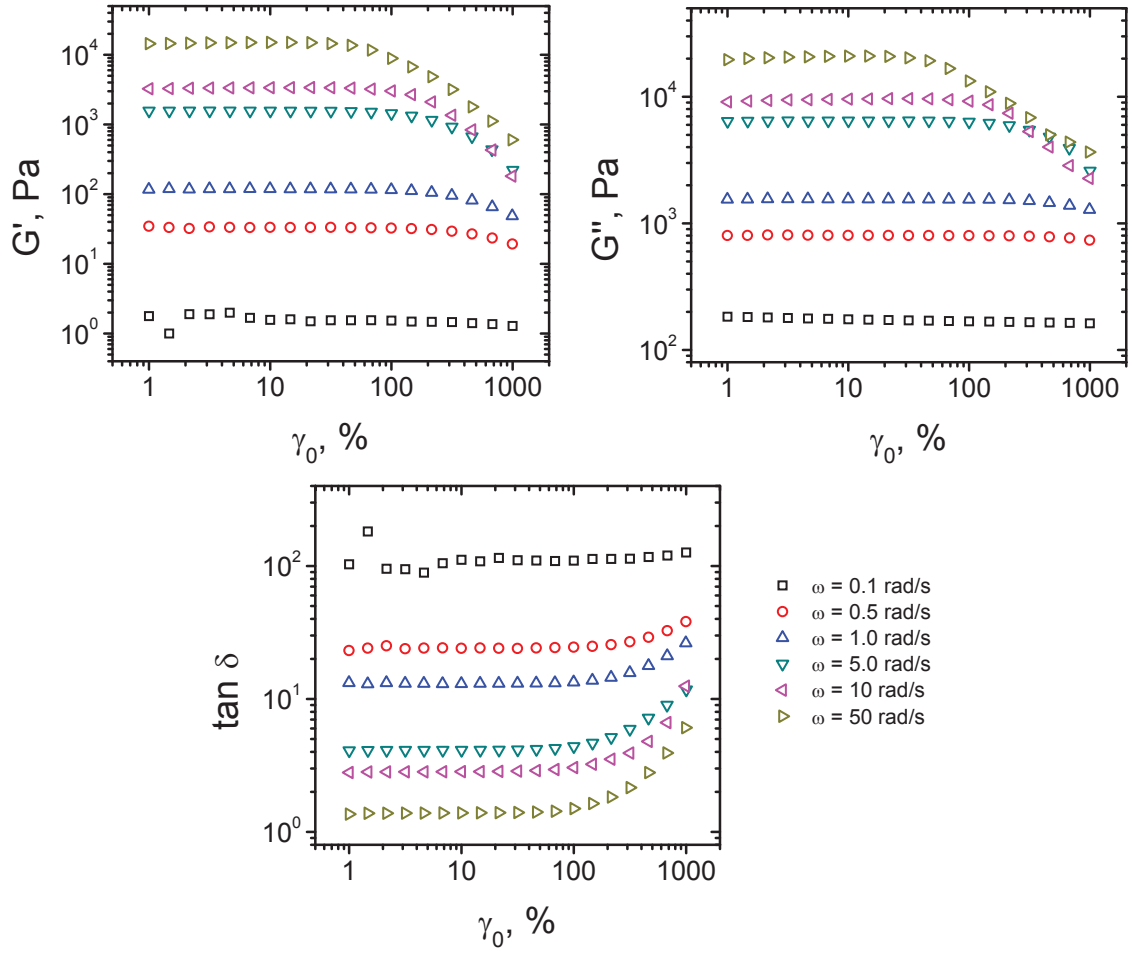

Figure D.2: Dynamic moduli and $\tan\delta$ as a function of strain amplitude for SAN10 measured at different frequency values. The symbol descriptions are common for all three plots.

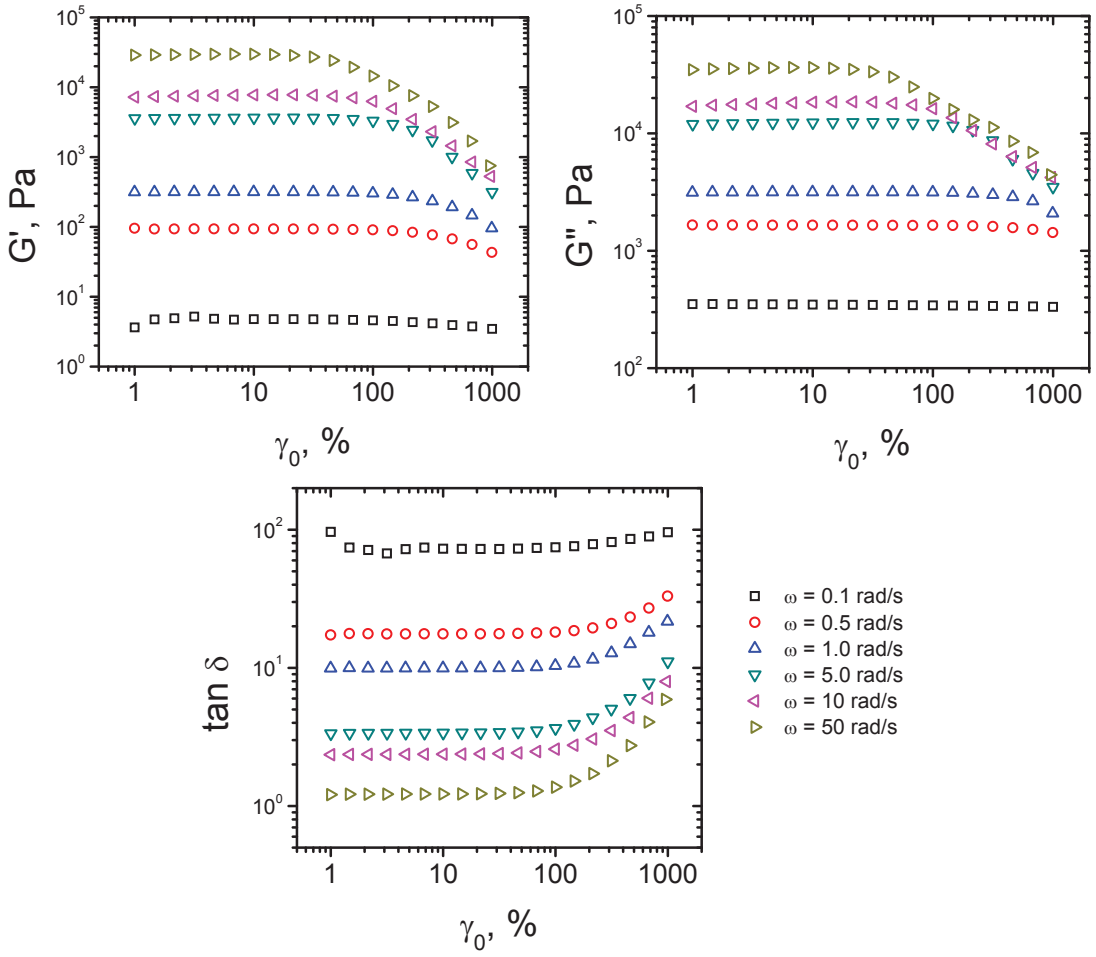

Figure D.3: Dynamic moduli and $\tan\delta$ as a function of strain amplitude for SAN20 measured at different frequency values. The symbol descriptions are common for all three plots.

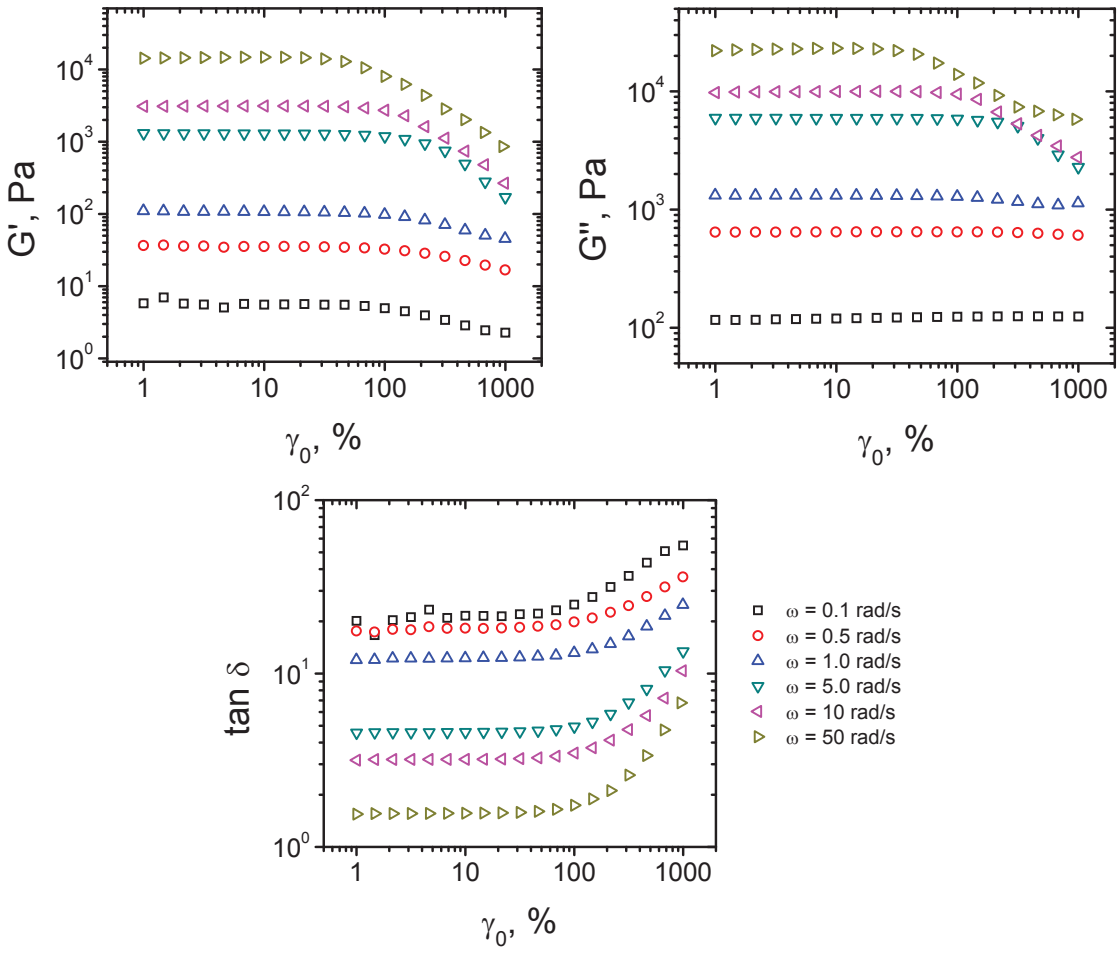

Figure D.4: Dynamic moduli and $\tan\delta$ as a function of strain amplitude for FLPS/SAN10 w/1% BC measured at different frequency values. The symbol descriptions are common for all three plots.

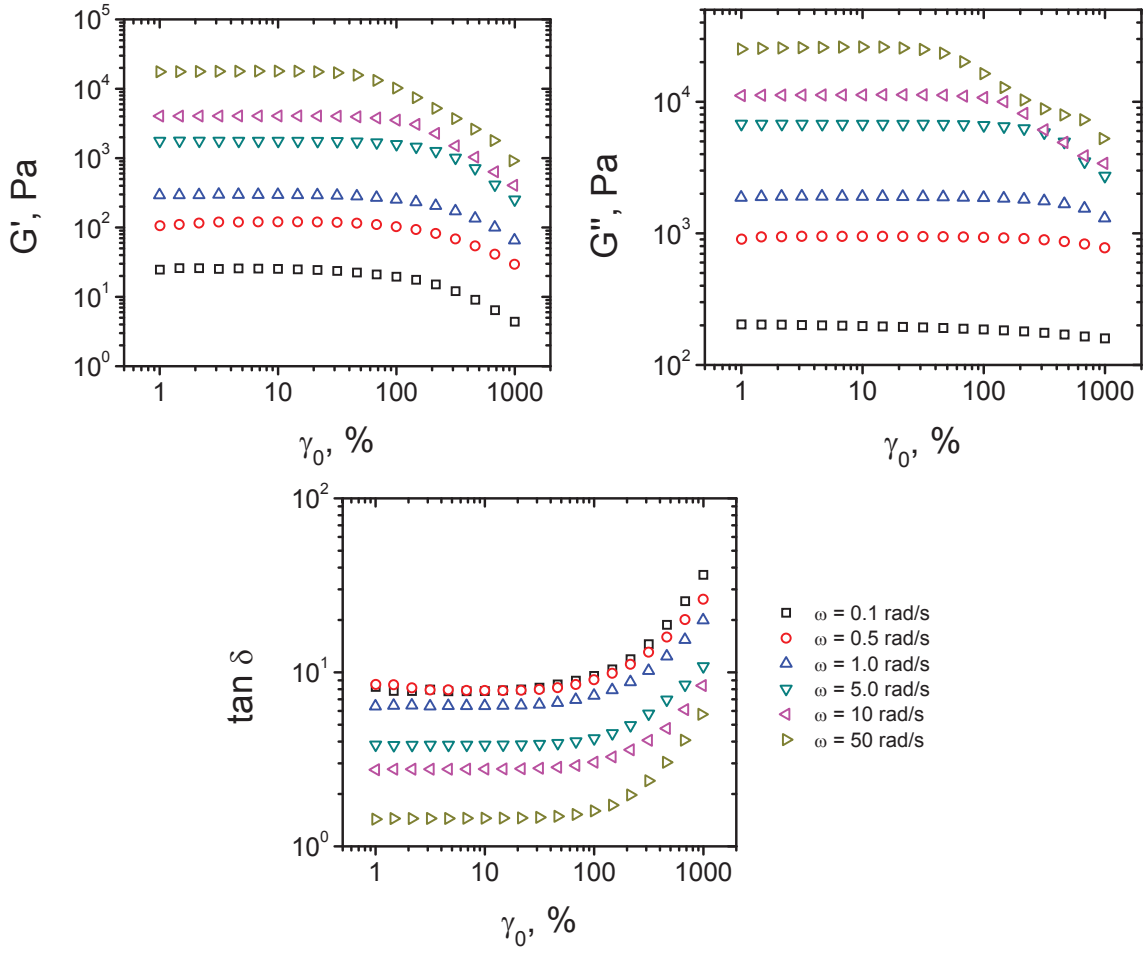

Figure D.5: Dynamic moduli and $\tan\delta$ as a function of strain amplitude for FLPS/SAN20 w/1% BC measured at different frequency values. The symbol descriptions are common for all three plots.

Figure D.6 shows the strain ans stress wave forms normalized with the corresponding amplitudes. As indicated in the inset, the wave form in Figure D.6a correspond to a data point in the linear regime ($\gamma_0 = 10\%$ and $\omega = 0.5$ rad/s), whereas Figure D.6b correspond to a point in the non-linear region ($\gamma_0 = 1000\%$ and $\omega = 50$ rad/s). The stress waveform in the linear regime has the sinusoidal shape typical for SAOS measurements. By contrast, the stress waveform in Figure D.6b cannot be described with a single trigonometric function, as expected for LAOS measurements [202].

The periodic rate strain, $\dot{\gamma}(t)$, was computed by numerical derivation of the data from the strain wave forms. Figure D.7 shows the periodic stress response, $\sigma(t; \gamma_0, \omega)$ parametrically plotted against $\gamma(t)$ and $\dot{\gamma}(t)$. The projections of the curves on the $\sigma - \gamma$ and $\sigma - \dot{\gamma}$ planes give the elastic and viscous Lissajous–Bowditch (LB) curves [206]. These curves are commonly used to represent raw data from LAOS measurements. In general, perfect elliptic shapes of these curves indicate a linear viscoelastic response, while distortion of the ellipse represents deviations from the linear behavior.

The plot in Figure D.7a shows data for the FLPS measured with γ_0=10 % and ω = 0.5 rad/sec. Notice that both LB curves display perfect elliptical shapes, which indicates linear response. Figures D.7b, D.7c and D.7d show data for the FLPS, FLPS/SAN10 and FLPS/SAN20 blends, respectively, measured with γ_0=1000 % and $\omega = 50$ rad/sec. The distorted shapes indicate non-linearities generated in all three materials.

To have a clearer view of the onset of the nonlinearities, both the viscous and the elastic LB curves are displayed in a Pipking diagram [214], with coordinates ω and γ_0 as suggested by Ewoldt et al. [206]. Figures D.8 – D.10 show such diagrams for FLPS and the blends FLPS/SAN10 and FLPS/SAN20, respectively. LB curves in the low-ω low-γ_0 zone of the diagram show the expected perfect elliptical shapes corresponding to the linear regime, while in the non linear regime, i.e. in the high-ω high-γ_0 zone, LB curves become distorted. From these plots, it is not possible to identify the onset of non linear regime without further analysis.

It is noteworthy that all the LB curves in the Figures D.8 and D.9 are very similar, which may indicate that the non linearities of low interfacial blend (FLPS/SAN10) came entirely from the component, i.e. the interface does not contribute. On the other hand, the FLPS/SAN20 LB curves at $\gamma_0 = 1000\%$ (shown in Figure D.10) display loops whose origin is not clear, but seem to represent an effect of the interface, since they are not

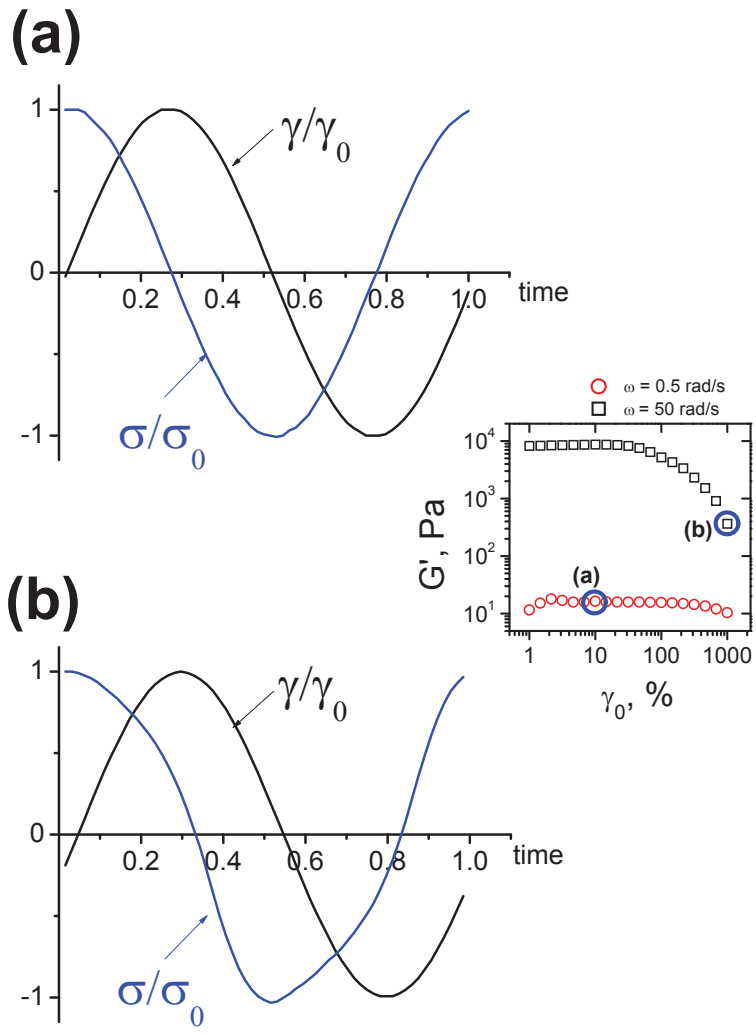

Figure D.6: Waveforms of transient strain and stress raw data during oscillatory measurements of FLPS as given by the rheometer ARES G2 (TA Instruments). Measurements were carried out at (a) $\gamma_0 = 10\%$ and $\omega = 0.5$ rad/s and (b) $\gamma_0 = 1000\%$ and $\omega = 50$ rad/s. The inset shows the frequency sweeps at frequencies 0.5 and 50 rad/s with the data point corresponding to the wave forms marked by the (blue) circles.

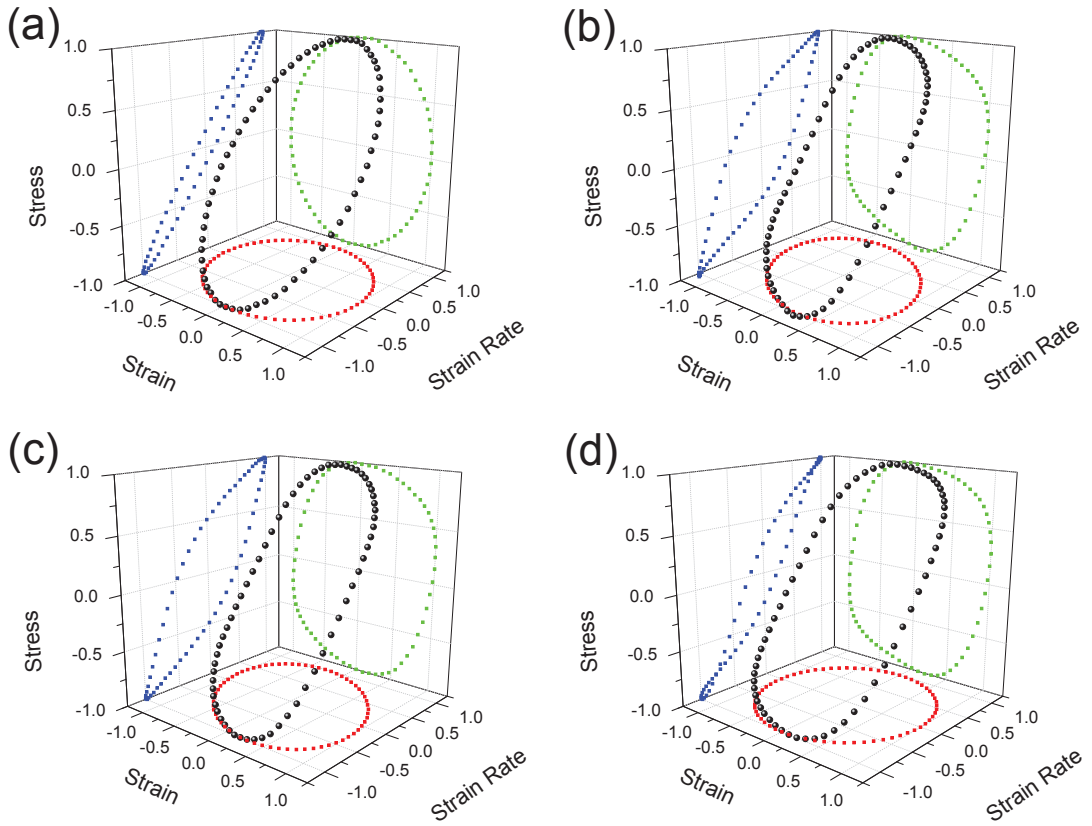

Figure D.7: Parametric plots of periodic stress as a function of strain and strain rate constructed from the raw data obtained from the rheometer ARES G2. (a) and (b) show data of FLPS measured at ($\gamma_0 = 10\%$, $\omega = 0.5$rad/s) and ($\gamma_0 = 1000\%$, $\omega = 50$ rad/s), respectively. (c) and (d)show data measured at ($\gamma_0 = 1000\%$, $\omega = 50$ rad/s) for FLPS/SAN10 and FLPS/SAN20, respectively.

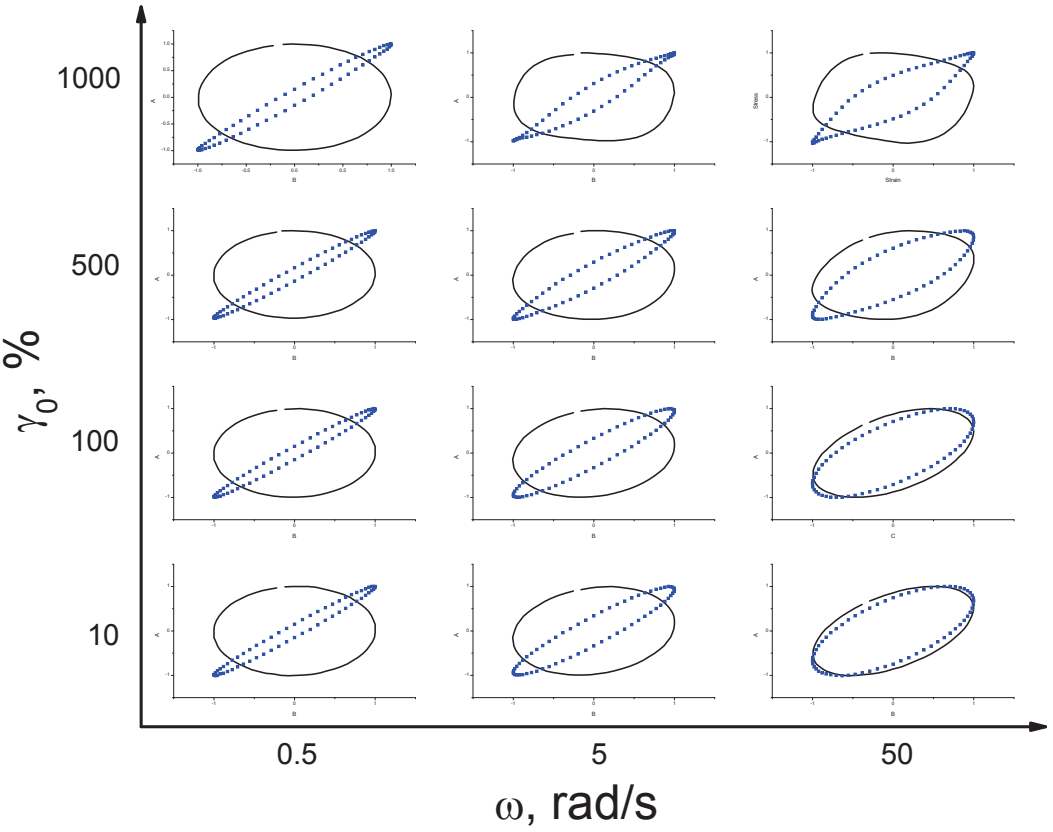

Figure D.8: Elastic (solid lines) and viscous (dotted lines) Lissajous-Bowditch curves for FLPS measured at different values of frequency and strain amplitude.

observed in the curves corresponding to the components. Further research is required to verify this hypothesis.

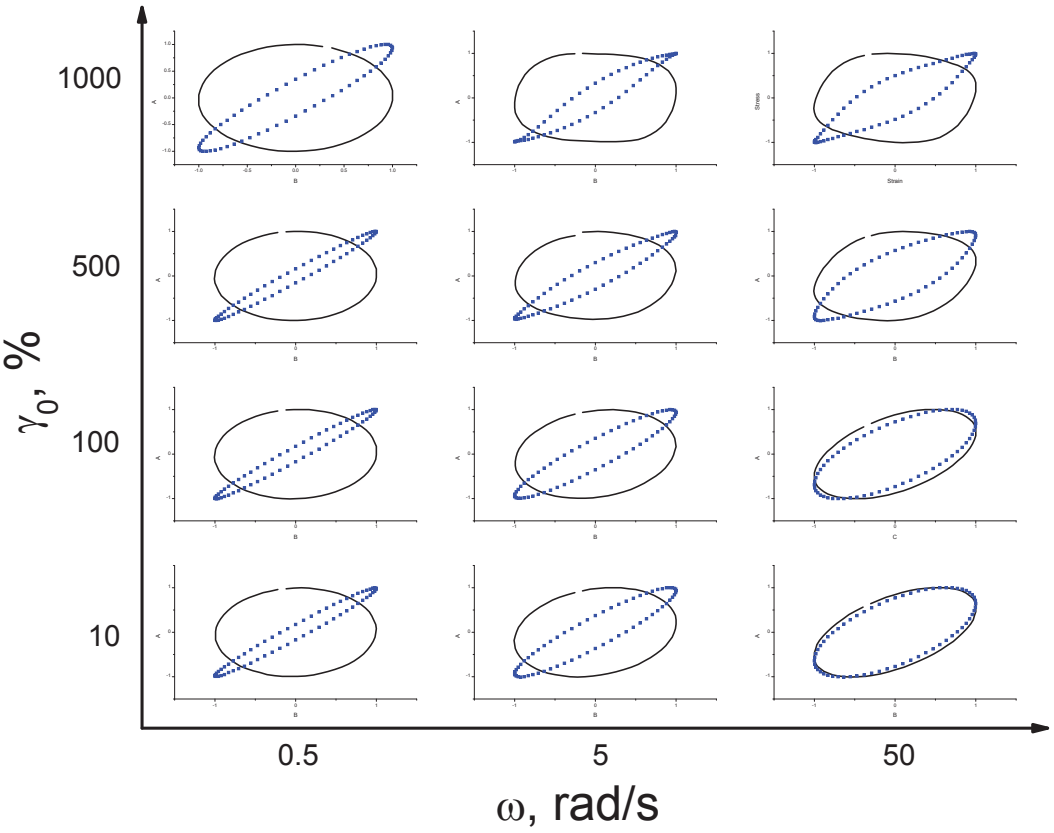

Figure D.9: Elastic (solid lines) and viscous (dotted lines) Lissajous-Bowditch curves for 50/50 FLPS/SAN10 blend with 1% BC measured at different values of frequency and strain amplitude.

Figure D.11 shows the ratios of the intensity 2nd and 5th harmonics with the fundamental one for the compatibilized FLPS/SAN10 blend, I_2/I_1 and I_5/I_1. In the literature, even harmonics are associated to wall slip phenomena [215, 216] or to defects in the experiments [217]. We can assume that these defects are not present in our experiments, since the values of I_2/I_1 are very small. The I_5/I_1 values are also small, however, they seem to grow with γ_0. No apparent correlation with ω was observed. Note that the data measured at $\gamma_0 \lesssim 100\%$ represent only noise since in that region no non-linearities

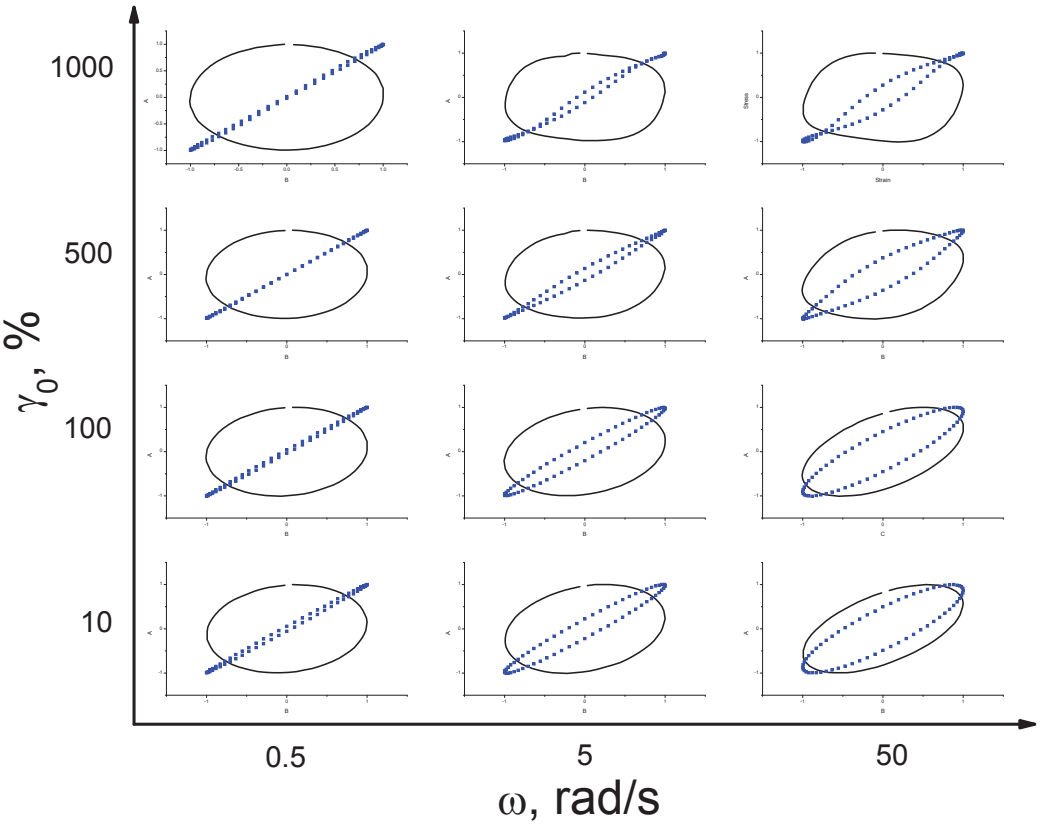

Figure D.10: Elastic (solid lines) and viscous (dotted lines) Lissajous-Bowditch curves for 50/50 FLPS/SAN20 blend with 1% BC measured at different values of frequency and strain amplitude.

are expected. The same applies for I_3/I_1 data (Figure D.12).

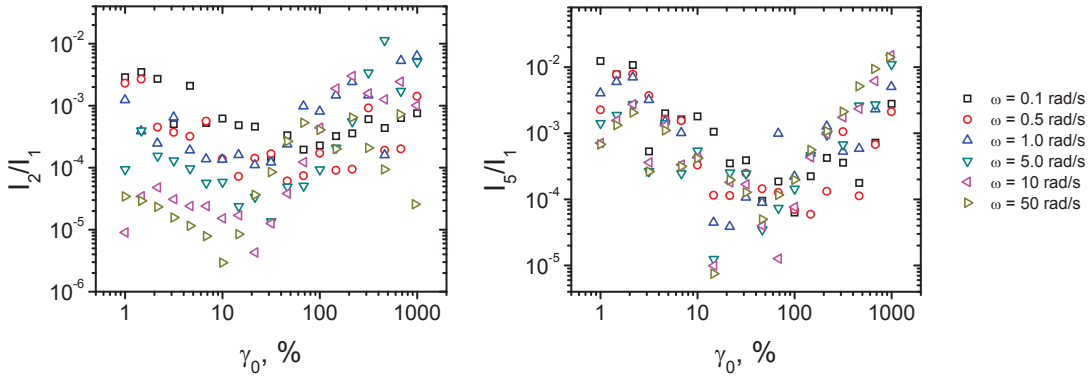

Figure D.11: Relative intensity of 2nd and 5th harmonics as a function of amplitude and frequency during oscillatory measurements of 50/50 FLPS/SAN10 blend with 1% BC.

The high harmonic with higher intensity is the 3rd one [202], which is evident in the plots of I_3/I_1 versus γ_0 (shown in Figure D.12). Notice that the value of I_3/I_1at high frequencies have very similar values for the components and the blends, but at low frequencies, the blends show higher values, most notably in the high interfacial tension blend (FLPS/SAN20). Similar to the LB curves, this may indicate a contribution of the interface to the non linear response of the blends.

D.3.2 Time sweeps

Figure D.13 shows the extra contribution to the elastic modulus due to the blend interface of the PS/SAN20 (without) blend as a function of annealing time. The time sweeps were performed using ten different strain amplitudes, ranging from 1 to 1000 %. Measurements performed at $\gamma_0 < 50\%$ were insensitive to the strain amplitude. This was not surprising because that strain range corresponds to the linear viscoelastic regime, as shown in Figure D.5. Using strains bigger than 50% produced a more marked decrease of G'_{int}, reaching negligible values at very high values of γ_0. This can be due to the distortion of the micostructure as shown in Figure D.14.

Figure D.14a show the heterogeneous morphology generated after a single strain

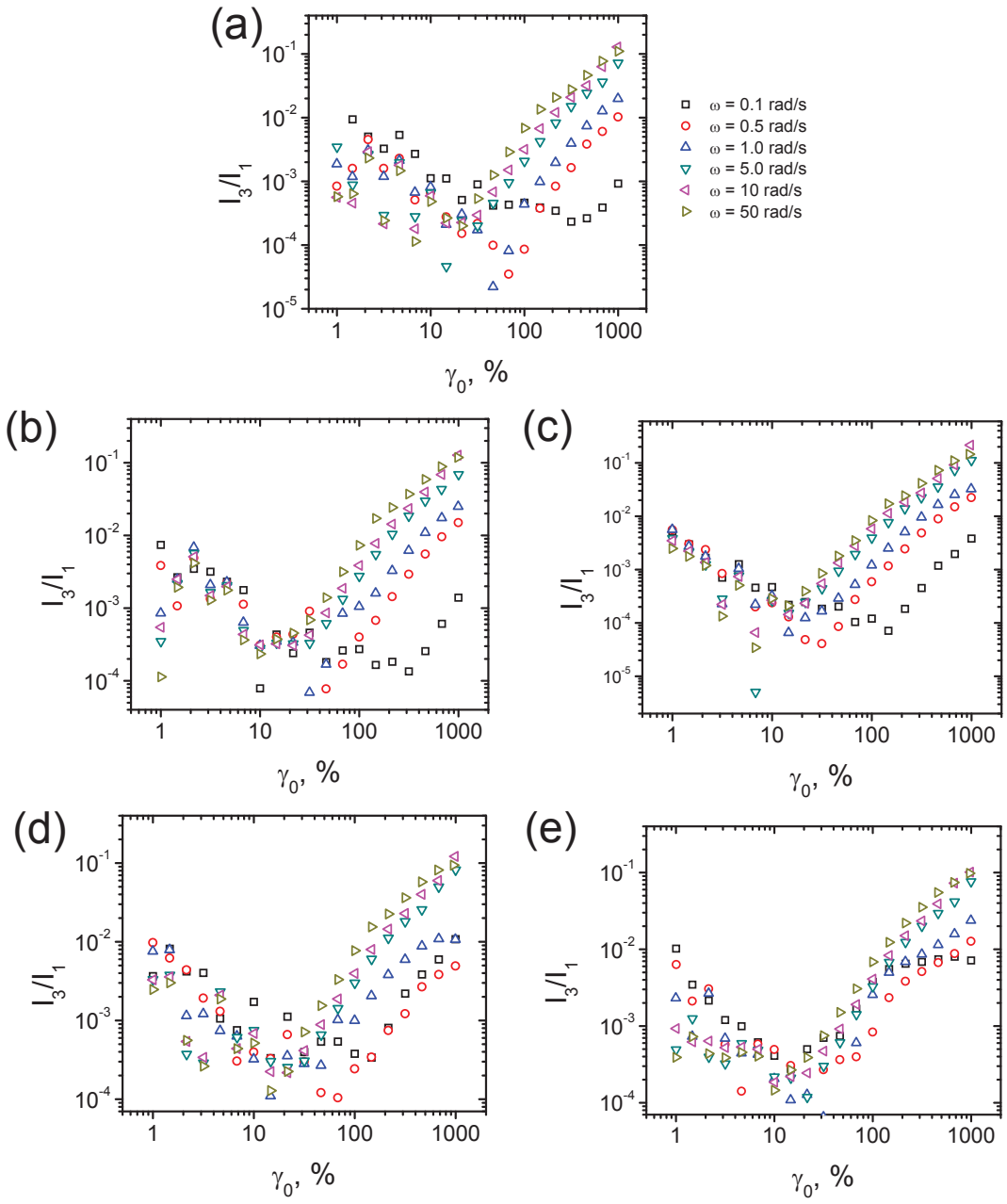

Figure D.12: Relative intensity of the 3rd harmonic as a function of strain amplitude and frequency during oscillatory measurements for (a) FLPS, (b) SAN10, (c) SAN 20, (d) 50/50 FLPS/SAN10 blend with 1% BC and (e) 50/50 FLPS/SAN20 blend with 1% BC.

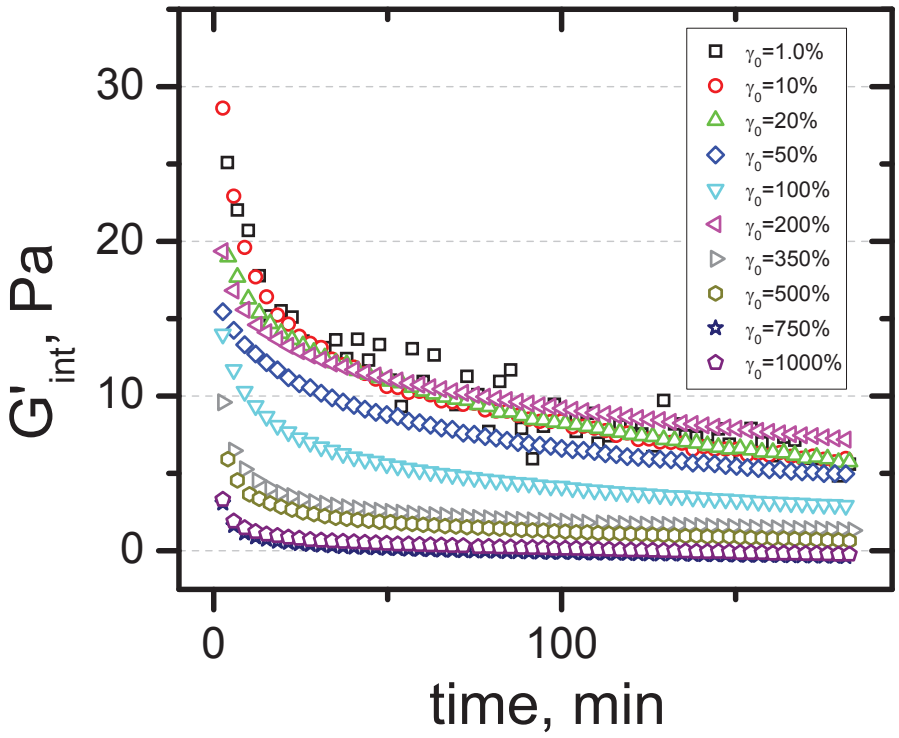

Figure D.13: Interface contribution to the elastic modulus of PS/SAN20 blend as a function of time and strain amplitude. Measurements were carried out at 200 °C and $\omega = 0.1$ rad/s.

step with $\gamma = 100\%$. This catastrophic response to large external deformation has been observed in many structured materials, such as soft gels and glasses [218], liquid crystals [219], foams [220], suspensions [221] and micelar solutions [222, 223]. These heterogeneities are commonly manifested as shear banding, which is what we observed in Figure D.14a. The distortion is even more catastrophic for higher strains, as shown in Figure D.14b. Whether these heterogeneities produces the marked decrease in the elastic modulus is not certain and requires further work to be confirmed.

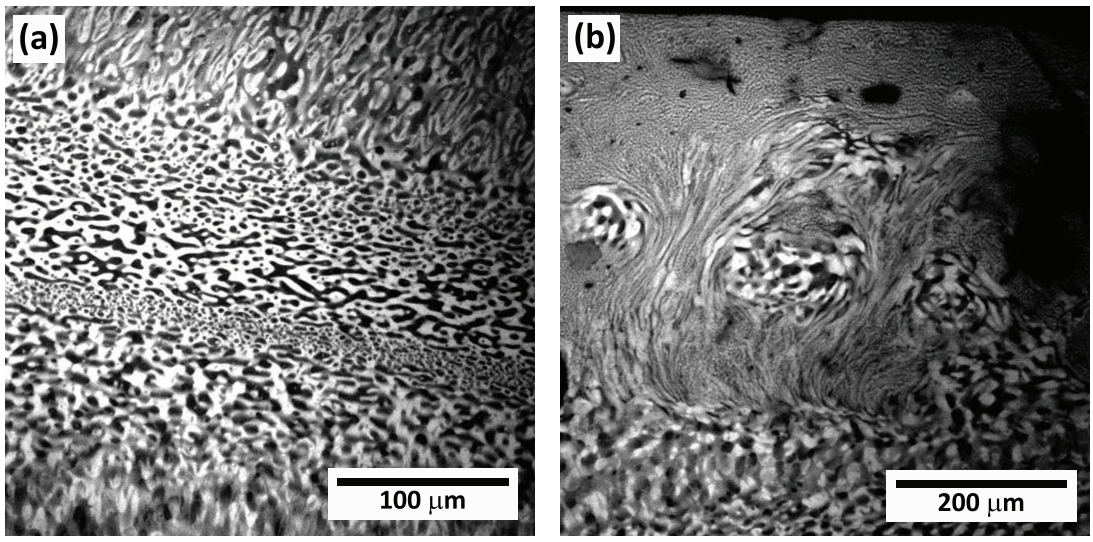

Figure D.14: Confocal micrograph of FLPS/SAN20 blend after annealing for 10 min at 200 ° and a single strain step with (a) $\gamma = 100$ % and (b) $\gamma = 500$ %.

Figure D.15 shows the evolution of the the relative intensity of the third harmonic during the time sweeps at different strain amplitudes. The measurements performed with $\gamma_0 = 10\%$ generates negligible values of I_3/I_1, which is the expected behavior since that strain lies in the linear regime. A gradual increase of the third harmonic is observed during the first 70 minutes of the time sweep performed at $\gamma_0 = 100$ % after which time, it reaches a plateau. This could reflect the distortion of the microstructure (driven by the large deformations) which increases during the tests until it reaches a steady state. Similar behavior was observed in the tests at higher strain amplitudes, but with an initial higher value of I_3/I_1, which signifies that the distortion develops faster as the

deformation is larger.

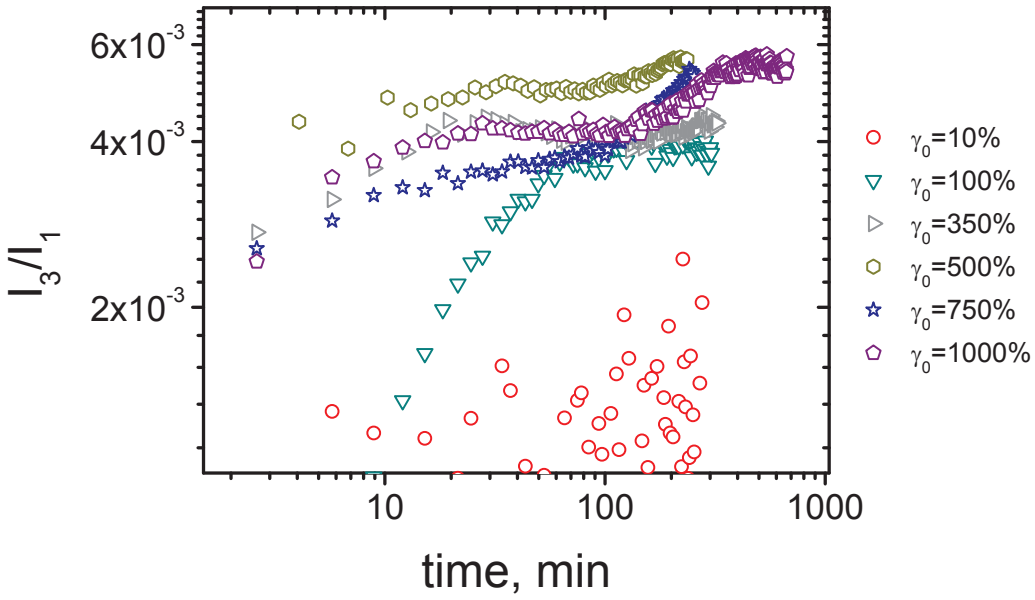

Figure D.15: Relative intensity of 3rd harmonic, for PS/SAN20 blend, as a function of time and strain amplitude. Oscillatory measurements were performed at 200 °C and $\omega = 0.1$ rad/s.

D.4 Conclusions

Dynamic strain and time sweeps were performed in cocontinuous blends and their components using a range of strain amplitudes covering linear and non linear viscoelastic regimes. Comparing LAOS response of the components with that of the the blends suggest that the microstructure has a contribution to the non linearities of the blends. The evolution of the morphology during coarsenings was also signaled by an increase in the third harmonic. More work, both experimental and theoretical, is needed to interpret the results presented here and understand the relation between LAOS measurements and morphology.